University of Glasgow

Investigating the innate immune barriers that constrain the transmission of coronaviruses

Emma Louise Davies BA.

Submitted in fulfilment of the requirements for the degree of Doctor of Philosophy in Virology

March 2025

MRC-University of Glasgow Centre for Virus Research
School of Infection and Immunity
College of Medical, Veterinary and Life Sciences
University of Glasgow

Abstract

Since the turn of the century, the emergence of three highly pathogenic coronaviruses highlights the importance of understanding coronavirus-host interactions. If sufficient cellular factors are available for a virus to complete its life cycle, genome-encoded post-entry blocks to replication may determine whether virus replication is successful. One such barrier is the interferon response, a signalling pathway upregulating hundreds of interferon-stimulated genes (ISGs), many of which encode proteins with specific and potent antiviral activity. The presence and timing of a functional interferon response is important in controlling coronavirus infection. Thus, identifying ISGs with antiviral activity can provide insights into genetic risk factors associated with coronavirus disease severity and the barriers to coronavirus zoonosis. To identify ISGs that inhibit unmodified coronaviruses, I optimised an arrayed ISG expression screening protocol that utilises immunostaining of the dsRNA replication intermediate and quantification of virus infection by plate-based image cytometry. I screened the endemic coronavirus HCoV-OC43 against multiple ISG libraries encoded into lentiviral vectors, including three published species libraries (human, macaque, bovine) and two newly generated libraries (mouse, bat). This revealed ISGs with known and novel antiviral activity against coronaviruses, including 2'-5'-oligoadenylate synthetase 2 (OAS2). OAS proteins classically activate RNase L via the synthesis of 2'-5'-oligoadenylates, resulting in the degradation of cellular and viral RNA. Alternative splicing generates two OAS2 isoforms, p69 and p71, exhibiting differential antiviral activity. I show that the p69 isoform restricts HCoV-OC43, while the p71 isoform restricts the unrelated picornavirus Cardiovirus A (EMCV) via different mechanisms. The OAS gene family thus enhances antiviral breadth in the host genome by both gene duplication and alternative splicing. This research has provided insights into how coronaviruses interact with the innate immune system.

Table of Contents

List of Tables

List of Figures

Publications

Davies EL, Sowar H, Balci A, … Fletcher AJ. Alternative splicing broadens antiviral diversity at the human OAS2 locus. bioRxiv. 2025 Feb 25 639105. doi:10.1101/2025.02.24.639105

Wickenhagen A, Sugrue E, Lytras S, …**Davies EL**, …Wilson SJ. A prenylated dsRNA sensor protects against severe COVID-19. Science. 2021 Oct 29;374(6567): eabj3624. doi: 10.1126/science.abj3624

Acknowledgements

Starting my PhD during the COVID-19 pandemic and completing it after an unexpected change in my lab group, this journey has truly been a rollercoaster! Throughout the highs and lows, I want to acknowledge the people who have supported me with their kindness, companionship, and guidance.

Thank you to Professor Sam J Wilson for allowing me to join his lab and for his advice and support for the first three years of my PhD. I am very grateful to Dr Adam Fletcher, who adopted me into his lab for my final year. My creativity and independence really developed under his supervision. Thank you to Professor Massimo Palmarini for agreeing to be my secondary supervisor and for his advice on developing my research. I am grateful to my assessors, Dr Chris Boutell and Dr Clare Harding, for checking in with me and their guidance on my PhD and career.

I have been fortunate to belong to two lab groups filled with great people. Special shout out to Main Man Matt (aka Dr Matthew Turnbull) – without your training, wisdom and dad jokes, I would not have gotten through this PhD. Without Dr Arthur Wickenhagen's kindness and knowledge of ISG libraries, I would have been lost. D-Money (aka Douglas Stewart), I only got through making the mouse ISG library with your help and humour. Thank you to all other members of the Wilson/Rihn group – Dr Suzannah Rihn, Dr Spyros Lytras, Dr Innes Jarmson, Dr Elena Sugrue, Dr Simon Swingler, Hollie Jackson Ireland, Ulad Litvin and Yongtao He. Thank you to the Fletcher group – Dr Arda Balci, Hanna Sowar and Eilidh Rivers – for welcoming me into their group. You guys were a pleasure to chat and work with.

I am grateful for the guidance and assistance from everyone in the CVR, from the washroom staff to the cleaning and admin teams. In particular, I would like to thank Dr Colin Loney, Dr Meredith Stewart, Dr Khalid Zakaria, Dr Rute Pinto, Dr Ed Hutchinson, Sarah Cole, Dr Marko Noerenberg, Dr Vanessa Cowton, Donna

Macpherson, Fiona Graham. Thank you for the support and camaraderie of the CVR PhD community, especially the Hutchinson group.

Thank you to the Wellcome Trust IIB management team, especially Dr Megan MacLeod, Dr Gill Douce and Jacqueline Meiklejohn. I would not have had the support I had during my lab transition if I had been part of another PhD programme.

In the third year of my PhD, my health deteriorated, and I had to suspend my studies. Thank you to the NHS staff who diagnosed my condition and helped me become healthy enough to resume my research. At this time and throughout my PhD, I truly appreciated my incredible friends - Sofia, Vicky, Charlotte, Rhi, Delia, Jake, Amelia and Caija. These friends travelled across countries and continents to check on me, kept me supplied with snacks and were always there with a hug and listening ear when I needed it. I am so grateful for your support and friendship, past and present. My lunchtime walks with Colin and Rhi really helped me settle back into the CVR. Thank you to my yoga and birding communities – you are all so welcoming and kept me sane during my final year and thesis writing.

Finally, thank you to my amazing family. My parents have been constantly supportive throughout this PhD and my health struggles. They were always on the phone for the good news and bad times, and I could not have done it without them. I have not managed to list all the people I am grateful for during the last few years, but this journey would not have succeeded without you. Thank you!

Author's Declaration

March 2025

I confirm that this thesis presented for the degree of Doctor of Philosophy in Virology has

i) been composed entirely by myself

ii) been solely the result of my own work unless clearly indicated

iii) not been submitted for any other degree or professional qualification

Emma L. Davies

General abbreviations

2-5A	2’-5’-linked oligoadenylates
AAT	A549-ACE2-TMPRSS2
ACTB	Actin beta
ATP	Adenosine triphosphate
bp	Base pairs
C-terminal	Carboxy-terminal
cDNA	Complementary DNA
CFK	Proposed oligomerisation motif in OAS proteins
cLSM	Confocal laser scanning microscopy
COVID-19	Coronavirus disease 19
CRISPR	Clustered regularly interspaced short palindromic repeats
DI	Domain I of an OAS protein
DII	Domain II of an OAS protein
DMSO	Dimethyl sulfoxide
DMV	Double membrane vesicle
DNA	Deoxyribonucleic acid
dNTP	Deoxyribonucleotide triphosphate
dsRNA	Double-stranded RNA
ER	Endoplasmic reticulum
GAPDH	Glyceraldehyde 3-phosphate dehydrogenase
GFP	Green fluorescent protein
gRNA	Guide RNA
IFN	Interferon
IRF	Interferon regulatory factor
ISG	Interferon-stimulated gene
ISRE	Interferon-stimulated response element
MIS-C	Multisystem inflammatory syndrome in children
MOI	Multiplicity of infection
mRNA	Messenger RNA
N-terminal	Amino-terminal
nsp	Non-structural protein
OAS	2'-5'-oligoadenylate synthetase
ORF	Open reading frame
PAMP	Pathogen associated molecular pattern
PCR	Polymerase chain reaction
PDE	Phosphodiesterase
PFU	Plaque forming units

Poly(I:C)	Polyinosinic:polycytidylic acid
PRR	Pattern recognition receptor
RdRp	RNA-dependent RNA polymerase
RFP	Red fluorescent protein
RIP-seq	RNA immunoprecipitation sequencing
RNA	Ribonucleic acid
rRNA	Ribosomal RNA
RT-qPCR	Reverse transcription- quantitative PCR
RTC	Replication-transcription complex
RUX	Ruxolitinib
sgmRNA	Sub-genomic mRNA
siRNA	Small interfering RNA
SNP	Single nucleotide polymorphism
ssRNA	Single-stranded RNA
UTR	Untranslated region
WT	Wildtype

Virus abbreviations

AdV	Adenovirus
BCoV	Bovine coronavirus
BoHV	Bovine herpesvirus
BTV	Bluetongue virus
BUNV	Bunyamwera orthobunyavirus
CHIKV	Chikungunya virus
CHPV	Chandipura virus
CVB	Coxsackie B virus
DENV	Dengue virus
EAV	Equine arterivirus
EBOV	Ebola virus
EMCV	Cardiovirus A
HCMV	Human cytomegalovirus
HCoV-229E	Human coronavirus 229E
HCoV-HKU1	Human coronavirus HKU1
HCoV-NL63	Human coronavirus NL63
HCoV-OC43	Human coronavirus OC43
HCV	Hepatitis C virus
HIV-1	Human immunodeficiency virus type 1
HMPV	Human metapneumovirus
HSV-1	Herpes simplex virus 1
IAV	Influenza A virus
JEV	Japanese encephalitis virus
MERS-CoV	Middle East respiratory syndrome coronavirus
MeV	Measles virus
MHV	Mouse hepatitis virus
NDV	Newcastle disease virus
ONNV	O'nyong'nyong virus
PIV3	Human parainfluenza virus type 3
PIV5	Human parainfluenza virus type 5

PRRSV	Betaarterivirus suid 1
PRV	Pseudorabies
PV	Poliovirus
RSV	Respiratory syncytial virus
RVFV	Rift Valley fever virus
SARS-CoV-1	Severe acute respiratory syndrome coronavirus 1
SARS-CoV-2	Severe acute respiratory syndrome coronavirus 2
SeV	Sendai virus
SFTSV	Dabie bandavirus
SFV	Semliki Forest virus
SINV-A	Sindbis virus AR86
SINV-G	Sindbis virus Girdwood
TBEV	Tick-borne encephalitis virus
USUV	Usutu virus
VEEV	Venezuelan equine encephalitis virus
VSV	Indiana vesiculovirus
WNV	West Nile virus
YFV	Yellow fever virus
ZIKV	Zika virus

1. Introduction

1.1. The innate immune response to viruses

1.1.1. The interferon response

The innate immune response is a crucial frontline defence against an invading pathogen. In 1957, Alick Isaacs and Jean Lindenmann studied the process of virus interference, where infection by one virus can inhibit infection by another. The addition of inactivated influenza virus to the highly vascularised membrane of a chick egg, the chorioallantoic membrane, resulted in the release of an agent that inhibited subsequent infection, which they named 'interferon' (IFN) (Isaacs and Lindenmann, 1987). IFNs are a group of signalling proteins that trigger an antiviral state within cells and are a key component of the innate immune response.

Since this initial discovery, IFNs have been classified into three groups (Type I, Type II and Type III) based on amino acid sequence homology and receptor usage. In humans, the type I family includes 13 subtypes of IFN-α and single subtypes of IFN-β, IFN-ε, IFN-κ and IFN-ω (Lazear et al., 2019). The type III family consists of four subtypes (-λ1, -λ2, -λ3 and -λ4) (Wack et al., 2015). The type II family consists of only IFN-ɣ, mainly produced by natural killer cells and T lymphocytes. IFN-ɣ plays an important role in the innate and adaptive immune response against pathogens but also has pro-inflammatory and immunomodulatory functions and will not be discussed further (Alspach et al., 2019).

Type I and type III IFNs are induced by viral infection, via similar signalling pathways and activate similar gene expression programmes, but have notable biological differences. The receptor for type III IFNs is mainly restricted to epithelial cells. Thus, this IFN type is protective in barrier tissues, such as the respiratory and gastrointestinal tract (Wack et al., 2015). The type I IFN receptor is widely expressed, as it is presented on nucleated cells. It is thought that IFN-λ, as well as IFN-β, are produced by virus-infected cells, with the localised type III-

dominant response being less inflammatory. When this is not enough to confine the infection, the production of large amounts of IFN-α by immune cells prompts a systemic IFN response (Lazear et al., 2019).

1.1.2. Induction of interferon

IFN production generally relies on pattern recognition receptors (PRRs), which recognise specific pathogen molecules known as pathogen-associated molecular patterns (PAMPs). Pathogen detection activates signalling cascades, resulting in the production of cytokines, such as interferon (IFN). Regarding viral infection, the most common PAMP is foreign nucleic acid, such as double-stranded RNA (dsRNA). Most viruses produce dsRNA during their replication cycle, due to their genome structure, as a replication intermediate, or (by)products of transcription (Chen and Hur, 2022).

Interferon production results from the recognition of nucleic acid structures uncommon in the host or in abnormal locations, mainly via three types of PRRs that differ in localisation and ligand specificity (Fig 1-1). Endosomal toll-like receptors (TLRs) can recognise dsRNA (TLR3) or single-stranded RNA (ssRNA) species (TLR7 and TLR8) (Kawai et al., 2024). Cyclic GMP-AMP synthase (cGAS) is located in the cytoplasm and recognises dsDNA in this abnormal location. Also in the cytoplasm, retinoic acid-inducible gene (RIG)-I-like receptors (RLRs) are most relevant for the positive-sense ssRNA viruses discussed in this project and include RIG-I (DDX58) and melanoma differentiation-associated gene 5 (MDA5) (Goubau et al., 2013); the RNA structures recognised by RLRs differ, with RIG-I mainly recognising base-paired RNA that has a 5'-triphosphate group (5'ppp) while MDA5 recognises long dsRNA molecules.

Upon receptor binding, downstream signalling occurs via adaptor proteins; in the case of RLRs, this adaptor protein is mitochondrial antiviral signalling protein (MAVS), which is predominantly found on the outer membrane of mitochondria. MAVS activates cellular kinases such as TANK-binding kinase 1 (TBK1), resulting in the phosphorylation of interferon regulatory factor (IRF)3

and/or IRF7. MAVS can also activate the NF-κB pathway, which involves dissociation and degradation of IκB so that NF-κB is released. Similarly, TLRs activate these signalling cascades using the adaptor proteins MyD88 or TRIF. The IRF or NF-κB transcription factors can then migrate to the nucleus to bind to IFN gene promoters (Dalskov et al., 2023).

IRF3 is constitutively expressed, while IRF7 is expressed in plasmacytoid dendritic cells (the primary producers of IFNα) and induced in other cells in response to IFN stimulation by positive feedback. It is suggested that IRF3, along with NF-κB, are the predominant transcription factors for IFN-λ1 and IFN-ß expression. In contrast, the IFNα promoter can bind multiple IRFs, with IRF7 being the major controller. Full activation of IFN promoters is thus complicated, as the most studied IFN-ß promoter is believed to require the cooperative binding of multiple transcription factors (ATF-2/c-Jun, IRF3, IRF7 and NF-κB) to the promoter to form what is known as the 'enhanceosome' (Dalskov et al., 2023; Panne et al., 2007; Randall and Goodbourn, 2008). Considering the pro-inflammatory nature of type I and type III interferons, this complicated regulation is likely necessary to balance control of virus infection with the pathological effects of IFN induction.

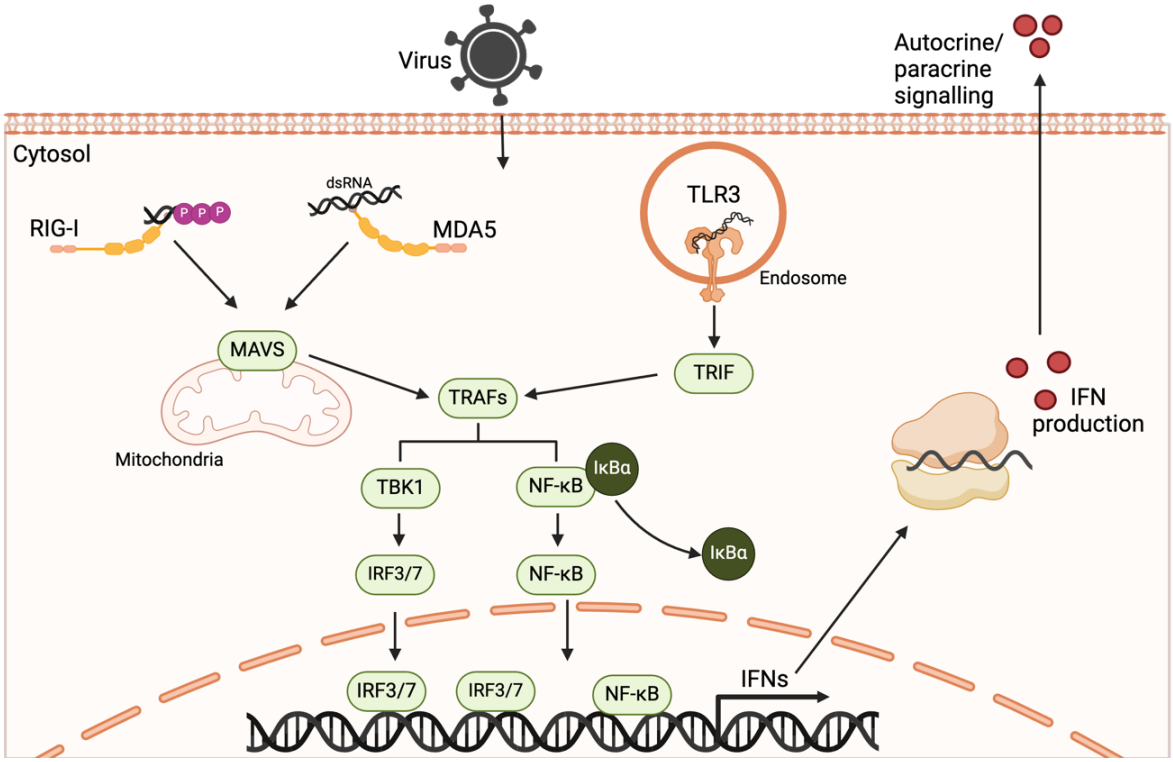

Figure 1-1: Sensing of viral nucleic acids leads to IFN production. dsRNA is sensed by PRRs, such as cytosolic RIG-I and MDA5 and the endosomal TLR3. RIG-I and MDA5 signal through the adaptor protein MAVS, which activates IRF3/7 and NF-κB signalling. These pathways are also activated by TLR3, which signals through the adaptor protein TRIF. Secreted IFN can act on the same cell or adjacent cells to induce an antiviral state.

1.1.3. Interferon signalling

After the translation of IFN proteins, these cytokines are secreted and induce their transcriptional programmes via their respective receptors. Type I IFNs signal through a heterodimeric receptor (IFNAR) consisting of IFNAR1 and IFNAR2 subunits. Type III IFNs also signal via a heterodimeric receptor (IFNLR) consisting of IFNLR1 (IL28Rα) and IL10Rβ. Despite the difference in receptors, downstream signalling can occur through a canonical pathway. The binding of the IFN ligand to the receptor activates Janus kinase 1 (JAK1) and tyrosine kinase 2 (TYK2); these receptor-associated protein tyrosine kinases phosphorylate the IFN receptor. This facilitates the recruitment of signal transducer and activator of transcription 1 (STAT1) and STAT2 proteins which are subsequently phosphorylated. IRF9 and these phosphorylated STAT proteins form the transcription complex IFN-stimulated gene factor 3 (ISGF3). After translocating

into the nucleus, ISGF3 binds IFN-stimulated response elements (ISREs), which induces an antiviral state by the upregulation of hundreds of interferon-stimulated genes (ISGs). These ISG protein products can exhibit specific and potent antiviral activity (Park and Iwasaki, 2020; Randall and Goodbourn, 2008).

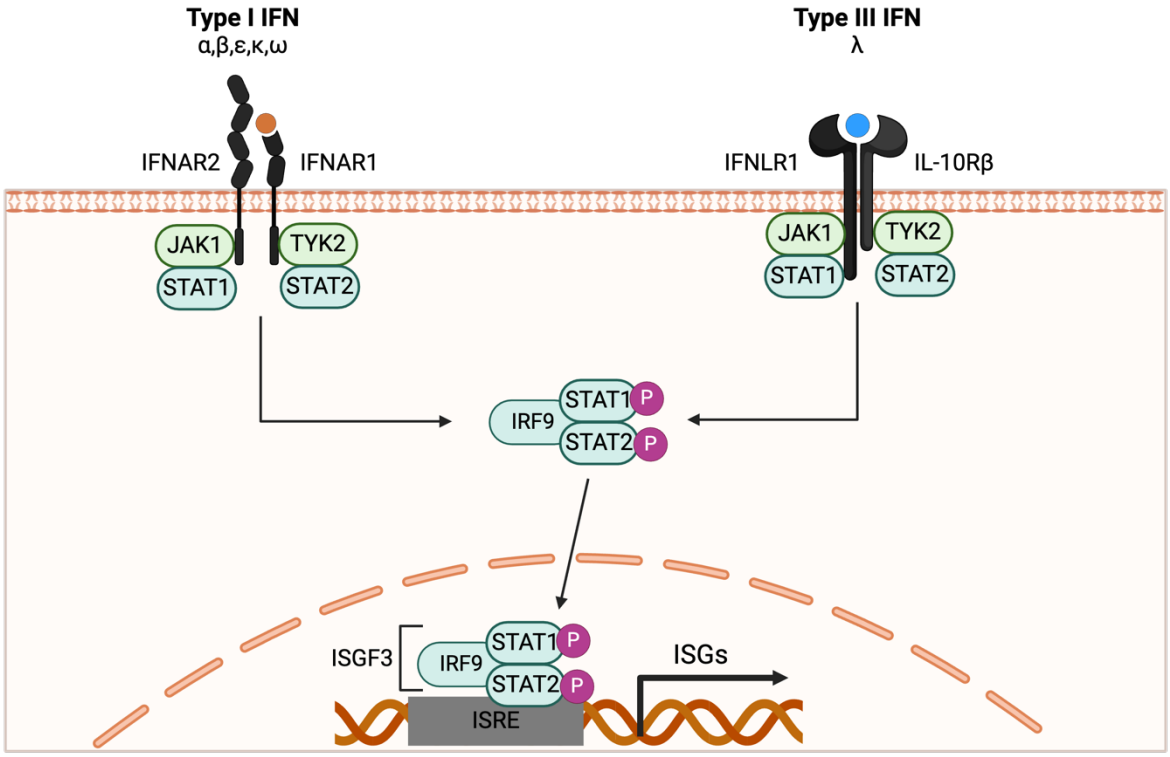

Figure 1-2: Canonical interferon signalling pathway. IFNs bind and activate their respective receptors. The tyrosine kinases JAK1 and TYK2 phosphorylate STAT1 and STAT2 proteins, leading to the formation of the ISGF3 complex. ISGF3 translocates to the nucleus, where it binds interferon-stimulated response elements (ISRE), leading to the transcription of hundreds of interferon-stimulated genes (ISGs).

1.1.4. Interferon-stimulated genes

As discussed in (Schoggins, 2019), defining an ISG is complex. The basic definition would be a gene that is induced by IFN signalling. More explicitly, an ISG is a gene whose expression is increased because of ISGF3 binding – or IFN-ɣ activated factor (GAF) in the case of type II IFNs. However, many ISGs are also direct targets of IRFs or NF-κB, so can be induced independently of IFN signalling. Some ISGs are not expressed without IFN signalling, while others have basal expression levels and are also IFN-inducible; the latter includes genes like *PLSCR1* and *DAXX* (described in section 3.1.4). To complicate terminology further, some

genes are downregulated due to the IFN response. This thesis will focus on genes that are upregulated in response to interferon. ISGs can utilise diverse mechanisms to exhibit broad or highly specific antiviral activity against DNA and RNA viruses. ISGs have evolved to target most stages of the virus replication cycle, and in some cases, an individual ISG can target a different cycle stage depending on the virus. In the following sections, I will provide examples of ISGs (Fig 1-3), particularly those targeting RNA viruses and their mode of inhibition.

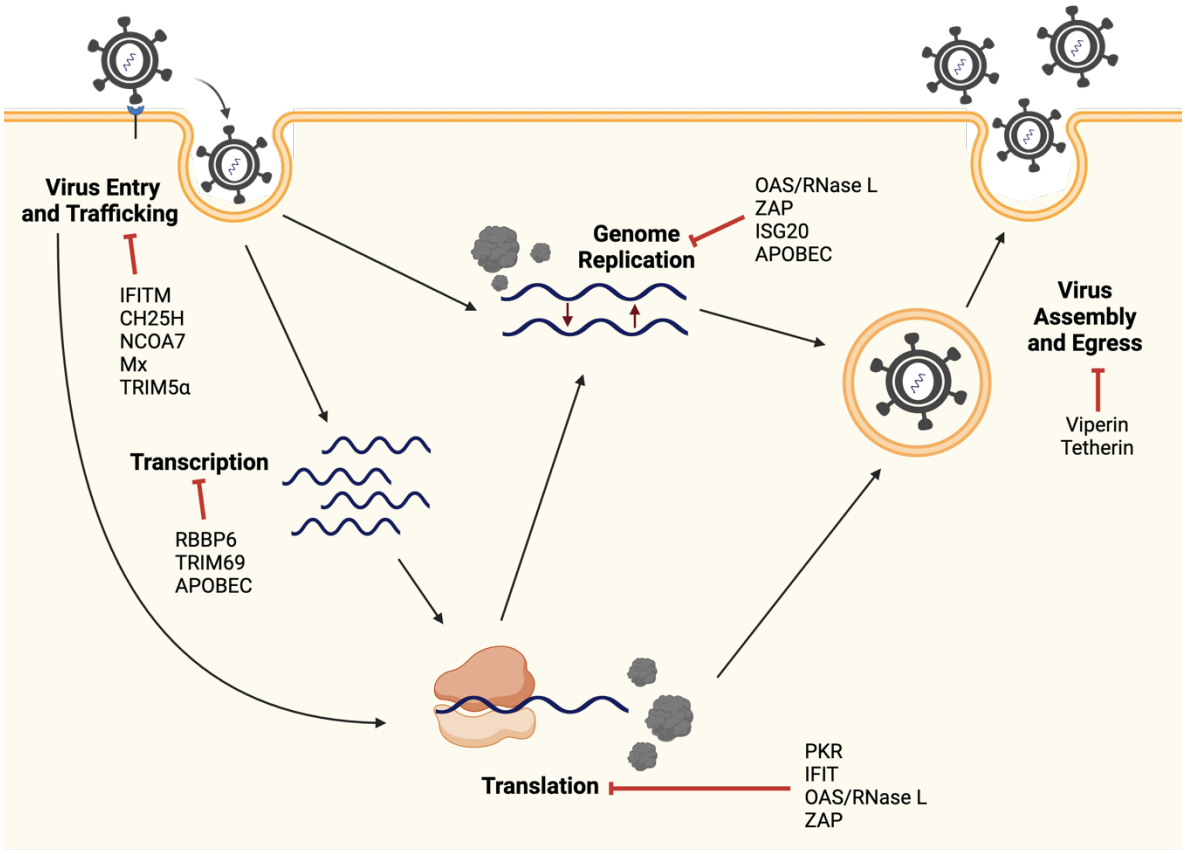

Figure 1-3: Examples of ISGs targeting stages of the virus replication cycle. ISGs have evolved to target the different stages of the virus replication cycle. Note that a given ISG can target a different stage depending on the virus.

1.1.5. ISGs targeting viral entry and trafficking

A virus must bind to and enter the host cell to begin its replication cycle. Many ISGs have evolved to target this process. A prime example is the IFN-inducible transmembrane (IFITM) proteins, which have been shown to interfere with the entry of a diversity of viruses, including orthomyxoviruses, flaviviruses and coronaviruses. IFITM3 was identified as a restriction factor of influenza A virus (IAV) in a siRNA genetic screen, and subsequent experiments using virus pseudotypes discovered the antiviral block was occurring prior to release of the viral genome into the cytosol (Brass et al., 2009). Given its localisation to endosomes, IFITM3 is most potent against viruses that enter cells via the endocytic pathway. Although its exact mechanism of action is still being ascertained, it is thought that IFITMs can affect membrane fluidity, which interferes with virus-cell membrane fusion, as well as enhancing the trafficking of virion-containing vesicles to lysosomes for degradation (Diamond and Farzan, 2013; Spence et al., 2019). Other ISGs that affect virus-cell membrane fusion include cholesterol-25 hydroxylase (CH25H) and nuclear receptor co-activator protein 7 (NCOA7), which are discussed later in section 3.1.2 (Majdoul and Compton, 2022)

For viruses that replicate in the nucleus, nuclear import of viral genomes is an essential step which can make these viruses susceptible to the antiviral activity of several ISGs. The Mx dynamin-like GTPases Mx1 and Mx2 are localised to the cytoplasm and nuclear pore, respectively. Mx1 exhibits anti-IAV activity by interfering with the translocation of viral genomes into the nucleus, in addition to inhibiting viral gene expression. Meanwhile, Mx2 is a potent restriction factor of retroviruses, such as HIV-1, by binding the capsid protein and inhibiting nuclear uptake and subsequent genome integration (Haller et al., 2015). Another ISG that restricts retroviruses is TRIM5α, which binds to and forms a lattice around the viral capsid, resulting in capsid disassembly prior to nuclear import (Ganser-Pornillos and Pornillos, 2019).

1.1.6. ISGs targeting viral RNA processes

Given the universal inability of viruses to translate their proteins, the requirement of host cell machinery to complete the replication cycle means ISGs have evolved to target these processes. Negative-sense RNA viruses must transcribe their genomes first, so blocking transcription can be successfully inhibitory. The E3 ligase Retinoblastoma binding protein 6 (RBBP6) binds to VP30, the transcriptional regulator encoded by Ebola virus (EBOV). This prevents the interaction of VP30 with the viral nucleoprotein, inhibiting transcription (Batra et al., 2018). Another E3 ligase, tripartite motif containing 69 (TRIM69) inhibits Indiana vesiculovirus (VSV) by association with the viral phosphoprotein (P), a cofactor of the viral polymerase, thus inhibiting transcription of viral mRNAs (Kueck et al., 2019; Rihn et al., 2019).

Positive-sense RNA viruses must translate their genomes to generate the proteins required for replication. Thus, ISGs targeting protein translation can be particularly effective restriction factors for this virus group. Protein kinase R (PKR) is activated by the PAMP dsRNA. In its best-characterised mechanism, PKR phosphorylates the eukaryotic translational initiation factor subunit eIF2α, which prevents cap-dependent translation (Hur, 2019). This global protein shut-off also occurs when the oligoadenylate synthetase (OAS)/RNase L pathway is activated, which results in the degradation of cellular mRNA and viral RNA, including genomes of ssRNA viruses (Bisbal and Silverman, 2007)(described in section 4.1).

Interferon-induced proteins with tetratricopeptide repeats (IFIT) proteins can also interfere with protein translation by binding to eIF3 (Diamond and Farzan, 2013). Additionally, IFIT proteins recognise 5’ppp and unmethylated capped viral transcripts, which would be absent on host mRNA, and prevent their translation. Viruses have evolved methyltransferases to evade this restriction and appear more host-like. Indeed, mutating West Nile virus to impair its 2’O-methyltransferase activity impairs its ability to infect mouse cells, but replication is enhanced when Ifit1 is absent (Daffis et al., 2010).

ISGs can also exhibit antiviral activity through the degradation of viral RNA. One example is zinc finger antiviral protein (ZAP), encoded by the *ZC3HAV1* gene. ZAP recognises CG dinucleotides in viral sequences (Takata et al., 2017), which are present in lower-than-expected numbers in vertebrate genomes, and targets them for degradation by recruiting co-factors TRIM25 and endonuclease KHNYN. Additionally, ZAP can inhibit viral protein translation of alphaviruses by recruitment of TRIM25 to ubiquitinate host proteins (Yang and Li, 2020). ISG20, a 3' to 5' exonuclease, can also degrade viral RNA genomes (Espert et al., 2003).

Retroviruses must convert their RNA genome into DNA by reverse transcription for successful replication. Apolipoprotein B mRNA-editing enzyme catalytic polypeptide-like (APOBEC) proteins, especially APOBEC3G, are cytidine deaminases that mutate deoxycytidine to deoxyuridine and can target this process. The resulting hypermutated viral DNA leads to impaired gene expression and replication (Chemudupati et al., 2019).

1.1.7. ISGs targeting virion assembly and egress

After genome replication, this genetic material must be assembled into the virion before trafficking and egress from the host cell. Far fewer ISGs have been identified that target this replication cycle; whether this is due to it being harder to identify late-acting ISGs or not many exist is unclear. One example is tetherin, encoded by the gene *BST2*. Early studies showed HIV-1 virions lacking the accessory protein Vpu accumulated at the cell surface, and it was hypothesised that Vpu evaded a host protein that caused this adherence. This led to the discovery of the transmembrane protein tetherin (Neil et al., 2008), which can anchor virions to the plasma membrane, thereby preventing their release. Another example is *RSAD2*-encoding viperin; this lipid droplet and ER-localised protein inhibits the enzyme farnesyl diphosphate synthase (FPPS), which is involved in the synthesis of sterols. The resulting changes in membrane fluidity affect the formation of lipid rafts, structures from which IAV virions bud (Wang et al., 2007).

1.1.8. Negative regulation of IFN signalling

Type I interferonopathies, such as Aicardi-Goutières syndrome, are inherited autoimmune diseases resulting from excessive and/or unregulated IFN signalling (Crow and Stetson, 2022). Genes involved in these diseases are involved in nucleic acid metabolism, nucleic acid sensing and negative regulation of the IFN response. Other autoimmune diseases, such as systemic lupus erythematosus (SLE), also show increased type I IFN production. These rare disorders cause complex pathologies, particularly affecting the brain and skin, reflecting the importance of negative regulation of the IFN response. For example, excessive IFN signalling can result in sustained activation of antigen-presenting cells, thus increasing recruitment and activity of B and T cells. This predisposes to the production of autoantibodies and the development of autoimmune disease (Ivashkiv and Donlin, 2014). Additionally, some ISGs are involved in the induction of apoptosis or proinflammatory cytokines, so prolonged IFN signalling promotes tissue damage that worsens disease pathology (McNab et al., 2015).

Cell intrinsic mechanisms to downregulate the IFN response include endocytosis of IFN receptors and dephosphorylation of activated JAK and STAT proteins. However, some ISGs themselves are negative regulators of IFN signalling. Phosphorylated tyrosine residues on IFN receptors and JAK1/2 are bound by Suppressor of cytokine signalling (SOCS) proteins; this prevents further binding of STAT proteins. Perhaps the most well-known negative regulator is ubiquitin-specific peptidase 18 (USP18), which binds to the intracellular side of the IFNAR2 receptors and changes its conformation; this change impairs the binding of Type I IFNs and downstream JAK-STAT signalling (Schneider et al., 2014).

Activation of the interferon response is a key barrier in the innate immune response, as the induction of hundreds of ISGs targeting different stages of the viral replication cycle can hinder the spread of an invading virus until an adaptive immune response can be mobilised. Concurrently, the upregulation of negative regulators creates a feedback loop to limit signalling so that the cytotoxic effects

of a prolonged IFN response do not outweigh the pathogenic impact of virus infection.

1.2. Coronaviruses

1.2.1. Introduction to human coronaviruses

Coronaviruses (Order *Nidovirales*, family *Coronaviridae*) are named after the crown-like appearance of the virion, due to the spike attachment protein on the surface. They are classified into four genera: alpha and beta coronaviruses mainly infect mammalian species, whereas gamma and delta coronaviruses mainly infect avian species (Alluwaimi et al., 2020). The first human coronavirus was described in 1965; this sample, named B814, was isolated from a child displaying common cold symptoms and could not be cultivated using traditional cell culture techniques (Tyrrell and Bynoe, 1965). David Tyrrell, the virologist leading the research at the Common Cold Unit in Salisbury, England, sent samples to the pioneering virologist June Almeida, who successfully imaged the virus for the first time. Almeida had previously imaged viruses causing infectious bronchitis in chickens (Infectious bronchitis virus (IBV)) and liver inflammation in mice (Mouse hepatitis virus (MHV)) and realising the similarities between their structures, discovered a new group of viruses – coronaviruses (Almeida and Tyrrell, 1967). Two human coronaviruses that are endemic today, HCoV-229E and HCoV-OC43 (a strain of Betacoronavirus 1), were identified soon after in 1966 and 1967. These isolates were sensitive to chemical ethers, suggesting the viruses had lipid envelopes. The other endemic coronaviruses, HCoV-NL63 and HCoV-HKU1, were discovered in the early 2000s (D. X. Liu et al., 2021).

The prevalence of these four endemic or “seasonal” coronaviruses peaks in winter and early spring, with HCoV-OC43 being the primary causative agent (Talbot et al., 2009). These viruses generally result in mild upper respiratory tract infections, but like many viruses, age, immune status, and underlying health conditions determine disease severity; pneumonia and bronchiolitis have been

reported in infants, the elderly and immunocompromised individuals (Gaunt et al., 2010).

Three highly pathogenic coronaviruses have emerged since the start of the century. Severe acute respiratory syndrome-related coronavirus (SARS-CoV)-1 first appeared in Guangdong Province, China in 2002 (Drosten et al., 2003); this outbreak was controlled by extensive public health measures with a ~9% case fatality. In 2012, the first case of Middle East respiratory syndrome-related coronavirus (MERS-CoV) was confirmed in samples taken from a patient in Saudi Arabia (Zaki et al., 2012); this virus has been associated with a ~35% case fatality rate. SARS-CoV-2, the causative agent of the recent coronavirus disease 19 (COVID-19) pandemic, emerged in late 2019 in Wuhan, China (Zhu et al., 2020). Disease varied from asymptomatic, mild upper respiratory disease to severe, lower respiratory disease, with >770 million cases reported as of January 2025 ("WHO COVID-19 dashboard," 2025). This range of symptoms meant control of SARS-CoV-2 was more difficult than SARS-CoV-1, as virus transmission occurred before symptom onset, unlike with SARS-CoV-1. More intense public health measures were thus required, such as quarantining infected individuals and their contacts, widespread testing and nationwide lockdowns. Given that natural infection or vaccination against SARS-CoV-2 does not provide life-long immunity, it can be argued that SARS-CoV-2 has transitioned to an endemic coronavirus (Harrison et al., 2023; Rabaan et al., 2023).

Before the COVID-19 pandemic, the prototypic betacoronavirus was MHV, which commonly infects laboratory mice. This project focuses on the related betacoronavirus HCoV-OC43, and the following sections will highlight the biology of this virus when possible.

1.2.2. Coronavirus genome organisation and structure

Coronaviruses have non-segmented, positive-sense, single-stranded RNA genomes that range from 27 to 32 kilobases (kb), thus have the largest genome sizes for RNA viruses; the coding region is flanked by structured 5' and 3'

untranslated regions (UTRs). Mimicking host mRNA, these genomes have a 5'-cap and are polyadenylated, enabling their immediate translation to produce viral proteins required for replication. The 5' end of the genome encodes ~16 non-structural proteins (nsp1-16) in two overlapping open reading frames (ORF1a and ORF1b); ORF1a is translated directly into the polyprotein pp1a while a -1 ribosomal frameshifting event produces the second polyprotein pp1ab (Fig 1-4). The polyproteins are processed by autoproteolytic cleavage by viral proteases papain-like protease (PL^{Pro}) and main protease (M^{Pro}), encoded by nsp3 and nsp5, respectively (D. X. Liu et al., 2021).

Structural and accessory proteins are encoded in the 3' end of the genome. Most coronaviruses encode four structural proteins – spike (S), envelope (E), membrane (M) and nucleocapsid (N) (Siu et al., 2008). S protein decorates the virion surface and is required for virus entry and attachment. The M protein is the master conductor orchestrating virion assembly, via its interaction with the other structural proteins; the E protein is incorporated to a lesser extent into the lipid envelope (Fig 1-4). Finally, the N protein encapsidates the viral genomic RNA. Embecoviruses are a subgroup of betacoronaviruses that include HCoV-OC43, HCoV-HKU1 and MHV, and encode an additional structural protein – haemagglutinin-esterase (HE). HE can possess sialic acid-binding activity and sialate-O-acetylesterase activity, which equips the virus with receptor-binding and receptor-destroying activity, respectively. A study utilising HCoV-OC43 infectious clones with depleted or impaired HE protein found that the presence of a functional HE protein contributes to the efficient production and dissemination of infectious virions *in vitro* (Desforges et al., 2013).

The number and location of accessory proteins within or between structural genes varies between coronaviruses. Although many are dispensable *in vitro*, they have important roles in antagonising host systems that affect their replication *in vivo*, such as the interferon response, stress response and apoptosis (Fang et al., 2021). HCoV-OC43 has two characterised accessory proteins – ns2a and ns5a. The NS2/NS2a protein of HCoV-OC43 exhibits phosphodiesterase activity that can

antagonise the OAS/RNase L pathway (discussed in section 4.1.6). ns5a/ns12.9 encodes a protein that oligomerises to form ion channels, known as a viroporin, and is involved in virion morphogenesis (Zhang et al., 2015). Interestingly, SARS-CoV-1 ORF3a and HCoV-229E ORF3a also encode viroporins between the S and E genes; these accessory proteins can rescue replication of HCoV-OC43 mutants lacking ns12.9, suggesting these viroporins have a conserved and vital role in coronavirus infection.

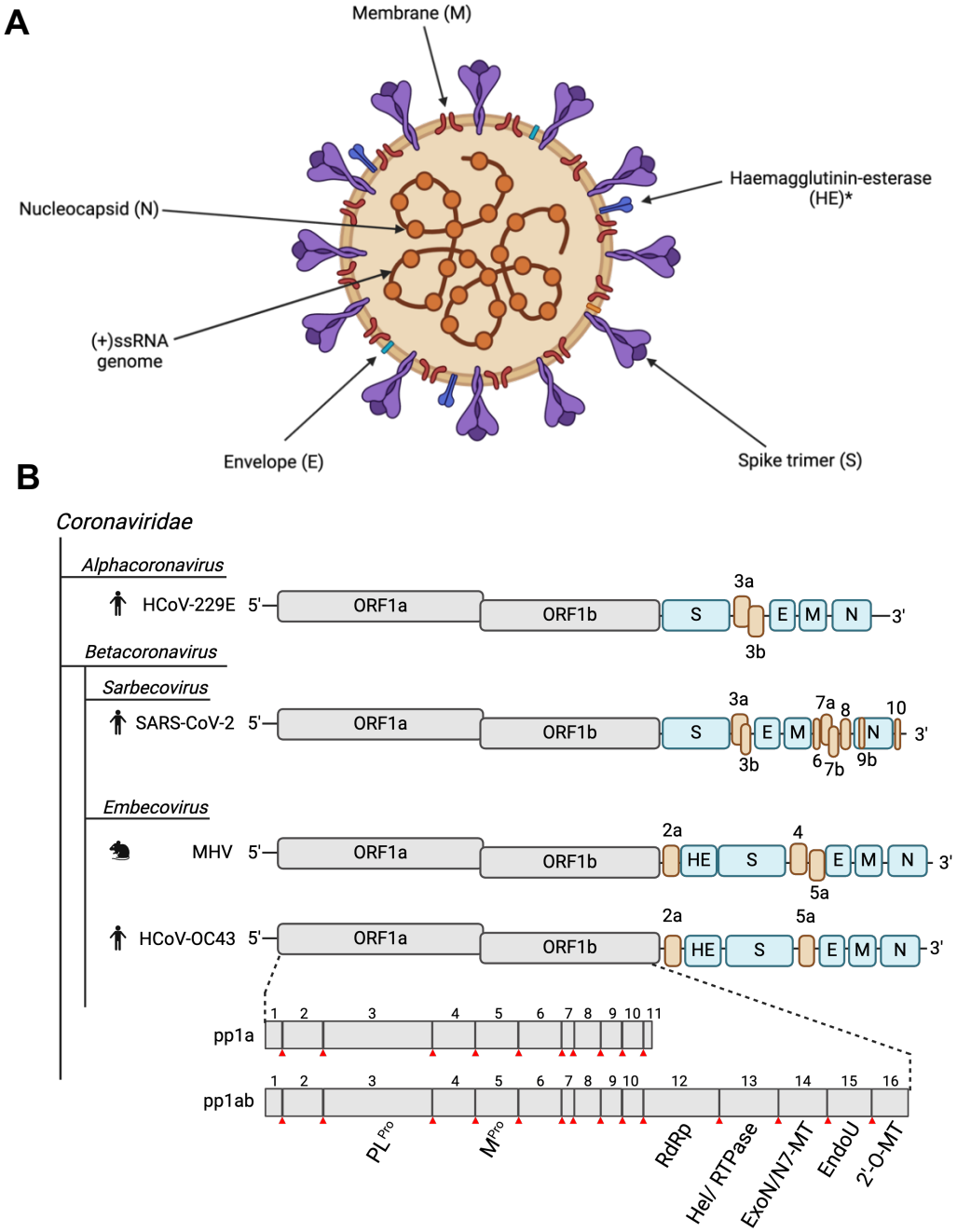

Figure 1-4: Coronavirus virion and genome structure. (**A**) Schematic representation of a coronavirus virion with structural proteins and genomic RNA labelled. *Only some betacoronaviruses express haemagglutinin-esterase (HE). (**B**) Schematic representation of the genome structure of alphacoronavirus HCoV-229E and the betacoronaviruses SARS-CoV-2, MHV and HCoV-OC43 are shown, with the open reading frames for non-structural proteins (grey), structural proteins (light blue) and accessory proteins (orange) labelled. The pp1a and pp1ab replicase polyproteins are represented at the bottom of the figure, with red triangles indicating where cleavage occurs. Papain-like protease (PL^{Pro}); main protease (M^{Pro}); RNA-dependent RNA polymerase (RdRp); Helicase (Hel); RNA 5'-triphosphatase (RTPase); Exonuclease (ExoN); N7-methyltransferase (N7-MT); Endoribonuclease (EndoU); 2'-O-methyltransferase (2'-O-MT).

1.2.3. Coronavirus replication cycle: virus entry

The first stage of the coronavirus replication cycle is binding of the spike protein to a cellular receptor to mediate virus entry into the cell. The spike protein exists as a homotrimer that undergoes cleavage into the S1 and S2 domains by host proteases; the S1 domain is responsible for receptor binding, whilst the S2 domain mediates membrane fusion. Many human coronaviruses utilise peptidases as receptors, such as angiotensin-converting enzyme 2 (ACE2; SARS-CoV-1, SARS-CoV-2, HCoV-NL63), aminopeptidase N (APN; HCoV-229E) and dipeptidyl peptidase 4 (DPP4; MERS-CoV) (D. X. Liu et al., 2021). However, it is widely accepted HCoV-OC43 and HCoV-HKU1 bind 9-O-acetylated sialic acids on glycan based-receptors (Hulswit et al., 2019); supporting this, CASD1, an enzyme involved in the biosynthesis of such sialic acids, was revealed as an HCoV-OC43 dependency factor in a loss-of-function CRISPR screen (Poston et al., 2022). Alternatively, major histocompatibility complex (MHC) Class I and transmembrane protease, serine 2 (TMPRSS2), have been implicated as protein receptors for HCoV-OC43 and HCoV-HKU1, respectively (Collins, 1994; Saunders et al., 2023).

Fusion of viral and cellular membranes can occur at the cellular or endosomal membrane. This has been well-documented for SARS-CoV-2 (Jackson et al., 2022); the SARS-CoV-2 spike protein has two sites that must be cleaved for successful fusion. The S1/S2 site is cleaved by furin during virion maturation in the virus-producing cell, while the S2' site (within the S2 domain) requires cleavage at the target cell. This can occur at the cell membrane if suitable proteases, such as TMPRSS2, are expressed at sufficient levels on the surface. Otherwise, the ACE2/SARS-CoV-2 spike complex undergoes clathrin-mediated endocytosis, where cathepsin L or B can mediate cleavage following endosome acidification.

The HCoV-OC43 replication cycle, including its entry stages, has not been as extensively studied. *In vitro* experiments suggest HCoV-OC43 enters the cell via caveolin-mediated endocytosis, which involves bulb-like invaginations of the cellular membrane abundant in cholesterol and other lipids (Owczarek et al.,

2018). Perhaps supporting this entry route, several loss-of-functions CRISPR screens reveal genes involved in cholesterol metabolism and glycosylphosphatidylinositol (GPI)-anchored protein biosynthesis as important host proteins facilitating HCoV-OC43 replication. Many genes involved in intracellular trafficking and endosome maturation, such as *VPS29*, *RAB7A* and *WDR81*, were also identified as host dependency factors in these screens (Poston et al., 2022; Schneider et al., 2021; Ruofan Wang et al., 2021). Successful release of the coronavirus genome into the cytosol, no matter the location of membrane fusion, is the starting point for viral protein synthesis and genome amplification.

1.2.4. Coronavirus replication cycle: RNA synthesis

As discussed previously, the coronavirus genome is immediately translated, and the non-structural proteins are released from the polyprotein, so that the viral replication transcription complex (RTC) can be formed. Some of these non-structural proteins initiate extensive remodelling of intracellular membranes, especially the endoplasmic reticulum (ER), into convoluted structures, such as double-membrane vesicles (DMV), which anchor the RTCs (Knoops et al., 2008). Supporting this, the ER-localised transmembrane protein 41B (TMEM41B) was identified as a pan-coronaviral host factor as it was required for the efficient replication of SARS-CoV-2, HCoV-OC43, HCoV-NL63 and HCoV-229E; it is also important in flavivirus replication and due to its subcellular localisation, it has been hypothesised to be involved in ER remodelling (Schneider et al., 2021). In addition to concentrating the RTC for RNA synthesis, the formation of these DMVs likely acts as an immune evasion mechanism to shield dsRNA replication intermediates from cytosolic sensors, such as RIG-I and MDA5.

Viral RNA synthesis occurs via a negative-sense RNA intermediate, which acts as a template to produce genomic and subgenomic mRNAs (sgmRNAs); subgenomic mRNAs are translated into the structural and accessory proteins. Genomic amplification is a continuous process with nsp12 encoding the RNA-dependent RNA polymerase (RdRp), synthesising RNA with assistance from the nsp7 and nsp8 co-factors. The large RNA genome is maintained by the 3'-5'-

exonuclease (nsp14), which provides coronaviruses with its proofreading activity. Nsp13, nsp14 and nsp16 act as RNA 5'-triphosphatase, N7-methyltransferase and 2'-O-methyltransferase, respectively, to add the 5'cap to the viral RNA (V'kovski et al., 2021) .

In contrast, the production of a nested set of sgmRNAs involves a discontinuous transcription process unique to viruses in the *Nidovirales* order. These sgmRNAs are co-terminal to the virus genome at the 5' and 3' ends; the 5' end contains a common leader sequence present at the 5' end of the genome. This process requires transcription-regulating sequences (TRS) located proximal to the leader sequence (TRS-L) or before the viral gene, known as the body (TRS-B). Due to the complementarity between the TRS-B on the negative-sense strand and the TRS-L on the positive-sense genome, a template switch can occur, facilitating the fusion of the non-contiguous leader and body sequences. This negative-sense subgenomic RNA is then used to produce positive-sense sgmRNAs which are subsequently translated into structural and accessory proteins (Sola et al., 2015).

1.2.5. Coronavirus replication cycle: assembly and egress

The structural proteins M, E and S are translated by ribosomes of the ER and accumulate at the ER-Golgi intermediate compartment (ERGIC). N protein is translated by cytosolic ribosomes and associates with the viral genomic RNA. The N-encapsidated genomes bud into the ERGIC where coronavirus assembly occurs (Katiyar et al., 2024; Stertz et al., 2007). It was initially thought that coronaviruses egress by exocytosis via the biosynthetic secretory pathway. Recent work studying the egress of MHV and SARS-CoV-2 suggests that betacoronaviruses exit the cell via the lysosomes, which are deacidified in infected cells (Ghosh et al., 2020).

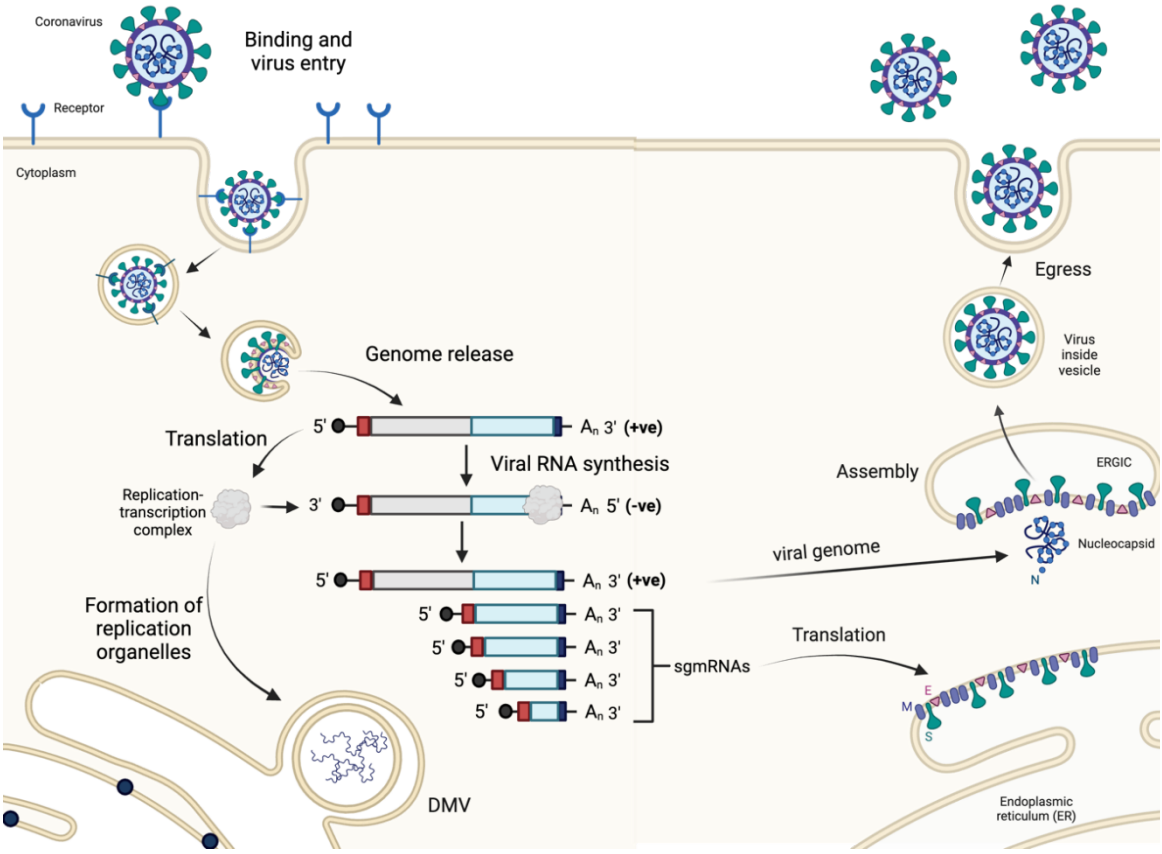

Figure 1-5: Coronavirus life cycle. Coronavirus virions bind to their cellular receptors via the spike (S) protein, resulting in conformational changes that facilitate fusion at the cellular or endosomal membrane. The positive-sense single-stranded RNA genome is released into the cytoplasm and is translated by ribosomal frameshifting to produce two polyproteins pp1a and pp1ab. These polyproteins are processed into 16 non-structural proteins (nsps) that generate the replication-transcription complex (RTC). The nsps induce remodelling of the endoplasmic reticulum (ER) to induce double-membrane vesicles (DMVs) and other membrane structures to anchor the RTC. A negative-sense intermediate acts as a template for synthesising viral genomic RNA and a nested set of subgenomic mRNA (sgmRNAs). The sgmRNAs are translated into the viral structural and accessory proteins, with nucleocapsid (N) translated in the cytoplasm and S, envelope (E) and membrane (M) proteins translated in the ER. The N-encapsidated viral genomes and structural proteins assemble at the ER-Golgi intermediate compartment (ERGIC) by budding. Mature virions egress from the infected cell by exocytosis.

1.2.6. Evolutionary hosts of coronaviruses

The ancestral hosts of all human coronaviruses are thought to be bats or rodents, with zoonotic transmission to humans via an intermediate mammalian host (Corman et al., 2018). Perhaps the most accepted evolutionary history of a human coronavirus is HCoV-OC43; unlike other human coronaviruses, HCoV-OC43 is not a stand-alone species but a strain of Betacoronavirus 1, which includes other viruses from a diversity of hosts, such as bovine coronavirus (BCoV), porcine hemagglutinating encephalomyelitis virus (PHEV) and canine respiratory coronavirus (CRCoV). Betacoronavirus 1 exists in the coronavirus subgenus *Embecovirus*, which includes rodent-related viruses such as MHV, suggesting rodents are also ancestral hosts. The most recent common ancestor for HCoV-OC43 and BCoV is predicted to be the late 19th/early 20th century, when it emerged into humans via livestock species, such as cattle (Shaw and Gatherer, 2023). The evolutionary history of HCoV-HKU1 is not well understood, but its presence in the *Embecovirus* subgenus suggests rodents are also the ancestral host.

The remaining seasonal coronavirus (HCoV-229E, HCoV-NL63) and emerging coronaviruses (SARS-CoV-1, MERS-CoV, SARS-CoV-2) have ancestral links to bats. Viruses related to HCoV-229E have been identified in alpacas, camels and bats, suggesting this virus emerged from Hipposiderid bat species into humans, via a camelid intermediate host (Harrison et al., 2023). Similar parallels can be seen with MERS-CoV, as dromedary camels have been implicated as the zoonotic source of the outbreak (Müller et al., 2014).

SARS-CoV-1 and SARS-CoV-2 belong to the *Sarbecovirus* subgenus, which includes many SARS-like coronaviruses found in horseshoe bats (*Rhinolophus* spp.). The SARS-CoV-1 outbreak started in a wildlife market, with masked palm civets implicated as the intermediate host facilitating transmission into humans (Cui et al., 2019). The wildlife trade has also been associated with the spillover of SARS-CoV-2; there is no widely accepted intermediate host for SARS-CoV-2 yet, but mammals commonly associated with these wildlife markets, such as raccoon dogs, have been suggested (Crits-Christoph et al., 2024).

1.2.7. Role of interferon in coronavirus infection

The presence and timing of a functional interferon (IFN) response is important in controlling coronavirus infection, with delayed type I IFN signalling enhancing inflammation in infected individuals (Channappanavar et al., 2016; Park and Iwasaki, 2020). Accordingly, autoantibodies against type I IFNs and genetic errors in IFN signalling effectors have been identified in patients with severe COVID-19 (Bastard et al., 2020; Zhang et al., 2020), highlighting the importance of interferon-stimulated genes during coronavirus infection. Before the COVID-19 pandemic, few ISGs that inhibited human coronaviruses had been investigated (Liu et al., 2014; Zhao et al., 2018).

Despite this, coronaviruses, including SARS-CoV-1, SARS-CoV-2 and MHV, appear to show poor induction of the IFN response, at least *in vitro* (Blanco-Melo et al., 2020; Roth-Cross et al., 2007; Ziegler et al., 2005) . The relationship between IFN and HCoV-OC43 is particularly complex. A recent transcriptomic and proteomic analysis of HCoV-OC43 infected cells revealed that HCoV-OC43 effectively suppressed interferon signalling pathways, but the ER stress response is highly induced (Bresson et al., 2025). In mice challenged with HCoV-OC43, it was found that alveolar macrophages are critical in protection against severe pneumonia (Zhong et al., 2025). Interferon has been shown to enhance HCoV-OC43 infection in some cell lines; this is thought to be due to the upregulation of IFITM proteins (section 1.1.5)(Zhao et al., 2014), which have been proposed to act as entry factors for HCoV-OC43. However, the addition of exogenous type I IFNs in cell culture can successfully restrict coronaviruses (Blanco-Melo et al., 2020; de Wilde et al., 2013), suggesting systemic interferon responses or IFN therapy could be protective in infected individuals.

Unsurprisingly, coronaviruses encode numerous mechanisms to interfere with interferon induction and signalling. Such mechanisms have mainly been identified for SARS-CoV-1, SARS-CoV-2 and MERS-CoV, and have been extensively reviewed (Park and Iwasaki, 2020; Znaidia et al., 2022). In SARS-CoV alone, at least 12 proteins have been shown to perform such evasion mechanisms (Sa Ribero

et al., 2020); this includes structural, non-structural and accessory proteins showing the multi-functional nature of their activities and the importance of inhibiting the interferon response for successful replication.

As described previously, remodelling of the ER into double membrane vesicles and binding of N protein to the coronavirus genome can help mask inflammatory RNA from host sensors. However, coronaviruses can limit IFN induction by targeting these sensors directly. It has been shown that activation of MDA5 requires conjugation of the ubiquitin-like protein ISG15. SARS-CoV-2 nsp3 (encoding PL^{Pro}), can antagonise this ISG15-dependent activation using its deISGylating activity (G. Liu et al., 2021). Nsp3 can also target IFN induction downstream of nucleic acid sensors; SARS-CoV-1 nsp3 can interact with the transcription factor IRF3, preventing its phosphorylation and nuclear translocation (Devaraj et al., 2007). Understandably, IRF3 is a prime target with several proteins of MERS-CoV (M, ORF4a, ORF4b, ORF5), SARS-CoV-1 (nsp3, ORF3b, ORF6) and SARS-CoV-2 (nsp3, nsp5, ORF3b, nsp13) also interfering with its phosphorylation, nuclear translocation and function (Sievers et al., 2024; Yang et al., 2013).

Coronaviruses also encode multiple evasion mechanisms targeting JAK/STAT signalling triggered by IFN. SARS-CoV-1 ORF3a can downregulate IFNAR1 by inducing its phosphorylation, which subsequently leads to translocation to lysosomes for degradation (Minakshi et al., 2009). SARS-CoV-2 nsp14 similarly targets IFNAR1 for degradation (Hayn et al., 2021). Coronaviruses can also hijack the host's own negative regulators of IFN signalling for evasion, as SARS-CoV-2 ORF3a can increase expression of SOCS1 (section 1.1.8) (Rong Wang et al., 2021), hampering STAT1 activation. STAT1 and/or STAT2 activation is also hindered by SARS-CoV-2 ORF7a and ORF7b which block its phosphorylation (Xia et al., 2020). ORF6 proteins of SARS-CoV-1 and SARS-CoV-2 are also potent IFN antagonists, as they prevents translocation of STAT1 into the nucleus; for SARS-CoV-2, this inhibition was mediated by localisation of ORF6 to the nuclear complex where its interacts with Nup98-Rae1 (Miorin et al., 2020).

Coronaviruses can also evade the immune response by shut down of host translation. The best-studied example is Nsp1. During SARS-CoV-2 infection, Nsp1 binds to the 18S ribosomal subunit, blocking the mRNA entry channel and subsequent translation of cytokines and ISGs. The importance of the interferon response in coronavirus infection is therefore highlighted by the diversity of mechanisms that coronaviruses have evolved to evade it.

1.3. Aims and approaches

The overall aim of this project was to identify ISGs that hinder the transmission of coronaviruses within the human population. At the Centre for Virus Research and elsewhere, arrayed ISG expression screening has been used successfully to identify such ISGs. Although some ISG libraries were already available, as part of this project, it was planned to expand them to include genes of additional species relevant to coronavirus transmission. Since many viruses of present and future clinical importance do not have reporter viruses available, Chapter 3 describes an immunostaining screening approach using an antibody that targets a PAMP widely produced during virus replication, to quantify virus infection. I aimed to validate this optimised protocol by performing a large-scale ISG screen against HCoV-OC43.

HCoV-OC43 is increasingly being considered as a low-risk model to study human coronaviruses and their interactions with the host. Firstly, it is an endemic human coronavirus that mainly causes minor symptoms, so it does not require biosafety level 3 (BSL-3) containment, unlike the “emerging” coronaviruses SARS-CoV-1, SARS-CoV-2 and MERS-CoV. Given its predicted spillover into humans almost 150 years ago, the transition of HCoV-OC43 to a common cold virus with seasonal prevalence can provide insights into the future evolution of SARS-CoV-2, which also belongs *Betacoronavirus* genus. Since I planned to screen thousands of ISGs for antiviral activity, HCoV-OC43 was an attractive choice as such large-scale experiments can be optimised and performed more efficiently and safer in lower containment labs. Additionally, no virus from the *Embecovirus* subgenus had been

screened and I thought it could enhance our knowledge of ISGs that target coronaviruses, especially those with ancestral rodent origins.

In the final year of my PhD studies, Professor Sam Wilson, my primary supervisor, relocated his lab to Cambridge. I abruptly joined the research group of Dr Adam Fletcher, who specialises in studying host defence enzymes, such as E3 ubiquitin ligases. Given the different expertise of my new lab, it was decided to end the ISG screening component of my project and undertake experiments to characterise the antiviral activity of a 'hit' identified in the screen against HCoV-OC43. In Chapter 4, various approaches were used to investigate the mechanism by which the dsRNA sensor OAS2 inhibits HCoV-OC43. Finally, Chapter 5 describes the use of infection assays to assess fluorescent tag retention in reporter viruses, to assist in other research projects performed by collaborators at the Centre for Virus Research.

Overall, this thesis describes my efforts to provide new information on the interactions of human coronaviruses with the innate immune system and further enhance our understanding of new mechanisms by which already well-studied ISGs exhibit antiviral activity.

2. Materials and Methods

2.1. Materials

2.1.1. Mammalian cell lines

Human Embryonic Kidney 293T (HEK 293T) cells were received from Paul Bieniasz. A549, a human adenocarcinoma alveolar basal epithelial cell line, and 17cl1, a mouse fibroblast cell line, were propagated from a lab stock. A549-ISRE:GFP, expressing eGFP under the control of an ISRE promoter, were received from Richard E. Randall. A549-ACE2-TMPRSS2 (AAT) have been previously described (Rihn et al., 2021). VeroE6, interferon-deficient kidney epithelial cells from an African green monkey, were received from Michele Bouloy. BHK21, baby hamster kidney cells, were purchased from ECACC. Huh7.5, a human hepatocellular carcinoma cell line, were propagated from laboratory stocks.

2.1.2. Viruses

Betacoronavirus 1 strain OC43 (ATCC-1558) was purchased from ATCC. HCoV-OC43 was propagated in VeroE6 (Chapter 3) or Huh7.5 (Chapter 4) at 33°C. The SARS-CoV-2 virus strain CVR-GLA-1 was produced at the Centre for Virus Research and the stock used in this work (Chapter 4) was propagated by Dr Arthur Wickenhagen. Mouse hepatitis virus encoding a GFP reporter (MHV-GFP) was kindly gifted by Dr Volkel Thiel and propagated in 17cl1 cells at 33°C. Encephalomyocarditis Virus/Cardiovirus A (EMCV) was purchased from ATCC and propagated in VeroE6 cells at 37°C. PR8-GFP11-WT and PR8-GFP11-Mutant viruses (based on a reverse genetic system of A/Puerto Rico/8/1934 (H1N1)) were generated by Dr Matthew Turnbull.

2.1.3. Bacterial cultures

Propagation of DNA plasmids was carried out in DH10B (Chapter 3) or DH5-Alpha competent *E. coli* (NEB) (Chapter 4); bacteria were cultured in Luria Bertani (LB) agar and broth (E&O Laboratories).

2.1.4. Cell culture reagents

Table 2-1: List of cell culture reagents used and their suppliers.

Reagent	Supplier
Dulbecco's Modified Eagle Medium (DMEM)	Thermo Fisher Scientific (31966021)
10x Minimum Essential Medium (MEM)	Thermo Fisher Scientific (11430030)
Opti-MEM	Thermo Fisher Scientific (31985047)
Phosphate-buffered Saline (PBS)	Thermo Fisher Scientific (14190094)
Fetal Calf Serum (FCS)	Thermo Fisher Scientific (10082147)
Bovine Serum Albumin (BSA)	Sigma Aldrich (A7638)
0.05% Trypsin-EDTA (1x)	Thermo Fisher Scientific (25300054)
0.5% Trypsin-EDTA (10x)	Thermo Fisher Scientific (15400054)
TPCK-treated trypsin	Sigma Aldrich (T1426)
Gentamicin 50 mg/mL	Melford Laboratories (G0124)
Penicillin/Streptomycin 10000 U/mL	Thermo Fisher Scientific (15140122)
Puromycin 2 mg/mL	Melford Laboratories (P330020)
Blasticidin S 10 mg/mL	Melford Laboratories (B12150)
G418 200 mg/mL	Melford Laboratories (G64000)
Doxycycline	Sigma Aldrich
Polyethylenimine (PEI)	PolySciences (23966-1)
Lipofectamine LTX with PLUS reagent	Thermo Fisher Scientific (15338030)
Polybrene 8 mg/mL	Merck (107689)
Avicel RC-591	FMC Biopolymer
TRIzol Reagent	Thermo Fisher Scientific (15596026)
Ruxolitinib	Stratech Scientific (S1378)
Human interferon beta 1b	Stratech Scientific (11415-1)
Human interferon alpha H2	Stratech Scientific (11145-1)

2.1.5. Molecular kits

Table 2-2: List of molecular kits and their suppliers.

Kit	Supplier
QIAprep Spin Miniprep kit	Qiagen (27104)
Plasmid Midi Kit	Qiagen (12143)
RNeasy Mini Kit	Qiagen (74104)
PureLink Quick Gel Extraction kit	Thermo Fisher Scientific (K210012)
QIAquick Gel Extraction Kit	Qiagen (28704)

2.1.6. Buffers and solutions

Protein Sample buffer: NuPAGE 4X Bolt LDS Sample Buffer (Thermo Fisher Scientific) with 5% 2-Mercaptoethanol (Sigma-Aldrich).

SDS Running Buffer: 20X NuPAGE MES SDS Running Buffer (Thermo Fisher Scientific).

TAE Buffer: To prepare 1L of 10X solution, add 48.5 g TRIS, 11.4 mL acetic acid and 20 mL 0.5M EDTA.

PBS-T: To make 2 L of a 10X solution, add 35 g $Na_2HPO_4 \bullet 2H_2O$, 4.8 g KH_2PO_4, 160 g NaCl and 4 g KCl into dH2O. After dilution to 1 L, add 1% Tween-20 (v/v) to give 1X PBS-T.

Ethidium Bromide: Dissolved in dH_2O to make 10 mg/mL stock solution (Sigma-Aldrich). Used at 0.5 µg/mL concentration in agarose gels.

Cell freezing mix: Filter-sterilised FCS containing 10% DMSO (Sigma-Aldrich). Stored at -20°C until use.

Coomassie Stain: For 500 mL, add 1 mL Coomassie Brilliant Blue R-250 (Thermo Fisher Scientific), 250 mL Ethanol, 37.5 mL Acetic acid and 212.5 mL dH_2O.

Ampicillin: 100 mg/mL ampicillin stock was made by dissolving 5 g of ampicillin salt (Melford, A40040) in 50 mL dH_2O and stored at -20°C until use.

2.1.7. Antibodies

Table 2-3: Primary and secondary antibodies used in this project.

Antibody	Application	Source
Mouse monoclonal anti-GAPDH	WB: 1:10000	Thermo Fisher Scientific (AM4300)
Rabbit monoclonal anti-vinculin (E1E9V)	WB: 1:1000	Cell Signalling Technologies (13901)
Rabbit monoclonal anti-RNase L (D4B4J)	WB: 1:1000	Cell Signalling Technologies (27281)
Rabbit polyclonal anti-OAS1	WB: 1:1000	Proteintech (14955-1-AP)
Rabbit polyclonal anti-OAS2	WB: 1:1000 IF: 1:500	Proteintech (19279-1-AP)
Mouse monoclonal anti-OAS2 (G-9)	WB: 1:100	Santa Cruz Biotechnology (sc271117)
Rabbit monoclonal anti-phosphoSTAT1 (Tyr701) (58D6)	WB: 1:1000	Cell Signalling Technologies (9167)
Sheep polyclonal HCoV-OC43 Nucleocapsid	WB: 1:5000	MRC Protein Phosphorylation and Ubiquitylation Unit (DA116)
Mouse monoclonal anti-dsRNA (J2)	IF: 1:1000	Nordic-MuBio (10010500)
Mouse monoclonal anti-58K	IF: 1:500	Abcam (ab27043)
Mouse monoclonal anti-calnexin (AF18)	IF: 1:500	Thermo Fisher Scientific (MA3-027)
Donkey anti-sheep IgG (H+L), HRP	WB: 1:5000	Thermo Fisher Scientific (A16041)
Goat anti-rabbit IgG (H+L), HRP	WB: 1:5000	Cell Signalling Technologies (7074)
Horse anti-mouse (H+L), HRP	WB: 1:5000	Cell Signalling Technologies (7076)
Mouse IgG Fc Binding Protein, HRP	WB: 1:5000	Santa Cruz Biotechnology (sc-525409)
Goat anti-mouse IgG2a Alexa Fluor™ 488	IF: 1:1000	Thermo Fisher Scientific (A21131)
Goat anti-rabbit IgG (H+L) Alexa Fluor™ 488	IF: 1:1000	Thermo Fisher Scientific (A32731)
Goat anti-rabbit IgG (H+L) Alexa Fluor™ 568	IF: 1:1000	Thermo Fisher Scientific (A11011)
Goat anti-mouse IgG (H+L) AlexaFluor™ 488	IF: 1:1000	Thermo Fisher Scientific (A11001)
Hoechst 33342	5 µg/mL	Thermo Fisher Scientific (H3570)

2.2. Methods

2.2.1. Mammalian cell culture

All cell lines were maintained in Dulbecco's Modified Eagle Medium (DMEM), supplemented with 10% FCS and 10 µg/mL gentamicin (Chapter 3, 5) or 100 U/mL penicillin/100 µg/mL streptomycin (Chapter 4).

2.2.2. Polymerase chain reaction (PCR)

PCR was used to amplify commercially purchased gene blocks or for *in vivo* assembly (IVA) to modify plasmids. Gene blocks were amplified using custom made forward and reverse primers complementary to the N-terminus and the C-terminus, respectively. Herculase II DNA polymerase (Agilent) was used according to manufacturer's protocols in 25 µL (IVA) or 50 µL (gene blocks) total volumes. For gene blocks, DNA was usually amplified at 95°C for 1 min, followed by 35 cycles (95°C for 15 sec, 55°C for 20 sec and 68°C for 1 min/kb) and a final extension at 68°C for 3 min. For IVA, DNA was usually amplified at 95°C for 30 sec, followed by 18 cycles (95°C for 10 sec, 60°C for 30 sec and 72°C for 15 sec/kb) and a final extension at 72°C for 10 min.

2.2.3. Gel electrophoresis and purification

PCR products and restriction digest fragments were resolved by agarose gel electrophoresis. 1% (w/v) agarose gels were made by dissolving UltraPure agarose powder (Thermo Fisher Scientific) in 1x TAE buffer using microwave heating, followed by addition of 8 µL ethidium bromide or 5 µL SYBR™ Safe DNA gel stain (S33102, Thermo Fisher Scientific). DNA excised from the gel was purified using PureLink Quick Gel extraction kit or QIAquick gel extraction kit, according to manufacturer's protocols. DNA was eluted with 50 µL dH_2O.

2.2.4. Molecular cloning

Modified plasmids pLV-EF1a-IRES-*SfiI*-Puro-TagRFP and pLV-EF1a-IRES-*SfiI*-Neo-TagRFP have been described previously (Wickenhagen et al., 2021). The following cDNA were ordered as gene blocks (IDT DNA) with flanking *SfiI* sites: human OAS2 p71 (NM_016817.3) and OAS2 p69 (NM_002535.3), mouse Oas1a (NM_145211), Oas1b (NM_001083925.1), Oas1c (NM_033541.4), Oas1d (NM_133893.3), Oas1e (NM_001347450.1), Oas1f (NM_145153.3), Oas1g (NM_011852.3), Oas1h (NM_145228.2), $Oas2^{751}$ (NM_001347448.1) and $Oas2^{741}$ (NM_145227.3). These gene blocks were PCR amplified (section 2.2.2) and gel purified (section 2.2.3). To generate the OAS2-$p71^{G2A}$ and OAS2-$p69^{G2A}$ myristoylation mutants, the parental gene blocks were PCR amplified with primers that mutate the glycine residue at position 2 to alanine.

SfiI (New England BioLabs, NEB) was primarily used to linearise 5 µg vector plasmid and to create complementary ends in the insert, according to manufacturer's protocols. Linearised plasmid was treated with alkaline phosphatase (NEB) to prevent self-ligation. Digested plasmid and insert were gel purified and eluted with 50 µL of dH_2O. For standard ligation reactions, 1 µL vector and 3.5 µL insert was mixed with 5 µL 2x T4 Buffer and 0.5 µL of T4 DNA Ligase (Promega) for a final volume of 10 µL. The ligation mixture was incubated for 4 h at room temperature or 4°C overnight before bacterial transformation (section 2.2.5). Post DNA extraction, *HindIII*-HF (NEB) restriction digestion was primarily used for screening colonies for sequencing.

The OAS2-$p69^{D481A}$, OAS2-$p69^{CAFAKA}$, OAS2-$p69^{R374E/K378E}$ and OAS2-$p69^{R529E/R533E}$ plasmids were generated by *in vivo* assembly using overlapping primers (Table 2-4). The PCR mixture contained 1 ng of pLV-EF1a-IRES-*SfiI*-OAS2-p69, 200 µM dNTPs (Promega), 100 nM primers (Table 2-4), 3% DMSO, 5 µL 5x Herc II buffer, 0.5 µL Herculase II (Agilent) and 14.75 µL water. After PCR amplification, template DNA was degraded using 1 µL FastDigest *DpnI* (Thermo Fisher Scientific) for 15 minutes at 37°C. 2 µL PCR mixture was used for bacterial transformation.

Table 2-4: Primers used for in vivo assembly.

Primer	Sequence
OAS2-p69^{D481A} Fwd	5'-CCTCAACGAAAGTGTCAGCTTTGCAGTGCTTCCTCCTTTAATGCACTGGG-3'
OAS2-p69^{D481A} Rev	5'-AAAGCTGACACTTTCGTTGAGGACTTTGG-3'
OAS2-p69^{CAFAKA} Fwd	5'-GGAATGGTTATCCTCTCCCGCCGCCGCGGATGGGACTGGAAACCCAATACCACC-3'
OAS2-p69^{CAFAKA} Rev	5'-GGGAGAGGATAACCATTCCTTTGCTTC-3'
OAS2-p69$^{R374E/K378E}$ Fwd	5'-ATTGACAGTGCTGTTAACATCATCGAAACATTCCTTGAAGAAAACTGCTTCCGACAATCAACAG-3'
OAS2-p69$^{R374E/K378E}$ Rev	5'-GATGATGTTAACAGCACTGTCAATCTGCTC-3'
OAS2-p69$^{R529E/R533E}$ Fwd	5'- CTGTTTCACAGTCCTGCAGGAAAACTTCATTGAATCCCGGCCCACCAAACTAAAGG-3'
OAS2-p69$^{R529E/R533E}$ Rev	5'-CTGCAGGACTGTGAAACAGGTAGAAAAC-3'

2.2.5. Transformation of *E. coli*

DH10B or DH5-Alpha competent *E. coli* were thawed on ice for 30 minutes. 10 µL ligation mix was added to 100 µL bacteria for ligation reactions. 1-2 µL of plasmid was added to 50 µL bacteria for plasmid propagation. After a 30-minute incubation on ice, the bacteria were subject to a heat shock at 42°C for 30 seconds. The bacteria were chilled on ice for ≥ 2 minutes prior to addition of 150-200 µL SOC media (NEB), then incubated at 30°C (DH10B) or 37°C (DH5-Alpha) for > 45 minutes, with shaking. Bacteria were then plated on pre-warmed LB agar plates containing 200 µg/mL ampicillin and incubated overnight at 30°C (DH10B) or 37°C (DH5-Alpha).

2.2.6. Extraction of plasmid DNA

For generating plasmid DNA for the mouse ISG library, 500 ng of 372 SCRPSY plasmids (GenBank accession no. KT368137.1, synthesised by BioBasic) were transformed individually into DH10B competent bacteria, using standard protocols (section 2.2.5). Individual colonies were inoculated into 3.5 mL Terrific Broth (TB)

medium (Sigma-Aldrich), supplemented with 200 µg/mL ampicillin (Melford) in 14 mL round bottom polypropylene test tubes with caps (Corning). Glycerol stocks of each plasmid were made by mixing 0.5 mL culture with 0.5 mL 80% glycerol (Fisher Chemical). DNA was extracted from 2 mL culture using QIAprep Spin MiniPrep Kit. DNA concentration was measured using NanoDrop Microvolume Spectrophotometer (Thermo Fisher Scientific) and normalised to 25 ng/µL. For transduction troubleshooting, 250 ng DNA or 5 µL neat miniprep DNA was digested for 2 h using *HindIII*-HF (NEB) and visualised by agarose gel electrophoresis (section 2.2.3).

For small-scale DNA preparations, an individual colony was inoculated in 3-5 mL of LB broth containing 200 µg/mL ampicillin and grown overnight with shaking at 30°C (DH10B) or 37°C (DH5-Alpha). DNA was extracted using the QIAprep Spin Miniprep kit and eluted in 50 µL dH_2O. Concentrations were measured on the NanoDrop Microvolume Spectrophotometer.

For medium-scale DNA preparations, an individual colony was inoculated in 175 mL of LB broth containing 200 µg/mL ampicillin and grown overnight with shaking at 30°C. DNA was extracted using the Plasmid Midi Kit, eluted in 200 µL dH_2O and concentrations was measured on the NanoDrop Microvolume Spectrophotometer.

2.2.7. Retroviral vectors and cell modification

Lentiviral vectors were produced by transient transfection. 5 µg vector plasmid (described in section 2.2.4), 5 µg HIV-1 gag-pol (pNLGP) and 1 µg vesicular stomatitis virus glycoprotein expression plasmid (pVSVg) were mixed with 500 µL serum-free DMEM by vortex, in the presence of PEI. This transfection mixture was incubated for 30 minutes, then added dropwise to a confluent 10 cm dish of HEK 293T. The media was replaced 16-24 h post-transfection and lentiviral vector containing supernatant was harvested and filtered using a 0.45 µm pore-size-filter at 48 h post-transfection. Supernatant was stored at -80°C before use.

To generate stable cell lines, A549 cells were seeded at a density of ~$5x10^5$ cells/well in 6-well plates. The next day, cells were transduced with 0.5 to 1 mL lentivirus-containing supernatant. Cells underwent antibiotic selection 48 h post-transduction and remained in antibiotic-containing media until all cells were dead in the mock-transduced control; puromycin was used at a concentration of 2 µg/mL and blasticidin was used at a concentration of 5 µg/mL. Success of gene expression or depletion was determined by Western blotting (section 2.2.9).

2.2.8. Gene editing by CRISPR Cas9

LentiCRISPRv2-Puro and lentiCRISPRv2-Blast plasmids were used to knockdown expression of OAS2 and RNase L, respectively (Sanjana et al., 2014). CRISPR guides were designed using the CHOPCHOP tool (https://chopchop.cbu.uib.no). Seven guides were subcloned into the lentiCRISPRv2 system and the three best guides for depleting target protein expression were used for subsequent experiments. The following guides are included in this thesis: OAS2 (guide 1: 5'-GTC TTA AGA GGC AAC TCC GA-3' , guide 2: 5'-GGA CGG AAA ACA GTC TTA AG-3' , guide 3: 5'-GCT TAC TCA GAG CGT TGA AGG-3') and RNase L (guide 1: 5'-GCC GAG TTG CTG TGC AAA CG-3', guide 2: 5'-TTA TCC TCG CAG CGA TTG CG-3', guide 3: 5'-CTA TAG GAC GCT TCG GAA TG-3', guide 4: 5'-TAT AGG ACG CTT CGG AAT GT-3', guide 5: 5'-TAG TCA TCT TCA GCC GCT AT-3', guide 6: 5'- TTT ATC TCG CAG CGA TTG C-3', guide 7: 5'-GCA ATC GCT GCG AGG ATA AA-3'). Lentiviral supernatants were generated and used for transduction as described before (section 2.2.7). OAS2 CRISPR guides were transduced into A549 cells and RNase L CRISPR guides were transduced into A549-OAS2-p69 or A549-OAS2-p71 cells.

2.2.9. Western blot

Cells were pelleted, washed once with PBS then lysed on ice for 15 minutes; the lysis buffer contains 50 mM Tris-HCl pH 7.5, 10 mM sodium 2-glycerophosphate, 5 mM sodium pyrophosphate, 270 mM sucrose, 50 mM NaCl, 200 µM phenylmethylsulfonyl fluoride (PMSF), 1 mM benzamidine, 10 µM Tris(2-

carboxyethyl)phosphine hydrochloride (TCEP) and 1% NP-40. Samples were centrifuged at 12000 x G for 15 minutes at 4°C and supernatant was collected. Protein concentration was measured using Pierce™ Bradford Plus Protein Assay Reagent (Thermo Fisher Scientific) and sample concentrations were normalised. NuPAGE 4X Bolt LDS Sample Buffer (Thermo Fisher Scientific), containing 5% 2-Mercaptoethanol (BME) was then added, to a final concentration of 1X sample buffer, 1.25% BME.

Proteins were separated on NuPage 4-12% BisTris polyacrylamide gels and transferred onto nitrocellulose membranes using the iBlot 2 (Invitrogen). After blocking in 5% milk (Sigma-Aldrich), membranes were probed with primary antibodies (Table 2-4), in 5% BSA (Millipore). Membranes were then stained with species IgG-specific secondary antibodies conjugated to horseradish peroxidase (Table 2-4). After addition of Pierce™ ECL substrate (Thermo Fisher Scientific) or Amersham ECL Select™ (Cytiva), membranes were scanned using the LI-COR Odyssey XF scanner or using High Performance Chemiluminescence Film (Cytiva) on the SRX-101A Medical Film Processor (Konica Minolta).

2.2.10. Rescue of infectious virus

BHK-21 cells were seeded at a density of $3x10^5$ cells/well in 6-well plates. The following day, media was changed to DMEM containing 2% FCS and transfected with 3 µg pCC1-4K-SARS-CoV-2-alpha-WT or pCC1-4K-SARS-CoV-2-alpha-ZsGreen and 3 µL Lipofectamine® LTX (Thermo Fisher Scientific), with 3 µL PLUS™ reagent in Opti-MEM media. Following a 20 minute incubation, transfection mix was added dropwise to cells. 48 h post transfection, supernatant was transferred to T25 flasks containing VeroE6 cells. The virus stock was harvested 2-4 days post infection, according to cytopathic effect or fluorescence levels. Infectious titre, including fluorescent tag stability, was determined by plaque assays (section 2.2.11, 2.2.12).

2.2.11. Virus infection

For HCoV-OC43 plaque assays, transduced A549 cells were seeded at $4x10^5$ cells/well in a 12-well plate and grown to confluency overnight. Cells were inoculated with 250 µL HCoV-OC43 serially diluted 10-fold in serum-free DMEM and incubated at 33°C for 1 h. An overlay of 1:1 Avicel (1.2%) and 2x MEM, supplemented with L-Glutamine, Sodium Bicarbonate 7.5% (Thermo Fisher Scientific), Gentamicin and 4% FCS was then added. Cells were incubated for 5 days and fixed with a final concentration of 2% Formaldehyde solution, washed twice with PBS then stained with Coomassie Blue for plaque visualisation. SARS-CoV-2 and EMCV plaque assays were performed under the same conditions but incubated for 3 days at 37°C. For MHV plaque assays, 17cl1 cells were seeded at $2x10^5$ cells/well and incubated for 30 h at 33°C.

For PR8-GFP11 virus plaque assays, MDCK-GFP1-10-Hs.ANP32A cells were seeded at a density of $1.8x10^6$ cells/well in 6-well plates and treated with 125 ng/mL doxycycline. Cells were infected with a 10^{-6} dilution of virus stock so that discrete plaques formed and an overlay of 1:1 Avicel (2.4%) and serum-free DMEM (supplemented with final concentrations of 1 µg/mL TPCK-treated trypsin, 125 ng/mL doxycycline, and 0.14% BSA) was added. 48 hpi, cells were fixed with a final concentration of 2% formaldehyde.

For infections for RT-qPCR and western blot analysis, multiplicity of infection (MOI) was calculated using virus titre calculated by plaque assay on A549 cells. Unless otherwise stated, A549 derivative cells were infected at MOI 0.01 and incubated for 72 h prior to cell collection. For experiments involving pretreatment with Ruxolitinib (RUX) or interferon, concentrations and incubation times are indicated in figure legends.

For virus titrations, virus was usually serially diluted 3- or 4-fold in serum-containing media. Media was removed from cells and replaced with diluted virus. Cells were fixed with formaldehyde 24-96 h post-transduction.

Infection experiments typically represent 3 technical replicates (Chapter 3 optimisation experiments) or at least two biological replicates, calculated as an average of two technical replicates, unless stated otherwise in the figure legend.

2.2.12. Quantifying retention of fluorescent tags in reporter viruses

Fixed cells were washed twice with PBS and scanned for GFP fluorescence on the Celigo Imaging Cytometer (Exposure ≈ 300 ms, Gain = 200). Cells were then stained with Coomassie Blue to visualise all plaques in the brightfield channel and then scanned again (Exposure = 4 ms, Gain = 200). The percentage of GFP-positive plaques was calculated by counting the total number of Coomassie-stained plaques then examining these counted plaques for GFP fluorescence in the green channel - small plaques on the very edge of the wells were excluded from this count as GFP fluorescence could not be confidently determined from the image scans due to high levels of autofluorescence. Images showing GFP fluorescence were colourised green using ImageJ software. For the PR8-GFP11 plaque assays, brightness and contrast were consistently adjusted for the GFP images shown in order to facilitate visualisation.

2.2.13. RNA extraction

Infected cells were lysed with 500 µL TRIzol reagent, frozen on dry ice and stored at -80°C. Samples were thawed on ice prior to addition of 100 µL of chloroform. Samples were shaken vigorously by hand and centrifuged at 12000 x G and 4°C for 15 minutes. The upper aqueous layer was collected and mixed with an equivalent volume of 70% ethanol. RNA was extracted using the Qiagen RNeasy kit with an on-column DNase treatment, following manufacturer's instructions. Samples were eluted in 50 µL dH_2O heated to 50°C, then concentration was measured on a Nanodrop Spectrophotometer.

2.2.14. First-strand (cDNA) synthesis

cDNA was synthesised using SuperScript IV Reverse Transcriptase (Thermo Fisher Scientific) with random hexamers primers, following manufacturer's instructions. Briefly, 1 µg RNA in an 11 µL volume was mixed with 1 µL random hexamers (50 µM, Thermo Fisher Scientific) and 1 µL dNTPs (10 mM, Promega). The mixture was heated at 65°C for 5 minutes then incubated on ice for > 1 minute. 4 µL 5X SSIV Buffer, 1 µL 0.1 M DTT, 1 µL RNase OUT and 1 µL SuperScript IV (Thermo Fisher Scientific) was then added to each sample. The reactions were incubated at 23°C for 10 minutes, 55°C for 10 minutes then 80°C for 10 minutes. Remaining RNA was degraded by adding 1 µL *E. coli* RNase H (Thermo Fisher Scientific) at 37°C for 20 minutes. Samples were stored at -20°C until use.

2.2.15. RT-qPCR

Host and viral gene expression was measured using TaqMan Fast Universal Master Mix (Applied BioSystems, 4366072) and specific TaqMan probes listed below on the QuantStudio 3 Real-Time PCR machine (Thermo Fisher Scientific). Each 20 µL reaction mix contained 1 µL cDNA, 10 µL 2x TaqMan Master Mix and 1 µL 20X Primer/Probe mix. The qPCR cycling parameters are 50°C for 2 min, 95°C for 10 min followed by 40 cycles (95°C for 15 seconds, 60°C for 1 min). Using the $2^{-\triangle\triangle Ct}$ method, viral transcript levels were normalised to ACTB, then normalised to input viral transcripts at 2 h in the respective cell line or at 48 h/72 h in the control cell line.

The following primers and probes were used: ACTB (Hs01060665_g1, Thermo Fisher Scientific), ISG15 (Hs00192713_m1, Thermo Fisher Scientific), IFIT1 (Hs03027069_s1, Thermo Fisher Scientific), HCoV-OC43_N_Fwd: 5'-CTA CTT CGC GCA CAT CCA G-3', HCoV-OC43_N_Rev: 5'-GTC AGG TGT TAC ACC AGA GG-3', HCoV-OC43_N_Probe: 5'-AGC CTC TAG TGC AGG ATC GCG TAG-3', HCoV-OC43_ORF1a_Fwd: 5'-ATG TGG TGT AAA GCA GGA AC-3', HCoV-OC43_ORF1a_Rev: 5'-GCA AGA ACA GTC CAC GGT ATA-3', HCoV-OC43_ORF1a_Probe: 5'-TAC TGG TCT GGA CGC TGT TAT GC-3'. Reactions were performed in duplicate.

2.2.16. Generation of ISG library supernatant

ISG cDNA libraries encoding human, macaque and bovine genes have been described previously (Hardy et al., 2023; Kane et al., 2016; Rihn et al., 2019). cDNAs for the mouse ISG library were generated as part of this project (section 3.2.4), alongside the cDNAs for the bat ISG library generated by Yongtao He. Briefly, libraries were generated in HEK-293T seeded in 96-well plates at a density of $3.5x10^5$ cells/well. HEK-293T were transfected with pSCRPSY, pNLGP and pVSVg at a ratio of 125 ng:25 ng:5 ng, in the presence of PEI. Supernatant was collected at 48, 72 and 96 h post-transfection and replaced with fresh medium. Leftover supernatant was pooled and used as a validation mix for screening optimisation.

2.2.17. Arrayed ISG expression screening

A549 cells were seeded in 96-well Pheno plates (PerkinElmer) at a density of ~$5x10^3$ cells/well and grown overnight. For optimisation experiments only, A549 cells were treated with 8 µg/mL polybrene. Cells were transduced with 50 µL library lentivirus supernatant and spinoculated at 500 x G for 1 h. Cells were infected 48 h post-transduction with HCoV-OC43 diluted in DMEM supplemented with 2% FCS (~$5x10^4$ PFU). After incubation at 33°C for 72 h, cells were fixed with a final concentration of 2% formaldehyde for 30 minutes, washed with PBS then permeabilised with 0.2% Triton X-100 (Sigma-Aldrich) for 5 minutes.

After cells were washed and blocked with 1% BSA for 1 h, cells were incubated with mouse anti-dsRNA IgG2a overnight at 4°C. After repeating washing and blocking steps, cells were incubated with goat anti-mouse IgG2a AlexaFluor488 and Hoechst 33342 for 1 h. Screening plates were scanned and analysed on the Celigo Imaging Cytometer (Nexcelom Biosciences) (section 2.2.16). Transduced and infected cells were gated using FlowJo v10.8. Formulae used to analyse ISG data are provided below (Table 2-5), using RStudio (Appendix 1). ISGs with <10% transduction efficiency were excluded from hit selection. For

the HCoV-OC43 miniscreen, data was normalised to the mean of 8 SCRPSY-EMPTY controls.

Table 2-5: Formulae used to analyse ISG data.

	Formula
UL	TagRFP+ dsRNA- gated population
UR	TagRFP+ dsRNA+ gated population
Percent_transduction	UL + UR
Ratio	UR ÷ Percent_transduction
Percent_VirusGrowth	(Ratio ÷ library mean) × 100
Z-score	(Ratio – library mean) ÷ library standard deviation

To measure cytotoxicity and ISRE induction, A549-ISRE:GFP cells were transduced with 50 µL/well of miniscreen library supernatant and spinoculated for 1 h at 500 x G. 120 h post-transduction, supernatant was collected and tested with the CytoTox-Glo™ Cytotoxicity assay (Promega, G9290) following manufacturer's protocols. Cells were fixed with formaldehyde and GFP+ cells were measured using the Guava EasyCyte flow cytometer (MilliPore). Data was normalised to SCRPSY-EMPTY controls.

2.2.18. Image cytometry

For ISG screening experiments, fluorescence was measured on the Celigo Imaging Cytometer (Nexcelom Biosciences) using the Expression Analysis: Target 1 + 2 + Mask setting, with the mask being the blue channel (nuclei). Cells were imaged in 3 channels: Blue 377/447 [Exposure = 50000, Gain = 200], Red 531/629 [Exposure = 3000, Gain = 200] and Green 483/536 [Exposure = 50000, Gain = 200]. Image scans were subject to the following analysis settings: % Well Mask = 97, Intensity threshold = 4, Dilation Radius = 6, Background Correction, Separate Touching Objects. Data was exported as .fcs files and gated using relevant controls on FlowJo v10.8 software.

2.2.19. Flow cytometry

The percentage of RFP+ cells and GFP+ cells were quantified using the Guava easyCyte flow cytometer (Millipore). Cells were trypsinised with 50 µL 10X trypsin-EDTA for 5 minutes at 37°C. 150 µL of DMEM was added and mixed to form a single-cell suspension. 100 µL cells were transferred into a round bottom 96-well plate containing 100 µL 4 % formaldehyde. On the flow cytometer, 10000 events/well were acquired and data was subsequently analysed using FlowJo v10.8 software.

2.2.20. Myristoylation click-chemistry reaction

A549 cells expressing RFP, p71, p69, $p71^{G2A}$ or $p69^{G2A}$ were incubated with 25 µM Myristic Acid, Azide (Thermo Fisher Scientific, C10268) for 6 h. Cells were trypsinised, washed three times with PBS and lysed in 200 µL lysis buffer (described in section 2.2.9, without TCEP) for 15 minutes on ice. Lysates were centrifuged at 12000 x G (4°C, 15 minutes) and supernatant was harvested and normalised to 1 mg/mL. Click chemistry reactions were then performed following manufacturer's protocols using Biotin Alkyne and Click-iT™ Protein Reaction Buffer Kit (Thermo Fisher Scientific), followed by methanol/chloroform precipitation. Protein was resuspended in buffer (50 mM Tris-HCl pH 8, 100 mM NaCl, 0.1% SDS) and 20 µL of equilibrated Pierce™ magnetic streptavidin beads (Thermo Fisher Scientific) were added per sample. After rotating for 1 h at room temperature, beads were washed four times before addition of 2X Bolt LDS Sample Buffer (Thermo Fisher Scientific), containing 5% BME. Samples were heated at 85°C for 3 minutes before immunoblotting for OAS2 (section 2.2.9).

2.2.21. Confocal laser scanning microscopy

A549 or modified cells were seeded at a density of $5x10^4$ cells/well onto glass coverslips. Cells were pre-treated with 1000 U/mL IFNß or infected with HCoV-OC43 at MOI 10 for 24 h (see figure legends). After washing with PBS and fixing with 4% formaldehyde for 15 minutes at room temperature, cells were permeabilised in buffer containing 0.2% BSA and 0.2% Triton X-100 in PBS for 20

minutes at room temperature. Antibodies were diluted in permeabilization buffer (see Table 2-3). Coverslips were incubated for 1 h with primary antibody followed by secondary antibody and Hoechst for 1 h. Maximum intensity projection images of cell monolayers were acquired with an Airyscan Fast detector fitted to a Zeiss LSM880 confocal microscope. Acquired images were analysed using ZEN software.

2.2.22. Modelling OAS2-RNA interactions

OAS2-dsRNA complex structural predictions were generated using AlphaFold3 public server (www.alphafoldserver.com) (Abramson et al., 2024). The server generates 5 ranked models per complex and the top ranked model (_0) was used for forming testable hypotheses. Structural analysis and figure preparation were performed with ChimeraX (version 1.8).

2.2.23. Software

Protein sequences were analysed using ClustalW on DNADynamo (Blue Tractor Software LTD). Graphs were generated using GraphPad Prism v10. Schematic illustrations were generated using BioRender software (BioRender.com). Image and flow cytometry data were gated using FlowJo v10.8. ISG screening data was analysed using RStudio. Fluorescent plaque assay images were edited with ImageJ and GIMP2 software v.2.10.32.

2.2.24. Statistical analysis

Statistical analyses were performed using GraphPad Prism v10, on figures with 3 biological replicates. Details of statistical tests are indicated in the figure legends. $^{ns}p > 0.05$, *$p < 0.05$, **$p < 0.01$, ***$p < 0.001$, ****$p < 0.0001$.

3. An ISG screening platform utilising dsRNA immunostaining

3.1. Introduction

One of the first ISGs identified was *Mx1*; mice homozygous for the Mx1 gene were resistant to influenza infection but succumbed to infection when treated with antibodies against interferon (Haller et al., 1979). Like Mx1, the link between expression of an individual gene and resistance to viral infection was how many of the first ISGs were discovered. Developments in sequencing technologies have accelerated our knowledge of genes upregulated in response to interferon, which in turn has informed ISG screening approaches against viruses. These ISG screens have enabled the antiviral potency and specificity of ISGs to be characterised through two main approaches: gain-of-function or loss-of-function screens (Jones et al., 2021). This introduction will particularly highlight ISGs identified in recent screens that target coronaviruses (Le Pen and Rice, 2024), most of which were performed against SARS-CoV-2 during the COVID-19 pandemic.

3.1.1. Methods of ISG screening: Gain of function

Gain-of-function screens, also known as overexpression or cDNA screens, involve examining the effect of ectopic expression of ISGs on viral infection. The first larger scale ISG screens involved transducing an ISG lentivirus library, containing 389 human ISGs, into cells prior to virus infection (Schoggins et al., 2011). Many ISG libraries are now based on the SCRPSY lentiviral vector which enables dual expression of both an ISG ORF and TagRFP, from an early, spliced HIV-1 mRNA and a late, unspliced HIV-1 mRNA, respectively (Fig 3-1 A). Additionally, a puromycin resistance gene is encoded in the same ORF as TagRFP, separated by a 2A ribosomal skipping peptide, allowing for antibiotic selection of transduced cells.

The standard arrayed expression screening approach involves transducing cells with the lentiviral vector (one ISG per well) before infection with a reporter virus encoding a green fluorescent protein (GFP). Virus infection is measured using flow cytometry, by determining the ratio of GFP+ cells in the total TagRFP+ positive population; TagRFP expression is thus used as a proxy for ISG expression. This approach can be modified (Table 3-1), by immunostaining with an antibody specific to the virus being screened, followed by a secondary antibody conjugated to a fluorescent dye and measuring infection by flow cytometry or image cytometry (Fig 3-1 C).

The ISG lentivirus library has also been expanded by adding ISGs from other species. At the Centre for Virus Research, in addition to 543 human ISGs, there are now 345 macaque, 289 bovine, 372 mouse and 82 bat ISGs (Hardy et al., 2023; Kane et al., 2016; Rihn et al., 2019); there are multiple copies or different isoforms of some of the ISGs, so the number of ORFs in each library is even higher (Fig 3-1 B). The yet unpublished mouse and bat ISG libraries have been developed throughout this project (section 3.2.4), to represent coronavirus reservoir species. Indeed, the ISGs from the bat library originate from horseshoe bats of the *Rhinolophus* genus, implicated in the origin of SARS-CoV-2 (Zhou et al., 2021).

GOF screens identify regulatory ISGs (exerting positive or negative feedback on the immune response) and ISGs with a direct antiviral effect. To further focus screening on characterising directly acting ISGs instead of ISGs triggering antiviral signalling, modified cell lines deficient in IFN signalling have been used. Such cell lines include STAT1-deficient or IRF3-deficient fibroblasts, or IRF3-deficient A549 cells (Lin et al., 2020; Schoggins et al., 2011; Wickenhagen et al., 2021). This can also be examined post-screening, by transducing the entire ISG library or select ISGs into reporter cell lines modified to express luciferase or GFP under the control of an IFNß promoter or ISRE (Kane et al., 2016; Wickenhagen et al., 2021).

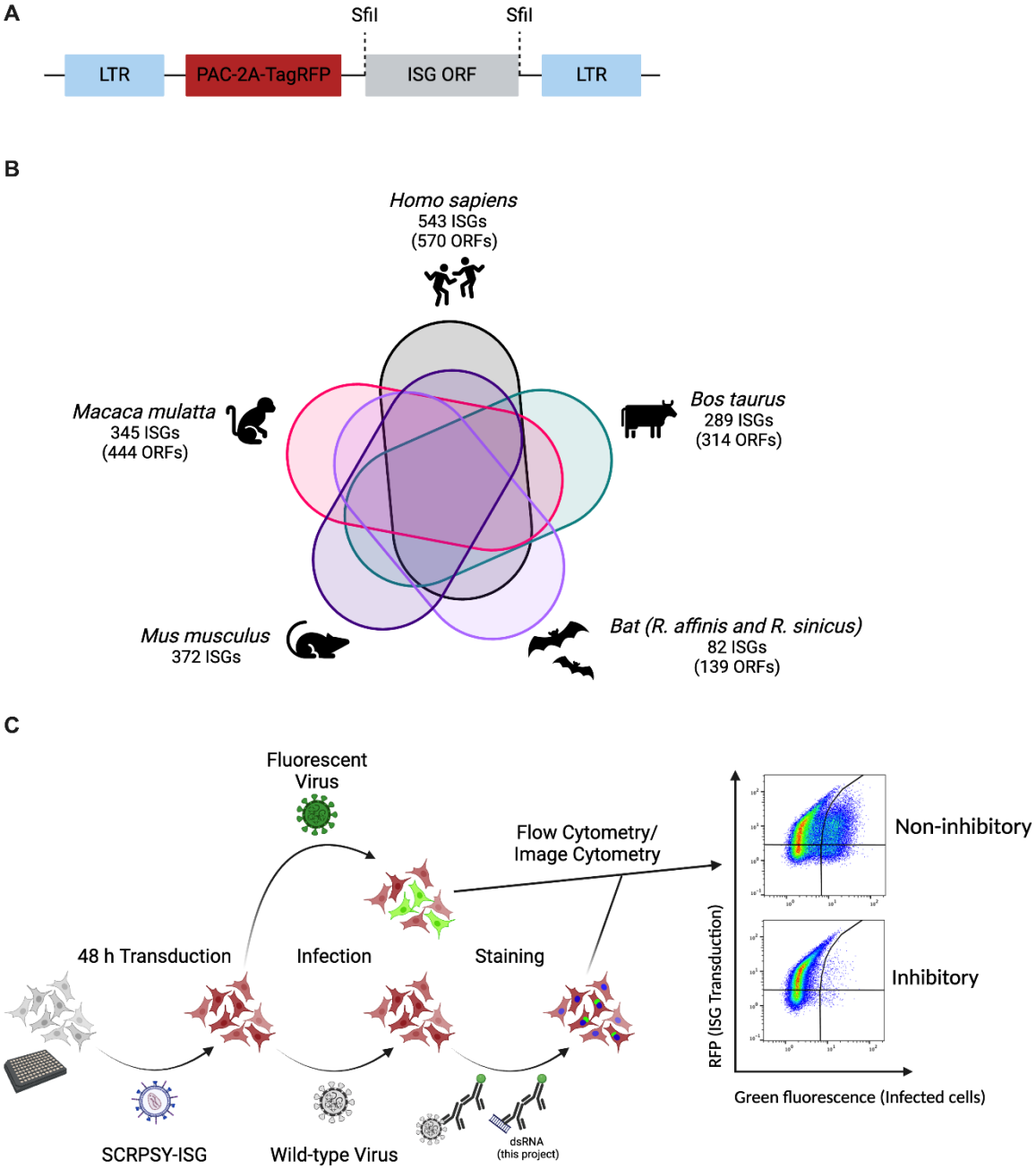

Figure 3-1: Methodology for gain-of-function screens.(**A**) Schematic of the SCRPSY lentiviral vector encoding an individual ISG and TagRFP under different promoters. (**B**) Number of genes and open reading frames for the different ISG libraries available at the Centre for Virus Research. (**C**) Schematic of approaches used for cDNA screening with the SCRPSY ISG library to identify antiviral genes.

Table 3-1: Gain-of-function screens and methods of virus quantification.

Viruses screened	Quantification						Reference
	Flow Cytometry	Image Cytometry	Microplate reader	Fluorescent Reporter Virus	Virus-specific antibody	Luciferase reporter	
CHIKV, HCV, HIV-1, VEEV, WNV, YFV	Y			Y			(Schoggins et al., 2011)
BUNV, CVB, EAV, HMPV, IAV, MeV, NDV, ONNV, PIV3, PV, RSV, SINV-A, SINV-G, VV	Y			Y			(Schoggins et al., 2014)
IAV		Y			Y Nucleoprotein		(Dittmann et al., 2015)
HIV-1	Y			Y			(Kane et al., 2016)
BUNV	Y			Y			(Feng et al., 2018)
VSV	Y			Y			(Rihn et al., 2019)
EBOV			Y			Y	(Kuroda et al., 2020)
HCoV-229E		Y			Y Nucleocapsid		(Pfaender et al., 2020)
HCMV			Y	Y			(Lin et al., 2020)
WNV	Y			Y			(Hanners et al., 2021)
SARS-CoV-2	Y			Y			(Wickenhagen et al., 2021)
HCV			Y			Y	(Bamford et al., 2022)
BTV	Y			Y			(Hardy et al., 2023)
IAV	Y			Y			(Pinto et al., 2023)
USUV, WNV	Y				Y Envelope		(Zoladek et al., 2024)

Bluetongue virus (BTV); Bunyamwera virus (BUNV); Chikungunya virus (CHIKV); Coxsackie B virus (CVB); Equine arterivirus (EAV); Ebola virus (EBOV); Human coronavirus 229E (HCoV-229E); Hepatitis C virus (HCV); Human cytomegalovirus (HCMV); Human immunodeficiency virus type 1 (HIV-1); Human metapneumovirus (HMPV); Influenza A virus (IAV); Measles virus (MeV); Newcastle disease virus (NDV); O'nyong'nyong virus (ONNV); Human parainfluenza virus type 3 (PIV3); Poliovirus (PV); Respiratory syncytial virus (RSV);Severe acute respiratory syndrome coronavirus 2 (SARS-CoV-2); Sindbis virus AR86 (SINV-A); Sindis virus Girdwood (SINV-G); Usutu virus (USUV); Venezuelan equine encephalitis virus (VEEV); Indiana vesiculovirus (VSV); West Nile virus (WNV); Yellow fever virus (YFV).

3.1.2. Anti-coronaviral ISGs identified by gain-of-function screening

One ISG identified as having anti-coronaviral activity through gain-of-function screening is lymphocyte antigen 6 complex locus E (*LY6E)*. In this study, Huh7 cells were transduced with a human ISG lentivirus library and infected with HCoV-229E (Pfaender et al., 2020). LY6E was subsequently stably expressed in cells and was found to be antiviral against HCoV-OC43, MERS-CoV, SARS-CoV-1, SARS-CoV-2 and MHV. This effect was also observed *in vivo*, with mice generated with immune cells deficient in *Ly6e* showing increased susceptibility to MHV

infection. This antiviral effect is thought to be due to LY6E interfering with spike-mediated membrane fusion.

Another ISG identified to interfere with coronavirus entry is cholesterol 25-hydroxylase (*CH25H*), which converts cholesterol into 25-hydroxycholesterol. This was identified in a small-scale overexpression screen, involving 57 human ISGs, against VSV-SARS-CoV-1 and VSV-SARS-CoV-2 pseudotypes (Zang et al., 2020). It has been hypothesised this is due to endosomal and plasma membranes having reduced cholesterol, affecting virus-cell membrane fusion.

ISGs inhibiting coronaviruses post-entry have also been identified by GOF screening, including *OAS1*. One such study used the standard overexpression screening method, where A549-ACE2-N^{pro} cells were transduced with the human and macaque ISG libraries and infected with a GFP-expressing SARS-CoV-2 reporter virus (Wickenhagen et al., 2021); N^{Pro} is a protein expressed by bovine viral diarrhoea virus (BVDV) that binds IRF3 and targets it for degradation, hence making the cells IRF3-deficient (Hilton et al., 2006). Further investigation revealed this OAS1-mediated inhibition occurred via the canonical pathway involving downstream activation of RNase L (Wickenhagen et al., 2021). This discovery of the anti-SARS-CoV-2 activity of OAS1 was supported by another gain-of-function screen that utilises CRISPR activation (CRISPRa). In this alternative approach, 1266 guide RNAs directed a catalytically inactive Cas9 fused to transcriptional activators, which enhanced expression of 414 downstream ISGs (Danziger et al., 2022). Both screens also identified LY6E and nuclear receptor coactivator 7 (NCOA7) as a restriction factor against SARS-CoV-2. In a separate study, ectopic expression and gene depletion confirmed the antiviral activity of the short isoform of NCOA7; it was proposed that NCOA7 targets the endocytic route of SARS-CoV-2 entry by interaction with the vacuolar H^+-ATPase (V-ATPase) resulting in acidification of the vesicle (Khan et al., 2021).

3.1.3. Methods of ISG screening: Loss-of-function

The development of CRISPR/Cas9 technology has advanced our understanding of virus-host interactions and has increasingly become the primary method of identifying host restriction factors of viruses, in addition to host factors the virus depends on for replication. To "knockout" genes, a complementary single guide RNA (gRNA) directs the Cas9 enzyme to the gene of interest, resulting in DNA cleavage. These double-stranded breaks in the DNA are repaired by non-homologous end joining (NHEJ); this error-prone pathway introduces insertions and deletions into the gene of interest, which can disrupt gene function (Doudna and Charpentier, 2014).

Like cDNA screens, CRISPR/Cas9 screens first involve transducing a lentiviral vector encoding antibiotic resistance genes, a gRNA and Cas9. Many screens have utilised genome-wide human CRISPR KO libraries such as the GeCKO v2 library (123,411 gRNAs targeting 19,050 genes (Sanjana et al., 2014)) or the Brunello library (76,441 gRNAs targeting 19,114 genes (Doench et al., 2016)). More targeted human ISG CRISPR KO libraries were also developed, containing 15,416 gRNAs targeting 1,902 ISGs (Roesch et al., 2018). In contrast to SCRPSY-based screens, these libraries can be used in arrayed or pooled format, the latter being cheaper to perform and less labour intensive. Arrayed approaches are more effective at examining proviral and antiviral genes in one screen, and there is no competition between gene KO, which could result in non-essential genes being depleted in pooled format and appearing essential.

An example CRISPR KO screen, based on methods of recent screens, is described next (Mac Kain et al., 2022; McDougal et al., 2023; Xu et al., 2023). Successfully transduced cells are selected for by addition of the relative antibiotic, usually puromycin. For screens aimed at identifying restriction factors, cells are pre-treated with or without IFN before infection with the virus of interest; many screens have used reporter viruses encoding fluorescent proteins or antibodies specific for viral proteins. Infected cells were then obtained by fluorescence-activated cell sorting (FACS). Genomic DNA was extracted, PCR

amplified and subjected to next-generation sequencing to identify enriched gRNAs.

3.1.4. Anti-coronaviral ISGs identified by loss-of-function screening

Two LOF screens identified phospholipid scramblase 1 (PLSCR1) as a restriction factor of SARS-CoV-2. In one study, Huh7.5 and A549-ACE2 cells were transduced with the pooled GeCKO v2 library and subject to IFN-ɣ pretreatment before SARS-CoV-2 infection (Xu et al., 2023). The other study performed an arrayed CRISPR screen in Huh7.5 cells, using the human genome Edit-R crRNA library (targeting 16,790 genes) and pre-treatment with IFN-α before infection with SARS-CoV-2 (Le Pen et al., 2024). Only 56 significant gene hits overlapped between these screens, and anti-coronaviral ISGs discussed in this introduction (DAXX, IFI6, LY6E) differed in their hit status between screens, likely due to differences in methods. However, both screens concluded that PLSCR1, which is ubiquitously expressed but enhanced by IFN stimulation, inhibits spike-mediated entry of SARS-CoV-2. Further experiments by these authors, using pseudoviruses containing coronavirus spike proteins, suggest PLSCR1 possesses differential antiviral activity towards coronaviruses; MERS-CoV was potently inhibited, but only modest inhibition was observed with seasonal coronaviruses such as HCoV-OC43.

Another ISG whose basal expression is increased by IFN stimulation is Death domain-associated protein (DAXX). DAXX was identified as restricting SARS-CoV-2 replication in a LOF screen using a CRISPR KO library specifically targeting ISGs (Mac Kain et al., 2022); it should be noted that DAXX mRNA did not significantly increase upon IFN stimulation in A549-ACE2 used in this screen, so its “ISGness” is context-dependent, unlike classic ISGs like Mx1 and OAS1. The authors demonstrated that DAXX is located in the nucleus of uninfected cells, but upon SARS-CoV-2 infection, DAXX relocates to the cytoplasm. Cell entry of pseudotypes expressing SARS-CoV-2 spike was unaffected by DAXX KO, suggesting this antiviral mechanism targets a post-entry stage of the SARS-CoV-2 replication cycle.

Although not chosen as the hit characterised in the aforementioned studies, interferon alpha inducible protein 6 (IFI6) was identified as having antiviral activity in two LOF screens and two GOF screens against SARS-CoV-2 (Table 3-2). IFI6 is localised to the endoplasmic reticulum, where coronavirus replication occurs, and was also revealed to have anti-flaviviral activity in a genome-wide CRISPR KO screen against yellow fever virus (YFV) (Richardson et al., 2018). The study concludes IFI6 prophylactically impairs the ability of flaviviruses to form their single membrane invaginations in the ER required for genome replication. However, the flavivirus Hepatitis C Virus (HCV) and HCoV-OC43, which form double-membrane vesicles protruding from the ER, were unaffected by ectopic expression of IFI6. Therefore, it is not yet clear how IFI6 impairs SARS-CoV-2 replication.

Table 3-2: ISGs identified in genetic screens described in this section.

Study	Cell line	Virus	Screen type	Candidate antiviral hit?						
				CH25H	DAXX	IFI6	LY6E	NCOA7	OAS1	PLSCR1
(Pfaender et al., 2020)	Huh7	HCoV-229E	GOF	-	-	N	Y*	-	N	N
(Wickenhagen et al., 2021)	A549-ACE2-N^{pro}	SARS-CoV-2	GOF	-	-	Y	Y	Y	Y*	N
(Zang et al., 2020)	HEK293-ACE2	VSV-SARS-CoV-1 VSV-SARS-CoV-2	GOF	Y*	-	Y	Y	-	-	-
(Danziger et al., 2022)	A549-ACE2 (+/- △STAT1)	SARS-CoV-2	GOF	-	-	N	Y	Y	Y*	-
(Mac Kain et al., 2022)	A549-ACE2	SARS-CoV-2	LOF	N	Y*	Y	Y	N	N	N
(Xu et al., 2023)	Huh7.5 A549-ACE2	SARS-CoV-2	LOF	N	N	N	Y	N	N	Y*
(Le Pen et al., 2024)	Huh7.5	SARS-CoV-2	LOF	N	Y	Y	N	N	N	Y*

Hit (Y). Not-hit (N). Not present in library (-). Characterised in study (*).

3.1.5. Advantages of gain-of-function screens

Performing GOF screens to identify antiviral restriction factors has some advantages, with the most notable perhaps being the capacity for comparative screening given the adaptability of the approach. ISG overexpression screens

against six (-)ssRNA viruses and seven (+)ssRNA viruses revealed that similar ISGs targeted viruses with related genome types (Schoggins et al., 2014). Comparative screening can also reveal differences in the antiviral activity of ISGs against viruses of the same family. Usutu virus (USUV) and West Nile virus (WNV) are related flaviviruses transmitted by mosquitoes, but a SCRPSY-based miniscreen revealed WNV was inhibited by the 3'-5' exonuclease ISG20 while USUV was not. Subsequent characterisation revealed that USUV can resist ISG20-mediated genome degradation via a structure in the 3'-UTR of the genome (Zoladek et al., 2024).

The ability of an individual ISG to differentially restrict strains of the same virus can also be identified with cDNA screening. An ISG screen using the human and macaque lentivirus libraries against three influenza A virus strains discovered the ISGs BTN3A1 and BTN3A3 inhibited the avian strain (Mallard), whereas the mammalian strains (PR8 and Cal04) were resistant (Pinto et al., 2023). A residue in the viral nucleoprotein determines sensitivity to BTN3A3, and avian strains that have exhibited zoonotic transmission into humans have evolved to evade BTN3A3. Therefore, comparative ISG screening helped reveal BTN3A3 evasion as a potential risk factor for avian IAV spillover into humans.

The availability of multi-species ISG libraries increases the number of genes screened but also has the potential to identify species-specific differences in ISG activity. Human and macaque ISG20 was identified in an ISG screen as having antiviral activity against Bunyamwera orthobunyavirus (BUNV). Further testing against 15 bunyaviruses showed human ISG20 usually exhibited more potent restriction than macaque ISG20, except in the case of Capim orthobunyavirus (CAPV). These ISG20 orthologs only differ by four amino acids, suggesting these changes may influence virus specificity of the proteins (Feng et al., 2018). Since both orthologues were expressed against an isogenic background, any differences in antiviral specificity are presumed to stem from the protein itself.

cDNA screening is limited to testing only genes present in the library. This may be considered an advantage, as it focuses the screen on ISGs in many species,

whereas many CRISPR screens utilise genome-wide libraries from one species. Additionally, in screening experiments where virus inhibition by IFN is not substantial, ISGs having a moderate effect in the IFN-induced antiviral state are more likely to be identified using cDNA screening.

3.1.6. Disadvantages of gain-of-function screens

Many disadvantages of GOF screens relate to the transduction of the ISG-encoding vector. As gene expression is no longer at endogenous levels, this "artificial" expression may result in apparent virus restriction or cell death as an artefact of ISG-mediated toxicity. Additionally, the library is biased against the successful transduction of long genes owing to packaging limits of the lentiviral system. This means long transcripts are either excluded from the library preparation or suffer low viral titres and corresponding poor transduction efficiencies in the target cell population.

A significant limitation of GOF screens is that ISGs that work as part of a complex are not routinely identified. This is exemplified by GOF and LOF screens performed on the alphavirus Venezuelan equine encephalitis virus (VEEV). There was no apparent substantial reduction in VEEV infectivity in STAT1$^{-/-}$ fibroblasts when IFIT1 (67.2%) and IFIT3 (94.9%) were overexpressed (Schoggins et al., 2011). However, IFIT1 and IFIT3 appeared as hits in LOF screens against VEEV-infected U-2 OS cells transduced with the Brunello genome-wide library or an ISG CRISPR KO library (McDougal et al., 2023). IFIT1 binds cap0 RNA (capped RNA lacking 2'-O-methylation), minimising translation of viral RNA. It has been reported human IFIT3 associates with IFIT1 and enhances its recognition of cap0 RNA. Expression of IFIT1 in doxycycline-inducible 293T-IFIT1 cells did not restrict the VEEV strain TC83 when trans-complemented with a firefly luciferase control, but co-expression of IFIT3 resulted in a substantial decrease of VEEV infection (Johnson et al., 2018).

3.1.7. Advantages of loss-of-function screens

LOF screens are effective at targeting specific genes and reducing gene expression. Compared to cDNA libraries, CRISPR KO libraries are commercially available and can identify genes that work in a complex. Perhaps the main advantage of CRISPR KO screening compared to cDNA screening is that it examines the importance of specific gene expression at a physiological level; virus inhibition may be due to an artefact of gene overexpression, such as dysregulation of a cellular process, instead of direct antiviral activity. This gene knockout may be more reflective of disease states, as susceptibility to disease is often due to deleterious mutations of genes. Indeed, loss-of-function variants in genes involved in the type I IFN signalling pathway were identified in patients with severe COVID-19 (Zhang et al., 2020).

CRISPR KO libraries, including those designed to examine just ISGs, are generally more extensive than the cDNA libraries available, as they have less strict inclusion criteria, such as the fold change upon IFN stimulation. This enables the identification of more "intrinsic" ISGs, i.e. expressed at basal levels and only weakly induced by IFN, such as DAXX. DAXX was not included in any GOF screen libraries discussed in this section (Table 3-2), so its antiviral activity would not have been discovered without the larger CRISPR libraries.

3.1.8. Disadvantages of loss-of-function screens

LOF screens are more labour intensive – there is an absolute requirement for antibiotic selection, and the sequencing step means these screens require longer timeframes than cDNA screens. Large, complex data are generated, so extensive bioinformatic analysis is needed, especially if screening is conducted in pooled format.

Even though CRISPR/Cas9 technology is quite effective, there is still a high chance of off-target effects, meaning the Cas9 nuclease can target unpredicted genomic sites in addition to those to which it is intended to cut, which could result

in false hits. Knockout of essential genes can result in cell death, so if these genes possess antiviral activity, it would not be identified using this screening approach. The IFN response is also considerably redundant; multiple genes can perform the same or similar function, so when one gene is depleted, another gene can sometimes compensate for its loss, and then its antiviral effect may not be detected.

In summary, GOF and LOF screens are powerful approaches to identify antiviral genes, despite their different limitations. Here, I present a new methodology for GOF screening using previously described ISG lentivirus libraries. I develop a method of measuring virus infection by detecting infection-related dsRNA rather than virus-derived protein antigens, as frequently done before. The goal is to broaden the applicability of ISG screening methodology to allow the investigation of antiviral mechanisms against diverse viruses without needing virus-specific reagents. This independence from reporter virus constructs is enabled by the broad generation of dsRNA during infection by both DNA and RNA viruses. In contrast to CRISPR-based screening, this approach is easier to scale, especially if paired with automated pipetting stations during the immunostaining stage, at much lower costs. This is because it requires small volumes of readily available antibodies, in comparison to the higher costs associated with sequencing. It is therefore easier to modify this approach for comparative screening, by changing the cell line infected or by using different viruses/isolates of the same virus, in a cost-effective fashion. As described in the following section, this screening methodology can successfully identify ISGs that specifically target an RNA virus.

3.2. Results

3.2.1. Recognition of Contribution

Table 3-3: List of people and their contributions to experimental work.

	Contribution
Arthur Wickenhagen	Generation of the SARS-CoV-2 miniscreen library (previous lab project)
Douglas Stewart	Assistance in the transformations, overnight cultures and minipreps required to make the mouse ISG library
Yongtao He	Experiments optimising DNA extraction protocol for library generation Generating plasmid DNA for the bat ISG library

3.2.2. Measuring virus infection by dsRNA staining using the Celigo Imaging Cytometer

At the Centre for Virus Research, the standard protocol for ISG screening utilises a recombinant fluorescent virus to measure infection by flow cytometry. However, there were few, if any, reporter virus systems available for human seasonal CoVs, such as HCoV-OC43, at the beginning of my PhD (Shen et al., 2016). I therefore decided to design a new protocol for ISG screening that uses dsRNA immunostaining to measure virus infection (Fig 3-1 C). Other GOF studies previously screened wild-type coronaviruses using immunostaining with antibodies against specific protein components, such as the HCoV-229E N protein (Pfaender et al., 2020). Immunostaining a broad target like dsRNA is not frequently used for screening; one study that employed this tactic utilised dsRNA immunostaining in combination with fluorescence microscopy to identify host factors required for coronavirus replication (Schneider et al., 2021).

Like other (+)ssRNA viruses, coronaviruses replicate their genomes via a dsRNA replicative intermediate (V'kovski et al., 2021). dsRNA is an activator of the innate immune response, so it is not expressed at high levels in uninfected cells (Park and Iwasaki, 2020). A new ISG expression screening protocol was thus developed that utilises immunostaining of dsRNA with quantification of infection by image cytometry. dsRNA was chosen as a staining target over more virus-

specific antibodies so that this protocol could be adapted to screen other (+)ssRNA viruses that may not have readily available reporter virus systems or antibodies, such as emerging viruses or animal viruses. At the time, successful ISG screens had been performed against HCoV-229E and SARS-CoV-2, so I decided to use HCoV-OC43 as the model virus to optimise my protocol. This was because it was a betacoronavirus like SARS-CoV-2 but is instead thought to have an ancestral reservoir in a rodent (Corman et al., 2018); given the diversity in ISGs expressed by different species (Shaw et al., 2017), it is plausible that the ISGs that inhibit a given virus may have been influenced by the ancestral reservoir, as suggested in (Wickenhagen et al., 2021).

Using the Celigo Imaging Cytometer, immunostaining allows dsRNA staining to be measured in the green fluorescence channel via a secondary antibody conjugated to the AlexaFluor488 dye. Additionally, nuclei are stained with Hoechst and measured in the blue fluorescence channel. I then quantified virus infection from high-resolution scans of the whole well. To do this, the cell outline must first be defined in a fluorescence channel, known as a mask. Ideally, we would have used a cytoplasmic stain, but I did not have this during the preliminary experiments, so Hoechst was used instead. An individual cell is therefore identified by the Hoechst-stained nucleus, and the area is then dilated to include most of the cytoplasm (Fig 3-2 A). This approach worked well given that coronaviruses replicate in double-membrane vesicles derived from the ER, and thus dsRNA staining presents close to the nucleus (V'kovski et al., 2021)(Fig 3-2 B).

In a preliminary experiment to determine the suitability of this protocol for ISG screening, HCoV-OC43 was titrated on A549 cells and fixed at multiple timepoints (Fig 3-2 C). A549 cells were the cell line of choice because they are a lung adenocarcinoma line permissive to respiratory virus HCoV-OC43 replication. Moreover, the SARS-CoV-2 ISG screen, performed by my colleagues, used A549-derived cells, and I wanted to keep the protocols as comparable as possible (Wickenhagen et al., 2021). In this experiment, the signal-to-noise ratio was high,

with dsRNA+ cells increasing in number over time and with increasing doses of HCoV-OC43, while background staining remained low in uninfected controls. When A549 cells were pretreated with type I IFN for 24 h, the number of dsRNA+ cells was drastically reduced at the highest doses of IFNβ1, showing that HCoV-OC43 is sensitive to ISGs within these cells (Fig 3-2 D). Combined, these data demonstrate that dsRNA staining is a sensitive method for quantifying viral infection.

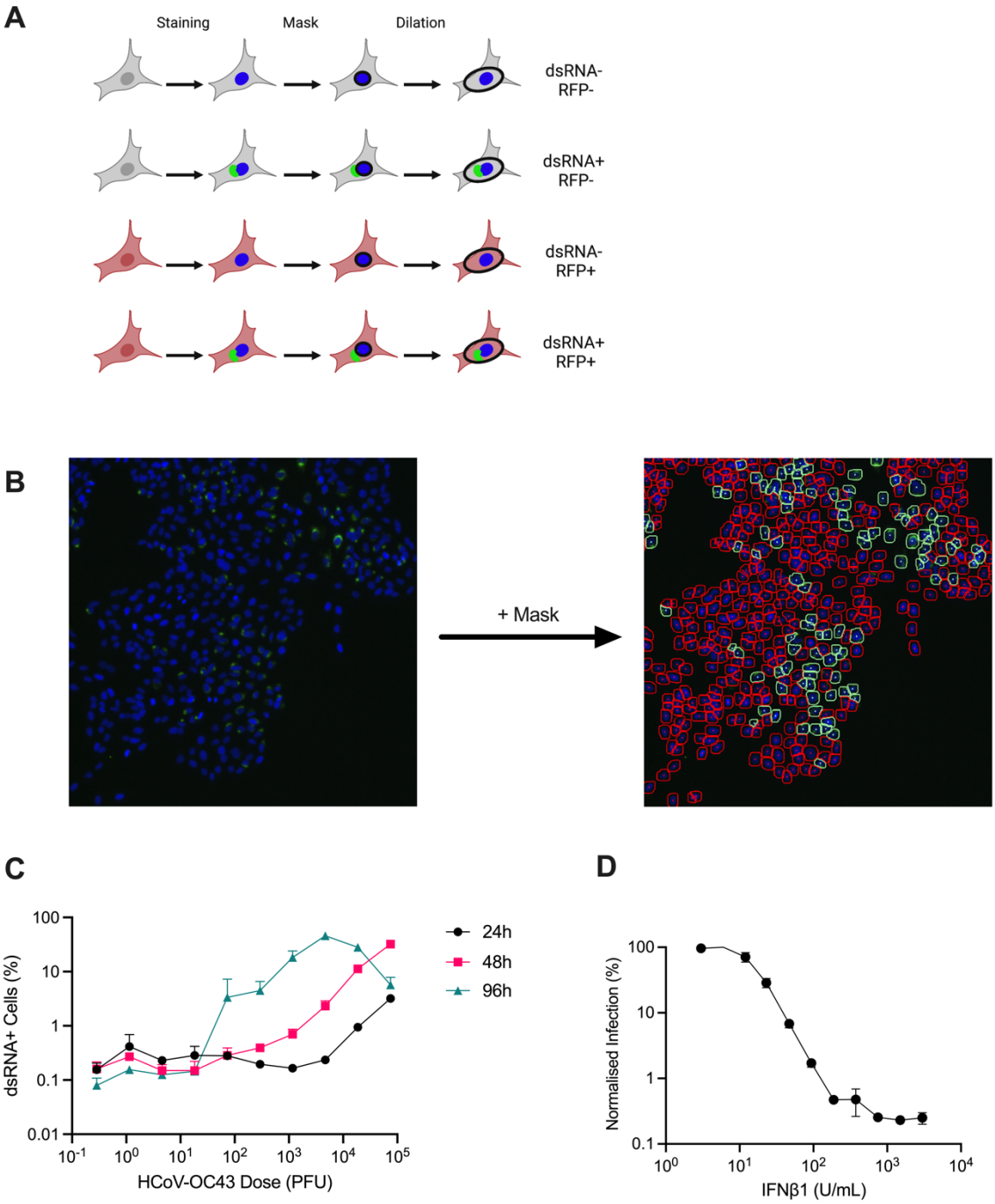

Figure 3-2: Quantifying HCoV-OC43 infection using the Celigo Imaging Cytometer. (**A**) Schematic representation of how the "mask" approach on the Celigo Imaging Cytometer is used to measure transduction efficiency and virus infection, via dsRNA staining. (**B**) Representative image of HCoV-OC43 infected A549 cells stained with anti-dsRNA (green) and nucleic acid stain Hoechst (blue). After Mask settings are applied, cells are categorised into uninfected (red outline) and infected (green outline). (**C**) A549 cells were infected with serial dilutions of HCoV-OC43, fixed at multiple timepoints, and stained with anti-dsRNA antibody and Hoechst before dsRNA+ cells were quantified. (**D**) A549 cells were pre-treated with increasing concentrations of IFNβ1 for 24 h prior to infection with HCoV-OC43 for 72 h (~5x10^4 PFU). Infected cells were quantified as in (C) and normalised to mock-treated cells. (**C-D**) The mean and SD of one independent experiment are shown.

3.2.3. Optimisation of conditions for ISG screening

For ISG screening, transduction with the SCRPSY lentiviral vector results in RFP expression, in addition to ISG expression, allowing transduction efficiency to be measured in the red fluorescence channel. Similar to flow cytometry, thresholds for transduction and infection are then set based on mock-transduced, mock-infected and transduced mock-infected controls, respectively (Fig 3-3 A). If red or green fluorescence is detected above threshold in this dilated area, the cells are classified as RFP+ and dsRNA+, respectively. These cells can be gated using the Celigo software or exported as .fcs files, and gating can be performed using flow cytometry software, such as FlowJo. As before, I titrated HCoV-OC43 on A549 cells, this time transduced with a fixed dose of SCRPSY-EMPTY lentivirus and fixed at multiple timepoints (Fig 3-3 B). The infection level was similar to mock transduced cells, confirming that transduction with a SCRPSY vector does not affect HCoV-OC43 replication. An infection level of 30-50% is optimal for ISG screening; this can be obtained in A549 cells with an incubation period of over 48 hours.

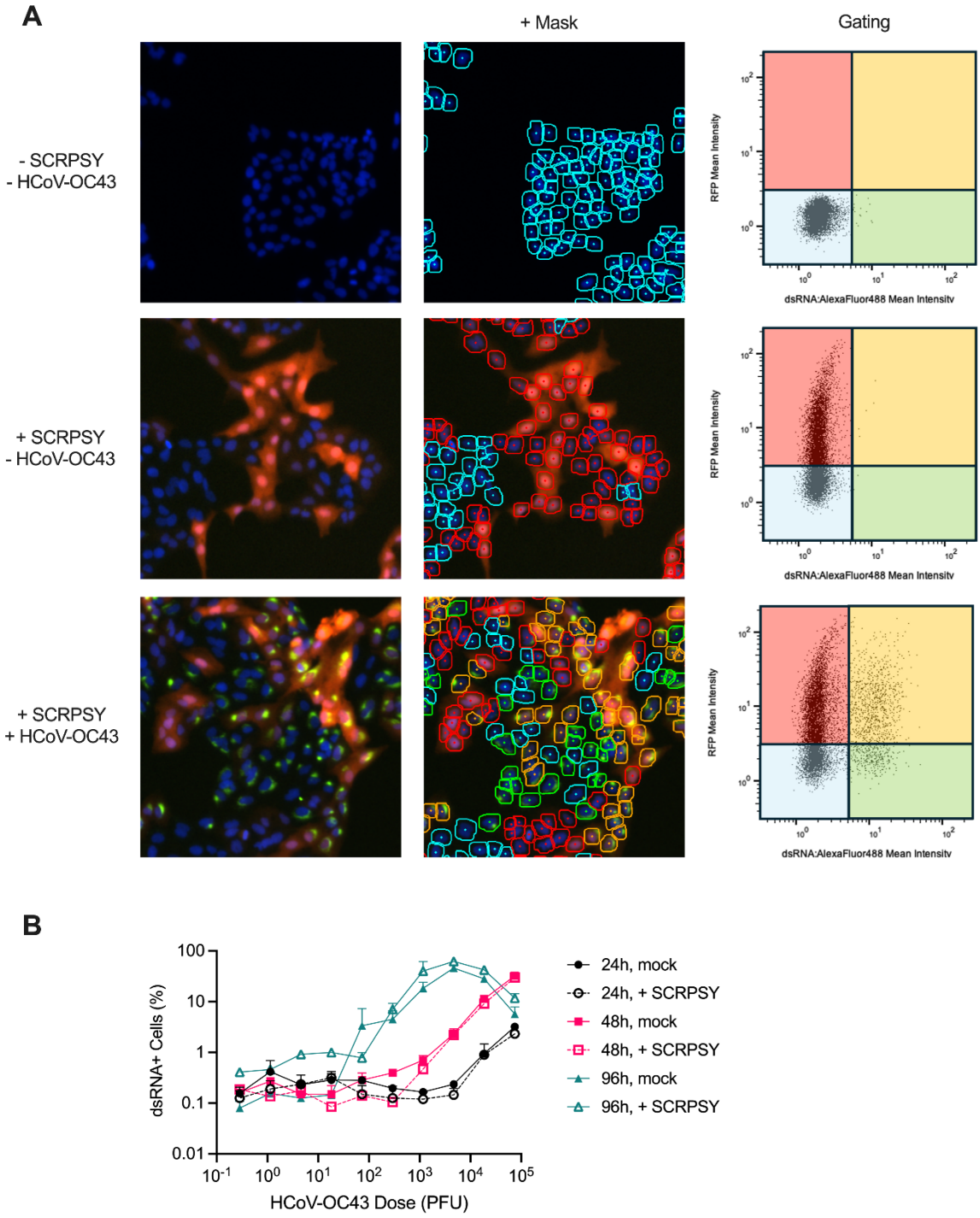

Figure 3-3: Quantifying ISG expression for screening experiments.(**A**) A549 cells were transduced with 20 µL/well of SCRPSY-EMPTY lentivirus-containing supernatant for 48 h prior to infection with 4-fold serial dilutions of HCoV-OC43. Fixed cells were stained with anti-dsRNA (green) and Hoechst (blue), then gated into the following classes on the Celigo Imaging Cytometer: RFP- dsRNA- (light blue), RFP+ dsRNA- (red), RFP+ dsRNA+ (orange) and RFP- dsRNA+ (green). Representative images of one independent experiment are shown. (**B**) Quantification of transduced (RFP+) dsRNA+ cells from (A) superimposed with mock-transduced infected cells from (Fig 3-2 C). The mean and SD for one independent experiment are shown.

Unlike flow cytometry, where cells are first dissociated from tissue culture surfaces before fixation, this protocol uses formaldehyde to fix A549 cells to the plate well for scanning. This means that the initial cell seeding density is of even greater importance because if the seeding density is too high, the Celigo software is unable to distinguish individual cells from a monolayer, resulting in inaccurate quantification of cell number. To determine the optimal seeding density, the experiment described above was performed with different input cell concentrations (Fig 3-4 A-B). From this, I concluded the optimum concentration was $5x10^3$ cells/well, as there was still space in the monolayer and there were approximately $4x10^4$ cells/well 120 h post-transduction, which is greater than the usual number of cells (~10000 events) analysed for screening by flow cytometry. As screening also requires a large volume of virus, a new stock of HCoV-OC43 was propagated for subsequent experiments. I titrated this stock on A549 cells and measured dsRNA+ cells at 48 h and 72 hpi (Fig 3-4 C); I decided on a virus dose of ~$5x10^4$ PFU/well and an incubation time of 72 h for screening to ensure the 30-50% infection optimum is satisfied.

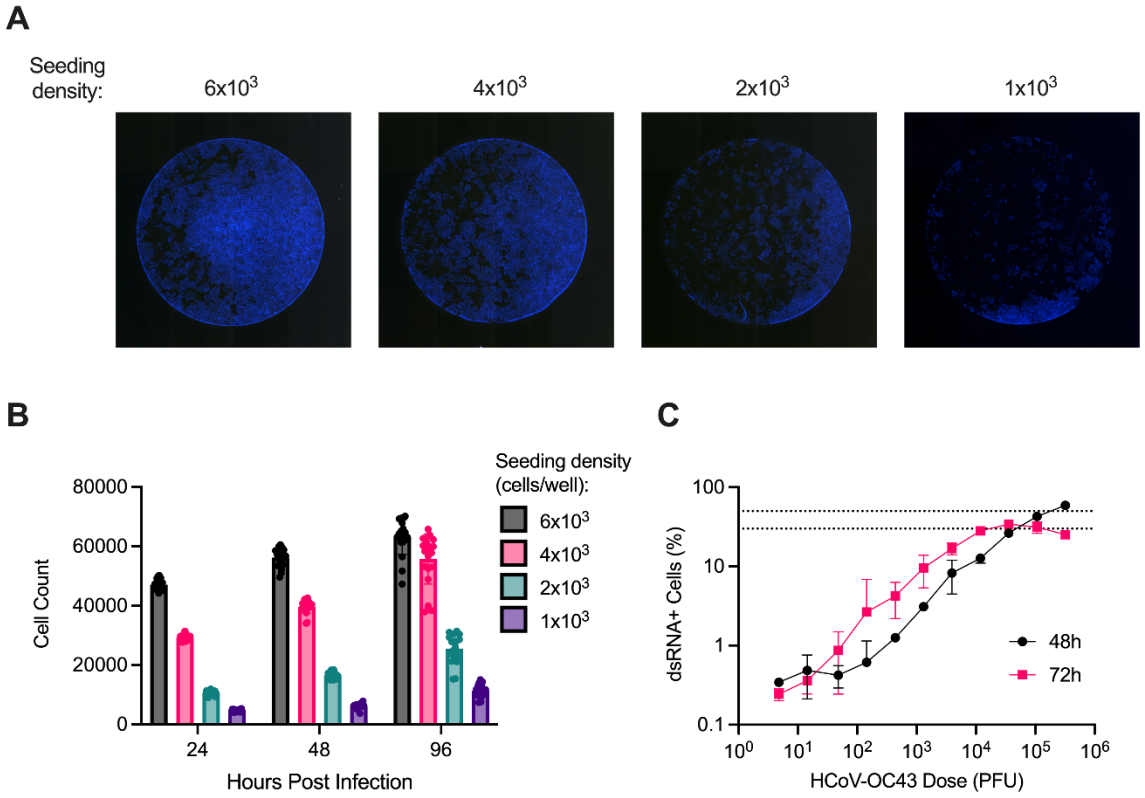

Figure 3-4: Optimisation of cell and virus conditions for screening. A549 cells were seeded at different densities and infected 24 h later with serial dilutions of HCoV-OC43, as in (Fig 3-3). (**A**) Representative well images of cell densities 48 hpi. (**B**) Cell number was quantified at multiple timepoints using the Celigo Imaging Cytometer. (**C**) A new HCoV-OC43 stock was propagated for screening experiments and titrated on A549 cells. dsRNA+ cells were quantified at 48 h and 72 hpi. The dashed lines indicate the optimal 30-50% range. (**B-C**) The mean and SD for one independent experiment are shown.

It should be noted that previous ISG screens have used the cationic polymer polybrene to increase the transduction efficiency of the SCRPSY-ISG vector (Wickenhagen et al., 2021), but I noticed HCoV-OC43 infection was decreased when polybrene was used (Fig 3-5 A-B). Polybrene acts by neutralising charge repulsion between lentiviruses and the cell surface, such as sialic acids. Since HCoV-OC43 uses N-acetyl-9-O-acetylneuraminic acid as a receptor (Hulswit et al., 2019), this may explain why there was a >3-fold reduction in HCoV-OC43 infection observed when the standard working concentration of 8 µg/mL polybrene was used (Fig 3-5 B).

With this protocol looking promising for screening HCoV-OC43, further optimisation was required prior to doing a multi-library screen. First, new human, bovine and macaque ISG lentivirus libraries were generated, consisting of 543, 289 and 345 genes, respectively. Prior to this, I extended the human library by 32 genes, including previously absent genes and different isoforms of genes already present in the library (data not shown). Supernatant remaining after lentivirus harvest can be pooled and used to determine the volume to add to reach the optimal >90% transduction efficiency. Since SCRPSY lentiviral plasmids also encode a puromycin resistance gene, antibiotic selection can be used to increase the level of transduction to reach the optimum (Fig 3-5 C). Given that the multi-species library screen would involve twenty 96-well plates and puromycin addition did not substantially increase the proportion of transduced cells, I decided against this additional step.

Since no ISG screen had been performed on the Celigo imaging cytometer before, I also wanted to check the transduction level was not being underestimated or overestimated; RFP+ cells were therefore measured in parallel on the Celigo image cytometer and Guava flow cytometer. Reassuringly, there was no considerable difference in RFP+ cells measured by both instruments at transduction levels required for screening (Fig 3-5 D). Given that 90% transduction efficiency was unlikely to be reached in A549 cells without polybrene, I decided to use a SCRPSY library supernatant volume of 50 µL/well for screening, which enabled a transduction efficiency of ~75%.

Prior to performing the multi-library screen for HCoV-OC43, I performed a miniscreen against HCoV-OC43, containing the gene hits from the published SARS-CoV-2 screen to optimise scanning and analysis settings on the Celigo Imaging Cytometer (Fig 3-5 E). The results of the miniscreen validated this new screening protocol as many expected genes inhibited HCoV-OC43 infection. These include *IFNB1* and *LY6E*, which have been previously shown to inhibit coronaviruses, including HCoV-OC43 (Fig 3-2 D)(Pfaender et al., 2020). Therefore, I have successfully optimised a protocol that enables the quantification of fluorescently labelled viral dsRNA in fixed cells using plate-based image cytometry, to screen ISGs for antiviral activity.

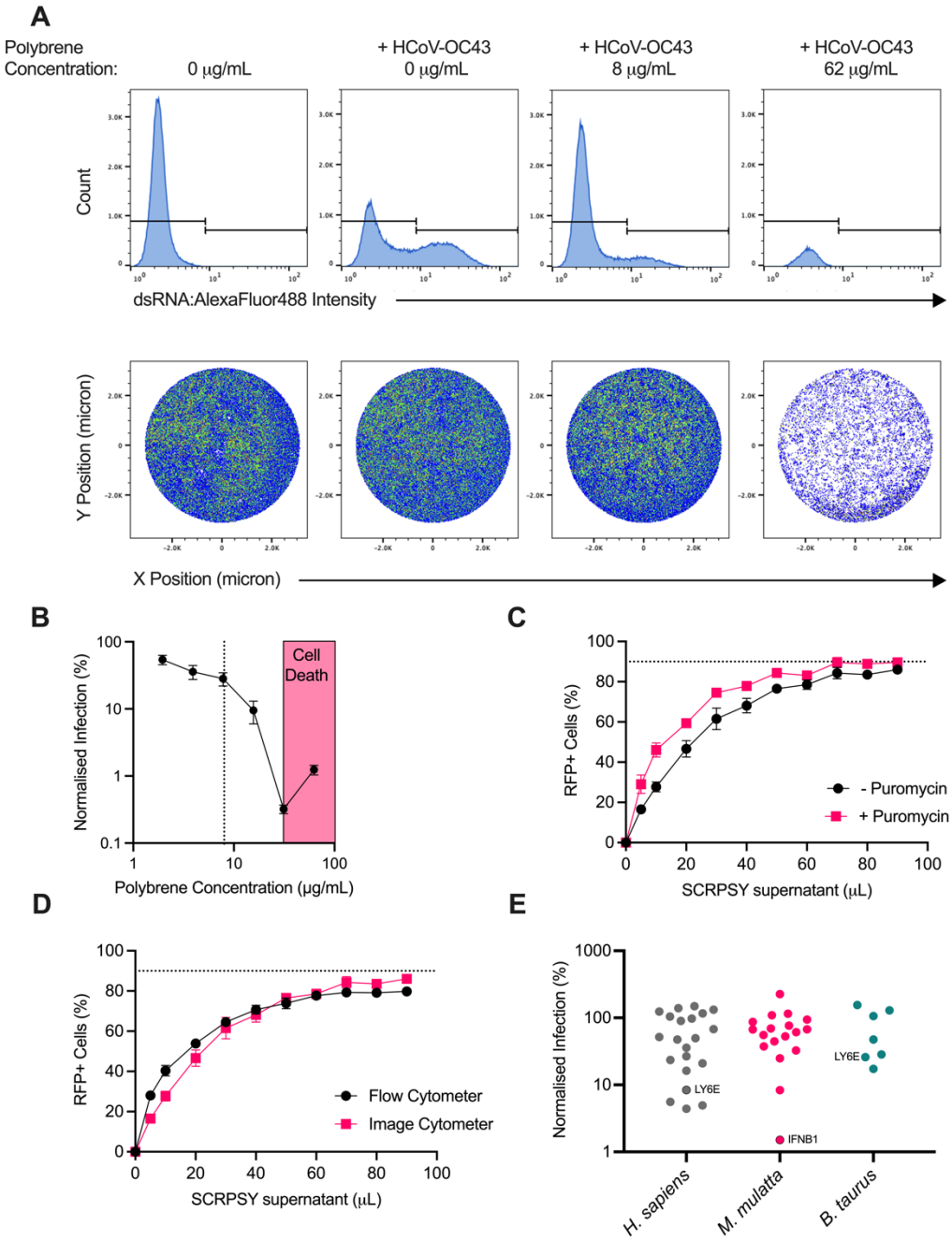

Figure 3-5: Optimisation of transduction conditions for screening. A549 cells were treated with polybrene for 48 h prior to addition of HCoV-OC43 in fresh medium for 72 h ($5x10^4$ PFU). (**A**) Representative histograms and nuclei mask well images at different polybrene concentrations. (**B**) Quantification of dsRNA+ cells post-polybrene treatment. Data normalised to mock-treated cells. The dashed line indicates the standard working concentration of polybrene (8 µg/mL). (**C**) A549 cells were transduced with SCRPSY lentiviral supernatant, then mock-treated or treated with 2 µg/mL puromycin 48 h later. 120 h post-transduction, RFP+ cells were quantified by flow cytometry. (**D**) Mock-treated A549 cells from (C) were measured for RFP expression in parallel by flow cytometry and image cytometry. (**E**) A549 cells were transduced with 50 µL/well of the SARS-CoV-2 miniscreen library generated by Wickenhagen *et al*., (2021) for 48 h prior to a 72 h infection with HCoV-OC43 ($5x10^4$ PFU). Fixed cells were stained with anti-dsRNA and Hoechst, and dsRNA+ cells were quantified using the Celigo Imaging Cytometer. Data normalised to SCRPSY-EMPTY controls. (**B-D**) Mean and SD of one independent experiment are shown.

3.2.4. Generation of a novel functioning mouse ISG library

During the optimisation of this screening protocol, a new mouse ISG library, containing 372 genes, was developed at the Centre for Virus Research. I wanted to screen HCoV-OC43 with this mouse library as, alongside the human and bovine library, this meant a species from every step involved in the proposed transmission of HCoV-OC43 (rodent → livestock → human) was represented in the screening process (Corman et al., 2018). This may provide insights into innate immune barriers that could have facilitated or hindered the emergence of HCoV-OC43 into the human population. This library was initially prepared using glycerol stocks provided by the biotechnology company Bio Basic, who synthesised the ISGs and ligated them into the SCRPSY vector. An ISG screen against HCoV-OC43 was performed with this new lentiviral library (Fig 3-6 A). Hits included *Ly6a,* although it should be noted that *Ly6e* is not present in the mouse ISG library.

Although these hits appeared valid, I quickly noticed an issue with the transduction efficiency of this library preparation; 161/372 genes had a transduction efficiency of <10%, which is the cutoff I use for my screens (Fig 3-6 B). I investigated how the initial DNA yield of the SCRPSY plasmid level related to transduction efficiency and found no correlation (Fig 3-6 C). There was also no correlation between transduction efficiency and HCoV-OC43 infection level (Fig 3-6 D). To troubleshoot this, normalised plasmid DNA for the first 24 ISGs from mouse library plate 1 were restriction digested and visualised by agarose gel electrophoresis (Fig 3-6 E). Half of these genes did not transduce above 10%, and faint or absent bands were seen for most of them. This suggests the original miniprep from the Bio Basic glycerol stocks was not good quality, and the DNA concentrations given by the Nanodrop spectrophotometer were inaccurate.

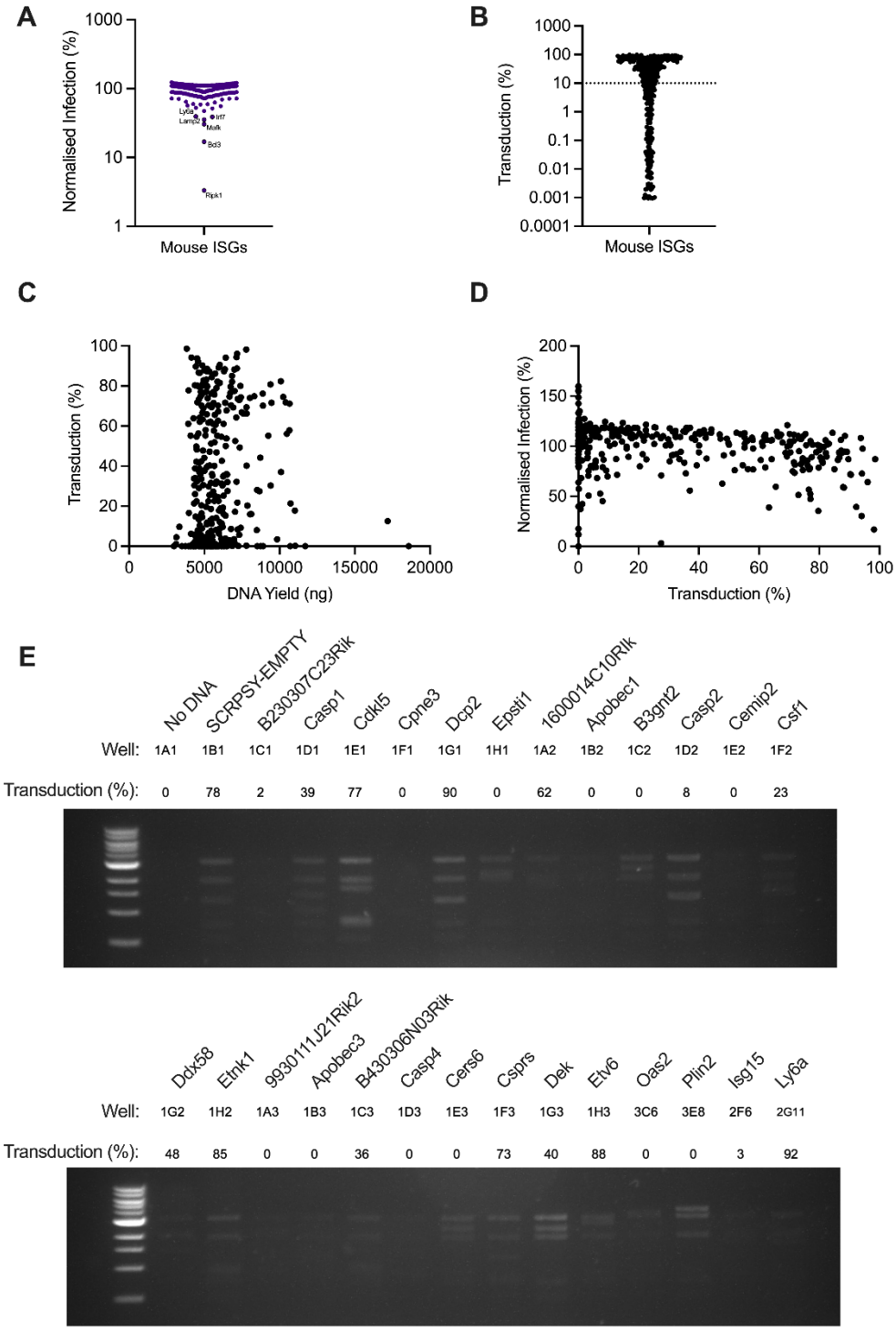

Figure 3-6: Troubleshooting the first mouse ISG library screen. A549 cells were transduced with 50 µL/well of mouse ISG library supernatant prior to a 72 h infection with HCoV-OC43 (5x10^4 PFU). Infected cells were quantified using the described screening protocol. (**A**) Hits with a z-score of < -2 are indicated. (**B**) Transduction efficiency of individual ISGs from the library are shown. The dashed line indicates the 10% transduction threshold. (**C-D**)The correlation between transduction efficiency and initial DNA yield (**C**) or HCoV-OC43 infection (**D**) is shown. (**E**) 250 ng of SCRPSY-ISG plasmid from a selection of mouse library ISGs were restriction digested prior to visualisation by agarose gel electrophoresis. The transduction efficiency is indicated for each gene.

With the assistance of Douglas Stewart, I redid the 372 SCRPSY plasmid minipreps for the mouse ISG library with initial bacterial transformation using 500 ng of plasmid DNA provided by BioBasic; this seems like a high amount of DNA, but even this did not give many isolated colonies post-transformation. The choice of media, incubation time and culture volume had to be optimised for this library preparation. This was performed by Yongtao He, who also made the new bat ISG library containing 67 ISGs from *Rhinolophus affinis* and 70 ISGs from *Rhinolophus sinicus*, alongside us.

Prior to normalising the new plasmid preparations, 5 µL of 24 DNA minipreps were restriction digested. Examining the gel revealed that all the genes had DNA bands, and the intensity of the bands largely correlated with the DNA concentration readout (Fig 3-7 A). Since I have previously observed high concentrations of DNA inhibiting lentivirus production during library preparation, the DNA minipreps of these 24 genes were serially diluted and transfected to make lentivirus to ensure the standard protocol amount of DNA was still appropriate for this new library. When using the standard plasmid amount of 125 ng for lentivirus production, 23/24 genes showed transduction efficiencies greater than the 10% cutoff in A549 cells (Fig 3-7 B); these transduction levels were from 50 µL/well of lentivirus-containing supernatant which is the usual dose for A549 cells. The only gene that doesn't pass the threshold is *Casp2*, which is unsurprising considering the involvement of this gene in apoptosis (Lopez-Cruzan et al., 2016). This was performed in parallel in 293T cells, commonly used for ISG screening, to determine whether the transduction efficiency is cell-type specific (Figure 3-7 C). In this case, 21/24 genes showed transduction efficiencies greater than the 10% cutoff, suggesting A549 cells were the preferable cell line to use for my screen.

Although most genes transduced above the 10% cutoff, optimal transduction efficiency for standard screening is >90%, which is not obtained here. Therefore, these transduction experiments were repeated at different cell seeding densities and with a higher volume of lentivirus supernatant. As expected, reducing seeding density to $5x10^3$ cells/well and adding >50 µL/well lentivirus increases the transduction efficiency but not substantially (Fig 3-8). Yongtao He found that

adding polybrene results in optimal transduction efficiencies with these new libraries (data not shown), but as discussed earlier (Fig 3-5 A-B), this is not possible with HCoV-OC43, so screening went forward without. Nevertheless, we successfully generated a novel functioning mouse ISG library that will provide insight into the antiviral activity of rodent ISGs.

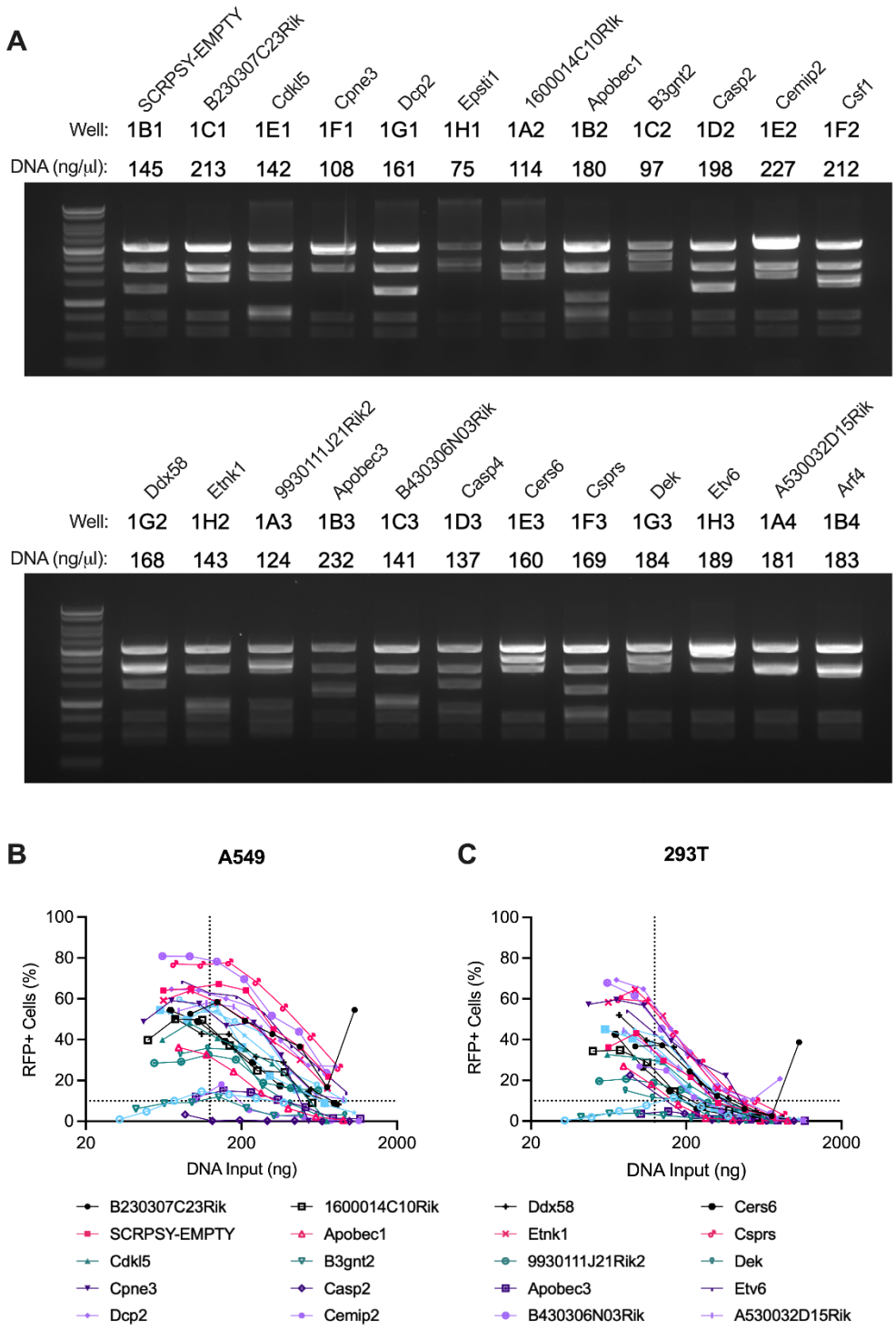

Figure 3-7: Testing the transduction efficiency of the newly generated mouse ISG library. SCRPSY-ISG plasmids were transformed into a lab bacterial stock, and DNA was extracted. (**A**) 5 µL of newly made SCRPSY-ISG plasmid for 24 mouse library genes was restriction digested and visualised by agarose gel electrophoresis. The miniprep DNA concentration is indicated for each plasmid. The plasmids for the above genes were serially diluted and transfected to produce lentivirus-containing supernatant. A549 (**B**) or 293T (**C**) cells were transduced with 50 µL/well of library and fixed 120 h post-transduction. RFP+ cells were measured by flow cytometry. The dashed line on the x-axis indicates the standard 125 ng input. The dashed line on the y-axis indicates the 10% transduction threshold.

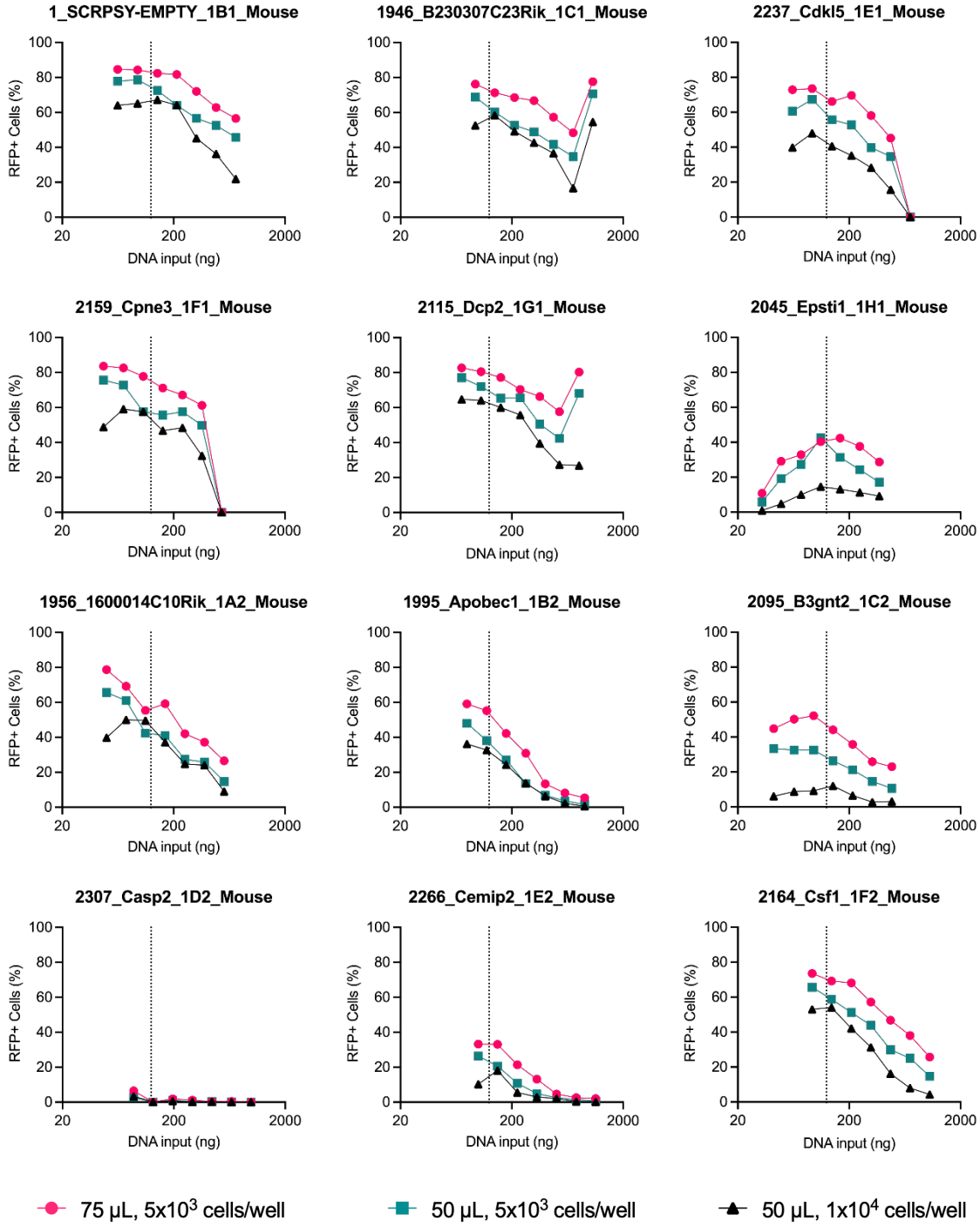

Figure 3-8: Transduction efficiency is improved by altering the lentiviral library volume or initial seeding density. The first 12 genes from (Fig 3-7) were transfected as before. A549 cells were seeded at $5x10^3$ or $1x10^4$ cells/well and transduced with 50 µL or 75 µL/well of library supernatant. RFP+ cells were measured 120 h post-transduction by flow cytometry. The dashed line indicates the standard 125 ng DNA input.

3.2.5. A multi-species library screen reveals genes with candidate antiviral activity against HCoV-OC43

Using this optimised protocol with new libraries, a multi-species ISG screen was performed to identify genes exhibiting antiviral activity against HCoV-OC43 at a late stage of infection (72 hpi). The ISG libraries consist of 543 human (*Homo sapiens*), 345 macaque (*Macaca mulatta*), 289 bovine (*Bos taurus*), 372 mouse (*Mus musculus*), 68 intermediate horseshoe bat (*Rhinolophus affinis*) and 70 Chinese rufous horseshoe bat (*Rhinolophus sinicus*) genes. To determine HCoV-OC43 infection in ISG-expressing cells, the cells were gated on FlowJo using a cell-only control (-SCRPSY, -HCoV-OC43) and a transduced, mock-infected control (+ SCRPSY-EMPTY, - HCoV-OC43). The gates were then checked using two additional controls: a transduced, infected control (+ SCRPSY-EMPTY, + HCoV-OC43) and a virus-only control (-SCRPSY, + HCoV-OC43) (Fig 3-9 A). Examining the cell-only control, it appears that there are multiple populations of cells. When gating these populations, the smaller population appears localised to the left edge of the well (Fig 3-9 B). For a 96-well plate, the Celigo Imaging Cytometer works by taking 16 images (fields of view) and stitching them together. This smaller population is likely a combination of higher density in that section of the well and the stitching process because it does not consistently occur in my experiments.

Using this screening protocol, some hits can be first identified visually by examining the well images, as a substantial reduction in dsRNA staining can be seen in the green channel, which correlates well with the FlowJo analysis (Fig 3-9 C). The transduction efficiencies were generally sufficient, although expectedly, many genes failed to pass the 10% transduction cutoff. In total, 8% human, 10% macaque, 27% bovine, 6% mouse, and 4% bat ISGs (*R. affinis* = 2 ISGs, *R. sinicus* = 4 ISGs) fell below this cutoff (Fig 3-9 D). Longer genes often fail to transduce, which could be due to poor packaging of the lentiviral vector genome, but ISG-mediated cytotoxicity can also contribute. ISGs that commonly fail to transduce are *EIF2AK2* (PKR), *APOBEC3G* and *MOV10,* and there have been suggestions that this is because they possess anti-retroviral activity and target the HIV-1-based vector in the producer cell (Schoggins et al., 2011).

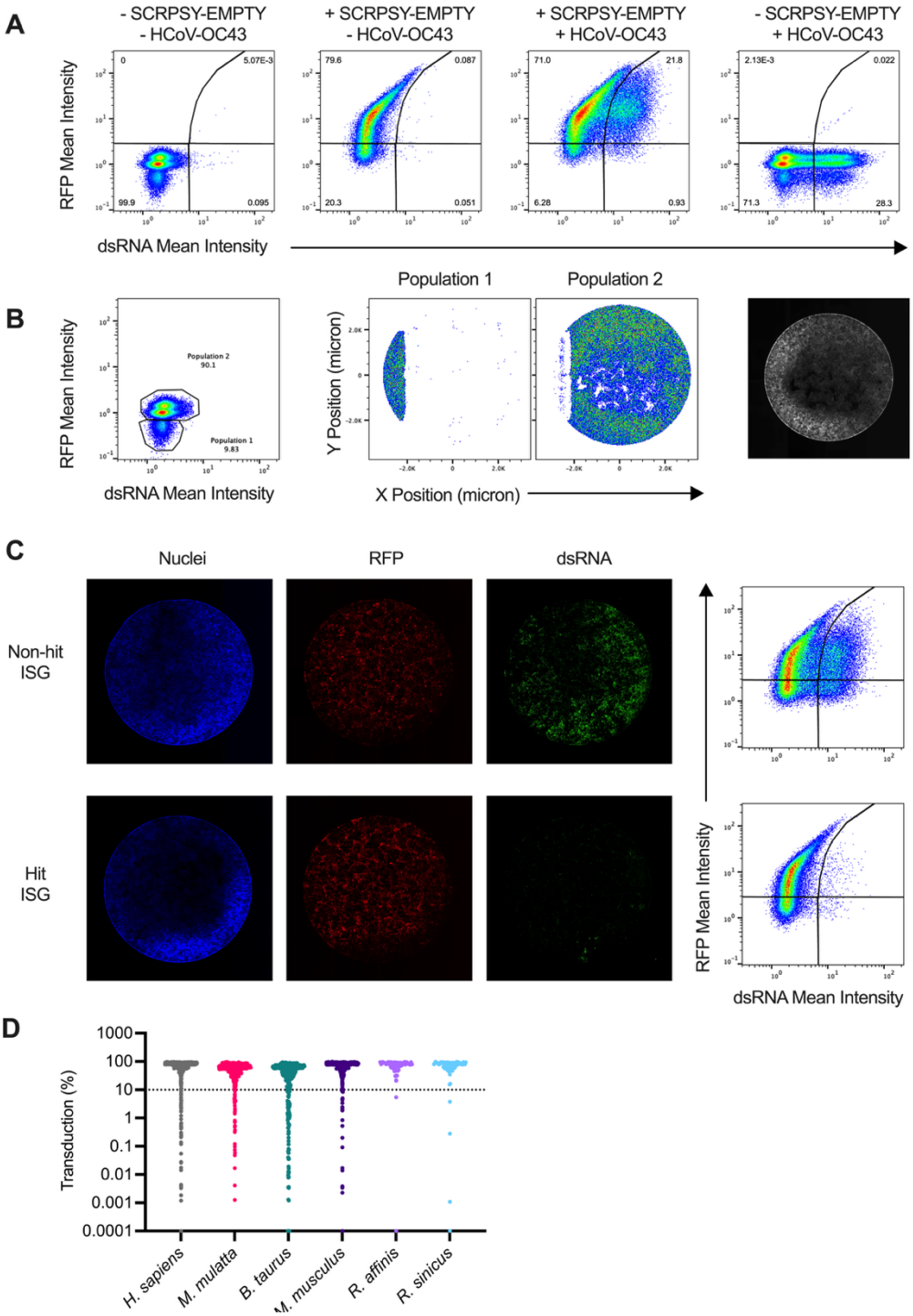

Figure 3-9: Gating strategies and transduction efficiencies of the multi-species library screen. A549 cells were transduced with 50 µL/well of supernatant from the following ISG libraries: human (*H. sapiens*), rhesus macaque (*M. mulatta*), cattle (*B. taurus*), mouse (*M. musculus*) and bat (*R. affinis* and *R. sinicus*). 72 hpi with HCoV-OC43, cells were stained for dsRNA and analysed using the protocol described. (**A**) Cells were gated on FlowJo first using the controls shown. The percentage of cells in each gated area is shown. (**B**) Gating, nuclei mask well image and Celigo well scan explaining the dual population observed in the cell-only (- SCRPSY-EMPTY, - HCoV-OC43) control. (**C**) Representative Celigo well scans and corresponding FlowJo analysis plot of an ISG hit and a non-hit. (**D**) Transduction efficiencies of all the ISGs tested. ISGs that fall below the 10% transduction threshold (dashed line) were excluded from hit analysis.

The data was normalised to the mean of the species library, with the mean for the human (30.9), macaque (36.2), bovine (34.6), mouse (45.0) and bat (*R. affinis* = 39.5, *R. sinicus* = 36.5) libraries all falling within the optimal 30-50% infection range. Despite SCRPSY-EMPTY being present on every 96-well plate, I do not believe this is an optimal control for normalisation for two reasons. Firstly, the SCRPSY plasmid does not have an ISG insert; it is considerably smaller than most plasmids in the library, so there is a tendency for over-transduction to occur. This sometimes results in cells over-expressing SCRPSY-EMPTY having lower infection levels than the mean infection level of the library. Secondly, the well position of SCRPSY-EMPTY on these library plates is H12. I have noticed that corner wells tend to have lower infection rates, which may be due to media evaporation.

To keep consistency with other published ISG screens outside of the Centre for Virus Research, z-scores for each ISG were calculated, and ISGs with a z-score < -2 were considered candidate antiviral genes (Fig 3-10). Additionally, ISGs that had a transduction efficiency of <10% were excluded from hit selection. The validity of this screening protocol is promising, as many hits from this HCoV-OC43 screen also appear in my colleague's previous screen of SARS-CoV-2 that used the standard reporter virus/flow cytometry protocol (Wickenhagen et al., 2021). Of note is the appearance of *LY6E* as a hit in the human, macaque, bovine and bat libraries. As mentioned previously, *LY6E* has been shown to have antiviral activity against many coronaviruses, including HCoV-OC43, making it an excellent positive control (Pfaender et al., 2020). Therefore, this optimised ISG screening protocol revealed 52 candidate ISGs from multiple species that can be further assessed for anti-HCoV-OC43 activity.

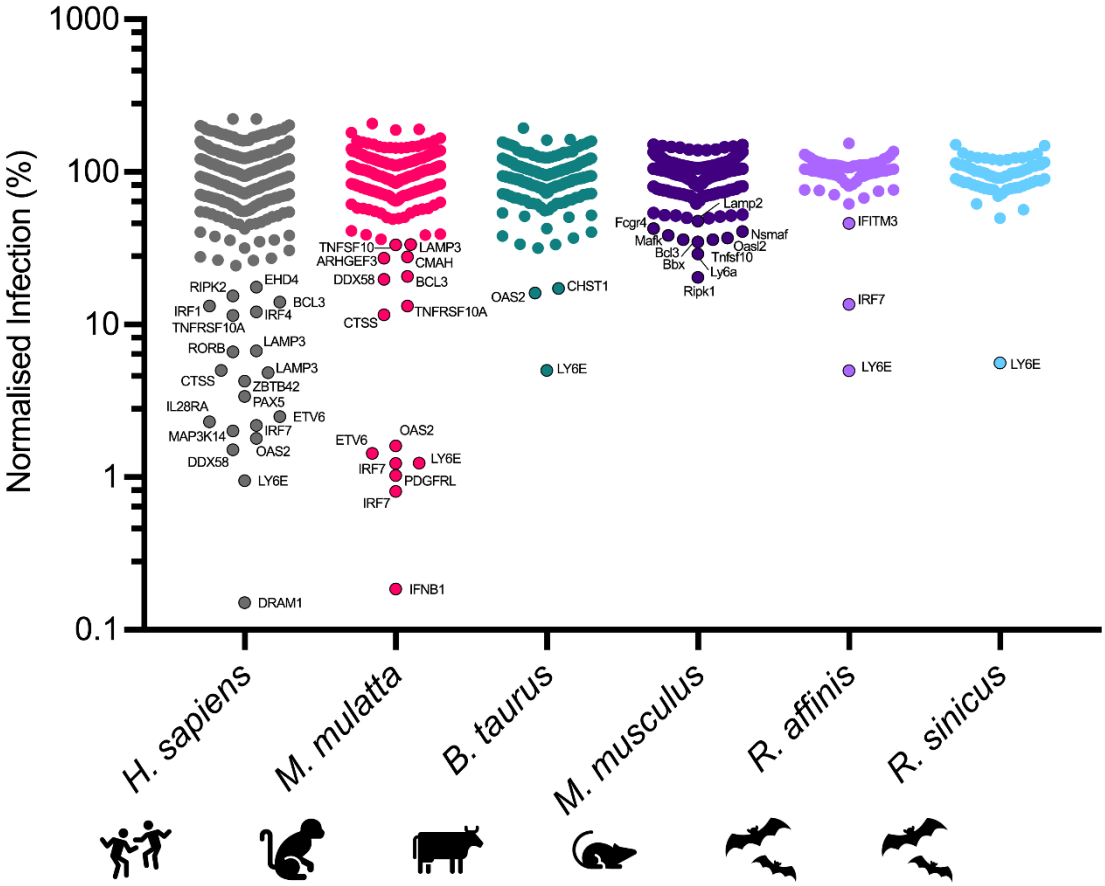

Figure 3-10: Identification of candidate ISGs with antiviral activity against HCoV-OC43. A549 cells were transduced with 50 µL/well of supernatant from each of the following ISG libraries: humans (*H. sapiens*), rhesus macaques (*M. mulatta*), cattle (*B. taurus*), mice (*M. musculus*) and two species of horseshoe bat (*R. affinis* and *R. sinicus*). The level of HCoV-OC43 infection after 72 h was measured after dsRNA immunostaining using the Celigo Imaging Cytometer. Data was normalised to the mean infection level of each species library. Hits with a z-score of < -2 are indicated.

3.2.6. Confirmation of the antiviral activity of candidate ISGs

Since the multi-species library screen was only performed once, miniscreens were performed to confirm the antiviral activity of the 52 candidate ISGs. This miniscreen included 20 human, 15 macaque, 3 bovine, 10 mouse and 4 bat genes (*R. affinis* = 3, *R. sinicus* = 1). As discussed in section 3.2.5, SCRPSY-EMPTY is not an optimal control, so I wanted to add ISGs to the miniscreen library that have not previously shown substantial proviral or antiviral activity. To do this, I collated ISG screening data from 28 independent screens, including my HCoV-OC43 screen, performed at the Centre for Virus Research. Given that there were no z-scores for the other 27 screens, I filtered ISGs with a normalised infection between 50-150%. These "non-hit" ISGs were removed if they had a transduction efficiency of <70% in the HCoV-OC43 screen, to ensure they had good ISG expression in the miniscreen. I then examined the normalised infection level of the remaining non-hit ISGs from other published screens (Pfaender et al., 2020; Schoggins et al., 2014). From this, I discovered 19 ISGs that are not proviral or antiviral against 37 diverse viruses with DNA, (+)ssRNA, (-)ssRNA and dsRNA genomes (Fig 3-11), suggesting together they could be a good control for normalisation. The fact that these ISGs have not shown antiviral activity (yet) in these screens is interesting as it begs the question of why some of these ISGs have evolved to be induced in response to IFN.

I normalised the infection level in the presence of candidate ISGs against the average infection level in the presence of 8 SCRPSY-EMPTY controls or the average infection level in the presence of 18 non-hits; the non-hit *GEM* was not included because the miniprep had a low DNA concentration. This gave similar values, suggesting the 18 non-hits are a good infection control for future screens (Fig 3-12 A-B). 34/52 ISGs showed a >2-fold reduction in HCoV-OC43 replication, although 5 of the ISGs that did not show this restriction had a transduction efficiency of <10% (Fig 3-12 C-H).

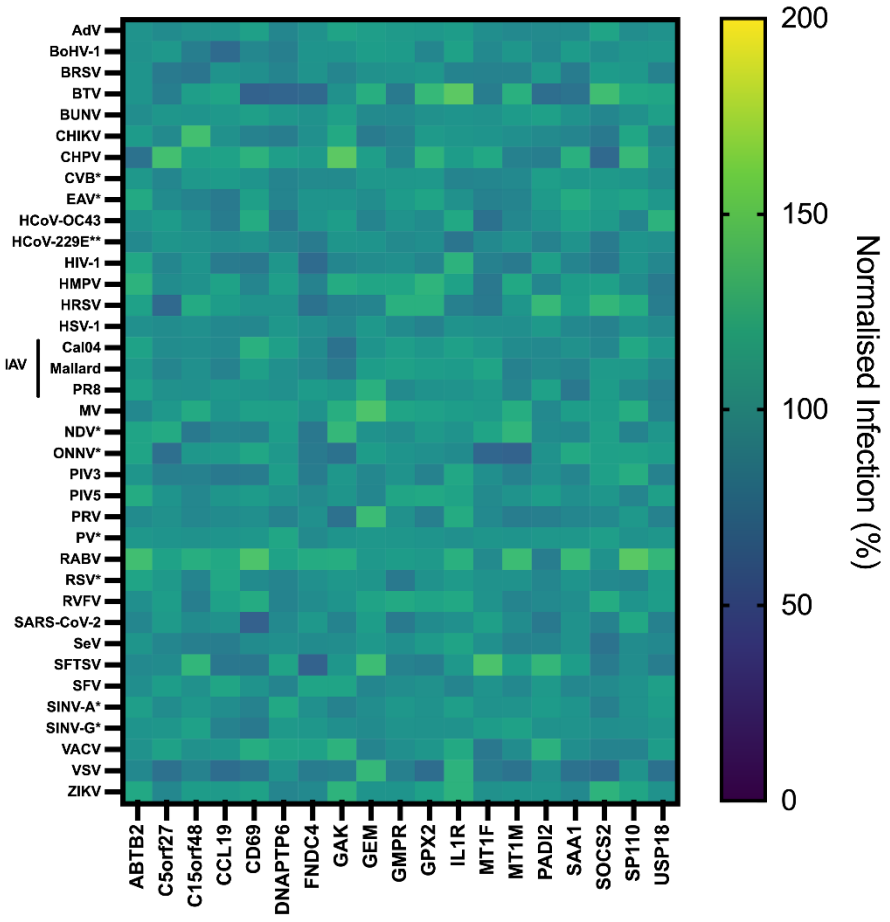

Figure 3-11: Identification of non-hits from ISG cDNA screens. Previous ISG screens performed by the Centre for Virus Research and from published ISG screens were analysed for ISGs that have never been substantially proviral or antiviral ("non-hits"). 19 genes were identified from ISG screens of 37 viruses and the normalised infection level is presented as a heatmap. *ISG screen described in Schoggins *et al*., (2014). **ISG described in Pfaender *et al*., (2020).

Several of these candidate ISGs also appear as hits in most screens the Centre for Virus Research has performed. This is because they are likely inhibiting viruses non-specifically. This can be due to the ISG causing cytotoxicity or inducing a general antiviral state. To investigate this, I transduced A549-ISRE:GFP cells with the miniscreen library. The cell supernatant was tested 120 h later with a commercially available cytotoxicity assay (Fig 3-13 A). This highlighted ISGs associated with cell apoptosis, such as *TNFRSF10A* and *TNFSF10,* which were removed from the candidate ISG list. I measured the percentage of GFP+ cells by flow cytometry and removed ISGs that induced >10% activation of the ISRE reporter, using GFP expression as a substitute (Fig 3-13 B); these genes were *IFNB1*, *IRF1*, *IRF4*, *IRF7* and *DDX58* (RIG-I), many of which play important roles in upregulating the IFN response.

Since HCoV-OC43 is an endemic virus in humans, I decided to focus primarily on human ISGs. It should be noted that the LAMP3 gene is duplicated in the human ISG library, which explains why it appears twice in the miniscreen (Fig 3-12 C). I additionally removed *LY6E*, due to its known anti-coronaviral activity, and *IL28RA*, due to it encoding a receptor for Type III interferons, from the candidate ISG list. Following this hit selection pipeline, I identified 7 ISGs (*CTSS*, *ETV6*, *LAMP3*, *OAS2*, *PAX5, RORB* and *ZBTB42*) that showed potent antiviral activity against HCoV-OC43, without causing cytotoxicity or substantial ISRE induction.

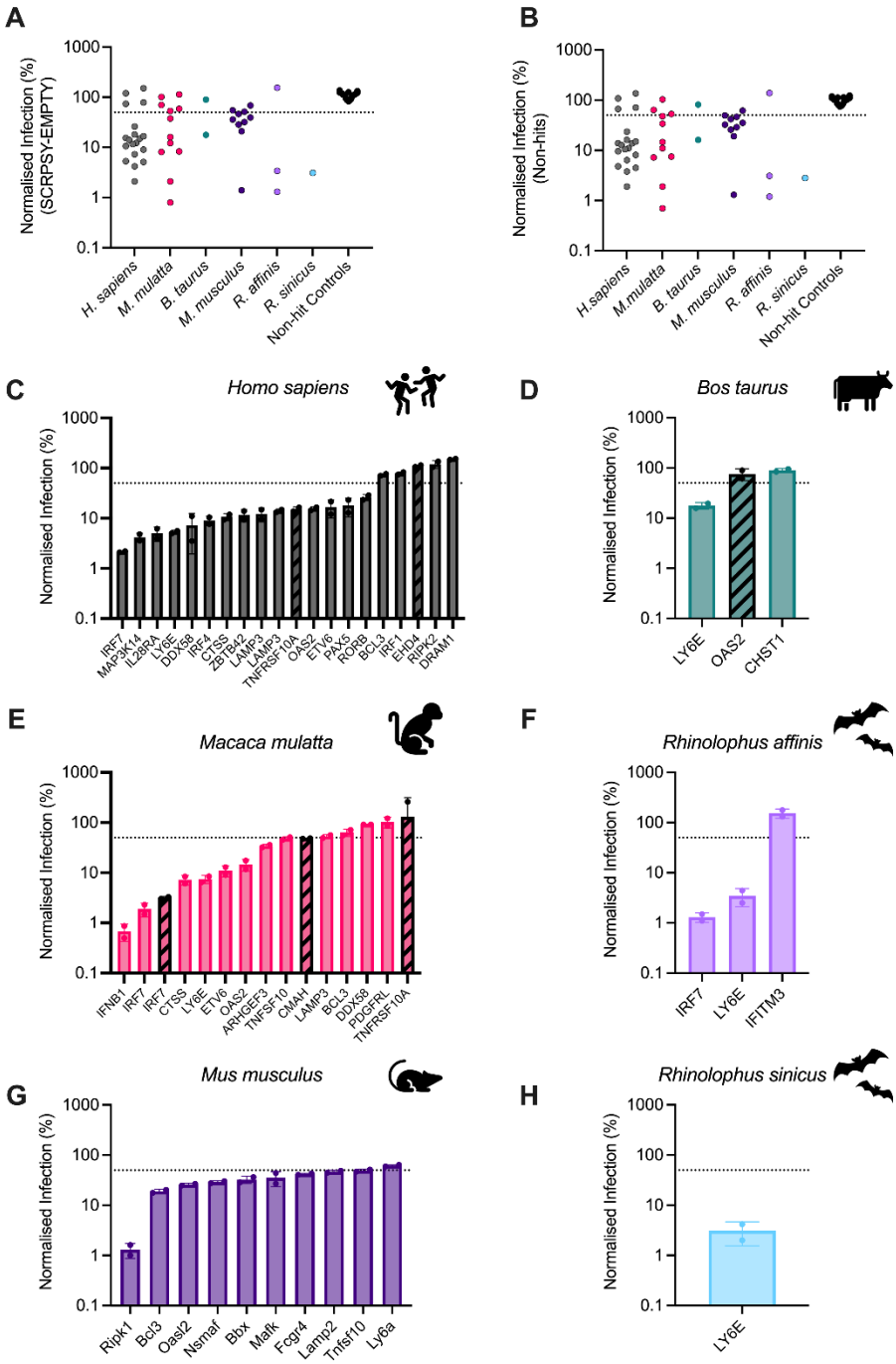

Figure 3-12: ISG miniscreen confirms anti-HCoV-OC43 activity of candidate genes. A549 cells were transduced with 50 µL/well of supernatant from the miniscreen library containing the ISG hits from (Fig 3-10), SCRPSY-EMPTY or 18 non-hits from (Fig 3-11). The level of HCoV-OC43 infection after 72 h was measured after dsRNA immunostaining, using the Celigo Imaging Cytometer. Data was normalised to SCRPSY-EMPTY controls (**A**) or the non-hit controls (**B**). The HCoV-OC43 infection level normalised to SCRPSY-EMPTY is shown for each ISG hit from the human (**C**), bovine (**D**), rhesus macaque (**E**), intermediate horseshoe bat (**F**), mouse (**G**) and Chinese rufous horseshoe bat (**H**) libraries. Dashed bars indicate genes that did not pass the 10% transduction threshold. The mean and SD for one independent experiment are shown. The dashed line indicates a 50% infection level.

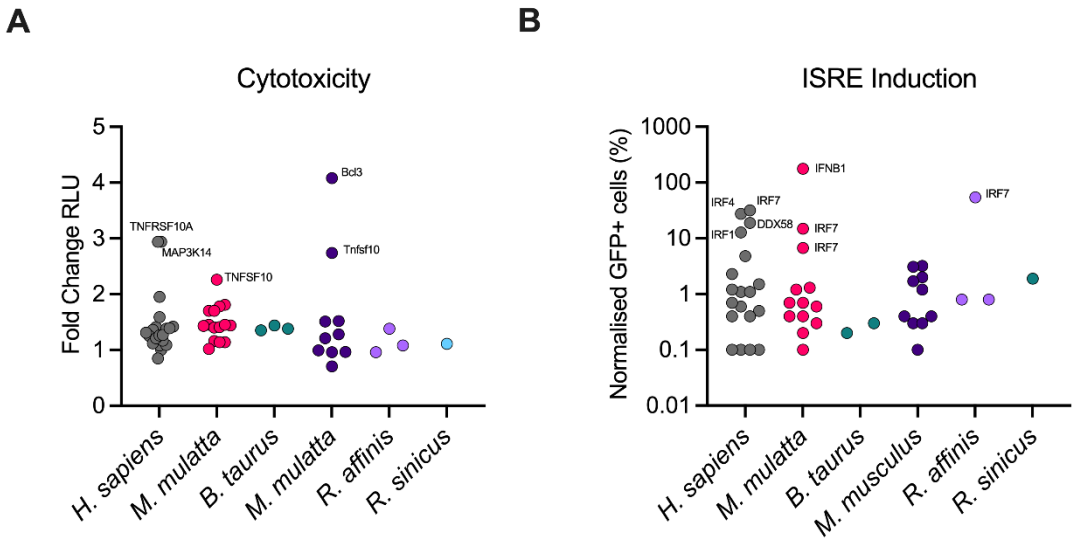

Figure 3-13: Identification of non-specific inhibitors of HCoV-OC43. A549-ISRE:GFP cells were transduced with 50 µL/well of supernatant from the ISG miniscreen library containing hits from (Fig 3-10). 120 h post-transduction, the supernatant was collected to measure cytotoxicity using the CytoTox-Glo™ Cytotoxicity assay kit (**A**). GFP+ cells were measured as a proxy for ISRE induction by flow cytometry (**B**). The data from one independent experiment are shown.

3.3. Discussion

In conclusion, measuring fluorescently labelled viral dsRNA using an image cytometer provides a quantifiable method for screening ISGs for antiviral activity, without the requirement for reporter viruses. HCoV-OC43 was an ideal model for optimising this new protocol as it is IFN-sensitive (Fig 3-2 D), can reach optimal infection levels (via dsRNA+ cells) in cells permissive to lentiviral transduction (Fig 3-2 C) and did not have a reporter virus readily available when these experiments were taking place. Although not covered in this project, imaging cytometry can provide visualisation of foci formation and changes in cell morphology, unlike flow cytometry, adding an extra dimension to ISG screening. This method has the potential to be adapted for other RNA viruses of clinical importance or at high risk of emergence in humans, such as flaviviruses.

After optimisation of seeding density, transduction methods and cytometer settings, a multi-species library screen was performed with three published ISG lentiviral libraries (human, macaque, cow) and two new ISG lentiviral libraries (mouse and bat) (Fig 3-10); as part of this project, we generated the mouse library containing 372 genes by transformation of 372 commercially purchased DNA preparations followed by transfection of extracted DNA to create the lentiviral library (Fig 3-7, 3-8). This screen revealed ISGs with candidate antiviral activity that have been hits in previous screens against coronaviruses SARS-CoV-2 and HCoV-229E (Pfaender et al., 2020; Wickenhagen et al., 2021). To rule out hits that can be antiviral through activation of the IFN signalling pathway, I transduced a miniscreen library into A549 cells modified to express GFP under the control of an ISRE; this identified *IFNB1*, *IRF1*, *IRF4*, *IRF7* and *DDX58* (RIG-I). ISGs that resulted in ISG-mediated cytotoxicity due to increased expression (*TNFSF10*, *TNFSF10A*, *MAP3K14*, *Bcl3*) were also excluded.

As expected, the coronavirus restriction factor *LY6E* was a top hit for most species in the miniscreen. The exception was the mouse library, which did not contain the *Ly6e* gene, but another member of the Ly6 gene family, *Ly6a*, was a hit. Human LY6E and mouse Ly6a are not orthologous but belong to the same gene

family with a characteristic disulphide bonding pattern; the human ortholog of *Ly6a*, *LY6S*, is an ISG discovered only recently (Shmerling et al., 2022). The human genes that were the top choices for further characterisation were *CTSS*, *ETV6*, *LAMP3*, *OAS2*, *PAX5*, *RORB* and *ZBTB42*; some of these hits showed antiviral activity in GOF and LOF screens described in the introduction (Table 3-4). Since these hits were identified by gene overexpression, we can only say they may be sufficient for reducing HCoV-OC43 infection. Only through LOF screening or depletion experiments can it be determined whether a gene is a necessary player in the antiviral defence against this virus – although, like all screens, these results will always be sensitive to cellular context.

Table 3-4: Presence of hits from the HCoV-OC43 screen in datasets from GOF and LOF screens discussed in the introduction.

Study	Cell line	Virus	Screen type	Hit in other genetic screens?						
				CTSS	ETV6	LAMP3	OAS2	PAX5	RORB	ZBTB42
(Pfaender et al., 2020)	Huh7	HCoV-229E	GOF	-	N	N	Y	-	-	-
(Wickenhagen et al., 2021)	A549-Npro-ACE2	SARS-CoV-2	GOF	N	N	N	Y	N	N	Y
(Zang et al., 2020)	HEK293-ACE2	VSV-SARS-CoV-1 VSV-SARS-CoV-2	GOF	-	-	Y	Y	-	-	-
(Danziger et al., 2022)	A549-ACE2 (+/- △STAT1)	SARS-CoV-2	GOF	Y	-	N	N	-	-	-
(Mac Kain et al., 2022)	A549-ACE2	SARS-CoV-2	LOF	N	N	N	Y	-	-	N
(Xu et al., 2023)	Huh7.5 A549-ACE2	SARS-CoV-2	LOF	N	N	N	N	N	N	N
(Le Pen et al., 2024)	Huh7.5	SARS-CoV-2	LOF	N	N	-	N	-	-	N

Hit (Y). Non-hit (N). Not present in library (-).

Cathepsin S (CTSS) is one of the cellular cysteine proteases present in the lysosome, like Cathepsin L (CTSL) and is involved in antigen processing and presentation (Yadati et al., 2020). CTSL has been implicated as an entry factor of SARS-CoV-2 when it enters the cell via the endosomal route (Jackson et al., 2022) and appears proviral in CRISPR screens discussed previously (Danziger et al., 2022; Le Pen et al., 2024). In addition to my HCoV-OC43 screen, CTSS showed significant inhibition of SARS-CoV-2 in the GOF CRISPR activation screen in both A549-ACE2 cells and those deficient in STAT1, suggesting this antiviral activity is independent of the IFN pathway (Danziger et al., 2022) (Table 3-4). The authors suggested that

this difference between CTSS and CTSL could be due to different cleavage specificity so that overexpression of CTSS suboptimally cleaves SARS-CoV-2 spike and/or interferes with spike cleavage by other cathepsins. However, CTSS was not a hit in the overexpression screen performed in A549-ACE2 cells deficient in IRF3 (Wickenhagen et al., 2021). It has been reported that cathepsins cleave TLRs into active forms; TLR3 can be cleaved by cathepsin B and H (Garcia-Cattaneo et al., 2012). Overexpression of CTSS could increase TLR-signalling during infection, which may induce antiviral effectors independent of IRF3. This could explain why CTSS was a hit in the HCoV-OC43 screen, as it used the same human lentiviral library except in parental A549 cells with functional immune pathways.

Overexpression of CTSS could also be interfering with coronavirus egress. It has been shown that betacoronaviruses exit the cell via a lysosomal-dependent pathway. MHV or SARS-CoV-2 infected cells had a decreased number of acidified lysosomes, and it was calculated that the mean lysosomal pH in uninfected cells was 4.7 but rose to pH 5.7 in MHV-infected cells (Ghosh et al., 2020). This can reduce the enzymatic activity of most cathepsins, which function optimally at acidic pH, but cathepsin S is enzymatically active at a broader pH range, up to weakly basic pH (Yadati et al., 2020).

Another hit in this screen was lysosome-associated membrane protein 3 (LAMP3), which has a tissue-restricted expression; LAMP3 is expressed in dendritic cells and lung type II pneumocytes and is involved in antigen processing (Akasaki et al., 2004). Given its lysosomal localisation, it could also interfere with coronavirus entry or egress. LAMP3 showed modest inhibition of pseudotype viruses expressing SARS-CoV-1 and SARS-CoV-2 spike proteins in a small GOF screen (Zang et al., 2020) (Table 3-4). In contrast, it has been reported that LAMP3 can be a proviral factor for influenza A virus in A549 cells, as its expression is induced upon infection and cells depleted of LAMP3 show decreased replication (Zhou et al., 2011).

ETV6 is a member of the ETS (E26-transforming specific) family of transcription factors. It commonly acts as a transcriptional repressor and is involved in blood cell production. In accordance, *ETV6* translocations and mutations have been associated with haematological malignancies (Rasighaemi and Ward, 2017). It has been reported that a closely related gene, *ETV7*, can negatively regulate the type I IFN response by targeting the expression of a subset of ISGs (Froggatt et al., 2021). Cells depleted in ETV7 showed decreased IAV replication, likely due to enhanced antiviral ISG expression. ETV6 may act as a transcriptional regulator in this HCoV-OC43 screen, and its downstream effect on the expression of specific genes may indirectly affect HCoV-OC43 replication. This screen is performed in A549 cells, and in hindsight, this screen should have been performed in parallel in A549 cells deficient in IFN signalling, such as via STAT1 knockout; (Fig 3-13 B) only revealed genes that can trigger ISRE in the absence of infection. If ETV6 appeared as a hit in A549 cells but not in A549$^{\Delta STAT1}$, it would suggest that ETV6 can act as a regulatory ISG.

Three other transcription factors showed candidate antiviral activity in the HCoV-OC43 screen. Paired box 5 (PAX5) is essential for the commitment of lymphoid progenitor cells into B cells, and due to its restricted expression, it is not likely a natural innate immune defence against a respiratory virus. However, Pax5 in mice targets many genes that are also transcriptional regulators, such as *Irf4* and *Irf8*, which can induce the expression of ISGs (Forero et al., 2013; McManus et al., 2011). A similar process may occur with RORB, a retinoid-related orphan receptor mainly restricted to the brain and retina, as it can act as a transcription factor upon ligand binding (Jetten, 2009). ZBTB42 is a member of the zinc finger and BTB-domain containing transcription factors and is expressed in skeletal muscles. ZBTB42 was also identified as a hit in the SCRPSY-based ISG screen against SARS-CoV-2 performed by my colleagues (Wickenhagen et al., 2021); ZBTB42 was not detected in lung tissues of patients with fatal COVID-19 infection, so its antiviral activity was not further characterised.

The final candidate antiviral gene is *OAS2*, which was chosen for further characterisation and will be discussed in more detail in Chapter 4. Briefly, OAS proteins polymerise ATP into oligoadenylate chains that activate RNase L. OAS2 also possessed antiviral activity in both GOF and LOF screens performed against HCoV-229E and SARS-CoV-2, discussed in the introduction (Table 3-4), suggesting broad anti-coronaviral activity. Another gene family member, OAS1, does not inhibit HCoV-OC43, and this was hypothesised to be due to HCoV-OC43 encoding an evasion mechanism against the OAS/RNase L pathway (Wickenhagen et al., 2021), suggesting OAS2 could be working via an RNase L independent mechanism.

In conclusion, a standard gain-of-function ISG screening workflow was modified to use antibodies against a broad viral molecule target. This protocol was optimised to successfully reveal candidate antiviral genes from six diverse species against a previously unscreened human coronavirus, HCoV-OC43. This screen supports results from previous studies with other coronaviruses. Although only OAS2 was characterised in the next chapter, investigating the additional putative restriction factors, particularly *CTSS*, could yield novel insight into human anti-coronavirus biology.

4. Identification of OAS2 as a restriction factor against HCoV-OC43

4.1. Introduction

4.1.1. The OAS gene family

The 2'-5'-oligoadenylate synthetase (OAS) family are interferon-stimulated genes important in the intracellular response to viral infection. These innate immune sensors are activated by binding to dsRNA, resulting in the polymerisation of ATP into 2'-5'-linked oligoadenylates (2-5A) (Justesen et al., 2000). These bind to and trigger the activation of RNase L, the only known 2-5A-dependent effector, resulting in the degradation of cellular and viral RNA within the cell (Fig 4-1). The synthesis of 2-5A is unique, as other template-independent RNA polymerases, including polyadenosine polymerase (PAP) and tRNA class I CCA adding enzymes (CCA), catalyse 3'-5' phosphodiester linkages (Torralba et al., 2008).

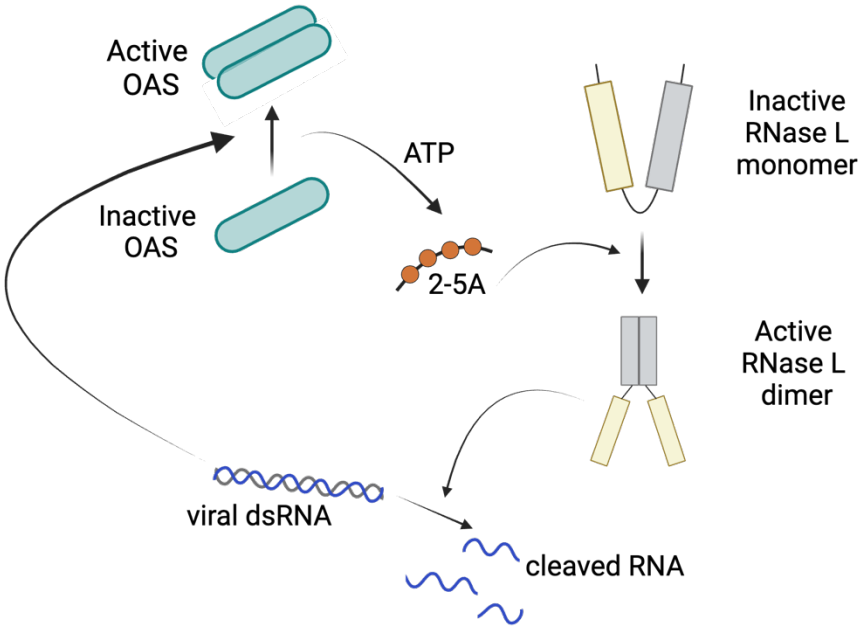

Figure 4-1: Schematic of the OAS/RNase L pathway. Binding dsRNA triggers conformational changes in OAS proteins, facilitating the production of 2-5A. This secondary messenger binds RNase L, inducing its dimerisation and activation.

The human OAS family includes four genes – *OAS1*, *OAS2*, *OAS3* and *OASL* on chromosome 12 (Fig 4-2). OAS1-3 are catalytically active and named according to the number of OAS domains they contain, each consisting of five exons (Justesen et al., 2000). In contrast, OASL has an N-terminal OAS domain and two C-terminal ubiquitin-like domains. To increase diversity further, multiple isoforms exist for OAS1 (p42, p44, p46, p48 and p52), OAS2 (p69 and p71) and OASL (p30 and p56-59), while only one splice variant exists for OAS3 (p100) (Fig 4-2) (Koul et al., 2024). The mouse Oas family on chromosome 5 comprises 12 genes, including eight *Oas1* genes (*Oas1a-h*), *Oas2*, *Oas3* and two *Oasl* genes (*Oasl1* and *Oasl2*) (Kakuta et al., 2002). Therefore, evolution has resulted in expanded sets of *OAS* genes in humans and mice via the mechanism of gene duplication, indicative of a central importance in antimicrobial defence.

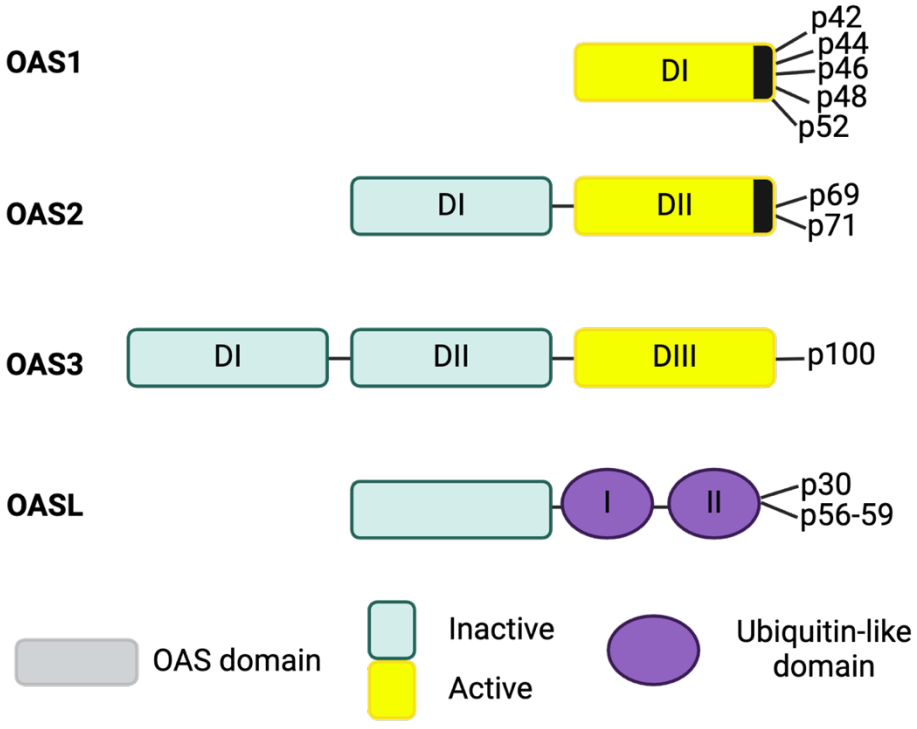

Figure 4-2: Domain organisation of the human OAS gene family. Rectangles represent OAS domains, with those indicated in 2-5A synthesis coloured yellow. There are many possible splice isoforms, generating variability in the C-termini (black box). Modified from Koul *et al*., (2024).

4.1.2. Activation of OAS proteins

OAS1, OAS2 and OAS3 require allosteric activation by dsRNA before they can catalyse 2-5A chains. Instead of using a dsRNA-binding fold, dsRNA binding occurs at a positively charged binding groove on the surface of the protein, where basic amino acids interact with the 2'-hydroxyl group of the dsRNA (Donovan et al., 2013) (Fig 4-3 A). The structure of the OAS proteins influences the minimum RNA length requirement they preferentially bind. In OAS1, this length requirement is 17 base pairs (bp) as its two dsRNA binding sites are approximately 30Å apart, enabling it to bind two neighbouring minor grooves in the dsRNA (Donovan et al., 2013). OAS2 can be activated by an intermediate length of 35bp, while a longer length of > 50bp can activate OAS3 (Donovan et al., 2015; Koul et al., 2020a).

Oligomerisation may be necessary for the enzymatic activity of OAS proteins, with reports that OAS1 can form monomers, dimers and tetramers, while OAS2 and OAS3 exist as dimers and a monomer, respectively (Ghosh et al., 1997; Ibsen et al., 2014; Koul et al., 2020a). Three residues in domain II (DII) of OAS2 (C668, F669 and K670 (CFK)) have been suggested to be an oligomerisation motif (Fig 4-3 B). Mutational studies of the CAFAKA mutant show conflicting evidence for the role of this CFK motif in the enzymatic activity of OAS2. $OAS2^{CAFAKA}$ purified from insect cells can no longer produce 2-5A, but $OAS2^{CAFAKA}$ from human cells was still catalytically active, although 2-5A levels did not reach that produced by $OAS2^{WT}$ (Koul et al., 2020b; Sarkar et al., 1999). The weak binding of domain I (DI) of OAS2 to the dsRNA mimetic poly(I:C), bound to sepharose beads, has led to suggestions that DI has lost the ability to bind dsRNA (Marié et al., 1999). Thus, the ~35bp binding preference for OAS2 makes sense given its existence as a dimer; it has been hypothesised that the four dsRNA-binding sites can be provided by the two DII domains of each OAS2 protomer (Koul et al., 2024). This could explain why the minimum dsRNA length requirement for OAS2 is double that of an OAS1 monomer (Fig 4-3 D).

Binding of dsRNA results in conformational changes that correctly position the catalytic triad residues for binding Mg^{2+} and the ATP substrates. The catalytic

triad consists of three conserved aspartic acid residues that are crucial for the synthesis of 2-5A chains (Koul et al., 2024). In OAS2, these residues are at positions D408, D410 and D481 (Fig 4-3 C), and OAS2^{D481A} mutants are incapable of producing 2-5A *in vitro* (Koul et al., 2020b; Sarkar et al., 1999). The OAS enzymes produce 2-5A of differing lengths, but only 2-5A trimers or longer oligomers can activate RNase L, which exists in its inactive monomeric form in the cytoplasm (Marié et al., 1997). OAS3 mainly produces 2-5A dimers, but recent studies show that it can produce longer oligomers of 2-5A (Dong et al., 1994; Donovan et al., 2015). OAS3 is also activated by a much lower concentration of dsRNA than OAS1 and OAS2 and is antiviral against a more diverse range of viruses; this has led some to hypothesise that OAS3 is necessary and sufficient for the activation of RNase L and the subsequent antiviral effect on virus replication (Donovan et al., 2015; Yize Li et al., 2016).

2-5A binding to RNase L results in dimerisation into its catalytically active conformation (Dong and Silverman, 1995). This results in the preferential cleavage of RNA at single-stranded UU and UA sequences (Dong et al., 1994). This has an antiviral effect by degrading viral genomic ssRNA and/or halting protein synthesis of viral mRNA or host mRNA encoding viral cofactors (Silverman, 2007). This cleavage also produces small self-RNAs that act as PAMPs for other PRRs, such as RIG-I and MDA5, which upregulate IFNß expression (Malathi et al., 2007).

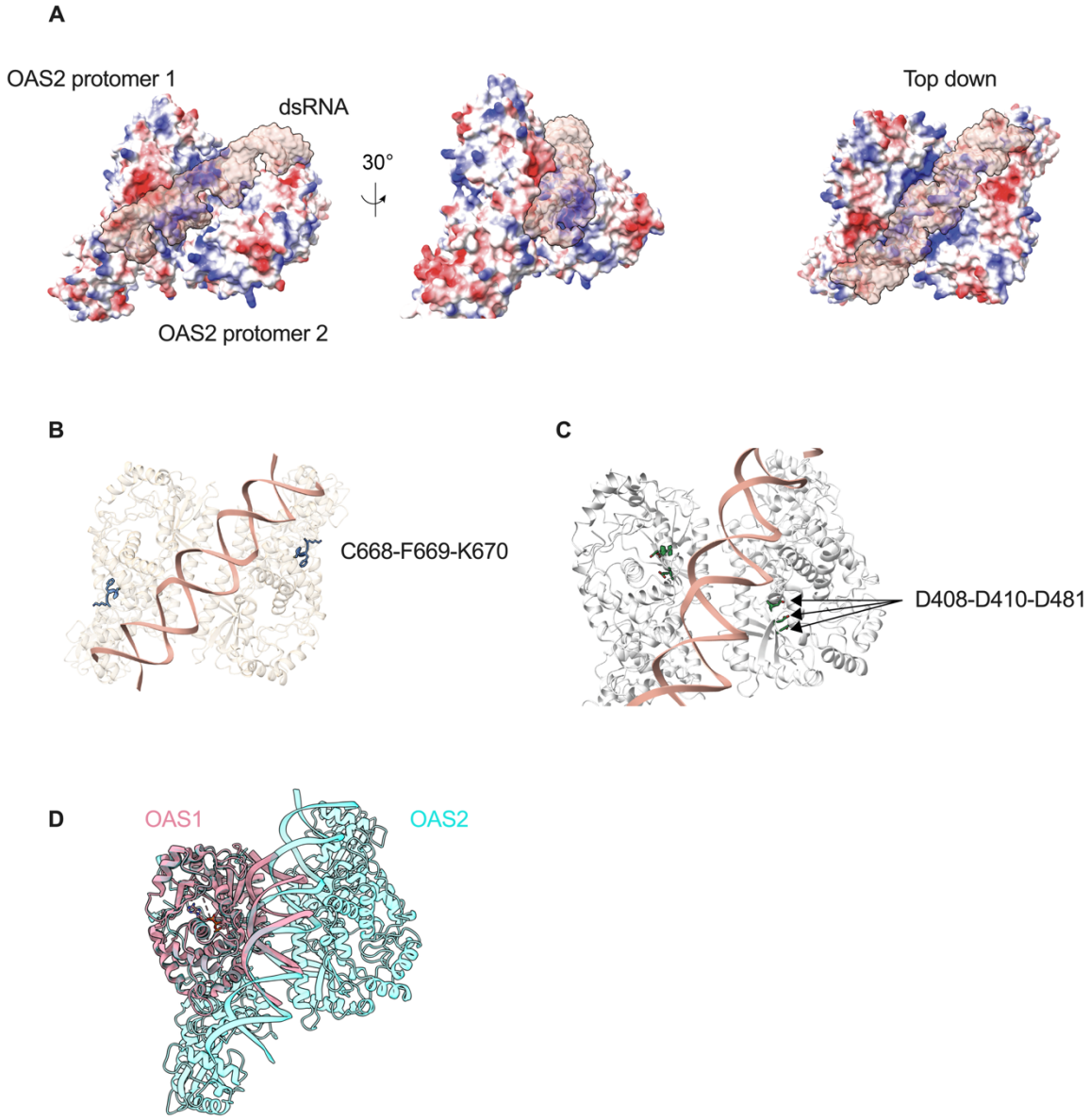

Figure 4-3: Key motifs of the OAS2 protein. AlphaFold structural predictions of OAS2 (p69 isoform) in complex with dsRNA described in (Koul *et al.*, 2020). (**A**) Electrostatic surface representation of an OAS2 dimer in complex with dsRNA shown from different orientations. Blue represents basic residues, while red represents acidic residues. (**B**) OAS2-dsRNA structure with proposed dimerisation motif (C668-F669-K670) highlighted. (**C**) OAS2-dsRNA structure with catalytic triad (D408-D410-D481) highlighted. (**D**) Superposition of the OAS1:18mer structure (Donovan *et al.*, 2013) (PDB: 4IG8) with the AlphaFold OAS2-dsRNA structure.

4.1.3. Virus restriction by the OAS family

The importance of the OAS/RNase L pathway is highlighted by the various families of viruses inhibited *in vitro* by overexpression or depletion of OAS and RNase L proteins, or through *in vivo* experiments using RNase $L^{-/-}$ mice (Kristiansen et al., 2011; Silverman, 2007). Most viruses shown to be inhibited by OAS proteins are RNA viruses, especially those with (+)ssRNA genomes, which is likely because their genomes are prime targets for RNase L (Table 4-1).

Table 4-1: Example viruses inhibited by the catalytically active OAS proteins.

Family	Virus	OAS1	OAS2	OAS3	*In vitro* evidence		Reference
					Overexpression	Depletion	
Arteriviridae	PRRSV		Y*		Y	Y	(Zhao et al., 2017)
Coronaviridae	SARSCoV2	Y			Y		(Wickenhagen et al., 2021)
Flaviviridae	DENV	Y		Y	Y		(Lin et al., 2009)
	HCV	Y		Y	Y	Y	(Kwon et al., 2013)
	JEV	Y*	Y*		Y	Y	(Zheng et al., 2016)
Paramyxoviridae	RSV	Y	Y			Y	(Behera et al., 2002)
Picornaviridae	EMCV	Y	Y	Y	Y	Y	(Marié et al., 1999; Wickenhagen et al., 2021)
Togaviridae	CHIKV			Y	Y		(Bréhin et al., 2009)
	SINV			Y		Y	(Yize Li et al., 2016)

Restriction (Y). OAS protein of porcine origin (*).

4.1.4. Localisation of human OAS proteins

Many viruses, especially (+)ssRNA viruses, generate membranous replication organelles, which can shield the dsRNA replicative intermediates from cytosolic viral RNA sensors (Romero-Brey and Bartenschlager, 2014). Therefore, localisation of OAS enzymes to membranes expands the range of pathogens that can be targeted. The OAS family utilises co- or post-translational modifications, such as lipidation, for this localisation. The two main isoforms of OAS1, p42 and p46, have

distinct C-termini, with p46 containing a CAAX-box motif that signals this protein to be prenylated (Soveg et al., 2021); such prenylation localises proteins to the cytosolic face of membranes within the endomembrane system (Wang and Casey, 2016). OAS1 p46 localises to the Golgi apparatus, and mutation of the CAAX-box revealed that this localisation is essential for its antiviral activity against SARS-CoV-2. In contrast, OAS1 p42 mainly localises to the cytosol and is unable to restrict this virus (Soveg et al., 2021; Wickenhagen et al., 2021). Some studies have suggested that p42 can also localise to the nucleus (Kondratova et al., 2020).

Both OAS2 isoforms contain an N-terminal myristoylation site, and previous studies, when OAS2 was referred to as the p69 form of OAS, show that OAS2 is indeed myristoylated (Marié et al., 1990). It has been hypothesised that this enables OAS2 to localise to the endoplasmic reticulum (Ghosh et al., 2000). Meanwhile, immunostaining of tagged OAS3 shows diffuse intracellular staining, consistent with being a cytosolic sensor (Cusic and Burke, 2024), although there have been suggestions that OAS3 contains a nuclear localisation signal (Malaguarnera et al., 2016).

4.1.5. Non-canonical mechanisms of action of OAS proteins

There is increasing evidence that OAS proteins can act independently of RNase L. Many lab mouse strains are highly susceptible to flaviviruses, such as West Nile Virus (WNV), compared to wild mice that are relatively resistant. Differing susceptibility was mapped to a single gene, later identified as *Oas1b* (Perelygin et al., 2002). Oas1b is one of the eight mouse Oas1 paralogs but is not catalytically active; only Oas1a and Oas1g have functional synthetase activity (Elkhateeb et al., 2016). Susceptible mice encode a truncated version of Oas1b, which lacks the C-terminal transmembrane domain that facilitates its localisation to the endoplasmic reticulum (Courtney et al., 2012; Perelygin et al., 2002). A yeast two-hybrid scheme identified ATP binding cassette protein 3, subfamily F (ABCF3), and oxysterol binding protein-related protein 1L (ORP1L) as binding partners of Oas1b, although the exact mechanism of how these protein interactions inhibit flaviviruses is yet to be determined (Courtney et al., 2012).

Another example of a catalytically inactive OAS protein with antiviral activity is OASL. It has been shown that OASL binds RIG-I and mimics polyubiquitin, enhancing RIG-I signalling and inducing the IFN response (Zhu et al., 2014). Maintaining the IFN response during viral infection appears to be an additional function of OAS proteins. A recent study showed that the human OAS1 p46 isoform inhibits WNV in an RNase L-independent manner (Harioudh et al., 2024). Using RNA immunoprecipitation sequencing (RIP-seq), the authors found OAS1 can bind cellular mRNAs, such as IFNß, through AU-rich elements and localises these mRNA to an endomembrane region. This prolongs the half-life of the mRNA and sustains IFN signalling. Mutations in the catalytic triad and RNase L depletion did not affect OAS1 p46 antiviral activity, whereas RNA-binding residues and the CAAX-box motif were required. Given that OAS1 p46 inhibits SARS-CoV-2 in an RNase L-dependent manner, this suggests the mechanism of antiviral activity of a given OAS protein is virus-specific and that one OAS enzyme can exert multiple antiviral effector functions via distinct mechanisms. Interestingly, this model of binding cellular mRNAs may explain data suggesting that OAS2 inhibits ZIKV through increased expression of IFNß (Liao et al., 2020).

4.1.6. Evasion of the OAS-RNase L pathway

The potent antiviral action of the OAS/RNase L pathway is highlighted by the diverse evasion mechanisms that viruses have evolved against it (Drappier and Michiels, 2015). Viral proteins can sequester dsRNA, so it cannot bind OAS proteins. TAR, a dsRNA structure in the HIV-1 genome, can bind and activate OAS, but the Tat protein binds to TAR, preventing such activation (Schröder et al., 1990).

Most evasion mechanisms act downstream of OAS binding to RNA. RNase L activity is regulated in the cell by an inhibitor (RLI), also known as ABCE1; this regulation process can be hijacked by viruses as RLI/ABCE1 expression is enhanced during EMCV infection (Martinand et al., 1998). Thelier's virus directly targets RNase L through direct interaction via its L* accessory protein (Sorgeloos et al.,

2013). Poliovirus (PV) is highly resistant to the RNase L restriction because of a highly structured region in the ORF of its proteinase $3C^{Pro}$; this cleavage-resistant region acts as a competitive inhibitor of RNase L (Han et al., 2007). Interestingly, IFN-resistant genotypes of Hepatitis C virus (HCV) have fewer UU and UA dinucleotides than predicted compared to genotypes more sensitive to IFN therapy (Han and Barton, 2002). This suggests that the particular sensitivity of an individual HCV genotype to IFN therapy is in part mediated by the susceptibility of HCV mRNA to RNase L cleavage.

Notably for this chapter, some coronaviruses express a 2'-5'-phosphodiesterase (PDE), which can degrade 2-5A, thus preventing RNase L activation. In MHV, this evasion mechanism was mapped to the NS2 protein, and catalytic mutations in NS2 ($NS2^{H126R}$) impair MHV replication and pathogenesis *in vivo* (Zhao et al., 2012). Expression of NS2 from HCoV-OC43 restores replication of MHV-$NS2^{H126R}$ *in vivo* (Goldstein et al., 2017); a similar rescue of replication was observed by expression of the MERS-CoV NS4b protein, which does not exhibit sequence homology to MHV or HCoV-OC43 NS2 (Thornbrough et al., 2016). The fact that multiple lineages of betacoronaviruses have retained a protein with PDE activity despite infecting diverse hosts underlies the importance of evading the OAS/RNase L pathway for successful infection.

4.1.7. OAS mutations and disease susceptibility

There has been increasing evidence of genetic mutations in the *OAS* gene family that affect susceptibility to viral infection (Gokul et al., 2023). This section will provide some examples of susceptibility to coronavirus infection and/or mutations in *OAS2*. Perhaps the most notable example showing how isoform variability affects the control of viral infection is the association between the single nucleotide polymorphism (SNP) rs10774671 (G>A) and severe COVID-19. rs10774671 acts as a splice-acceptor site for exon 7 of *OAS1*; individuals with a G allele express the p46 and p42 isoforms, whereas individuals with the A allele express only p42 (Wickenhagen et al., 2021). As mentioned in section 4.1.4, the p46 form is prenylated, enabling it to localise to the site of viral replication and

exert its antiviral activity. The A allele has also been linked to susceptibility to other viruses, including WNV infection (Lim et al., 2009), and this SNP is thought to be inherited from Neanderthals (Zeberg and Pääbo, 2021).

In some studies, *OAS2* has also been linked to severe COVID-19 infection. An autosomal recessive deficiency in *OAS2* was associated with a case of SARS-CoV-2-related multisystem inflammatory syndrome in children (MIS-C) (Lee et al., 2023). In a Mexican cohort, individuals with the C allele of the *OAS2* intronic SNP rs1293767 were less likely to develop COVID-19 symptoms (Perez-Favila et al., 2024). Another intronic SNP associating *OAS2* with infectious disease is rs1293762, present in intron 2 and associated with tick-borne encephalitis virus (TBEV), DENV and HCV infection (Gokul et al., 2023). These intronic SNPs may be involved in alternative splicing, although this requires testing. Unlike *OAS1* p42/p46, it is not yet clear what determines alternative splicing of *OAS2* into the p71 and p69 isoforms.

Another SNP previously associated with severe TBEV and DENV infection is rs15895, located in exon 9 of *OAS2* (Barkhash et al., 2010b). The A allele changes the tryptophan residue at position 720 to a stop codon, resulting in an eight amino acid truncation. There is variation in this SNP across ethnicities, with North Eurasian populations historically exposed to TBEV (Shorians, Tuvinians and Khakass) having lower frequencies of the A allele compared to lesser exposed populations (Russians and Germans); this led the authors to suggest that TBEV may act as a selection pressure on exposed populations to inherit the protective G allele (Barkhash et al., 2010a).

4.2. Results

4.2.1. Recognition of Contribution

Table 4-2: List of people and their contributions to experimental work.

	Contribution
Adam Fletcher	AlphaFold modelling of OAS2-RNA interactions and primer design
Arda Balci	Immunostaining, confocal microscopy and image analysis
Arthur Wickenhagen	Generation of OAS2 WT and G2A plasmids (previous lab project)
Innes Jarmson	Generation of RNase L CRISPR plasmids (previous lab project)
Matthew Turnbull	Generation of OAS2 CRISPR plasmids (previous lab project)

4.2.2. The p69 isoform of OAS2 restricts HCoV-OC43 at the protein and replication level

As described in Chapter 3, OAS2 was a hit in the human, macaque and bovine ISG library screens against HCoV-OC43 and did not substantially induce an IFN response or cause cytotoxicity. Given that HCoV-OC43 encodes a 2'-5'-PDE that antagonises the canonical OAS-RNase L pathway, I decided to investigate OAS2 further, as I hypothesised that restriction of HCoV-OC43 could be occurring via an RNase L-independent mechanism. The literature generally describes two transcripts of *OAS2*, giving rise to isoforms p71 and p69, which are identical for the first 683 amino acids with alternative splicing generating unique C-termini (Koul et al., 2024); p69 has a distinct 4-residue C-terminus, compared to the 36-residue C-terminus of p71 (Fig 4-4 B).

However, the Ensembl project describes 15 OAS2 transcripts, 7 of which are likely protein-coding (Dyer et al., 2025). Analysis of OAS2 transcript distribution across tissues, using the publicly available Genotype-Tissue Expression project (GTEx) dataset (GTEx Consortium, 2015), indicates only three of these transcripts show significant expression (Fig 4-4 A), which correspond to the OAS2 transcripts available on NCBI: p71 (ENST00000342315.8, NM_016817.3), p69 (ENST00000392583.7, NM_002535.3) and 'isoform 3' (ENST00000449768.2,

NM_001032731.2). Isoform 3 is identical to p71 and p69 for the first 150 amino acids but has a distinct 22-residue tail (Fig 4-4 A).

The human OAS2 "hit" in the ISG screen discussed in Chapter 3 was the p69 isoform. To determine whether OAS2 was inhibitory in non-screening experimental systems, stable cell lines were generated that ectopically express the canonical NCBI sequences of p71, p69 and isoform 3 in A549 cells – i.e. the same genetic background as used in the screens (Fig 4-4 C). As a control, A549 cells stably expressing RFP were also generated. Fortunately, the p71 and p69 isoforms exhibited marginally different electrophoretic mobility and could be distinguished by Western blot (Fig 4-4 C). OAS2 is not expressed at detectable levels by Western blot without IFN stimulation. Since it is unclear what determines OAS2 isoform expression in cells, parental A549 cells were stimulated with IFNß to examine endogenous OAS2 expression. By comparing the migration of the induced OAS2 band with the ectopic constructs, it appears that A549 cells naturally express the p69 isoform (Fig 4-4 C). Although I attempted to test its antiviral activity, protein expression of isoform 3 was not confirmed in the modified cells (Fig 4-4 C), as most commercially available anti-OAS2 antibodies would not be able to bind this isoform. Additionally, isoform 3 does not contain the key residues for catalytic activity and RNA binding, so it was decided to exclude this isoform from subsequent experiments.

I next titrated HCoV-OC43 on my transgenic A549 cells and determined viral titres by plaque assay. Compared to the RFP-expressing control line, the titre of HCoV-OC43 was 524-fold lower in the presence of p69, whereas p71 had minimal effect on viral replication (Fig 4-4 D). In addition to the significantly lower titre, there was a change in plaque morphology in p69-expressing cells. The plaque area was smaller, and the plaque shape was more heterogeneous, making plaques difficult to count (Fig 4-4 E).

Because of this, RFP-, p71- and p69-expressing cells were then infected with different doses of HCoV-OC43 and levels of nucleocapsid protein were

determined by Western blot. Nucleocapsid levels were substantially reduced in p69-expressing cells compared to the control (Fig 4-4 F). The magnitude of this inhibition was surprising given that OAS2, compared to OAS3, is not commonly discussed as a viral restriction factor. I assembled the data from >20 arrayed ISG expression screens performed at the Centre for Virus Research and analysed the effect of ectopic OAS2 p69 expression on a diverse range of viruses. OAS2 rarely appears as a hit; where it does, my screens above revealed the most potent antiviral activity (HCoV-OC43). Interestingly, SARS-CoV-2 came in second (Fig 4-4 G).

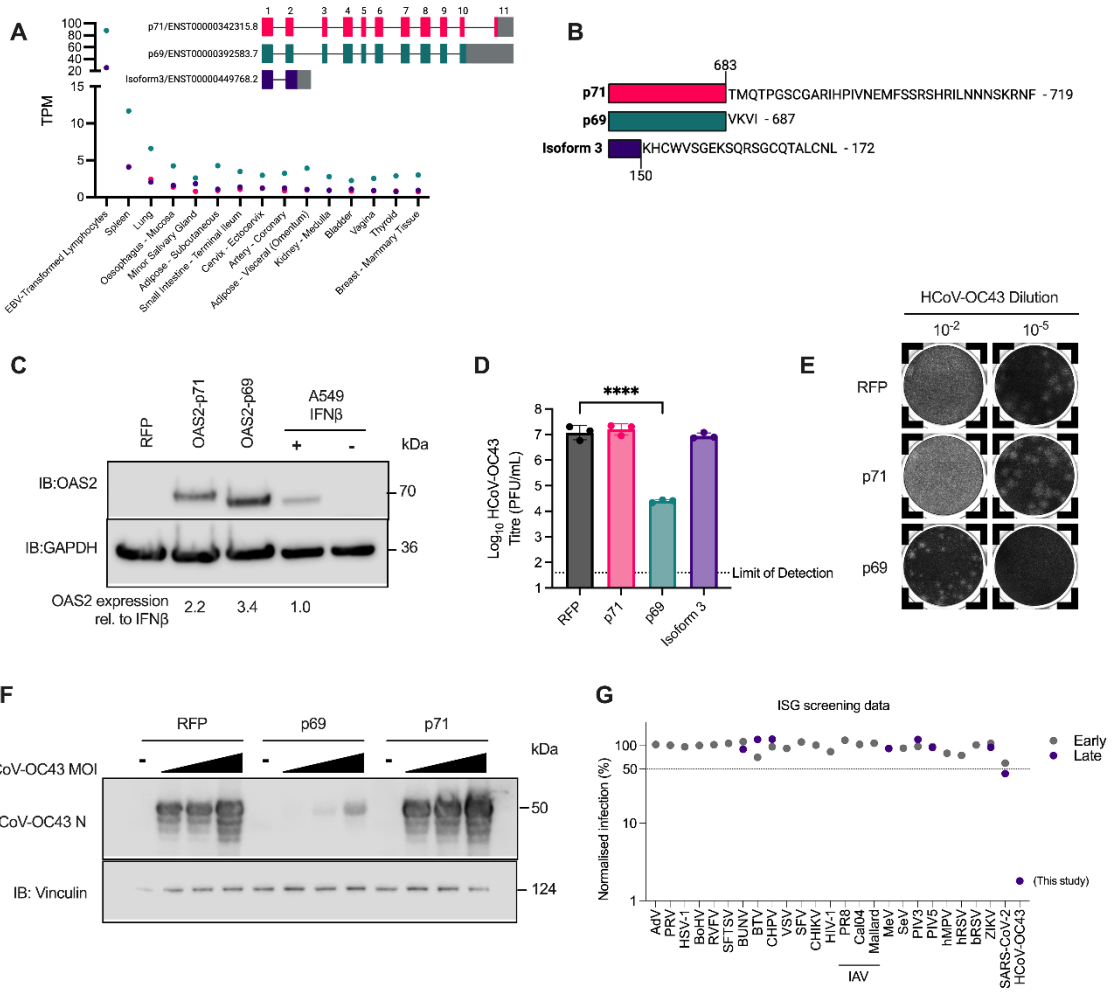

Figure 4-4: The p69 isoform of OAS2 restricts HCoV-OC43. (**A**) Diagrammatic representation of the exon structure of multiple OAS2 transcripts and their corresponding expression levels across tissues, examined using the GTEx database. Grey shading represents non-coding regions. (**B**) Schematic of OAS2 p71 (NM_016817.3), p69 (NM_002535.5) and isoform 3 (NM_001032731.2) protein sequences. The length and distinct C-termini are shown. (**C**) Immunoblot of A549 cells modified to express RFP, OAS2-p71 or OAS2-p69. A549 cells treated with 1000 U/mL IFNβ are shown. (**D**) The infectious titre of HCoV-OC43 on the modified cells in (C) was determined by plaque assay. Each data point represents one independent experiment. Data were analysed using one-way ANOVA with Dunnett's multiple comparison test (vs. RFP), where *p<0.05, **p<0.01, ***p<0.001, and ****p<0.0001. (**E**) Representative images of HCoV-OC43 plaques formed in (D). (**F**) Modified cells from (C) were infected with HCoV-OC43 at an MOI of 0.005, 0.01 and 0.05 and blotted for HCoV-OC43 Nucleocapsid (N) after 72 h (n=1). (**G**) Normalised infection levels in cells expressing the p69 isoform for diverse viruses, from arrayed ISG expression screening datasets performed at early and late timepoints of infection.

4.2.3. The p69 isoform of OAS2 restricts HCoV-OC43 at the transcript level

HCoV-OC43 does not cause substantial cytopathic effect in A549 cells, so I wanted to develop a more sensitive qPCR assay to quantify HCoV-OC43 replication and its inhibition by OAS2. Dual-labelled probes were designed to target the 5' end of the viral genome (within ORF1a) or the 3' subgenomic region (within the N ORF). Specifically, the ORF1a target quantifies the number of viral genomes, whereas the N target quantifies the number of genomes + the number of subgenomic RNAs. Levels of these transcripts were examined at multiple timepoints in A549 cells to determine optimal incubation times. ORF1a signal peaked at 48 hpi at all MOIs tested (Fig 4-5 A), whereas nucleocapsid signal was still increasing at 72 hpi for MOIs lower than 0.01 (Fig 4-5 B); this difference between the two targets indicates specific transcription of subgenomic RNA at later time points. For subsequent experiments, cells were infected at an MOI of 0.01 unless otherwise stated and harvested 48-72 hpi; the longer incubation takes into account that viral replication tends to be lower in transduced cells.

Supporting data from (Fig 4-4), ORF1a and nucleocapsid transcripts were significantly reduced in p69-expressing cells compared to controls (Fig 4-5 C-F). RT-qPCR data was analysed using the $2^{-\triangle\triangle Ct}$ method to calculate the relative fold gene expression change during the experiment. Actin beta (ACTB) was used as the housekeeping gene, but there were two choices for the control sample. Data can be normalised using a 2 h timepoint of the same cell line, which can be considered the amount of "input" genome or the RFP cell line at the same timepoint. Using the 2 h approach, ORF1a (Fig 4-5 C) and nucleocapsid (Fig 4-5 D) transcripts were 61- and 51-fold lower in p69-expressing cells compared to RFP. Using the RFP approach, ORF1a (Fig 4-5 E) and nucleocapsid (Fig 4-5 F) transcripts were 27- and 37-fold lower in p69-expressing cells.

It should be noted that viral transcripts are 1.5 to 3-fold higher in p71-expressing cells than the RFP control (Fig 4-5 C-F); this increase is statistically significant when normalised to the RFP cell line at the same timepoint. This

suggests that the p71 isoform may enhance HCoV-OC43 infection. However, it cannot be ruled out that RFP is a suboptimal control. As a much smaller gene, lentiviral vectors expressing RFP tend to “over-transduce” due to the high titres generated in the transfection protocol. This can cause a slight inhibition of viral replication in cells.

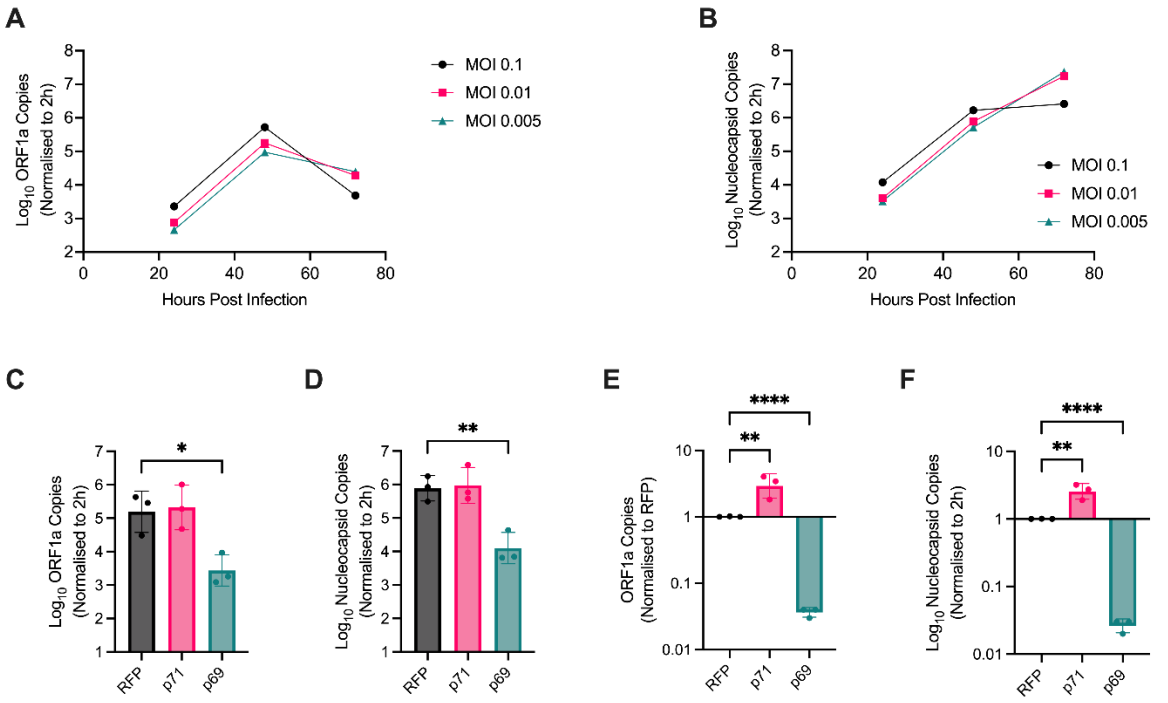

Figure 4-5: Reduction of HCoV-OC43 RNA in p69-expressing cells. A549 cells were infected with HCoV-OC43 at the MOIs indicated and transcript copies of ORF1a (**A**) and nucleocapsid (**B**) were quantified at multiple timepoints by RT-qPCR (n=1). (**C-D**) Quantification of HCoV-OC43 ORF1a (**C**) or nucleocapsid (**D**) of cells expressing RFP, p71 or p69 infected for 72 h (MOI 0.01) by RT-qPCR. Data was analysed using $2^{-\triangle\triangle Ct}$ method with viral gene copies at 2 h, in the respective cell line, as the control sample. (**E-F**) Quantification of HCoV-OC43 ORF1a (**E**) or Nucleocapsid (**F**) of cells expressing RFP, p71 or p69 infected for 72 h (MOI 0.01) by RT-qPCR. Data was analysed using $2^{-\triangle\triangle Ct}$ method with viral gene copies in RFP-expressing cells at 72 h as the control sample. (**C-F**) Each data point represents one independent experiment. Data were analysed using one-way ANOVA with Dunnett's multiple comparison test (vs. RFP), where *p<0.05, **p<0.01, ***p<0.001, and ****p<0.0001.

4.2.4. Myristoylation is required for the localisation and antiviral activity of OAS2 p69

In the subsequent section, Dr Arda Balci performed the immunostaining, microscopy and data analysis for (Figure 4-7).

Given that prenylation is required for the anti-SARS-CoV-2 activity of OAS1 (Wickenhagen et al., 2021), I hypothesised that N-terminal myristoylation has a similar role in the antiviral activity of OAS2. Myristoylation involves the addition of myristic acid to the N-terminal glycine residue after removal of the initiator methionine (Fig 4-6 A); in addition to the N-terminal glycine, the myristoylation consensus includes a serine or threonine residue at position 5 (G-X-X-X-S/T-X-X-X). The N-myristoylation site was mutated in both OAS2 isoforms (G2A) and stable cell lines were generated (Fig 4-6 B).

To test if OAS2 p69 is indeed myristoylated, these stable cell lines were incubated with a myristic acid azide substrate, which is incorporated into cellular myristoylated proteins. After cellular lysis, a click-chemistry reaction was performed upon the addition of a biotin alkyne. The newly biotinylated proteins were subjected to a streptavidin pulldown followed by immunoblotting for OAS2. There is a reduction in OAS2 protein pulled down in cells expressing the G2A mutants but not a complete loss as expected (Fig 4-6 D). Other groups have shown that p69 is myristoylated using radioactive isotopes (Marié et al., 1990), so this protocol requires optimisation. Previous work showing OAS1 p46 is geranylgeranylated used a similar approach (Soveg et al., 2021), but in those experiments, 293T OAS1 KO cells were transfected with FLAG-tagged OAS1 proteins 3 h after adding the azide substrate. This FLAG-tagged OAS1 was immunoprecipitated and the click-chemistry reaction was performed on-bead; their samples were enriched for the protein of interest, whereas my samples contained all proteins from a stable cell line. Despite this assay requiring optimisation, the data suggest that myristoylation is necessary for its antiviral activity against HCoV-OC43 because the infectious titre of the $p69^{G2A}$ mutant was equivalent to p71 (Fig 4-6 C).

Given the mislocalisation of OAS1 p46 upon mutation of its C-terminal prenylation site, I hypothesised that myristoylation of OAS2 resulted in its localisation to specific subcellular compartments. We stained the cell lines ectopically expressing p71, p69 and their respective G2A mutants for OAS2 and examined their localisation by confocal laser scanning microscopy (cLSM). p71 and p69 appeared to localise to perinuclear compartments. Co-staining with the Golgi marker 58K confirmed localisation of both isoforms to the Golgi apparatus (Fig 4-7 A-B) but not to the endoplasmic reticulum, as co-staining did not occur with the ER marker calnexin (Fig 4-7 D). Additionally, IFN-stimulated A549 cells were examined, confirming endogenous OAS2 localises in a similar fashion to ectopically expressed OAS2 (Fig 4-7 C).

Coronavirus replication organelles are formed by the modification of endomembrane compartments (Romero-Brey and Bartenschlager, 2014), and so I suspected that OAS2, as a viral dsRNA sensor, may localise to such sites of replication. Co-staining of OAS2 and dsRNA in HCoV-OC43 infected cells revealed that more co-localisation was observed with the p71 isoform than the p69 isoform (Fig 4-7 E-F). Even though cells were infected at a high MOI, it is unsurprising that p69 did not show convincing co-localisation given its antiviral activity; dsRNA is more noticeable in cells in which the ectopic expression of p69 is lower. Given both isoforms localise to the Golgi apparatus, p71 acts as a better control to determine co-localisation, but optimisation of this experiment is required to convincingly confirm OAS2 localises with dsRNA.

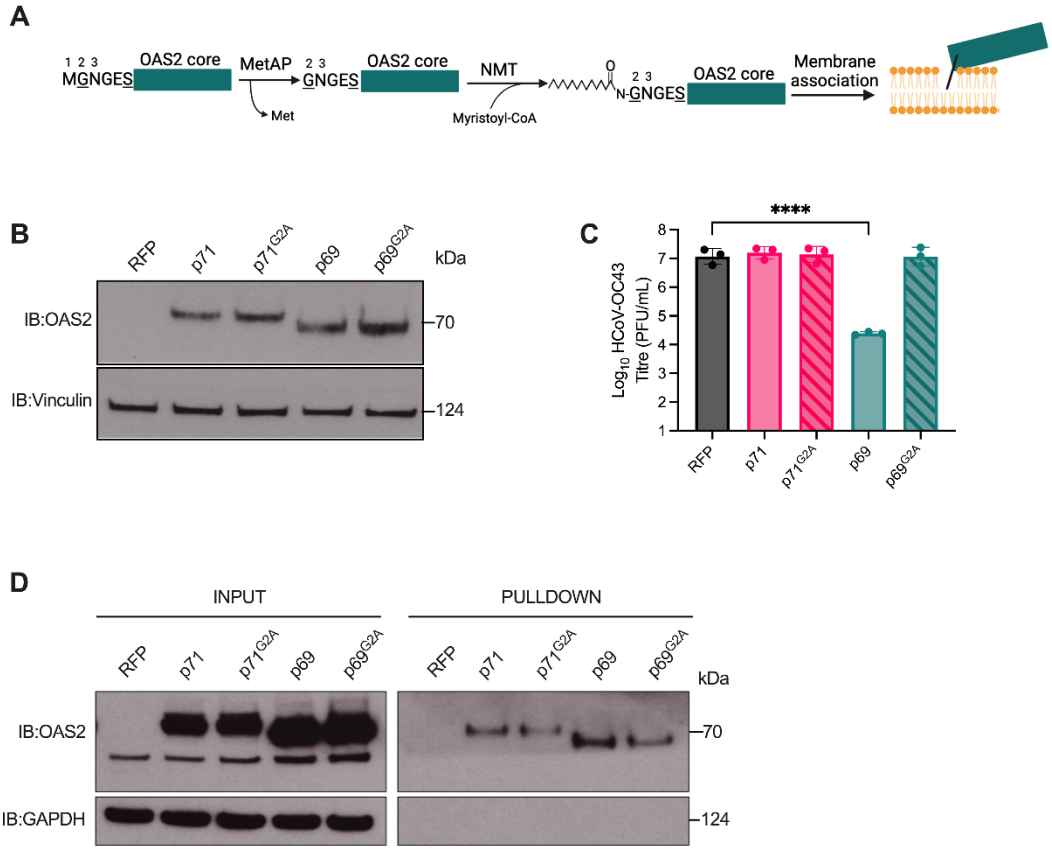

Figure 4-6: Myristoylation is required for the antiviral activity of p69. (**A**) Schematic representation of OAS2 myristoylation. Methionine aminopeptidase 2 (MetAP2) removes the initiator methionine before the addition of the myristoyl group by N-myristoyltransferase (NMT) to the subsequent glycine residue. Key residues of the myristoylation consensus sequences are underlined. (**B**) Immunoblot of cells expressing the OAS2 isoforms and their respective myristoylation site mutants. (**C**) Infectious titre of HCoV-OC43 in the modified cells in (B) was determined by plaque assay. Each data point represents one independent experiment. Data were analysed using one-way ANOVA with Dunnett's multiple comparison test (vs. RFP), where *p<0.05, **p<0.01, ***p<0.001, and ****p<0.0001.(**D**) Immunoblot of whole cell lysate (left) and streptavidin pulldown (right) of cells in (A) subjected to click-chemistry using a myristic acid azide and alkyne biotin (n=1).

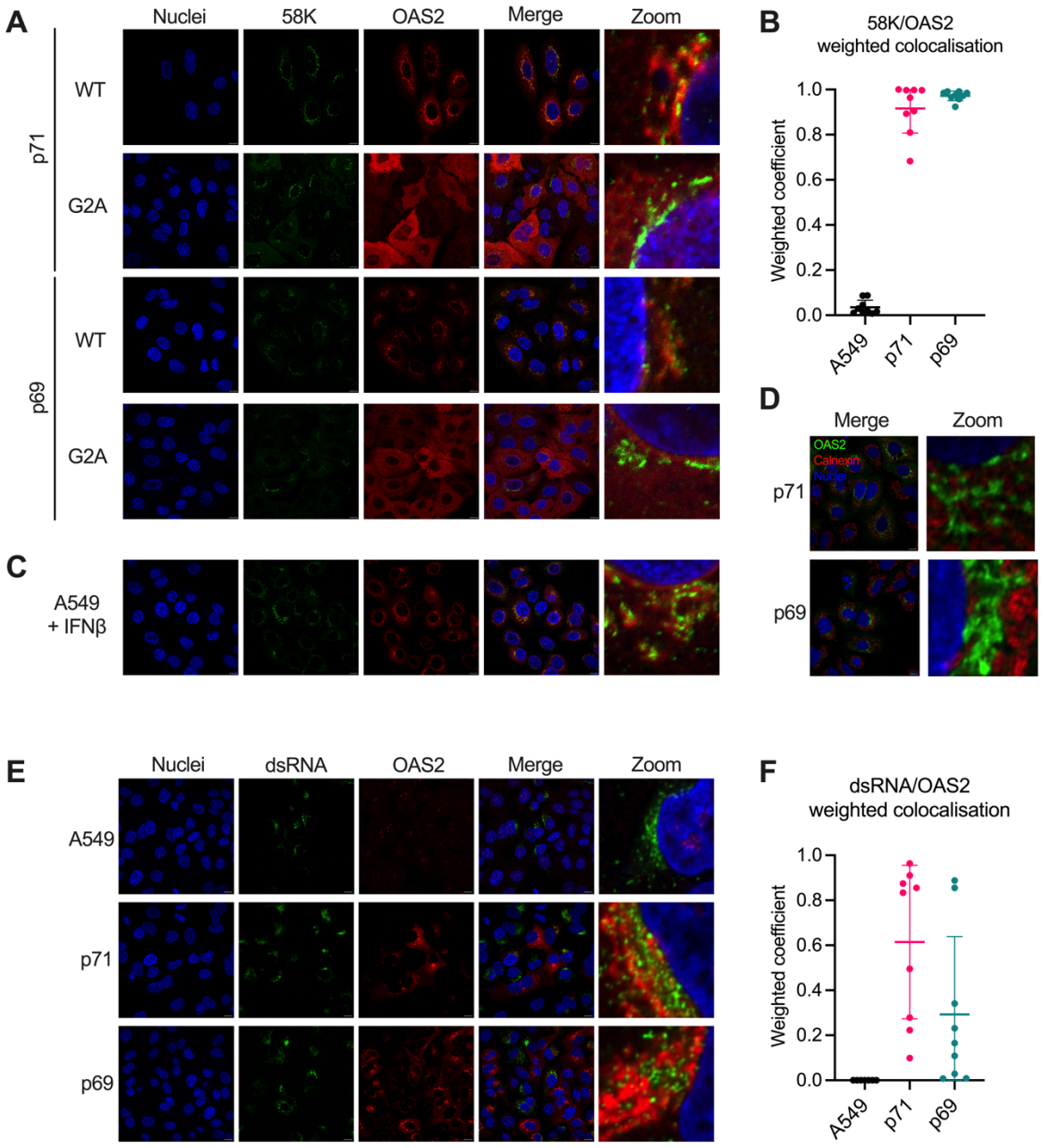

Figure 4-7: Myristoylated OAS2 localises to the Golgi apparatus. (**A**) Confocal micrographs of A549 cells expressing p71, p69 or their respective myristoylation site mutants stained with anti-58K (green), anti-OAS2 (red) and Hoechst (blue) (n=1). (**B**) Quantification of colocalisation of 58K with OAS2 in cells represented in (A). (**C**) A549 cells were treated with 1000 U/mL IFNβ for 24 h and stained as in (A) (n=1). (**D**) Confocal micrographs of A549 cells expressing p71 or p69 stained with anti-OAS2 (green), anti-Calnexin (red) and Hoechst (blue). (**E**) Confocal micrographs of parental, p71- or p69-expressing A549 cells infected with HCoV-OC43 for 24 h (MOI = 10). Cells were stained for anti-dsRNA (green), anti-OAS2 (red) and Hoechst (blue) (n=1). (**F**) Quantification of colocalisation of dsRNA with OAS2 in cells represented in (E). (**B, F**) Each data point represents an individual cell in one independent experiment.

4.2.5. The antiviral activity of p69 is not dependent on catalytic activity or RNase L

As described above, the antiviral activity of OAS proteins canonically occurs via synthesis of 2-5A, which activates RNase L. To determine whether the catalytic triad is required for the antiviral activity of p69 toward HCoV-OC43, a D481A substitution was introduced into the p69 isoform and stably expressed in A549 cells. As oligomerisation has been hypothesised to be involved in enzymatic activity, a CAFAKA substitution was also generated (Fig 4-8 A); $p69^{CAFAKA}$ expression was 2.4-fold lower than $p69^{WT}$ whereas $p69^{D481A}$ was equivalent to WT. At 72 hpi, HCoV-OC43 ORF1a transcripts were 89-, 137- and 74-fold lower in the $p69^{WT}$, $p69^{D481A}$ and $p69^{CAFAKA}$ cells, respectively, compared to the RFP control (Fig 4-8 B). Similarly, HCoV-OC43 nucleocapsid transcripts were 156-, 190- and 140-fold lower in the $p69^{WT}$, $p69^{D481A}$ and $p69^{CAFAKA}$ cells, respectively, compared to the RFP control (Fig 4-8 C). The higher fold change with $p69^{D481A}$, and vice versa with $p69^{CAFAKA}$, may reflect the difference in protein expression (Fig 4-8 A).

Recent *in vitro* studies have suggested that the CAFAKA mutation is not sufficient to disrupt OAS2 oligomerisation and is still catalytically active, so it could be that the mutation has not disrupted oligomerisation in my system; if so, it is perhaps unsurprising that antiviral activity has been maintained by the CAFAKA variant (Koul et al., 2020b). However, the same authors showed that D481A mutants cannot produce 2-5A, so we can be confident that this mutation ablates 2-5A synthesis. Therefore, these data support my hypothesis that the antiviral activity of p69 might not involve the classic pathway involving 2-5A and RNase L.

To confirm that p69 may act via an RNase L-independent mechanism, I sought to deplete RNase L and determine whether HCoV-OC43 replication was rescued in cells expressing p69. Firstly, lentiviral vectors expressing seven unique RNase L-specific CRISPR guides were transduced into RFP-expressing A549 cells, and their relative efficacy in RNase L depletion was assessed by Western blot (Fig 4-9 A). The most effective CRISPR guides were then used to deplete RNase L in

RFP- and p69-expressing A549 cells (Fig 4-9 B). These modified cell lines were infected with HCoV-OC43. Remarkably, potent RNase L depletion did not affect the ability of p69 to inhibit viral nucleocapsid protein expression (Fig 4-9 C).

To confirm this finding, I used RT-qPCR to measure viral RNA transcripts at 48 hpi. Viral RNA was normalised to the RFP empty vector control. Robust restriction of ORF1a and nucleocapsid transcription was maintained in p69-expressing cells depleted of RNase L, suggesting an RNase-L independent mechanism (Fig 4-9 D-E). It should be highlighted that HCoV-OC43 replication is 2- to 3-fold lower in the RFP-expressing cells depleted of RNase L, which could result from expressing this CRISPR guide in the cell. This might explain why replication of HCoV-OC43 in p69 cells depleted of RNase L is 2 to 7-fold lower than the p69 empty vector control. Nevertheless, RNase L depletion does not rescue HCoV-OC43 replication in the presence of p69, suggesting the OAS-RNase L pathway cannot, by itself, explain the antiviral activity of p69.

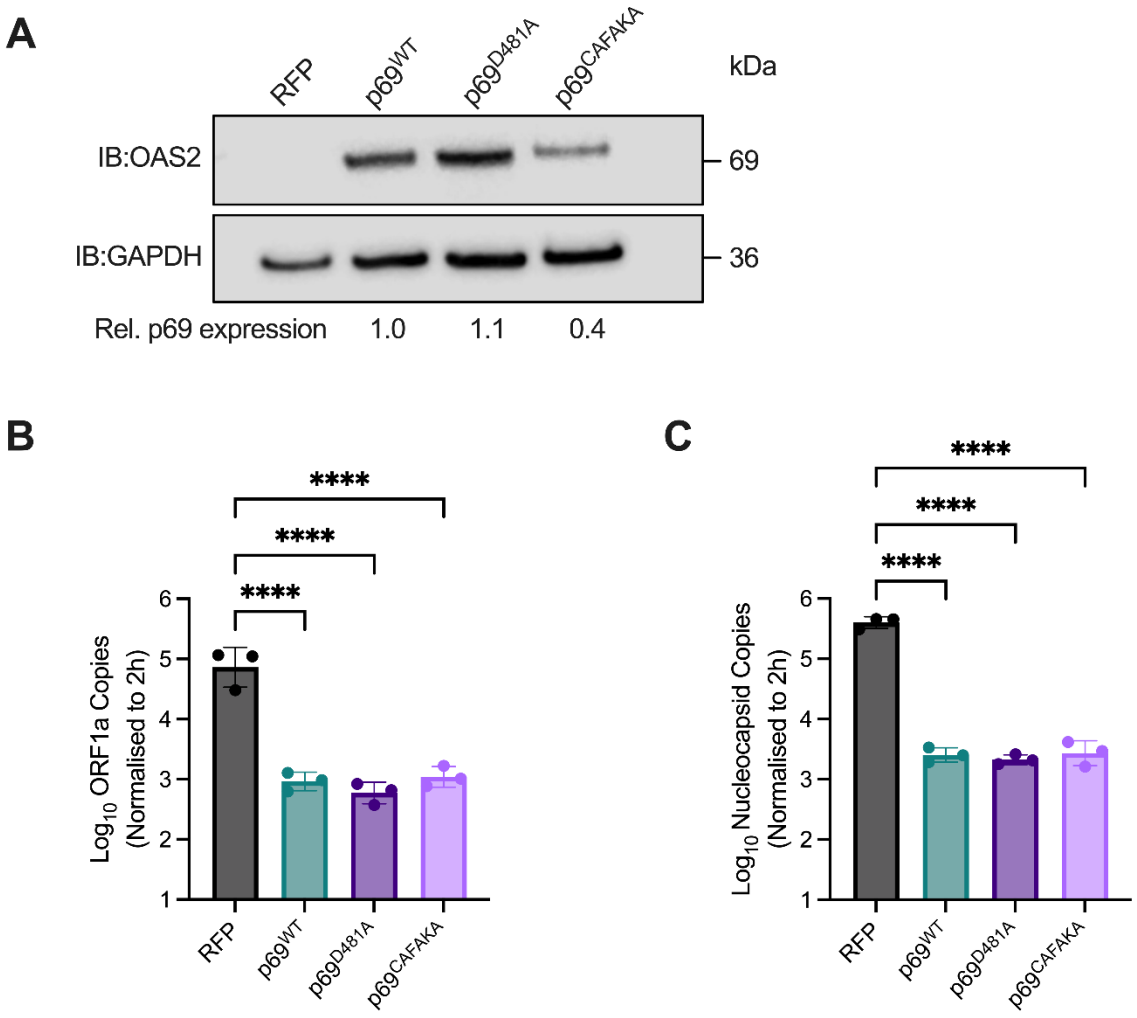

Figure 4-8: Catalytic mutants of p69 retain antiviral activity. (**A**) Immunoblot of A549 cells modified to express RFP, p69, p69^{D481A} or p69^{CAFAKA}. (**B-C**) Quantification of HCoV-OC43 ORF1a (**B**) and nucleocapsid (**C**) in modified cells from (A) infected for 72 h (MOI 0.01) by RT-qPCR. Data was analysed using the $2^{-\triangle\triangle Ct}$ method with viral gene copies at 2 h in the respective cell line as the control sample. (**B-C**) Each data point represents one independent experiment. Data were analysed using one-way ANOVA with Dunnett's multiple comparison test (vs. RFP), where *p<0.05, **p<0.01, ***p<0.001, and ****p<0.0001.

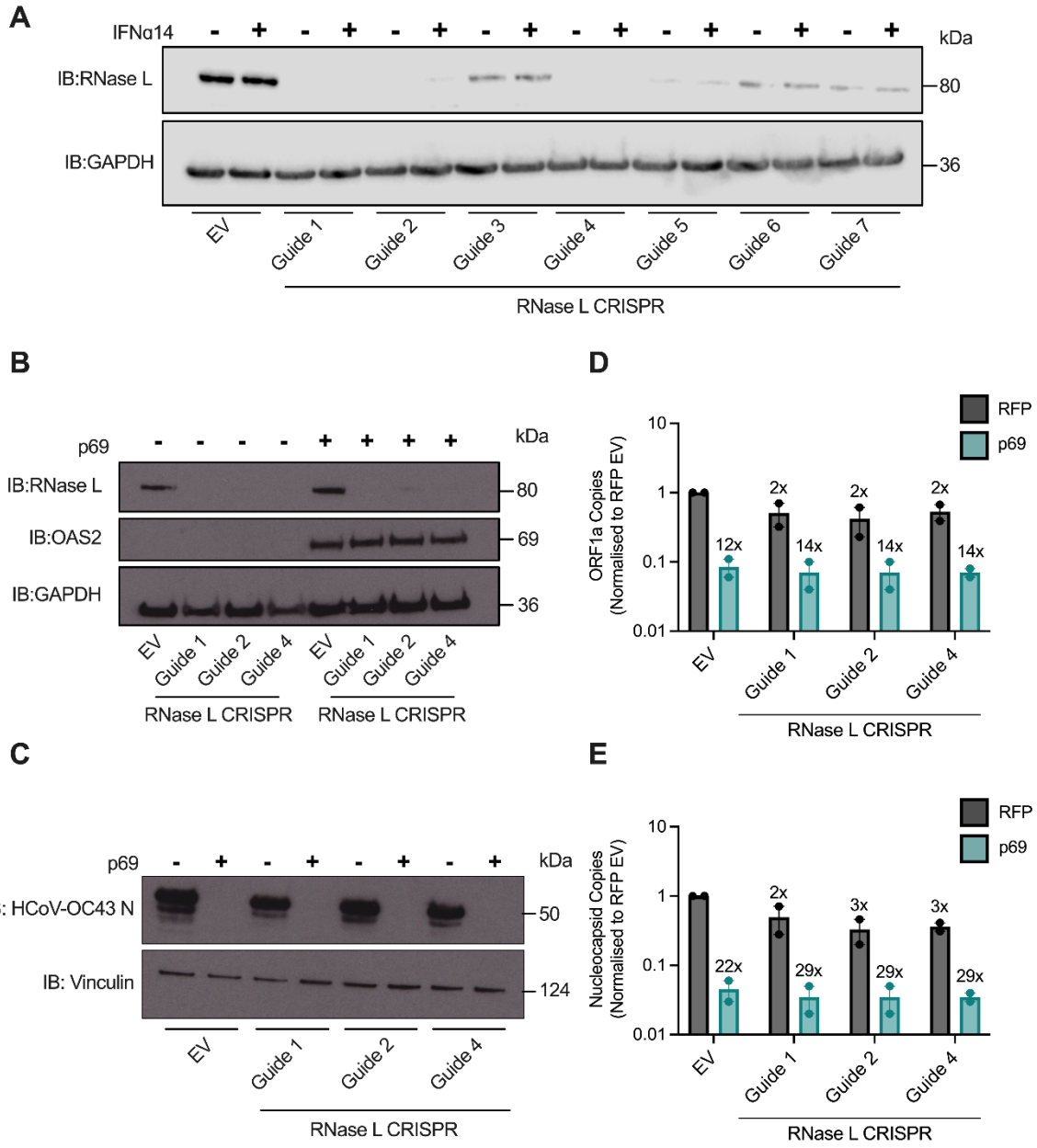

Figure 4-9: Loss of RNase L does not rescue HCoV-OC43 replication. (**A**) Immunoblot of RFP-expressing A549 cells with reduced RNase L expression using seven different lentiviral vector-derived CRISPR guides. (**B**) Immunoblot of A549 cells expressing RFP or p69 whose RNase L expression was reduced using the three most effective CRISPR guides from (A). (**C**) Modified cells from (B) were infected with HCoV-OC43 for 72 h and stained for HCoV-OC43 nucleocapsid; representative immunoblot of two independent experiments is shown. (**D-E**) Quantification of HCoV-OC43 ORF1a (**D**) and nucleocapsid (**E**) in RNase L knockdown cells from (B) infected for 48 h (MOI = 0.01) by RT-qPCR. Data was analysed using the $2^{-\triangle\triangle Ct}$ method, with the RFP empty vector cell line used as the control sample. Each data point represents one independent experiment. EV: Empty Vector.

4.2.6. Predicted RNA-binding mutations abolish the antiviral activity of p69

In the following section, Dr Adam Fletcher performed the AlphaFold modelling of OAS2 in complex with dsRNA.

To examine whether p69 binds viral dsRNA, mutations that should impair RNA binding were introduced. As an experimental OAS2-RNA model was unavailable, the interaction between an OAS2 dimer and RNA was modelled using a double-stranded 43mer that has been previously shown to activate OAS2 *in vitro* (Koul et al., 2020a), using the AlphaFold Server (Fig 4-10 A) (Abramson et al., 2024). Confidence intervals of the individual OAS2 protomers were relatively high, with the RNA molecule sandwiched between the protomers (Fig 4-10 A). At the OAS2-RNA interface, there are numerous lysine and arginine residues, forming a basic channel that interacts with RNA (Fig 4-10 B).

Binding of dsRNA enables OAS2 residues R529 and R533 to form hydrogen bonds with the phosphate backbone. A dual R194E/R198E mutant of porcine OAS1 displayed >10000-fold reduction in catalytic activity and was less able to bind a radioactive RNA ligand (Hartmann et al., 2003). As shown in the study, these residues align to R529 and R533 in human OAS2. R529 is also conserved in bovine and rodent species, although glutamine (Q) is present at position 533 in rodents (Fig 4-10 C). Similarly, OAS2 residues R374 and K378 are in close proximity to the RNA ligand; mutation of the equivalent latter residue in porcine OAS1 (K41E) resulted in a 63-fold reduction in catalytic activity. Together, this gives us confidence that mutating these residues will impair RNA binding. Non-conservative substitutions, aimed to ablate electrostatic interactions between protein and nucleic acid, were introduced into p69, and $p69^{R374E/K378E}$ and $p69^{R529E/R533E}$ mutants were ectopically expressed in A549 cells (Fig 4-10 D); note that the expression of the $p69^{R529E/R533E}$ mutant was 2.7-fold lower than $p69^{WT}$.

Next, I infected these cells and used RT-qPCR to monitor viral replication. As before, I observed a strong inhibition (141x) of ORF1a signal in the $p69^{WT}$-

expressing cells relative to the RFP control, compared to a 59-fold inhibition in ORF1a signal in $p69^{R374E/K378E}$ expressing cells. In contrast, a 3.3-fold increase in ORF1a transcripts was observed in $p69^{R529E/R533E}$ cells, compared to the RFP control (Fig 4-10 E), suggesting a total loss of viral restriction. Similarly, with nucleocapsid signal, I observed a strong inhibition (205x) in $p69^{WT}$ compared to the RFP control and this inhibition was lessened to a 61-fold reduction in $p69^{R374E/K378E}$ cells. In contrast, a 3.5-fold increase was observed in nucleocapsid transcripts in $p69^{R529E/R533E}$ cells (Fig 4-10 F). Therefore, both RNA-binding mutants appear to reduce HCoV-OC43 restriction, with the antiviral activity completely lost in the presence of $p69^{R529E/R533E}$. It is unlikely that the modestly lower protein expression of the $p69^{R529E/R533E}$ mutant explains this result. Moreover, the $p69^{CAFAKA}$ mutant had a similar reduction in expression level compared to WT, while retaining its antiviral activity (Fig 4-8 B). Thus, the positively charged RNA-binding residues R529 and R533 are necessary for the observed restriction of HCoV-OC43.

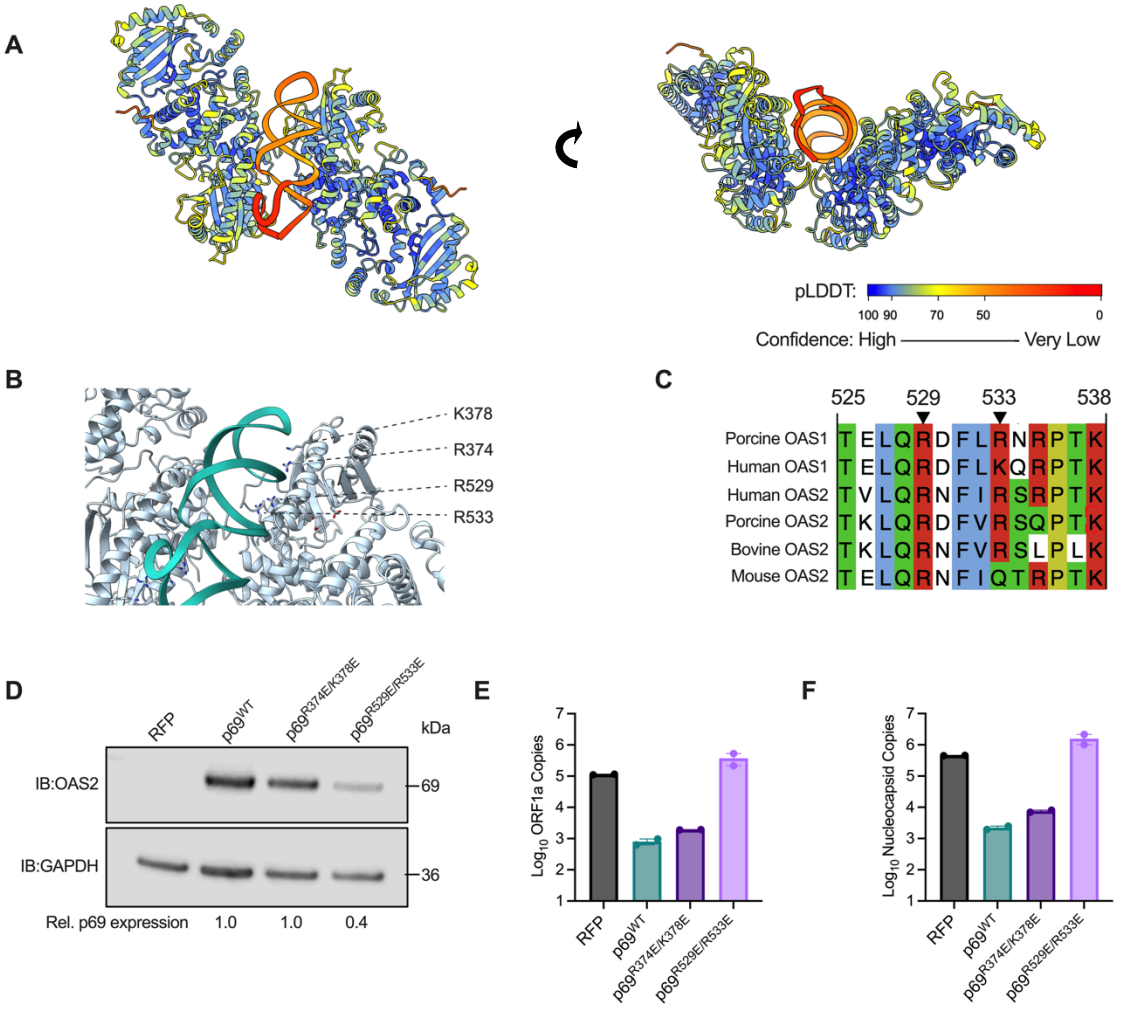

Figure 4-10: RNA-binding mutations abrogate the antiviral activity of p69. (**A**) Top-ranking AlphaFold3 model of OAS2 p69 in complex with 43mer dsRNA, described in Koul *et al*., (2020). The model is coloured according to pLDDT scores. (**B**) Position of OAS2 residues R374, K378, R529 and R533 in proximity to dsRNA in the model from (A). (**C**) Multiple sequence alignment of OAS1 and OAS2 proteins from several species, focusing on residues R529 and R533, which correspond to porcine OAS1 residues R194 and R198 tested in Hartmann *et al*., (2003). (**D**) Immunoblot of A549 cells modified to express RFP, p69, $p69^{R374E/K378E}$ or $p69^{R533E/R529E}$. (**E-F**) Quantification of HCoV-OC43 ORF1a (**E**) and nucleocapsid (**F**) in modified cells from (D) infected for 72 h (MOI 0.01) by RT-qPCR. Data was analysed using the $2^{-\triangle\triangle Ct}$ method with viral gene copies at 2 h in the respective cell line as the control sample. (**E-F**) Each data point represents one independent experiment.

4.2.7. The p71 isoform of OAS2 restricts EMCV in an RNase L-dependent manner

The data so far suggest that OAS2 p69 restricts viral infection in an RNase L-independent manner. I wanted to explore whether this was true for other viral targets of OAS2. I decided to use Cardiovirus A (EMCV); EMCV has previously been shown to be sensitive to the OAS-RNase L pathway and can be inhibited by OAS2 (Marié et al., 1999). Because EMCV, a picornavirus, also replicates in membranous organelles (Romero-Brey and Bartenschlager, 2014), it seemed plausible that OAS2 myristoylation enables antiviral activity against EMCV.

I infected cells expressing RFP, p69 or p71 with EMCV. Surprisingly, viral infectious titre was ~70-fold lower in p71 expressing cells than in the RFP control, whereas the p69 isoform did not show a statistically significant reduction (Fig 4-11 A). In addition to the lower titre, the difference in plaque phenotype between the OAS2 isoforms was substantial, with p71 causing a considerably smaller plaque area (Fig 4-11 C). As expected, myristoylation is important for this antiviral activity, with the $p71^{G2A}$ mutant having an infectious titre 15-fold higher than the wild-type p71 (Fig 4-11 B); this increase in replication was also reflected by the larger plaque area in cells expressing $p71^{G2A}$ (Fig 4-11 C). Despite not showing significant inhibition of EMCV in the experiment performed in (Fig 4-11 A), the $p71^{G2A}$ mutant has a 2.8-fold higher infectious titre and larger plaque area than p69. With this and the fact that the $p69^{G2A}$ mutant has a 1.4-fold higher titre than p69, it cannot be ruled out that p69 possesses some antiviral activity against EMCV.

The role of RNase L in this p71-mediated restriction of EMCV was determined by ablating RNase L from RFP- and p71-expressing A549 cells (Fig 4-12 A), using the most effective CRISPR guide from (Fig 4-9 B). Depletion of RNase L significantly increased the infectious titre in cells ectopically expressing p71, with a corresponding enlargement of plaque area (Fig 4-12 B-C); this increase was only 4-fold with the RFP control. The increase in titre in the RFP control is likely due to the restriction of EMCV by other OAS proteins. It has been shown that the OAS1

p46 isoform, but not the p42 isoform, inhibits EMCV in A549-derived cells (Wickenhagen et al., 2021). A549 cells possess the A allele at the SNP rs10774671 and can only express the OAS1 p42 isoform (Soveg et al., 2021). Therefore, it is likely that this enhancement of infection in RFP RNase L-depleted cells is due to the release of inhibition by OAS3. To confirm this, OAS3 should be depleted in the cells generated in (Fig 4-12 A). Because the fold increase upon RNase L depletion was larger in cells expressing p71 than in cells expressing RFP, and the RNase L-depleted cells all had a similar infectious titre, it is likely that this assay does indeed reflect RNase L-dependent restriction of EMCV by p71.

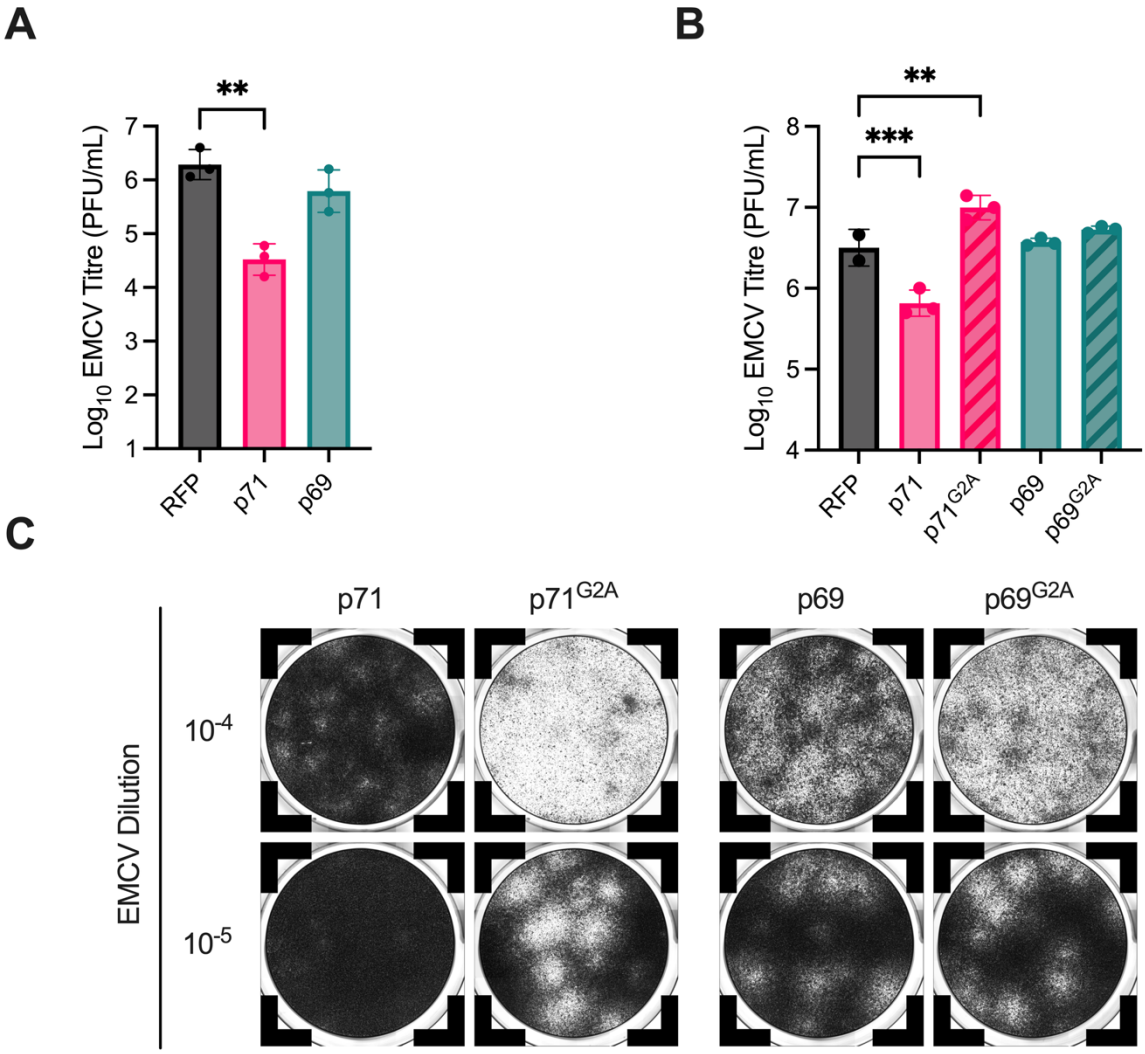

Figure 4-11: The p71 isoform of OAS2 restricts EMCV. (**A**) The infectious titre of EMCV in A549 cells expressing RFP, p71 or p69 was determined by plaque assay. (**B**) Infectious titre of EMCV in A549 cells expressing p71, p69 or their respective myristoylation site mutants was determined by plaque assay. (**C**) Representative images of EMCV plaques formed in (B). (**A-B**) Each data point represents one independent experiment. Data were analysed using one-way ANOVA with Dunnett's multiple comparison test (vs. RFP), where *p<0.05, **p<0.01, ***p<0.001, and ****p<0.0001.

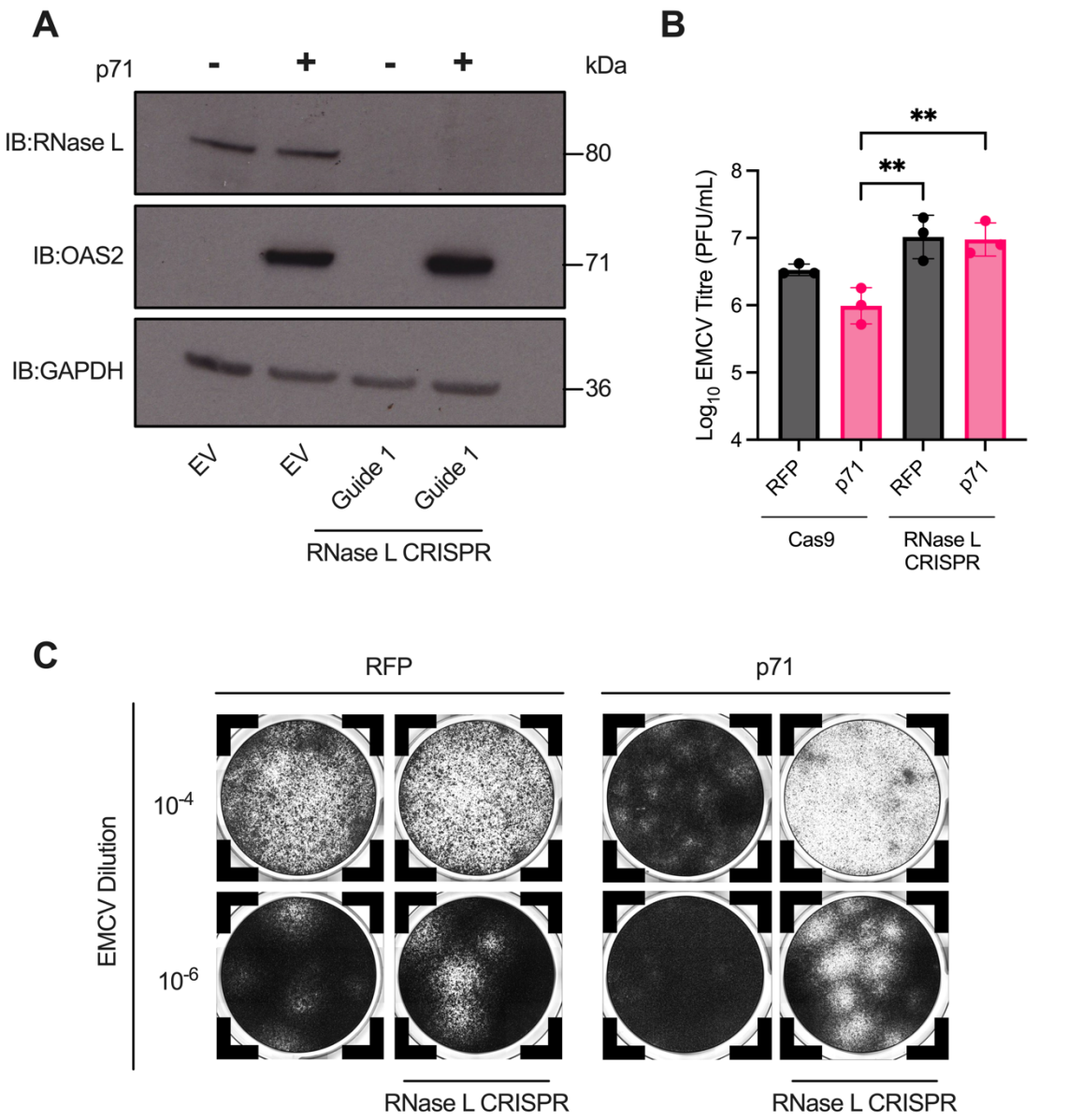

Figure 4-12: The antiviral activity of p71 against EMCV is RNase L-dependent. (**A**) Immunoblot of A549 cells expressing RFP or p71 whose RNase L expression was reduced using a lentiviral vector-encoded CRISPR guides. (**B**) The infectious titre of EMCV in RFP- or p71-expressing A549 cells depleted of RNase L was determined by plaque assay. Each data point represents one independent experiment. Data were analysed using one-way ANOVA with Dunnett's multiple comparison test (vs. RFP), where *p<0.05, **p<0.01, ***p<0.001, and ****p<0.0001.(**C**) Representative images of EMCV plaques formed in (B).

4.2.8. The JAK inhibitor Ruxolitinib inhibits HCoV-OC43 replication

It has been reported that OAS2 restricts Zika Virus (ZIKV) via activation of Type I IFN signalling (Liao et al., 2020). To investigate the role of IFN signalling in the p69-mediated restriction of HCoV-OC43, the JAK inhibitor Ruxolitinib (RUX) was used, which inhibits IFN signalling downstream of the IFN alpha/beta receptor (Quintás-Cardama et al., 2010). To determine optimal RUX concentrations, A549 cells were incubated with differing doses of IFNβ and RUX and stained for phosphorylated STAT1 protein levels after 24 h (Fig 4-13 A). Although 0.5 μM RUX greatly reduced phosphorylated STAT1, concentrations >2 μM were optimal for inhibiting IFN signalling.

RFP- and p69-expressing A549 cells were pre-treated with RUX prior to HCoV-OC43 infection. For both RFP and p69, HCoV-OC43 nucleocapsid protein was reduced with the addition of RUX (Fig 4-13 B). Infectious titre of RUX-treated cells was reduced 1.7- and 3.5-fold in cells expressing p71 and p69, respectively, compared to the DMSO control (Fig 4-13 C). This was opposite to what is expected, given IFN stimulation restricts HCoV-OC43 (Fig 3-3 D). However, some proposed entry factors for HCoV-OC43, like IFITM3, are IFN-stimulated, which could explain the reduced infection (Zhao et al., 2014). Alternatively, RUX may have off-target or cytotoxic effects, resulting in decreased HCoV-OC43 replication. A genetic rather than pharmacological approach to tackle this would be to additionally express the OAS2 isoforms in A549 cells deficient in STAT1 or IFNAR and compare HCoV-OC43 replication. This would confirm whether p69 is acting via upregulation of IFN signalling. However, the persistent restriction in cells treated with RUX suggests that OAS2 does not inhibit viral infection by inducing IFN secretion.

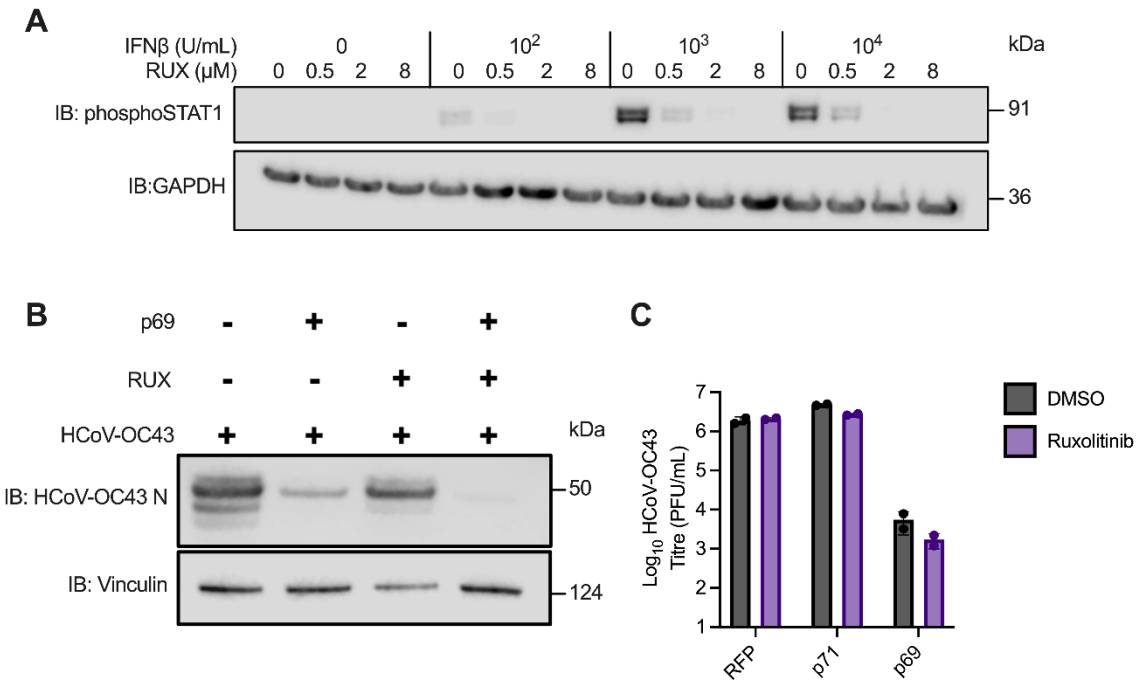

Figure 4-13: Ruxolitinib has an inhibitory effect on HCoV-OC43 infection. (**A**) Immunoblot showing expression levels of phosphorylated STAT1 induced by treatment of IFNβ for 24 h and the effect of simultaneous addition of the JAK inhibitor Ruxolitinib (RUX). (**B**) Cells expressing RFP or p69 were treated with 2 μM RUX for 2 h before 72 h HCoV-OC43 infection (MOI 0.01) and stained for HCoV-OC43 nucleocapsid; representative immunoblot of two independent experiments. (**C**) A549 expressing RFP, p71 or p69 were treated with 0.5 μM RUX for 1 h prior to infection with HCoV-OC43. The infectious titre was determined by plaque assay. Each data point represents one independent experiment.

4.2.9. p69 does not substantially change ISG upregulation during HCoV-OC43 infection

An alternative hypothesis is that OAS2 induces ISG expression independently of IFN – as reported for some pattern recognition receptors. To test this, I measured the expression levels of certain ISGs in A549-OAS2 infected cells by RT-qPCR. The data were analysed by the $2^{-\triangle\triangle Ct}$ method using either transcript copies at 2 h in the respective cell line or transcript copies in the RFP control at 72 h as the reference, as a check to determine whether the timepoint at which the control samples were taken vastly affected the results.

Using the 2 h approach, ISG15 transcripts were 3.9-fold higher or 3.5-fold lower in the presence of p71 or p69, respectively, compared to RFP (Fig 4-14 A). This was similar to the RFP approach; ISG15 transcripts were 5-fold higher or 3.5-fold lower in the presence of p71 or p69, respectively (Fig 4-14 B). The same direction and magnitude of transcript copies were observed with IFIT1, another ISG tested (Fig 4-14 C-D). CXCL10, IFNB1 and Mx1 were not consistently detectable at the timepoints tested.

It appears p71 has higher levels of ISG expression than the control. However, this may reflect that HCoV-OC43 replication is 1.5 to 3-fold higher in the presence of p71 at the same timepoint (discussed in 4.2.3). Given that p69 has lower ISG expression than the RFP control, this data does not suggest that an enhanced ISG response is causing the p69-mediated restriction of HCoV-OC43. However, these changes were only observed with two ISGs tested, and only the 72 h timepoint was examined, so more experiments should be performed to confirm this conclusion. For example, expressing the OAS2 isoforms in A549 cells modified with an ISRE-GFP/Luciferase reporter construct. This would allow ISRE activity to be measured in real-time during HCoV-OC43 infection in the presence of the OAS2 isoforms, using fluorescent plate readers like the CLARIOstar.

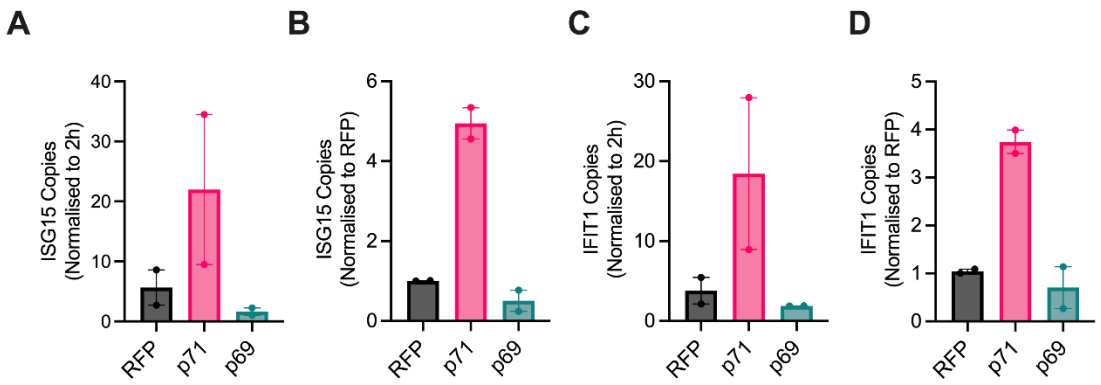

Figure 4-14: ISG induction in OAS2-expressing cells. (**A-D**) Quantification of ISG15 and IFIT1 copies in cells expressing RFP, p71 or p69 infected with HCoV-OC43 for 72 h (MOI 0.01) by RT-qPCR. For ISG15, data was analysed using the $2^{-\triangle\triangle Ct}$ method with ISG15 gene copies at 2 h in the respective cell line (**A**) or in RFP-expressing cells at 72 h (**B**) used as the control samples. For IFIT1, data was analysed using the $2^{-\triangle\triangle Ct}$ method with IFIT1 gene copies at 2 h in the respective cell line (**C**) or in RFP-expressing cells at 72 h (**D**) used as the control samples. Each data point represents one independent experiment.

4.2.10. The effect of endogenous OAS2 on HCoV-OC43 replication

Ectopic expression of p69 has shown that this isoform can restrict HCoV-OC43 replication. However, examining the role of endogenous OAS2 during an IFN response can tell us whether this ISG is part of the cell's antiviral arsenal against HCoV-OC43. The cell model for the experiments so far has been A549 cells, which express the p69 isoform upon IFN stimulation (Fig 4-4 A), so CRISPR-mediated targeting of the OAS2 locus should specifically deplete this isoform from the cell. Three different lentiviral vector-derived CRISPR guides were used to ablate OAS2 expression in A549 cells, and no OAS2 protein expression was detected by Western blot with any of the guides after IFN stimulation (Fig 4-15 A).

After pre-treatment with IFNβ, these CRISPR-targeted cells were infected with HCoV-OC43. Viral nucleocapsid transcripts were measured by RT-qPCR at multiple timepoints. At 24 hpi, there was a negligible difference between cells depleted of OAS2 compared to the control (Fig 4-15 B). At 48 hpi, nucleocapsid levels were 1.4 to 2.4-fold higher in OAS2-depleted cells compared to the control (Fig 4-15 C). At 72 hpi, OAS2-depleted cells exhibited 1.4-fold higher nucleocapsid levels than the control (Fig 4-15 D). These changes were not statistically significant, but given the large standard deviation between experiments repeating these experiments may change this. There is a trend of increased HCoV-OC43 replication at later timepoints under these experimental conditions, so it cannot be ruled out that endogenous expression of the p69 isoform may contribute to IFN-mediated restriction of this coronavirus.

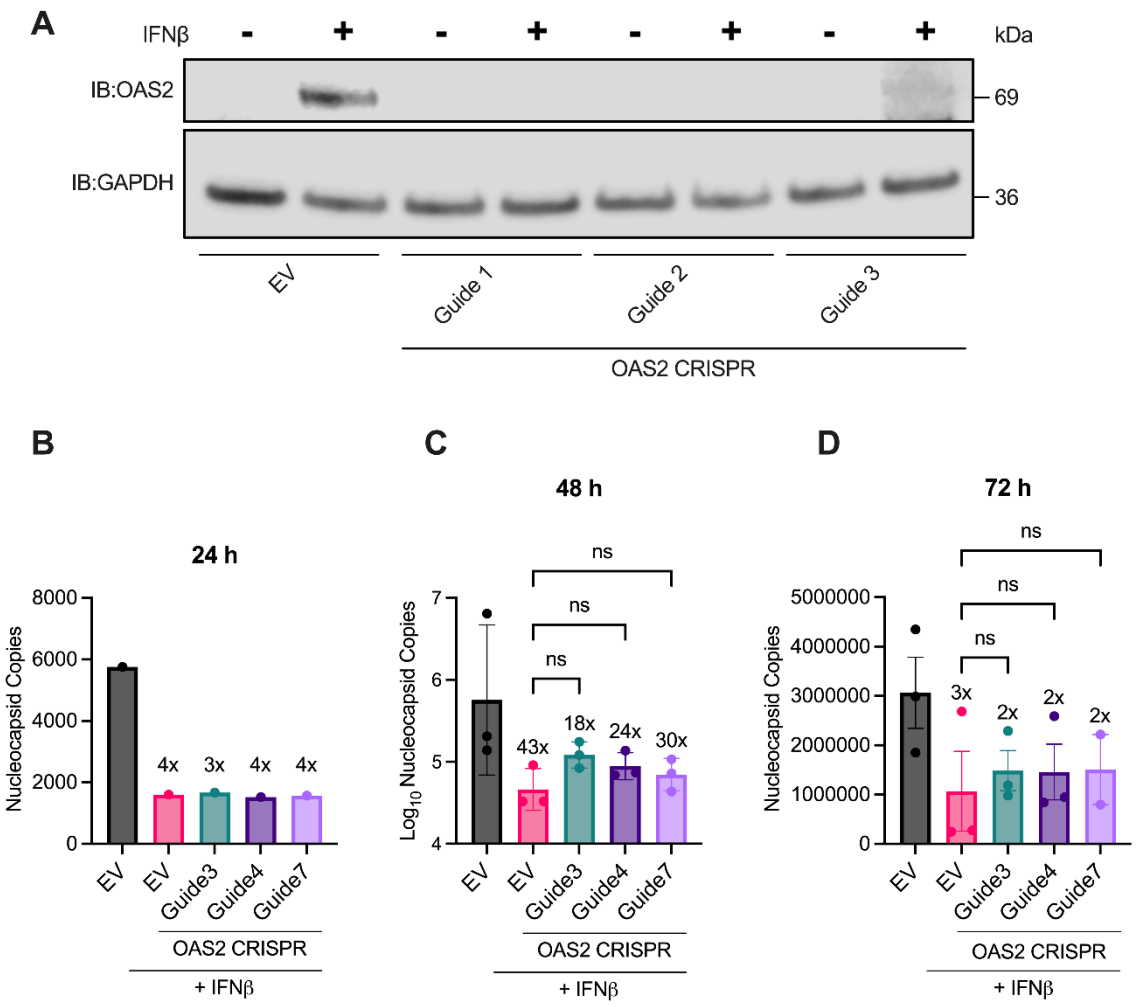

Figure 4-15: Endogenous OAS2 depletion may enhance HCoV-OC43 infection. (**A**) Immunoblot of A549 cells whose OAS2 expression has been reduced by three different lentiviral-vector derived CRISPR guides, with or without 100 U/mL IFNβ addition. (**B-D**) Quantification of HCoV-OC43 nucleocapsid levels in cells from (A), mock-treated or pre-treated with 100 U/mL IFNβ prior to infection with HCoV-OC43 for 24 h (MOI 0.1) (**B**), 48 h (**C**), or 72 h (MOI 0.01) (**D**) by RT-qPCR. Data was analysed using the $2^{-\triangle\triangle Ct}$ method with nucleocapsid copies at 2 h in the respective cell line as the control sample. Each data point represents one independent experiment. Data were analysed using one-way ANOVA with Tukey's multiple comparison test, where *p<0.05, **p<0.01, ***p<0.001, and ****p<0.0001. EV: Empty Vector.

4.2.11. Restriction of coronaviruses by murine Oas proteins

Since HCoV-OC43 is thought to have a rodent origin, the question of whether mouse Oas2 can restrict HCoV-OC43 was investigated next. There are two isoforms of mouse Oas2 annotated in UniProt; these will be named Oas2^{751} and Oas2^{742} based on the number of amino acids in the protein. Analogous to the situation in humans, these isoforms are identical for the first 722 residues but have distinct C-termini (Fig 4-16 A). Mouse Oas2 proteins have an extension to the N-termini that is not present in human OAS2 (Fig 4-16 B).

A549 cells stably expressing RFP, Oas2^{751} or Oas2^{742} were generated, but protein expression could not be detected by Western blot at the expected molecular weight ~85 kDa. A polyclonal anti-OAS2 antibody (19279-1-AP) raised against human OAS2 fusion protein Ag6170, which has been used for all other experiments, only detected non-specific bands (Fig 4-16 C). Another immunoblot was performed with a different monoclonal anti-OAS2 antibody (G-9), raised against an epitope mapping near the C-terminus of mouse Oas2, but no bands were detected (Fig 4-16 D). RNA was extracted from these modified cells, and PCR was performed using primers designed to amplify an 800-base pair region of mouse Oas2, which is present in both isoforms. DNA of expected length was detected in the cells generated to express Oas2^{751} or Oas2^{742} cells but not RFP, confirming these constructs were being transcribed (Fig 4-16 E). Validation of the ability of the anti-OAS2 (G-9) antibody to detect endogenous Oas2 in mouse cells has not been performed, so it is unclear whether this antibody will be useful for Western blot analyses.

Assuming the Oas2 isoforms are being expressed, the shorter Oas2^{742} isoform restricted HCoV-OC43 by 1.5-fold compared to RFP, whereas the infectious titre was 1.3-fold higher with Oas2^{751} (Fig 4-16 F). There were also no apparent changes in plaque phenotype between the Oas2 isoforms and RFP (data not shown). This fold reduction is negligible compared to the >500-fold decrease in HCoV-OC43 infectious titre observed with human p69 (Fig 4-4 D).

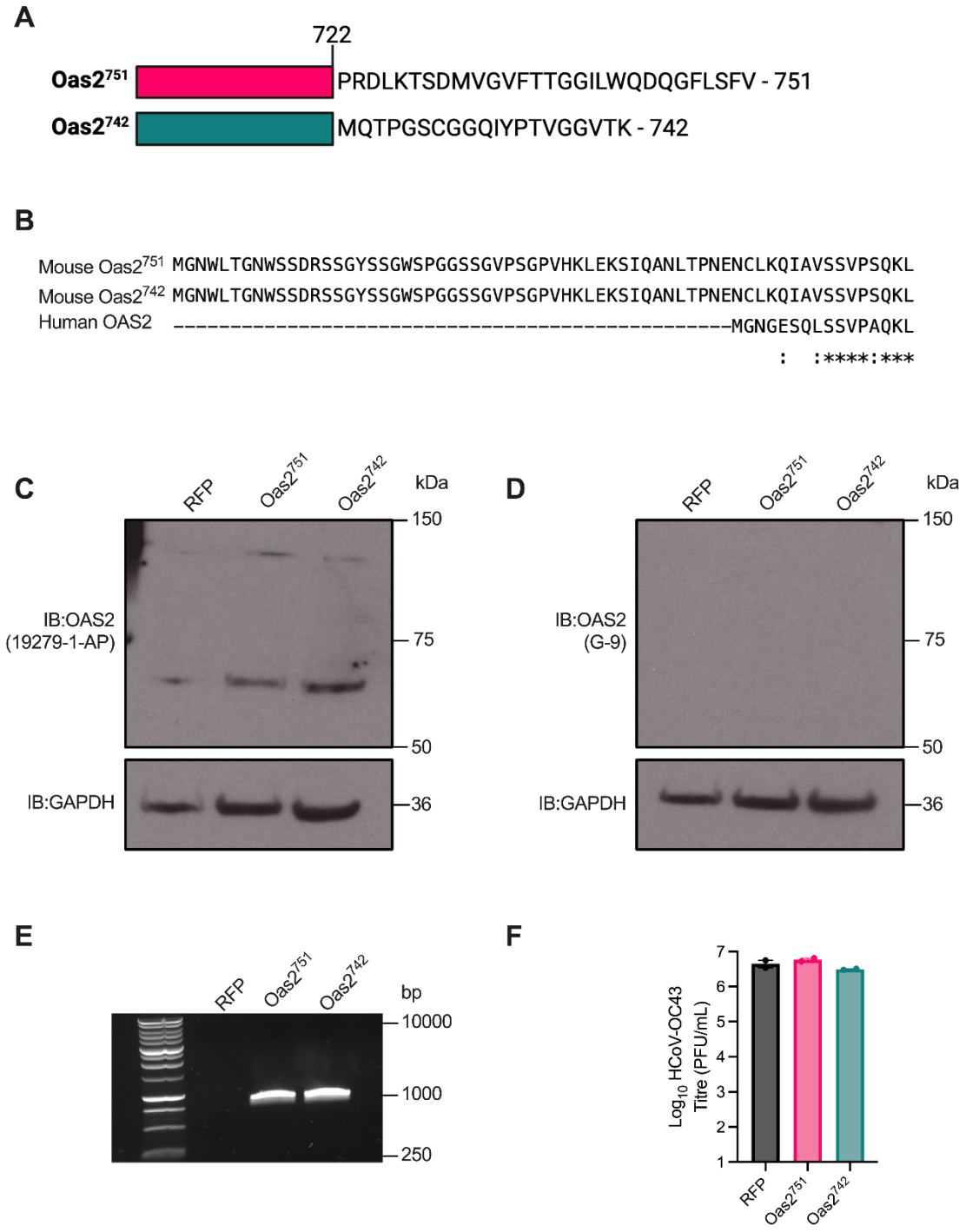

Figure 4-16: Mouse Oas2 isoforms do not appear to restrict HCoV-OC43. (**A**) Schematic of Oas2^{751} (NM_001347448.1) and Oas2^{741} (NM_145227.3) protein sequences. The length and distinct C-termini are shown. (**B**) N-terminal 65 residues of the mouse Oas2 isoforms aligned with the N-terminal 16 residues of human OAS2. (**C-D**) Immunoblot of A549 modified to express RFP or two mouse Oas2 isoforms (Oas2^{751} and Oas2^{742}). Cells were stained with two different commercial OAS2 antibodies: 19279-1-AP (**C**) or G-9 (**D**). (**E**) RT-PCR amplification of an 800 bp fragment of mouse Oas2 in cells from (C). (**F**) Infectious titre of HCoV-OC43 in cells from (C) was determined by plaque assay. Each data point represents one independent experiment.

Throughout this PhD, many stable cell lines have been generated using lentiviral modification, and the protein of interest has been consistently detected by Western blot after the cells had undergone antibiotic selection. It is possible that the murine Oas2 proteins were not detected because the coding sequence I used was not codon-optimised for human cells. However, previous experiments have examined the antiviral activity of the eight mouse Oas1 paralogs against coronaviruses. These Oas1 paralogs were successfully expressed in the human cell line A549-ACE2-TMPRSS2 (AAT) and the mouse 17cl1 cell line (Fig 4-17 A-B). Oas1b does not appear to be expressed in AAT cells, but the loading control is considerably lower than other paralogs; Oas1b was detected faintly in 17cl1, so binding of the anti-OAS1 antibody to this protein may be suboptimal.

Using these stable cell lines, it was discovered that only the Oas1a protein could restrict SARS-CoV-2 (Fig 4-17 C), but no paralogs showed antiviral activity against HCoV-OC43 (Fig 4-17 D) or MHV (Fig 4-17 E). Oas1a shares similarities with human OAS1 p46 in that it is catalytically active, has a CAAX-box motif and is highly induced by IFN; its restriction of SARS-CoV-2 is therefore predictable (Elkhateeb et al., 2016). It is likely that Oas1a does not show antiviral activity against HCoV-OC43 and MHV because they encode the 2'-5'-phosphodiesterases mentioned previously that allow evasion of the OAS-RNase L pathway (Goldstein et al., 2017).

This data suggests that mouse Oas proteins do not require codon optimisation to be successfully expressed in A549 cells. The expression of the murine Oas2 protein needs to be confirmed by alternative methods, such as mass spectrometry. Until then, it cannot be confirmed whether murine Oas2 proteins do or do not restrict HCoV-OC43 replication. It also remains possible that a murine cofactor for Oas2 is missing in the human cell system – although this was not the case for murine Oas1.

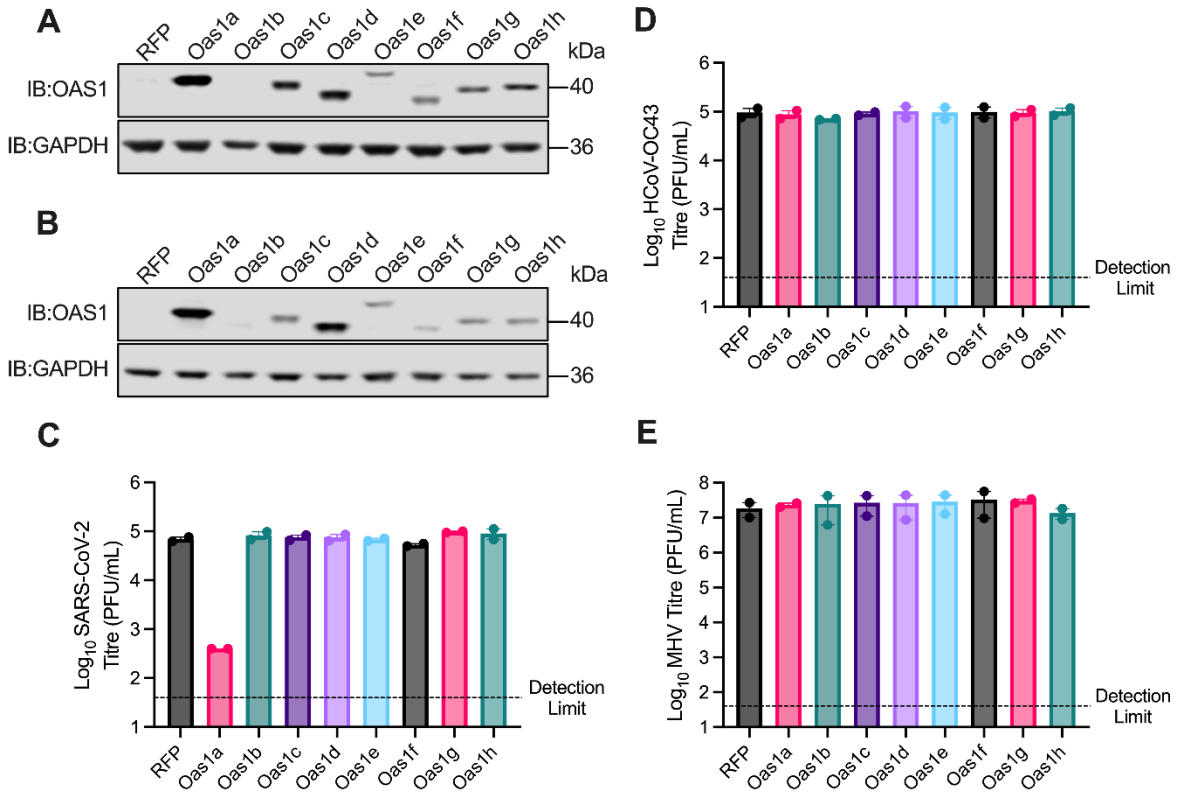

Figure 4-17: Mouse Oas1a restricts SARS-CoV-2. (**A**) Immunoblot of A549-ACE2-TMPRSS2 (AAT) cells modified to express RFP or the eight mouse Oas1 paralogs. (**B**) Immunoblot of 17cl1 cells modified to express RFP or the eight mouse Oas1 paralogs. (**C-D**) Infectious titre of SARS-CoV-2 (**C**) or HCoV-OC43 (**D**) in cells described in (A) was determined by plaque assay. (**E**) Infectious titre of MHV in cells described in (B) was determined by plaque assay. (**C-E**) Each data point represents one independent experiment.

4.3. Discussion

From these results, I can report that the shorter p69 isoform of human OAS2 significantly inhibits HCoV-OC43 at the level of viral RNA, protein and replication (Fig 4-4,4-5). This antiviral activity requires p69 localisation to the endomembrane system (Fig 4-6,4-7) and intact RNA-binding (Fig 4-10). Importantly, enzymatic activity and RNase L are unnecessary for HCoV-OC43 inhibition by p69 (Fig 4-8,4-9).

These experiments were performed in a cell line, A549, that induces the p69 isoform upon IFN treatment; CRISPR-Cas9-mediated depletion of OAS2 in this cell line results in a slight enhancement of HCoV-OC43 replication (Fig 4-15). Given that IFN stimulation was required for p69 expression, different doses of IFN or varying HCoV-OC43 MOI/incubation times may influence these results. It would be interesting to find a cell line that naturally expresses OAS2 without requiring IFN stimulation and determine the role of endogenous OAS2 in these cells. Given that HCoV-OC43 exhibits neurotropism (Desforges et al., 2020), the replication of HCoV-OC43 and the corresponding importance of OAS2 in neuronal cells should also be examined.

A new model being proposed in the ISG field suggests that the restriction of a particular virus is not mediated by an individual ISG but instead by numerous ISGs acting in unison. Using a combination of CRISPR screening and RNA sequencing, a study identified three genes (ZAP, IFIT1 and IFIT3) primarily mediate the restriction of Venezuelan equine encephalitis virus (VEEV) in response to IFN (McDougal et al., 2023). Indeed, VEEV replication was only modestly lower in cells depleted of ZAP, IFIT1 and IFIT3 compared to cells depleted of key proteins of the IFN pathway (IRF9, STAT1 and STAT2), suggesting that these three ISGs dominated the antiviral response. In contrast, this combination of ISGs had little antiviral effect on another alphavirus O'nyong'nyong virus (ONNV). Therefore, it can be argued that OAS2 is perhaps only one of a subset of ISGs required to restrict HCoV-OC43, which is reflected in the incomplete rescue to HCoV-OC43 replication following OAS2 depletion and IFN treatment. Given its potent anti-coronaviral

activity (Fig 3-11), LY6E is likely another member of this subset (Pfaender et al., 2020). Dually depleting LY6E and OAS2 to test whether these two act in synergy would be an interesting experiment here.

To my knowledge, the regulation of alternative splicing for OAS2 has not been elucidated. It would be interesting if OAS2 followed a similar pattern to OAS1, with a SNP determining isoform expression (Soveg et al., 2021). As discussed in section 4.1.7, intronic OAS2 SNPs, such as rs1293762, have been associated with increased susceptibility to viral infections, and it has been hypothesised that these SNPs may influence splicing. Given the difference in protein migration between p71 and p69, I plan to stimulate various cell lines with IFN and examine OAS2 isoform expression. In the meantime, we searched the Human Peptide Atlas, a repository for proteomics datasets, for peptides from the unique C-terminus of p71 that would be generated by trypsin cleavage (Table 4-3). These peptides have been regularly detected in various cell lines, including HeLa and Jurkat cells.

Table 4-3: Predicted p71 C-terminal peptides generated by trypsin cleavage.

Peptide accession	Peptide sequence	Times observed
PAp05476049	VPTMQTPGSCGAR	125
PAp01650513	IHPIVNEMFSSR	93
PAp11767730	ILNNNSKR	12

Data from https://peptideatlas.org/builds/human/ (accessed on 6 November 2024)

Since performing these experiments, I have re-analysed OAS2 SNPs and found that the canonical 719 amino acid p71 sequence, on NCBI, UniProt and Ensembl databases, is in fact the eight amino acid truncated protein caused by the A allele of the SNP rs15895 (Fig 4-18 A). The p71 construct analysed in this project, derived from these reference sequences, expresses this 719 amino acid protein ($p71^{719}$). However, the original paper identifying the p71 isoform isolated cDNA from Daudi cells, encoding a 727 amino acid protein, which will be referred to as $p71^{727}$ (Marié and Hovanessian, 1992). Interestingly, Daudi cells originate from a Burkitt's lymphoma patient of African descent, and the A allele occurs at

a lower frequency in African populations than in European populations (Gokul, Arumugam and Ramsuran, 2023). Examining the NCBI reference SNP report, the presence of the A allele appears considerably higher in European populations (Fig 4-18 B). Thus, owing to considerable sampling bias towards European populations, the truncated A-allele encoding p71^{719} has become the canonical p71 sequence in these databases.

This rs15895 SNP has been associated with increased susceptibility to severe DENV infection (in association with other OAS2 SNPs) and severe TBEV infection. This has created a disconnect between Genome-Wide Association Studies (GWAS) and *in vitro* research (which I am complicit in). For example, a study that ectopically expressed OAS proteins in A549 cells concluded that OAS1 p46 and OAS3 showed antiviral activity against DENV infection, but the OAS2 p71 and p69 isoforms did not (Lin et al., 2009). Another study examined HCV using a similar approach and made the same findings (Kwon et al., 2013). However, they also used the canonical GenBank sequence of p71^{719}; given the association of the truncated protein with disease severity, this shorter C-terminus likely influences antiviral activity.

Examining the sequence of the p71 C-terminus reveals 9 or 7 basic residues spaced throughout p71^{727} or p71^{719}, respectively (Fig 4-18 C); it is possible that these residues can interact with viral dsRNA and facilitate its binding into the positively charged groove of OAS2. AlphaFold cannot determine the structure of the C-terminus of p71 with high confidence, suggesting it is conformationally dynamic. However, the C-terminus does appear in close proximity to the dsRNA ligand (Fig 4-18 D), which could potentially facilitate its interaction with dsRNA and influence sequence/structure specificity. Given the difference in C-terminus must be responsible for the potent antiviral activity of p69 against HCoV-OC43, this suggests that changes in the C-terminal tail affect virus susceptibility both *in vitro* and *in vivo*.

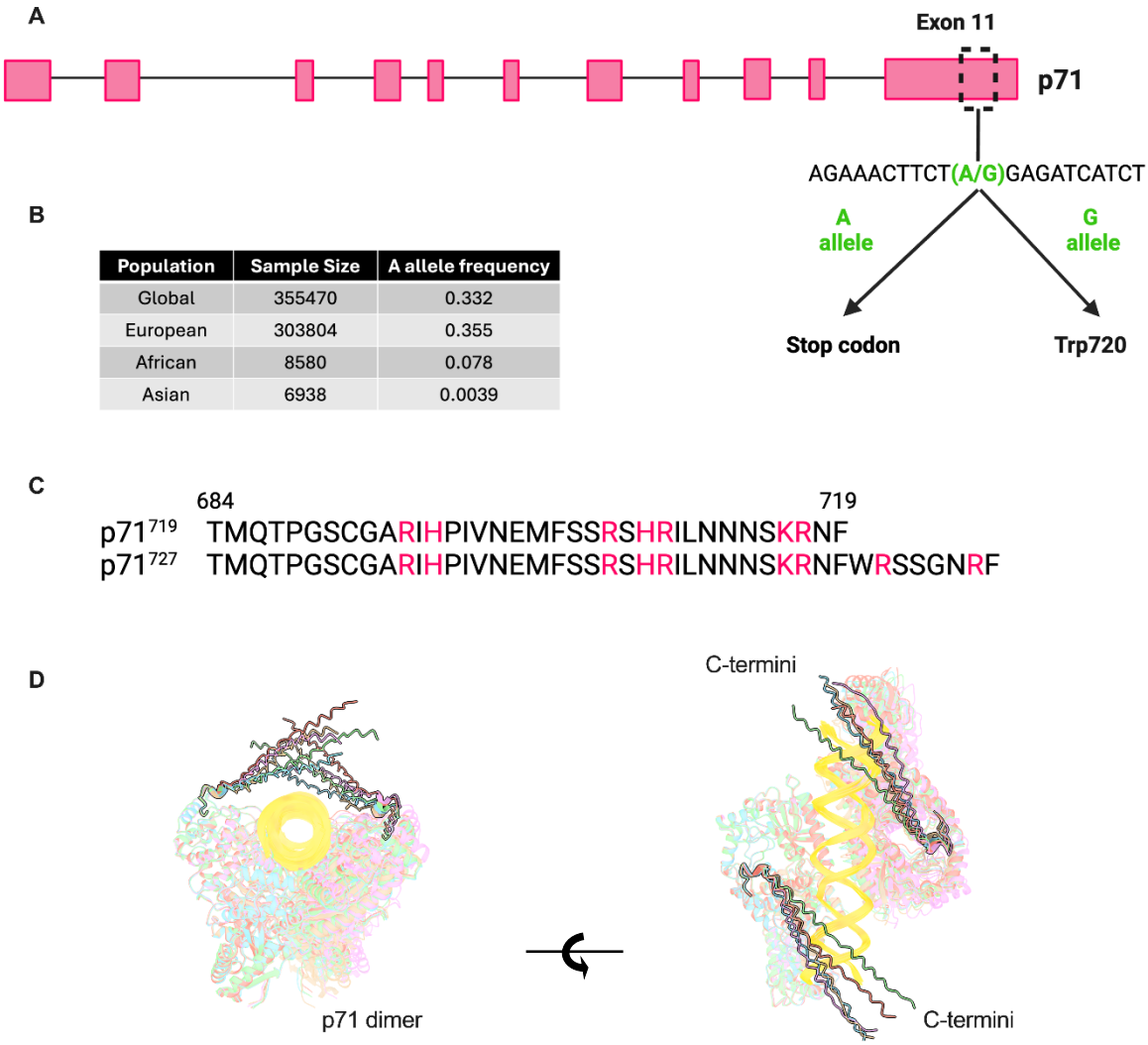

Population	Sample Size	A allele frequency
Global	355470	0.332
European	303804	0.355
African	8580	0.078
Asian	6938	0.0039

Figure 4-18: OAS2 C-terminal tail influences antiviral activity. (**A**) Schematic representation of the rs15895 SNP resulting in a truncated p71 protein. Pink squares represent the exons of the OAS2 p71 isoform. (**B**) The "A" allele frequencies recorded for different populations were obtained from NCBI dbSNP (accessed 22 January 2025). (**C**) C-terminal tail of $p71^{719}$ and $p71^{727}$ are shown with basic amino acid residues highlighted in pink. (**D**) Superposition of 5 AlphaFold structure predictions generated for OAS2 $p71^{719}$, with the C-terminus from residue T684 highlighted.

I wanted to determine whether the differential antiviral activity of the p71 and p69 isoforms existed with other coronaviruses, but few studies that have investigated OAS2 have explicitly noted what isoform was used. Two previous ISG screens on coronaviruses showed OAS2 as a potential hit. In the screen performed by my lab, the OAS2 p69 expression inhibited SARS-CoV-2 replication by 1.7- and 2.1-fold at timepoints of 14 h and 40 h, respectively (Wickenhagen et al., 2021). However, OAS2 did not reduce SARS-CoV-2 replication in a separate study that examined the antiviral activity of human OAS proteins (Danziger et al., 2022). I aligned the published primer sequences used to design the OAS2 expression constructs in this study with the OAS2 p71/p69 sequences. The reverse primer ended at residue 683 for both sequences, which is the last identical residue for the p71/p69 isoforms. This suggests the OAS2 protein expressed in this study lacked any unique C-terminus, explaining why no antiviral activity was observed.

OAS2 also inhibited HCoV-229E replication by 1.5- and 2.6-fold at 24 h and 48 hpi, respectively (Pfaender et al., 2020), but it is unclear which OAS2 isoform is being expressed in the cDNA library used for this screen. This restriction is modest compared to the 55-fold reduction observed in the ISG screen discussed in Chapter 3. Testing the differential antiviral activity of the OAS2 isoforms against pandemic and seasonal coronaviruses might tell us whether any genetic lineage or initial non-human host may predispose a coronavirus to OAS2 inhibition. Given that HCoV-OC43 is the most potently inhibited virus of 20+ viruses screened at the Centre for Virus Research (Fig 4-4 G), HCoV-OC43 seems to be particularly susceptible to p69-mediated restriction.

Several groups have reported OAS2-mediated restriction of other families of viruses (Table 3-1). It has been recently reported that ZIKV replication is inhibited by ectopic expression of OAS2 via upregulation of type I IFN signalling, so I checked what isoform was implicated in this. The reverse primer sequence used to amplify the OAS2 ORF from A549 did not align with either the p71 or p69 isoform. Further investigation revealed the reverse primer aligned to isoform 3, encoding the 172 amino acid protein (Fig 4-4 B). It does not contain the catalytic

triad, so it makes sense its antiviral response is not via the OAS/RNase L pathway. This short OAS2 isoform is not well studied and is not regularly described as an isoform of OAS2. The inconsistency in testing the antiviral activity of OAS2 means there is not a good understanding of what, and therefore how, viruses are inhibited by this protein.

I chose EMCV as a control to look at the antiviral activity of the OAS2 isoforms. It has been reported that murine NIH3T3 cells expressing p71 or p69 inhibit EMCV, with the p69-mediated restriction being more substantial (Marié et al., 1999). An examination of the methods of this paper suggests that the author used the $p71^{727}$ protein. My data confirms that $p71^{719}$, despite the C-termini truncation, still possesses modest antiviral activity against EMCV; this is likely via activation of RNase L given the higher fold-change in infection in p71-expressing RNase L depleted cells compared to control cells (Fig 4-11, 4-12). These findings do not replicate the antiviral activity of p69 against EMCV, which could be due to several reasons, such as a different cell type or EMCV strain. This confirms that OAS2 can work via the canonical OAS/RNase L pathway and an RNase L-independent mechanism. By screening a panel of diverse viruses with cells depleted of RNase L in future, it can be determined whether the mechanism of action is specific to the OAS2 isoform or if both isoforms can perform both antiviral mechanisms under the correct activating conditions, i.e. p69-mediated inhibition via 2-5A synthesis and p71-mediated inhibition via RNase L independent mechanisms.

The hypothesis that OAS3 is the dominant member of the OAS family that activates RNase L (Yize Li et al., 2016), with OAS1 and OAS2 performing alternative functions, supports and opposes this data. Given that HCoV-OC43 encodes a 2'-5'-PDE and p69-mediated inhibition does not require RNase L, this supports the idea that OAS2 can inhibit viruses by RNase L-independent mechanisms. However, this does not explain the p71-mediated inhibition of EMCV observed. In this paper, the authors used CRISPR-Cas9 to knockout OAS1, OAS2 or OAS3 in A549 cells, stimulated them with poly(I:C) and measured RNase L activation by monitoring

rRNA degradation. 18S and 28S rRNAs were intact in OAS3-KO cells but not in OAS1-KO or OAS2-KO cells. However, this result may be biased against OAS2 in two ways. Firstly, A549 cells appear to express only the p69 isoform (Fig 4-4 C). Therefore, the ability of the OAS2 p71 isoform to activate RNase L is not examined here. Secondly, the authors used poly(I:C), which may not be an optimal surrogate for dsRNA for OAS2. OAS proteins have different dsRNA length requirements, different binding affinities for dsRNA and are differentially sensitive to structure such as 3'-single stranded overhangs (Koul et al., 2024, 2020a); given OAS1 and OAS2 are compartmentalised, the accessibility of transfected poly(I:C) to the different proteins may differ. Therefore, a set concentration of a perfect dsRNA may give the appearance that OAS1 and OAS2 have minimal effect on RNase L activation in response to poly(I:C).

The authors also examined the replication of four diverse viruses in these OAS KO cells (SINV, CHIKV, IAVΔNS1, VACVΔE3L) and showed that OAS3 was the major factor dictating RNase L activation. As shown in (Table 3-1), most viruses reported to be susceptible to inhibition by OAS1 and OAS2 have ssRNA genomes. SINV and CHIKV are alphaviruses that utilise endosomes and lysosomes for replication, whereas influenza virus A (IAV) replicates in the nucleus (Dou et al., 2018; Romero-Brey and Bartenschlager, 2014). Given that OAS1 p46 and OAS2 isoforms localise to the endomembrane system, viral dsRNA derived from these viruses may not come into proximity to OAS1 and OAS2. Thus, it is likely that OAS1 and OAS2, with their subcellular localisation, do contribute to RNase L activation in viral infection, as exemplified here by EMCV restriction by OAS2 p71 and elsewhere by SARS-CoV-2 restriction by OAS1 p46 (Wickenhagen et al., 2021).

The data presented here have not yet untangled the RNase L-independent mechanism by which p69 restricts HCoV-OC43. Previous studies on OAS proteins provide some suggestions. Most promising is the recent study showing OAS1 p46 binds and stabilises cellular IFNß mRNA, enhancing IFN signalling and inhibiting WNV replication (Harioudh et al., 2024). This mechanism mirrors many of the details we see with OAS2 p69, as the OAS protein required RNA-binding capabilities

and endomembrane localisation, but not catalytic activity, to inhibit a (+)ssRNA virus. I examined the role of the IFN response by using the JAK inhibitor Ruxolitinib and found decreased replication in both p69-expressing and control cells (Fig 4-13). This suggests that either the activation of IFN response enhances HCoV-OC43 replication or the drug may have off-target effects on the cells, indirectly restricting viral replication. Nonetheless, RUX did not rescue from the p69 restriction, arguing against a requirement for IFN in the RNase L independent block. I also measured ISG expression in infected cells in the presence of ectopic expression of the OAS isoforms (Fig 4-14). Expression of two ISGs, ISG15 and IFIT1, was modestly lower at 72 hpi, when p69 was expressed; this timepoint is potentially too late during infection to reliably examine the IFN response. This data suggests that p69 is not restricting via the IFN response. Without further experiments, I do not think we can rule out that OAS2 p69 is inhibiting HCoV-OC43 via this IFN-dependent mechanism. This can be confronted through many different experiments, many of which were performed in the aforementioned study. For example, by incubating the cell lines that express p69 with poly(I:C) or HCoV-OC43 and measuring IFNB levels by RT-qPCR at early time points. Additionally, if the observed inhibition by p69 is lost in IFNAR KO cells or by incubating with an IFNAR-neutralising antibody, this would confirm that this mechanism requires a functioning IFN response.

Given the known protein-protein interaction of mouse Oas1b with ABCF3 in its antiviral mechanism against flaviviruses (Courtney et al., 2012), an avenue to pursue would be to search for binding partners of OAS2. OAS2 was identified as a binding partner of Nucleotide-binding and oligomerisation domain 2 (NOD2), using a proteomics approach and overexpression of NOD2 in THP-1 upregulated RNase L activation upon stimulation with poly(I:C) (Dugan et al., 2009). Investigating the role of NOD2 in OAS2 antiviral action through depletion in the cell lines generated during this project and identifying other possible binding factors by OAS2 pull-down experiments, followed by mass spectrometry, may also provide insights into the anti-HCoV-OC43 mechanism of p69.

Expression of ISGs, such as OAS2, can form a barrier to spillover of viruses from other animals into humans. As discussed (Wickenhagen et al., 2021), HCoV-OC43 encodes a 2'-5'-PDE that antagonises the OAS/RNase L pathway, and this suggests that reservoir species of such virus lineages encode OAS proteins that could inhibit these viruses; SARS-CoV-2 was sensitive to this pathway, suggesting it had not evolved an evasion mechanism. As shown in (Fig 4-17), SARS-CoV-2 was inhibited by expression of Oas1a, but rodent-originating coronaviruses, HCoV-OC43 and MHV were not. Examination of the OAS1 sequences in horseshoe bats, a proposed source of SARS-CoV-2, showed a retrotransposition event disrupted the CAAX motif in these species, so they cannot produce prenylated OAS1. SARS-CoV-2 thus lacked a selective pressure to evolve an OAS/RNase L evasion mechanism, which explains the increased susceptibility of COVID-19 in individuals that do not express the prenylated OAS1 p46 isoform.

I wanted to examine whether a similar effect was observed with OAS2, so I expressed two isoforms of mouse Oas2 in A549 cells; neither isoform appeared to restrict HCoV-OC43 (Fig 4-16). Despite showing the presence of mouse Oas2 transcripts in the cells, protein expression of Oas2 was not confirmed. It would be interesting if mouse Oas2 does not restrict HCoV-OC43 as this implies HCoV-OC43 did not need to evolve a mechanism to evade this RNase L-independent mechanism. A lack of restriction could also suggest that potential cofactors required for this undetermined mechanism cannot interact with mouse Oas2. This is plausible considering the extended N-terminus of mouse Oas2 that is not present in human OAS2 (Fig 4-16 B).

Towards the end of writing this thesis, a preprint was released examining the structure and antiviral activity of OAS2 (Merold et al., 2025). Interestingly, the authors suggested a new model for OAS2 activation based on cryo-electron microscopy and AlphaFold predictions, whereby OAS2 exists in an autoinhibited state as a dimer, mediated via a zinc-coordination site (C652 and H654). The binding of dsRNA monomerises OAS2 into its active form, with domain I (DI) being important for distinguishing the appropriate dsRNA length for activation. In

support of the data presented here, the authors show myristoylation localises OAS2 to the Golgi apparatus, and the RNA binding residues R529 and R533 are necessary for its 2-5A synthesis activity. Additionally, the antiviral activity of p71 was tested against an assortment of viruses, including flaviviruses, bunyaviruses, orthomyxoviruses and the dsDNA viruses herpes simplex virus 1 (HSV-1) and vaccinia virus (VACV). Only EMCV exhibited significant inhibition by p71 in an RNase L-dependent manner. Realising, like us, that OAS2 might specifically target viruses that replicate in double-membrane vesicles, HCoV-OC43 and HCoV-NL63 were shown to be substantially inhibited by OAS2 p69, whereas SARS-CoV-2 was only slightly inhibited; no data was provided for restriction of these viruses by p71 or the role of RNase L. Nevertheless, this increases the validity of my data as many of my conclusions on the characteristics of OAS2 have been independently confirmed by another group using different experimental systems. Although our investigations into OAS2 are similar, my thesis provides evidence of alternative splicing as a mechanism of diversifying the antiviral activity of OAS2, whilst Merold *et al*. have expanded our understanding of OAS2 regulation.

Taken together, I propose a model in which alternative splicing generates two isoforms of OAS2, p71 and p69, which can inhibit unrelated viruses by different mechanisms (Fig 4-19). p69 inhibits the seasonal coronavirus HCoV-OC43 independently of RNase L in a yet undetermined mechanism. p71 inhibits the picornavirus EMCV via canonical activation of RNase L. By alternative splicing of OAS2, the diversity of viruses the cell can inhibit is increased, providing a multifaceted immune response when a pathogen invades.

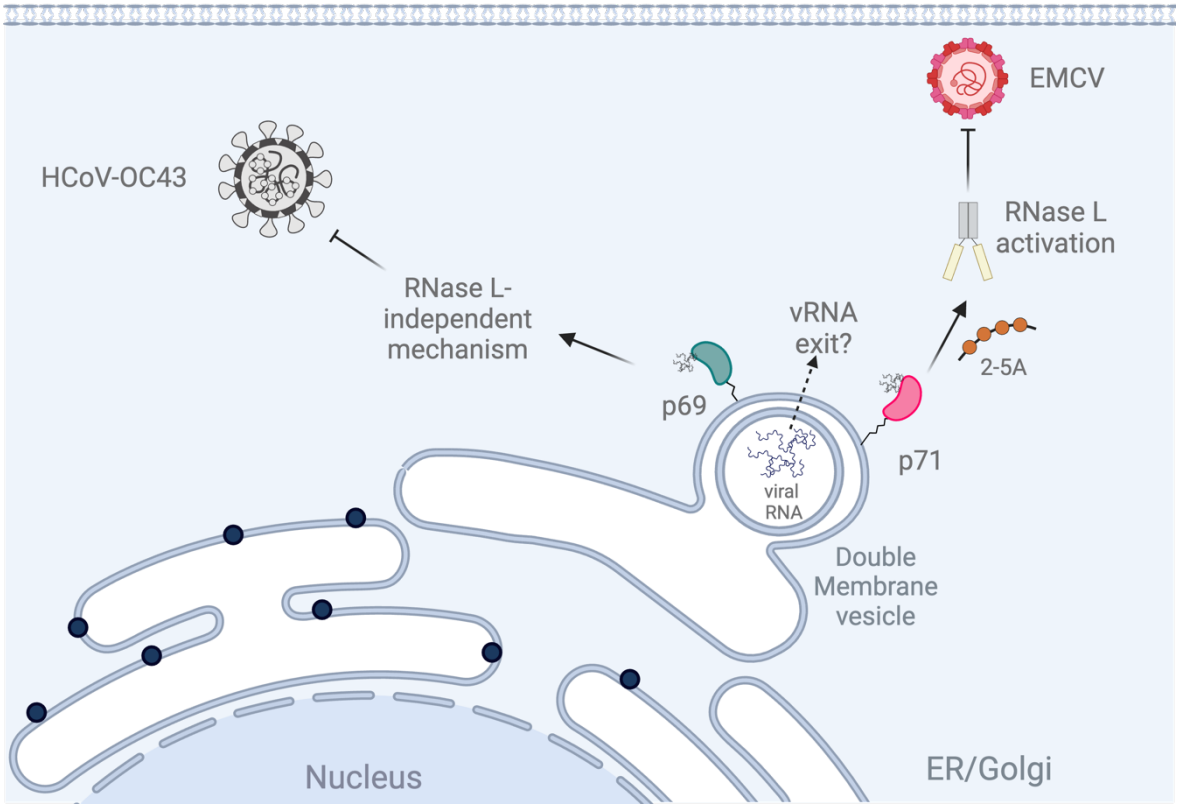

Figure 4-19: Overview of the distinct antiviral mechanisms of OAS2. OAS2 exists as 2 main isoforms, p69 and p71, with the canonical sequences encoding a distinct 4-residue or 36-residue C-terminus, respectively. N-terminal myristoylation localises the p71 and p69 isoforms to the site of virus replication, such as double-membrane vesicles. Both isoforms are activated upon binding dsRNA, triggering conformational changes that positions the catalytic triad to produce 2-5A. p71 inhibits EMCV via the canonical OAS/RNase L pathway, whereas p69 inhibits HCoV-OC43 independently of RNase L. These contrasting antiviral mechanisms is dependent on the unique C-terminus, which likely influences the discrimination of dsRNA length and/or structure between these two viruses.

5. Quantifying fluorescent tag retention in reporter viruses

5.1. Introduction

5.1.1. Design of reporter viruses

Methods to investigate replication of wild-type viruses, such as through immunostaining or indirectly through measurement of viral protein or RNA levels, can be time-consuming, costly and/or labour-intensive. Therefore, the generation of replication-competent reporter viruses has been instrumental in understanding virus infection dynamics and virus-host interactions. Such reporter viruses can encode a range of fluorescent proteins, most commonly green fluorescent proteins (e.g. eGFP, ZsGreen) or red fluorescent proteins (e.g. RFP, mCherry, dTomato). Alternatively, other reporter genes, such as bioluminescent Renilla luciferase, are also available (Yongfeng Li et al., 2016).

The increasing availability of reverse genetics (RG) systems for a diversity of viruses has facilitated the development of reporter viruses. For example, in-vitro ligation, bacterial artificial chromosome (BAC) and yeast artificial chromosome (YAC) systems were rapidly established for SARS-CoV-2 after its outbreak, which all increase the ease by which a reporter gene can be introduced into the viral genome (Kurhade et al., 2023). The reporter gene can be inserted into the viral genome in different ways. Firstly, the fluorescence gene can be fused to a viral protein, allowing direct monitoring of viral protein localisation within the cell; however, this approach can affect the normal functionality of the conjugate protein. So-called accessory genes, often essential *in vivo* but dispensable in tissue culture, can sometimes be replaced by a reporter gene (Zhang et al., 2002). Selection of the gene within the viral genome implies this protein likely plays a role *in vivo*, so this expression strategy may not be optimal if infecting animal models. Perhaps the optimal strategy is for the reporter gene to be expressed separately. This can occur through the introduction of an internal ribosomal entry site (IRES) or a self-cleaving peptide (2A); 2A peptides are 18-22

amino acid peptides, naturally occurring in the genomes of some viruses, that are inserted between proteins in a polypeptide that mediate co-translational cleavage, via a ribosomal skipping mechanism (Liu et al., 2017).

In response to the COVID-19 pandemic, a SARS-CoV-2 toolkit was developed, which included a single plasmid-based RG system where the reporter genes mCherry, ZsGreen or Nanoluciferase were cloned in-frame at the C-terminus of the ORF7a protein (Rihn et al., 2021); these proteins were separated by the 2A linker, mediating cleavage of the reporter protein from the viral protein. Another YAC-based system was used to develop a SARS-CoV-2 reporter virus where ORF7a was replaced by eGFP. Although this virus can replicate to high levels, it was attenuated compared to a clinical isolate, suggesting ORF7a is important for replication *in vitro*, highlighting caution must be taken when replacing viral genes (Thi Nhu Thao et al., 2020). Viruses with large genomes, such as herpesviruses, can encode multiple reporter genes; the Merlin reporter virus is based on the human cytomegalovirus (HCMV) strain Merlin cloned into a BAC. The immediate early gene UL36 and mCherry are separated by a 2A linker, while the UL32 gene, expressed late in infection, is fused to GFP by a six amino-acid linker (Houldcroft et al., 2020). This dual-reporter virus allows the quantification of infected cells at different stages of infection.

5.1.2. Applications of reporter viruses

Fluorescent reporter viruses are especially valuable for viruses that show minimal cytopathic effect as they allow infection to be quantified via fluorescence, using flow cytometry, image cytometry and microscopy. As discussed in Chapter 3, fluorescent reporter viruses are readily used for screening approaches and have helped identify potential antiviral drugs, host dependency factors, and restriction factors. SARS-CoV-2 reporter viruses expressing eGFP and mNeonGreen were used in screens to identify the antiviral activity of OAS1 and PLSCR1, respectively (Wickenhagen et al., 2021; Xu et al., 2023). Unlike pseudovirus systems that mainly limit studies to virus entry, the replication

competency of many reporter viruses means that factors that target post-entry stages of virus replication can also be studied.

Reporter viruses are valuable tools for tracking viral infection *in vitro* or *in vivo, a*s exemplified by studies on influenza viruses. One study developed a set of IAVs, nicknamed 'Color-flu,' in which the NS1 ORF was fused to mCherry, eGFP, eCFP, or Venus reporters. This allowed virus replication in the lungs of infected mice to be investigated (Fukuyama et al., 2015). IAV replication has also been tracked in real time in mice using an IAV reporter virus expressing nanoluciferase (Kim et al., 2022).

The diverse applications of reporter viruses are only valid if reporter gene expression is maintained. As a reporter gene does not benefit virus replication, selection pressures can result in its loss from the virus genome, e.g. via deletion of its coding region or mutations affecting its transcription. Therefore, it is important to check the 'stability' of the reporter gene to ensure that virus replication levels align with fluorescent/bioluminescent signals. GFP reporter gene retention in two coronaviruses is examined in this chapter.

5.1.3. Split-GFP system

An alternative method of monitoring virus-host interactions is to use a bimolecular fluorescence complementation approach, such as the split-GFP system. In this system, GFP is split into fragments: an N-terminal fragment containing 10 ß-strands (GFP1-10) and a C-terminal fragment containing a single ß-strand (GFP11). These fragments are fused to two different proteins (protein A and protein B) and are non-fluorescent when expressed independently (Kodaka et al., 2017) (Fig 5-1). When protein A and protein B interact, enabling the fragments to come into close proximity, the fragments spontaneously assemble with high affinity into a functioning fluorescent protein, and fluorescence can be measured.

Since some viruses have limited coding capacity, this split-GFP system can circumvent this as the GFP11 fragment is 16 amino acids, considerably smaller

than the full-length protein of 238 amino acids. This has been used to follow IAV infection; the GFP11 fragment was fused to the PB2 protein, while the GFP1-10 fragment was expressed via transfection (Avilov et al., 2012). A split-GFP system designed by my colleagues to study interactions between the IAV polymerase and a host protein is described in section 5.2.4.

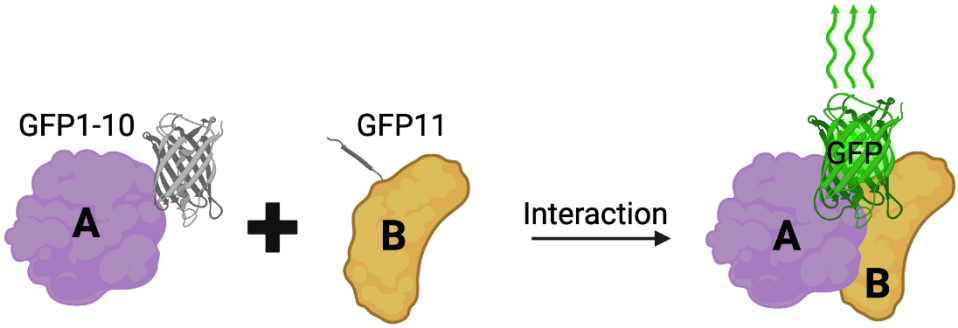

Figure 5-1: Schematic of the split-GFP system. The GFP1-10 and GFP11 fragments are separately fused to different proteins. Upon protein interaction, GFP reassembles to form the fluorescent protein.

5.1.4. Influenza A virus

Influenza A virus (IAV) is the primary causative agent of influenza, which causes substantial morbidity and mortality every year. IAV, of the *Orthomyxoviridae* family, has a (-)ssRNA genome comprised of eight segments (Fig 5-2 A). Within the IAV virion, the genome exists as viral ribonucleoproteins (vRNPs), where viral RNA is wrapped around oligomerised nucleoprotein capped on one end by the viral polymerase; the viral polymerase consists of the proteins PB1, PB2 and PA (Fig 5-2 B-C). On the virion surface are three transmembrane proteins called haemagglutinin (HA), neuraminidase (NA), and matrix protein 2 (M2) (Carter and Iqbal, 2024) (Fig 5-2 C).

HA interacts with sialylated cell surface receptors to mediate entry via endocytosis. Following membrane fusion, vRNPs are released into the cytoplasm before being imported into the nucleus. Viral mRNA transcription is required to synthesise viral polymerase proteins, which are also imported into the nucleus (Carter and Iqbal, 2024). Replication involves the synthesis of a (+)ssRNA

template, which requires an interaction between the viral polymerase and host ANP32 proteins to allow it to form the replication conformation (Carrique et al., 2020). Interaction with ANP32 proteins is species-specific, with avian IAVs needing to acquire the E627K mutation in PB2 to replicate in mammals (Zhu et al., 2023).

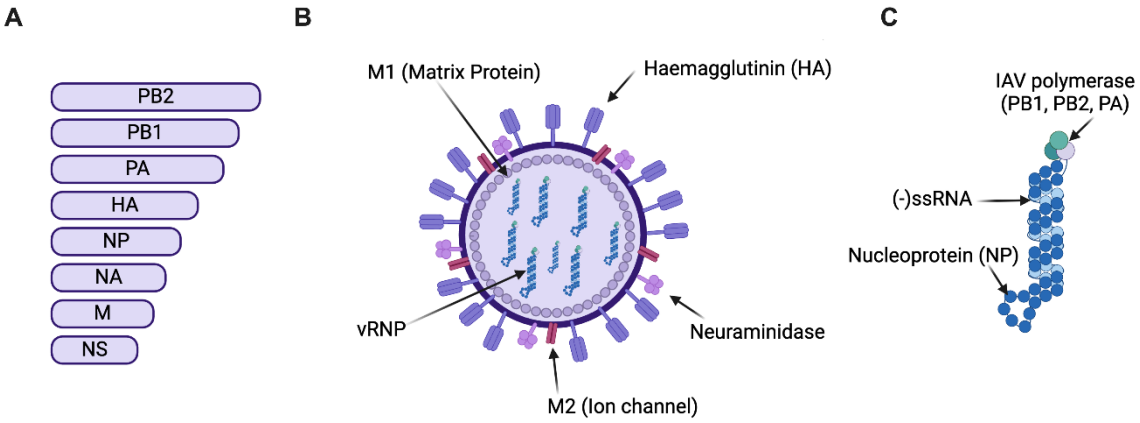

Figure 5-2: Influenza A virion and genome organisation. (**A**) Schematic of the eight segments of the negative-sense single-stranded IAV genome, which are wrapped in nucleoprotein and packaged into the IAV virion. (**B**) Schematic of the spherical form of the pleomorphic IAV virion. The IAV virion consists of a viral envelope including the glycoproteins HA, NA and M2, shielding an internal matrix layer. (**C**) Schematic of the IAV viral ribonucleoprotein. These helical structures are capped with the heterotrimeric viral polymerase.

5.2. Results

5.2.1. Recognition of Contribution

Table 5-1: List of people and their contributions to experimental work.

	Contribution
Douglas Stewart	Generation of pCCI-4K-alpha plasmid Generation of IAV/ANP32A split GFP system
Matthew Turnbull	Generation of pCCI-4K-alpha plasmid Generation of IAV/ANP32A split GFP system

5.2.2. Generation of a mouse hepatitis virus stock with a higher GFP+ plaque percentage

At the start of my PhD, we planned to perform ISG screening against a rodent or rodent-originating coronavirus. This was because hits characterised through ISG screens against bat-originating HCoV-229E and SARS-CoV-2 had recently been published, and we were interested in whether coronaviruses from a different ancestral host would have different restriction factors (Pfaender et al., 2020; Wickenhagen et al., 2021). It was proposed that mouse hepatitis virus (MHV) be screened, as we had just received a fluorescently tagged MHV from a collaborator. Therefore, we could perform the standard ISG screening protocol by measuring virus infection by flow cytometry.

The MHV-GFP virus described in this section is the A59 strain, with the accessory protein ORF4 completely replaced by GFP (Fig 5-3 A)(Züst et al., 2007); ORF4 appears to be dispensable for MHV replication *in vitro* (de Haan et al., 2002). I initially performed an MHV-GFP infection in murine 17cl1 cells, and examination under a fluorescence microscope showed substantial cytopathic effect with many cells not exhibiting a GFP signal. Plaque assays were performed to determine whether this MHV stock contained virus particles that had lost their GFP tag. Post-fixation, plate wells were scanned in the green channel using the Celigo Imaging Cytometer, then scanned again in the brightfield channel after staining with Coomassie to visualise all plaques. Comparison of these scans revealed that only

~38% of plaques were GFP-positive (Fig 5-3 B-C), suggesting this infection system was suboptimal for quantifying infection via fluorescence, as infection levels would be significantly underestimated.

To create a stock with an increased percentage of virus particles expressing the GFP protein, the MHV-GFP stock was serially diluted across 96-well plates, as in a limiting dilution assay. Over 72 h, each well was monitored for CPE +/- GFP signal using a fluorescent microscope. At a dilution of 1/59049, only 1/8 wells exhibited CPE and had a GFP signal, so this supernatant was harvested and used to inoculate a flask of 17cl1 cells. As before, plaque assays were performed to quantify the percentage of MHV stock with the fluorescent tag. Approximately ~91% of plaques were GFP+, so this stock was a more suitable reporter virus (Fig 5-3 D). The plaques had a smaller phenotype than the previous stock, possibly due to MHV-GFP virus particles having a growth disadvantage or the virus particles in the harvested supernatant having other genetic differences which affect replication kinetics (Fig 5-3 E). Perhaps a superior method to increase the GFP+ percentage would be to perform plaque purification. This would involve performing plaque assays with a solid agarose overlay instead of a liquid overlay, then, after discrete plaques have formed, “picking” a plaque and using this to inoculate a flask.

Although planned, ISG screens with MHV were not performed. The main reason was that MHV caused significant syncytia in cells early after infection, making quantification of individual infected cells difficult. This inspired the idea to generate a screening protocol that did not require reporter viruses or specific antibodies (Chapter 3).

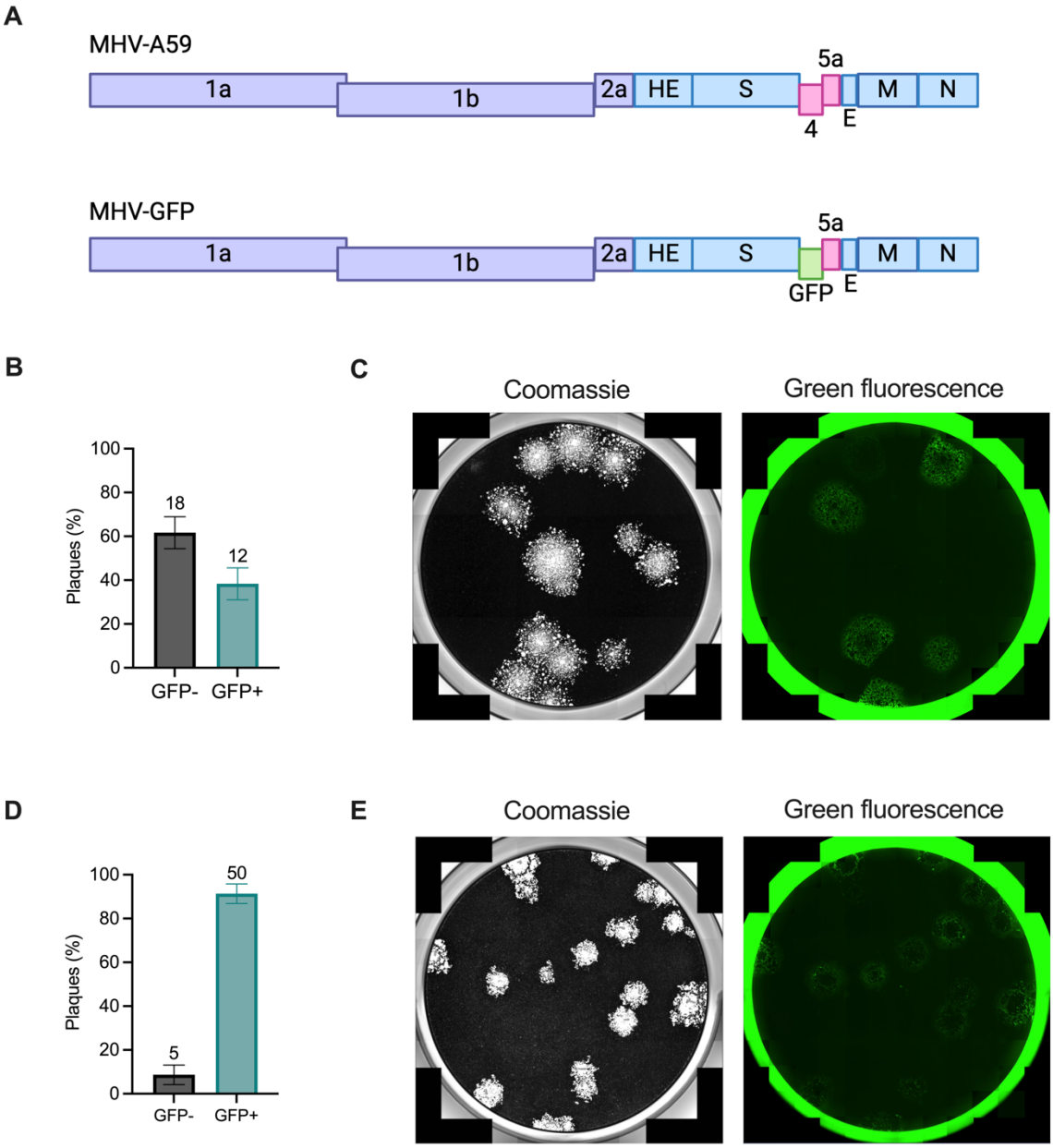

Figure 5-3: Generation of high percentage GFP+ MHV stock. (**A**) Schematic of the wild-type and GFP-containing genomes of the MHV strain A59. (**B**) Retention of the GFP tag in an MHV-GFP stock from a collaborator was measured by plaque assay. The number of GFP+ plaques was counted. (**C**) Example brightfield and green channel images of plaques formed from (B). (**D**) Retention of the GFP tag in a new MHV-GFP stock was measured by plaque assay. The number of GFP+ plaques was counted. (**E**) Example brightfield and green channel images of plaques formed in (D). (**B, D**) Mean and SD from one independent assay, performed in technical triplicate, are shown. Bars are labelled with the number of plaques counted.

5.2.3. Rescue of an infectious cDNA clone of the SARS-CoV-2 alpha variant

During the COVID-19 pandemic, there was a need to analyse the difference in emerging SARS-CoV-2 variants, which required molecular tools for such research. My colleagues developed a SARS-CoV-2 RG system, where transient transfection of a single plasmid facilitates rescue of infectious virus; such a system encoding the Wuhan-Hu-1 strain has been published (Rihn et al., 2021). It was planned to modify this RG system to generate B.1.1.7/alpha variant of SARS-CoV-2; the alpha variant was the first designated SARS-CoV-2 variant of concern and was discovered after a significant increase in new COVID-19 cases in England in late 2020 (Hill et al., 2022). To generate this RG system, my colleagues infected VeroE6-ACE2-TMPRSS2 cells with clinical samples, performed RNA extractions, and then synthesised cDNA fragments. The infectious cDNA (icDNA) of SARS-CoV-2-alpha was cloned into the pCC1-4K plasmid – both wild-type and a ZsGreen derivative were generated, with ZsGreen inserted at the C-terminus of ORF7a protein, after a 2A ribosomal skipping linker (Fig 5-4 A).

To rescue infectious virus, I transfected BHK-21 cells with the icDNA clones of WT and ZsGreen derivatives. 48 h later, culture supernatant was harvested to inoculate VeroE6 cells. The virus was harvested 48 h (WT) or 72 h (ZsGreen) post-infection. Plaque assays were performed to determine the titre and fluorescent tag retention of the virus stock. The titre of the WT stock was ~35-fold lower than the ZsGreen stock (Fig 5-4 B), likely owing to the earlier harvest time. Further optimisation of propagation conditions, such as longer incubations and using a VeroE6-ACE2 cell line, may facilitate the rescue of a higher titre stock. Using the Celigo Imaging Cytometer, the stability of the ZsGreen tag post-rescue was assessed by scanning plate wells in the green channel and then in the brightfield channel post-Coomassie staining. 96% of plaques were GFP-positive (Fig 5-4 C-D), similar to that observed with the Wuhan-Hu-1 RG system. To assess long-term stability, the virus should be passaged >5 times and ZsGreen+ plaques quantified. Nevertheless, infectious virus of the alpha variant was successfully rescued and used in subsequent experiments by colleagues.

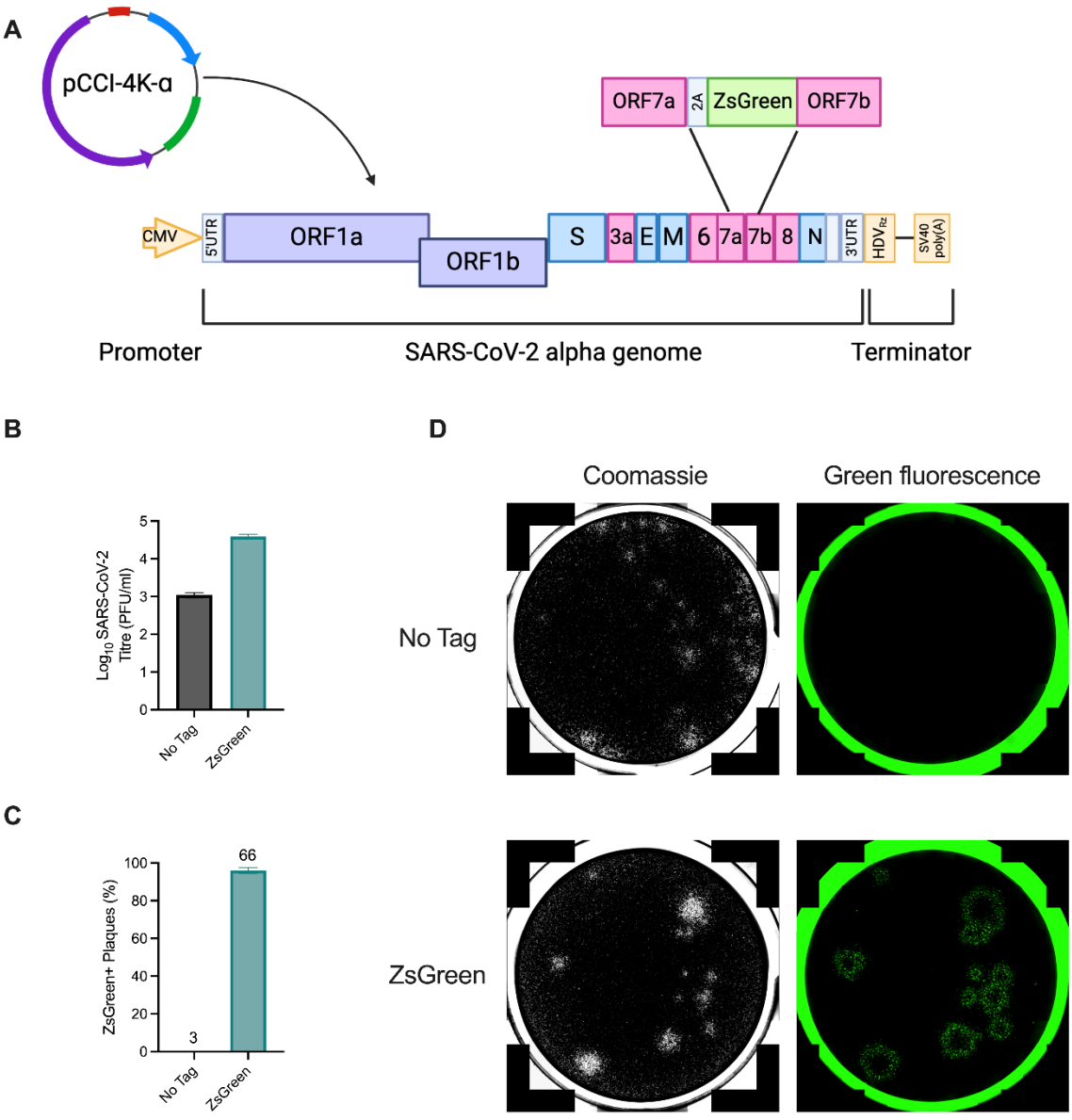

Figure 5-4: Rescue of icDNA-derived SARS-CoV-2 alpha variant. (**A**) Schematic of pCCI-4K-SARS-CoV-2-alpha-ZsGreen icDNA clone. (**B**) Infectious titre of WT and ZsGreen rescued alpha variant, measured by plaque assay on VeroE6 cells. (**C**) Retention of the ZsGreen tag in SARS-CoV-2 alpha passage 1 stock post-rescue, measured by plaque assay. The number of ZsGreen+ plaques was quantified. The number of plaques is indicated above the bar. (**D**) Example brightfield and green channel images of plaques formed by WT and ZsGreen rescued alpha viruses from (B). (**B-C**) Mean and SD from one independent assay, performed in technical duplicate, are shown.

5.2.4. Retention of a GFP11 tag in wild-type and mutant influenza A viruses

Dr Matthew Turnbull, my colleague at the Centre for Virus Research, implemented a split-GFP system for influenza A virus to generate a more stable reporter virus, with higher titres than the 'Color-Flu' described above. The split-GFP system was designed so that most of GFP (GFP1-10) was attached to ANP32A expressed in cells under the control of a doxycycline-inducible promoter. The last 16 residues of GFP were attached to the C-terminus of PB1 in a PR8 reporter virus, similar to that described in (Mistry et al., 2020). Therefore, when GFP1-10-ANP32A and PB1-GFP11 interact, green fluorescence can be measured (Fig 5-5 A).

As part of this project, I was recruited to assess the stability of the GFP11 tag in the wild-type PR8 reporter virus (PR8-PB1^{WT}-GFP11), as well as in a PR8-GFP11 that has two synonymous mutations in PB1 (PR8-PB1^{mutant}-GF11). Plaque assays were performed in doxycycline-treated MDCK-GFP1-10-ANP32A cells by infection with serially diluted PR8-GFP11. Post fixation, cells were scanned in the green channel, followed by the brightfield channel post-staining on the Celigo Imaging Cytometer, and then GFP+ plaques were quantified. Both the PB1^{WT} and PB1^{mutant} viruses had similar titres (Fig 5-5 B). This split-GFP system appears very stable; of 600+ plaques examined for both the PR8-PB1^{WT}-GFP11 and PR8-PB1^{mutant}-GFP11 viruses, the latter virus only exhibited 4 GFP- plaques (Fig 5-5 C-D). This is likely owing to how small the GFP11 fragment is compared to expressing a full-length fluorescent protein.

Thus, with >99% of plaques GFP-positive, this split-GFP system is a reliable way to investigate interactions between PB1 and ANP32A or for other screening applications.

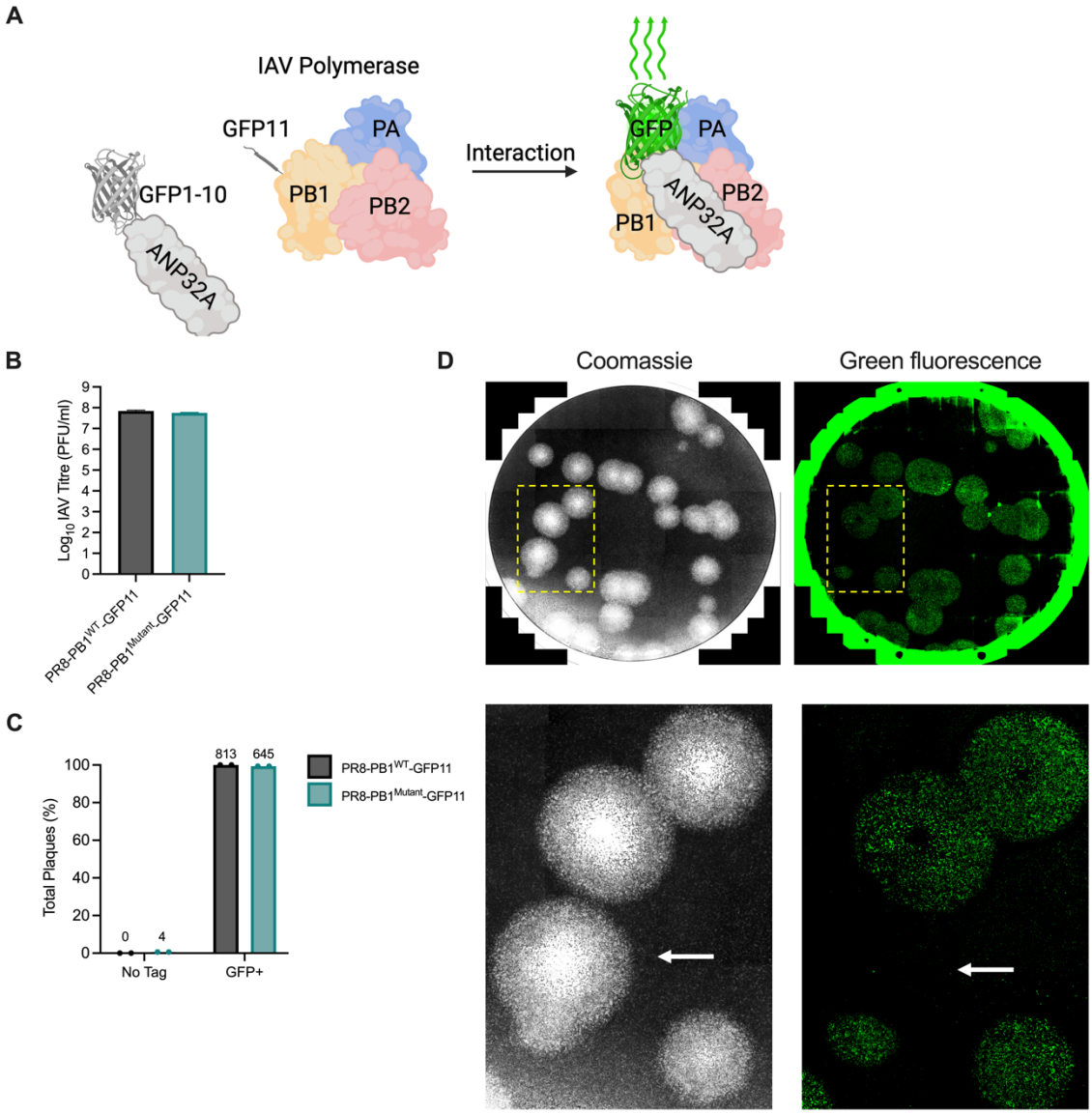

Figure 5-5: Assessing retention of a GFP11 tag encoded in PR8 viruses. (**A**) Schematic of the split-GFP system used to investigate interactions between host ANP32A and the IAV polymerase. (**B**) Infectious titre of the two PR8-GFP11 viruses, measured by plaque assay on MDCK-HsANP32A cells. (**C**) Retention of the GFP11 tag was measured by plaque assay. GFP+ plaques were counted and the total number of plaques are indicated above the bar. (**D**) Example brightfield and green fluorescence image of plaques from (C). A GFP-negative plaque is indicated by yellow box (top panel) or white arrow (bottom panel). (**B-C**) Mean and SD from two independent assays performed in at least technical triplicate are shown.

5.3. Discussion

Fluorescent reporter viruses have enhanced our understanding of viral infections, from small-scale *in vitro* experiments to high-throughput screening and animal models. However, their usefulness is dependent on the fluorescent tag being retained. This is exemplified by a stock of MHV-GFP; a direct comparison of plaques by fluorescence and Coomassie staining showed <40% of plaques expressed GFP. This percentage was raised to >90% after propagating a stock following a limiting dilution approach (Fig 5-3). This highlights the importance of checking the stability of fluorescent tags in reporter virus systems. This chapter shows that this can be done efficiently with plaque assays if the virus is permissive to such experiments. If not, another approach would be to infect cells with the reporter virus and stain the fixed cells with virus-specific antibodies, using secondary labelling with a different fluorophore and comparing the cells for dual fluorescence.

Considering the selective pressure to expel a reporter gene, the dsRNA-based imaging cytometry approach to screening discussed in Chapter 3 is of particular use, as it circumvents the need of such a reporter virus. In such screening experiments, cells overexpressing potential antiviral genes are challenged with a virus at low MOI to examine their effect on multi-cycle infection. Since encoding a reporter gene may be a hindrance to virus replication, this innate immune pressure may favour virions that have shed their reporter gene, potentially skewing experimental outcomes.

The reporter virus for the SARS-CoV-2 alpha variant had high ZsGreen retention post-rescue (Fig 5-4). Here, the stability of this ORF7a-2A-reporter cassette was not assessed after multiple propagations but has been done previously for the Wuhan-Hu-1 strain (Rihn et al., 2021). For 2 of 3 replicates, >95% of plaques were still positive for the reporter gene after five passages, but a reporter-negative population appeared and outnumbered the reporter-positive population in the final replicate. This might be what occurred with the MHV-GFP

stock and indicates the presence of the reporter gene should ideally be quantified after every virus propagation.

An alternative approach is the split-GFP system because the GFP11 tag is considerably smaller than a reporter gene. This system worked well in studying the association between host ANP32A and PB1 of IAV, with very high retention (Fig 5-5). Since HCoV-OC43 reporter systems have become available since the start of this project, adding the GFP11 tag to this virus is doable, so it would be an interesting approach to examining the localisation of viral proteins within the cell or potential binding partners with OAS2.

6. Discussion

If appropriate viral dependency factors, such as entry receptors, are available, the ultimate permissiveness of a cell to viral infection depends on the presence or absence of genome-encoded blocks to viral replication. Many of these virus restriction factors are interferon-stimulated genes. This PhD project aimed to identify ISGs that can act as these innate immune barriers, restricting the transmission of coronaviruses in humans. To do this, I optimised an ISG screening platform using dsRNA immunostaining to score infection with quantification by plate-based image cytometry (Chapter 3); previous approaches for cDNA screening involved the use of fluorescent reporter viruses, cytopathic effect or immunostaining of viral proteins. Using dsRNA staining is an effective quantification method for both genetic and drug screening, as it offers a readily adaptable and low-cost approach for rapid screening during novel virus emergence, compared to generating fluorescent clones. However, reporter viruses are incredibly valuable tools to study viral infection and can be utilised when available. This requires an assessment of the stability of the encoded reporter gene to ensure the data gathered is accurate. Such experiments were described for three reporter viruses used by my collaborators (Chapter 5).

By performing a multi-species ISG screen against the endemic coronavirus HCoV-OC43, followed by secondary screens and examining cytotoxicity and the ability to induce the IFN response, I obtained a shortlist of candidate ISGs with direct antiviral activity against HCoV-OC43. This included genes with independently characterised anti-coronaviral activity, such as *LY6E* and *CTSS*. The gene I was most intrigued by was *OAS2*; this member of the OAS gene family was discovered >30 years ago and is considered a broadly acting antiviral that exerts its inhibitory effects through activation of RNase L. Given the OAS/RNase L evasion mechanism encoded by certain coronaviruses, such as HCoV-OC43, it was not expected to be a hit in the screen. Therefore, I decided to further investigate the anti-HCoV-OC43 activity exhibited by OAS2.

In Chapter 4, I uncovered that the shorter p69 isoform of OAS2 shows potent restriction of HCoV-OC43 in an RNase L-independent mechanism. This restriction appears to be highly specific, with OAS2 p69 being only modestly antiviral against related SARS-CoV-2 but having no effect in 30+ other ISG screens targeting diverse viruses, including retroviruses, orthomyxoviruses, herpesviruses and bunyaviruses. Despite only differing in the C-terminus, the longer p71 isoform of OAS2 had no effect on HCoV-OC43 but was able to modestly inhibit the picornavirus EMCV via the canonical OAS/RNase L pathway.

The OAS gene family is a spectacular example of how antiviral breadth has become encoded into the host genome. OAS proteins are ancient and exist across Metazoa, from sponges to mammals (Chu et al., 2023). Perhaps to cope with increasing pathogen burden, gene duplication and gene fusion events have diversified the OAS repertoire in higher metazoan species, with four members in humans and twelve in mice. This has likely resulted in OAS proteins gaining novel functions, in addition to fine-tuning the structure and sequence specificity for the dsRNA substrate. Accordingly, lower metazoan species do not encode genes related to OAS induction and activity, such as IFN and RNase L (Hu et al., 2018). This suggests ancient OAS proteins had alternative cellular roles and gained basic residues at the protein/dsRNA-binding interface later in evolution to become the innate immune dsRNA sensors existing in higher metazoan species today. For that reason, increasing evidence of OAS proteins working in an RNase L-independent fashion is not surprising, as I describe here for OAS2 p69-mediated inhibition of HCoV-OC43.

In addition to gene duplication, the OAS gene family exhibits antiviral breadth through alternative splicing to expand the number of proteins expressed. Alternative splicing of OAS1 and OAS2 results in isoforms with distinct C-termini, resulting in additional antiviral effects (Soveg et al., 2021; Wickenhagen et al., 2021). For OAS1, inclusion of the CAAX motif in p46 facilitates the localisation of the protein to membranous sites of viral replication, compared to the p42 isoform. In contrast, all three isoforms of human OAS2 included on NCBI have a

myristoylation site, suggesting that no matter the function of the OAS2 isoform, localisation to intracellular membranes is essential. Compared to the C-terminus in OAS1, modification of the N-terminus might be required instead as, based on AlphaFold models of the OAS2 isoforms, the C-terminus may be involved in RNA-binding. Considering mouse Oas1b as well (Courtney et al., 2012), OAS proteins have harnessed the mechanisms of prenylation, myristoylation and transmembrane domains to associate with membranes, highlighting the importance of proximity to virus replication in antiviral activity. Therefore, the OAS gene family has harnessed both gene duplication and alternative splicing to influence the localisation of the antiviral proteins to different sites within the cell, from intracellular membranes to the cytoplasm and nucleus.

The role of alternative splicing in refining the antiviral response is not a novel concept. Splice variants of TLR3, RIG-I and MAVS lacking key domains have been documented and are thought to function by regulating IFN induction in a dominant-negative fashion (Liao and Garcia-Blanco, 2021). There are four isoforms of ZAP (ZAP-S, ZAP-M, ZAP-L and ZAP-XL), with ZAP-S and ZAP-L being the most abundant and studied (Li et al., 2019). Compared to ZAP-S, ZAP-L has an inactive poly (ADP ribose) polymerase (PARP) domain and a CAAX box in its C-terminus and has higher baseline expression levels. In contrast, ZAP-S is more readily induced by IFN. Differential antiviral activity has been observed with these isoforms, with ZAP-L and ZAP-XL being more potent against alphaviruses, whereas all isoforms showed similar restriction against EBOV. There is conflicting evidence on whether ZAP-S or ZAP-L is more potent against SARS-CoV-2. One study found ZAP-S inhibits SARS-CoV-2 by interfering with ribosomal frameshifting, whereas another found ZAP-L was more potent, and this required an intact CAAX motif, similar to OAS1 p46 (Kmiec et al., 2021; Zimmer et al., 2021). Similarly, the related protein PARP12 has two isoforms, with the longer isoform containing a C-terminal PARP domain; PARP12L exhibits antiviral activity against the alphavirus VEEV, whereas PARP12S does not (Atasheva et al., 2012).

Interestingly, IFN stimulation can also influence alternative splicing. The p110 isoform of adenosine deaminase acting on RNA 1 (ADAR1) is constitutively expressed and is mainly localised to the nucleus (Patterson and Samuel, 1995). An alternative IFN-stimulated transcriptional start site can be used, resulting in the inclusion of an exon containing an earlier AUG codon to produce the p150 isoform, that is predominantly localised to the cytoplasm. It is possible that IFN stimulation may alter isoform abundance instead of overall mRNA abundance, so there are likely more examples of such alternative splicing regulation. Therefore, the contrasting antiviral activities of OAS2 p71 and p69 described here further support isoform-specific antiviral behaviour as a method of enhancing antiviral breadth within the innate immune system.

Taking this into account, screening for antiviral ISGs comes with the caveat that the antiviral potential of a gene may not be identified if only one isoform is expressed in the gene library. This is especially important for cDNA screens but can also be an issue with CRISPR screens; the expression of some isoforms can be influenced by genetics, be cell-type specific or require certain stimuli, and so the cell background or experimental conditions may prevent this isoform-specific restriction being revealed. Indeed, if p71 was the only OAS2 isoform expressed in the human ISG library used here, the potent antiviral activity of p69 against HCoV-OC43 would not have been discovered. When subsequently characterising the chosen “hit” of a genetic screen, it is extremely valuable to examine the effect of the different isoforms in parallel, as this can help narrow down the essential domains or motifs required for the observed restriction; this was the case here, as it enabled the p69 C-terminus to be identified as the determinant of antiviral activity against HCoV-OC43 vs EMCV.

The mechanism by which OAS2 p69 inhibits HCoV-OC43 is yet to be elucidated. Some RNase L independent mechanisms have been described in Chapter 4, such as stabilisation of host mRNA and enhancing innate immune signalling proteins. A wealth of evidence suggests that OAS proteins likely had cellular roles, such as RNA metabolism, earlier in evolution. For example, OAS

proteins show structural similarity to CCA-adding enzymes found in Archaea (Torralba et al., 2008). Additionally, loss-of-function mutations in OAS1 genes are present in a variety of primates and as mentioned above, RNase L is not present in lower metazoans (Carey et al., 2019; Hu et al., 2018). These functions could still apply in mammalian OAS proteins and contribute to or be exploited to restrict HCoV-OC43. The involvement of OAS proteins in cellular processes is beginning to be untangled. It has been demonstrated that OAS1 p42 can add 2-5A to poly(ADP)ribose (PAR) (Kondratova et al., 2020). High levels of PAR in the cytoplasm initiate cell death; OAS1 p42 suppresses this PAR build-up to promote cell survival. Although interesting, it is unlikely that the addition of 2-5A to other molecules mediates the inhibition of HCoV-OC43, as catalytic activity was not required. OAS2 has also been associated with the regulation of lactation, and high mRNA expression has been associated with better prognosis in breast cancer patients (Oakes et al., 2017; Zhang and Yu, 2020). Further work is needed to determine whether p69-mediated restriction of HCoV-OC43 is direct or is a consequence of indirect signalling or regulation of other pathways.

The OAS proteins have been described as redundant, with OAS2 mainly considered to have a minor role in viral infection. However, certain characteristics of OAS2 suggest it has critical functions linked to the immune response. Firstly, evidence suggests OAS2 can be induced directly by IRF3 and thus could be produced independently of IFN (Grandvaux et al., 2002). Secondly, analysis of control and RNase L-depleted cells suggests that OAS2 mRNAs are resistant to RNase L-mediated mRNA turnover (Burke et al., 2019); other RNase L-resistant mRNAs identified include IFNβ1, IFIT2, CH25H and DDX58 (RIG-I), but not OAS1 or OAS3. Additionally, OAS2 has been shown to co-localise with stress granules (Reineke and Lloyd, 2015), which could indicate its involvement in innate immune signalling integrated by stress granules. Given this and the data displayed here, this suggests we have yet to discover the full importance of OAS2 as part of the innate immune response.

Overall, I hope the work I have presented here has provided insight into restriction factors affecting the transmission of coronaviruses and contributed to the increasing volume of work re-examining the role of OAS proteins in immunity, including the mechanisms by which OAS proteins function outside of the long-standing 'OAS/RNase L' dogma. This work has opened a new area of investigation that will expand our understanding of the co-evolution of host and virus and, perhaps, one day, inform novel approaches for therapeutics to ameliorate the worst pathologies associated with human coronavirus infections.

Appendix

Appendix 1 – R script for ISG screen analysis

```
 ##Analysis pipeline for ISG screens using a species library dependent mean##

#Libraries
library(dplyr)
library(ggplot2)
library(tidyr)
library(stringr)
library(ggrepel)
library(devEMF)

#enter details
user_name<-paste("ELD")
experiment_folder<-("EXP1-41_ANALYSIS_Zscore")
Experiment<-paste("EXP1-41")
virus<-paste("HCoV-OC43")
virus_strain<-paste("unknown")
virus_type<-paste("live")
Cell_line<-paste("A549")
Quantification1<-paste("AlexaFluor488")
Quantification2<-paste("NA")
#min growth represents a threshold cutoff for what classes as an antiviral gene.
#It automatically generates a table with genes under this threshold.
threshold_growth_to_be_antiviral<- -2

#set file path for general analysis folder

#switch to path for CSV file directory
setwd("/Users/emmadavies/OneDrive - University of Glasgow/PhD/Projects/Project 1_Rodent Originating CoVs/EXP1-41/CSV Files")
getwd()

#load all files with the extension .csv in that CSV files directory
temp = list.files(pattern="*.csv")

# get the data as a list of data frames
myfiles = lapply(temp, read.csv)

#change back to the general analysis folder
setwd("/Users/emmadavies/OneDrive - University of Glasgow/PhD/Projects/Project 1_Rodent Originating CoVs/EXP1-41/CSV Files")
getwd()

# collate the data frames
output = do.call(rbind,myfiles)

#Remove mean and SD rows from Table
colnames(output)[colnames(output)=="X"] <- "File_name"
output <- output[!(output$File_name=="Mean"|output$File_name =="SD"),]

#read in library summary
lib<-read.csv("/Users/emmadavies/OneDrive - University of Glasgow/PhD/ISG Library Documentation/ISG_Lib_For_R_v4_20230918.csv",
                      sep=",", na.strings = c("","NA"), header=T)

#change sample ID header to match library "UniqueNo.GeneName.Gene.Number.Species" or whatever is needed for database input
colnames(output)[colnames(output)=="SampleID"] <- "Well_Identifier"

#change column names of the four quadrants out of FlowJo
#This will work as long as the appropriate columns have capital UL, LL, UR, UL

cnames<-colnames(output)

for(i in 1:length(cnames)) {
  if(grepl("UL",cnames[i],fixed=TRUE)){
    cnames[i]="UL"
  }
  else if(grepl("UR",cnames[i],fixed=TRUE)){
```

```
    cnames[i]="UR"
  }
  else if(grepl("LL",cnames[i],fixed=TRUE)){
    cnames[i]="LL"
  }
  else if(grepl("LR",cnames[i],fixed=TRUE)){
    cnames[i]="LR"
  }
}
colnames(output)<-cnames

#change to numeric
output$UL <- as.numeric(gsub("%", "",output$UL))
output$UR <- as.numeric(gsub("%", "",output$UR))
output$LL <- as.numeric(gsub("%", "",output$LL))
output$LR <- as.numeric(gsub("%", "",output$LR))

#add experiment columns
output["Experiment_ID"]<-paste(Experiment,sep="")
output["Virus"]<-paste(virus,sep="")
output["Virus_strain"]<-paste(virus,sep="")
output["Virus_type"]<-paste(virus_type,sep="")
output["Cell_line"]<-paste(Cell_line,sep="")
output["Quantification1"]<-paste(Quantification1,sep="")
output["Quantification2"]<-paste(Quantification2,sep="")
output["Reason_for_Exclusion"]<-paste("NA")

#########################################################################
#removes space that is present at end of some rows
output$Well_Identifier <- trimws(output$Well_Identifier, which = c("right"))
lib$Species <- trimws(lib$Species, which = c("right"))

#merge files by row
output_merged<-dplyr::inner_join(lib,output,by="Well_Identifier")

#calculate total red (=percent transduction)
output_merged$Percent_transduction <- with(output_merged, UL + UR)

#calculate ratio
output_merged$ratio<-(output_merged$UR/(output_merged$UL+output_merged$UR)*100)

########
#remove rows containing specificed strings
#remove water controls (=B1)
output_nowater<-output_merged[!grepl("_Cells_",output_merged$Well_Identifier),]

#remove virus-only
output_nowater_novirus<-output_nowater[!grepl("_Virus_only_",output_nowater$Well_Identifier),]

#remove SCRPSY (but not SCRPSY infected)
output_nowater_novirus_noSCRPSY <- output_nowater_novirus[!grepl("_Empty-
SCRPSY_",output_nowater_novirus$Well_Identifier),]

####explore looking for various NA values#####
sum(is.na(output$Percent_inhibition))

write.csv(output_nowater_novirus_noSCRPSY,file=paste(experiment_folder,"_output_nowater_novirus_noSCRPSY.csv"))

############Subset the different libraries#####################################

#subset Cow Library
cow_lib <- output_merged[grepl("Cow", output_merged$Species),]

write.csv(cow_lib,file=paste(experiment_folder,"_cow_lib.csv"))

#subset Human Library
human_lib <- output_merged[grepl("Human", output_merged$Species),]

write.csv(human_lib,file=paste(experiment_folder,"_human_lib.csv"))

#subset Macaque Library
mac_lib <- output_merged[grepl("Macaque", output_merged$Species),]

write.csv(mac_lib,file=paste(experiment_folder,"_mac_lib.csv"))
```

```
#subset Mouse Library
mouse_lib <- output_merged[grepl("Mouse", output_merged$Species),]

write.csv(mac_lib,file=paste(experiment_folder,"_mouse_lib.csv"))

#subset R.affinis Library
Raffinis_lib <- output_merged[grepl("Rhinolophus affinis", output_merged$Species),]

write.csv(mac_lib,file=paste(experiment_folder,"_Raffinis_lib.csv"))

#subset R.sinicus Library
Rsinicus_lib <- output_merged[grepl("Rhinolophus sinicus", output_merged$Species),]

write.csv(mac_lib,file=paste(experiment_folder,"_Rsinicus_lib.csv"))


#Calculate Virus Growth and z-scores of Cow Library
cow_nowater_novirus_noSCRPSY <- output_nowater_novirus_noSCRPSY[grepl(
  "Cow", output_nowater_novirus_noSCRPSY$Species),]
cow_lib["mean_value"] <- mean(cow_nowater_novirus_noSCRPSY$ratio,na.rm=T)
cow_lib["standard_deviation"] <- sd(cow_nowater_novirus_noSCRPSY$ratio,na.rm=T)
cow_lib["zscore"] <- ((cow_lib$ratio - cow_lib$mean_value)/cow_lib$standard_deviation)
cow_lib$Percent_VirusGrowth<-((cow_lib$ratio/cow_lib$mean_value)*100)
write.csv(cow_lib,file=paste(experiment_folder,"_cow_lib.csv"))

#Calculate Virus Growth and z-scores of Human Library
human_nowater_novirus_noSCRPSY <- output_nowater_novirus_noSCRPSY[grepl(
  "Human", output_nowater_novirus_noSCRPSY$Species),]
human_lib["mean_value"] <- mean(human_nowater_novirus_noSCRPSY$ratio,na.rm=T)
human_lib["standard_deviation"] <- sd(human_nowater_novirus_noSCRPSY$ratio,na.rm=T)
human_lib["zscore"] <- ((human_lib$ratio - human_lib$mean_value)/human_lib$standard_deviation)
human_lib$Percent_VirusGrowth<-((human_lib$ratio/human_lib$mean_value)*100)
write.csv(human_lib,file=paste(experiment_folder,"_human_lib.csv"))

#Calculate Virus Growth and z-scores of Macaque Library
mac_nowater_novirus_noSCRPSY <- output_nowater_novirus_noSCRPSY[grepl(
  "Macaque", output_nowater_novirus_noSCRPSY$Species),]
mac_lib["mean_value"] <- mean(mac_nowater_novirus_noSCRPSY$ratio,na.rm=T)
mac_lib["standard_deviation"] <- sd(mac_nowater_novirus_noSCRPSY$ratio,na.rm=T)
mac_lib["zscore"] <- ((mac_lib$ratio - mac_lib$mean_value)/mac_lib$standard_deviation)
mac_lib$Percent_VirusGrowth<-((mac_lib$ratio/mac_lib$mean_value)*100)
write.csv(mac_lib,file=paste(experiment_folder,"_mac_lib.csv"))

#Calculate Virus Growth and z-scores of Mouse Library
mouse_nowater_novirus_noSCRPSY <- output_nowater_novirus_noSCRPSY[grepl(
  "Mouse", output_nowater_novirus_noSCRPSY$Species),]
mouse_lib["mean_value"] <- mean(mouse_nowater_novirus_noSCRPSY$ratio,na.rm=T)
mouse_lib["standard_deviation"] <- sd(mouse_nowater_novirus_noSCRPSY$ratio,na.rm=T)
mouse_lib["zscore"] <- ((mouse_lib$ratio - mouse_lib$mean_value)/mouse_lib$standard_deviation)
mouse_lib$Percent_VirusGrowth<-((mouse_lib$ratio/mouse_lib$mean_value)*100)
write.csv(mouse_lib,file=paste(experiment_folder,"_mouse_lib.csv"))

#Calculate Virus Growth and z-scores of R. affinis Library
Raffinis_nowater_novirus_noSCRPSY <- output_nowater_novirus_noSCRPSY[grepl(
  "Rhinolophus affinis", output_nowater_novirus_noSCRPSY$Species),]
Raffinis_lib["mean_value"] <- mean(Raffinis_nowater_novirus_noSCRPSY$ratio,na.rm=T)
Raffinis_lib["standard_deviation"] <- sd(Raffinis_nowater_novirus_noSCRPSY$ratio,na.rm=T)
Raffinis_lib["zscore"] <- ((Raffinis_lib$ratio - Raffinis_lib$mean_value)/Raffinis_lib$standard_deviation)
Raffinis_lib$Percent_VirusGrowth<-((Raffinis_lib$ratio/Raffinis_lib$mean_value)*100)
write.csv(Raffinis_lib,file=paste(experiment_folder,"_Raffinis_lib.csv"))

#Calculate Virus Growth and z-scores of R. sinicus Library
Rsinicus_nowater_novirus_noSCRPSY <- output_nowater_novirus_noSCRPSY[grepl(
  "Rhinolophus sinicus", output_nowater_novirus_noSCRPSY$Species),]
Rsinicus_lib["mean_value"] <- mean(Rsinicus_nowater_novirus_noSCRPSY$ratio,na.rm=T)
Rsinicus_lib["standard_deviation"] <- sd(Rsinicus_nowater_novirus_noSCRPSY$ratio,na.rm=T)
Rsinicus_lib["zscore"] <- ((Rsinicus_lib$ratio - Rsinicus_lib$mean_value)/Rsinicus_lib$standard_deviation)
Rsinicus_lib$Percent_VirusGrowth<-((Rsinicus_lib$ratio/Rsinicus_lib$mean_value)*100)
write.csv(Rsinicus_lib,file=paste(experiment_folder,"_Rsinicus_lib.csv"))

############Merge different species libraries together####################################

#merge mac_lib, human_lib, mouse_lib and cow_lib to one data.frame
```

```
complete_lib<-dplyr::bind_rows(cow_lib, human_lib, mac_lib, mouse_lib, Raffinis_lib, Rsinicus_lib)

#write csv of complete library to check
write.csv(complete_lib, file = paste(experiment_folder,"_complete_lib.csv"))


#Final Table using Library specific Medians
Final_table<-dplyr::select(complete_lib,Experiment_ID,Species,Well_Identifier, UniqueNo,
                      Gene,PROVISIONAL.ENSEMBL.ID,Plate,Row,Column,GeneName,zscore,
                      Percent_VirusGrowth,Count,LL,LR,UL,UR,Percent_transduction,
                      mean_value,standard_deviation,Reason_for_Exclusion,Log2FC,
                      Top300,mammCore,Antiviral,Virus,Virus_strain,Virus_type,
                      Cell_line,Quantification1,Quantification2)
Final_table<-dplyr::arrange(Final_table,by=zscore)

write.csv(Final_table,file=paste(experiment_folder, "_Final_List.csv"))

###############Final table - subset controls####################################

#water controls
water_controls<-Final_table[grepl("Cells",Final_table$GeneName),]
water_controls<-dplyr::arrange(water_controls,by=Species)
write.csv(water_controls,file=paste(experiment_folder,"_water_controls.csv"))

#virus controls
virus_controls<-Final_table[grepl("Virus_only",Final_table$GeneName),]
virus_controls<-dplyr::arrange(virus_controls,by=Species)
write.csv(virus_controls,file=paste(experiment_folder,"_virus_controls.csv"))

#SCRPSY controls
SCRPSY_controls<-Final_table[grepl("SCRPSY",Final_table$GeneName),]
SCRPSY_controls<-dplyr::arrange(SCRPSY_controls,by=Species)
write.csv(SCRPSY_controls,file=paste(experiment_folder,"_SCRPSY_controls.csv"))

##### subset high inhibitors ########################################

antivirals<-dplyr::filter(Final_table,zscore<threshold_growth_to_be_antiviral)
antivirals<-antivirals[!grepl("SCRPSY",antivirals$GeneName),]
antivirals<-antivirals[!grepl("Virus",antivirals$GeneName),]
antivirals<-antivirals[!grepl("Cells",antivirals$GeneName),]

write.csv(antivirals,file=paste(experiment_folder,"Genes_inhibiting_under_",threshold_growth_to_be_antiviral,"_-2_z-
score.csv"))

antivirals_transduction10 <-subset(antivirals, Percent_transduction > 10)
write.csv(antivirals_transduction10,file=paste(experiment_folder,"Genes_inhibiting_under_",threshold_growth_to_be_antivir
al,"_-2_zscore_higherthan10transduction.csv"))

##### plots ############################################################

#remove cells-only
genes_toplot<-complete_lib[!grepl("Cells",complete_lib$Well_Identifier),]

#remove virus-only
genes_toplot<-genes_toplot[!grepl("Virus",genes_toplot$Well_Identifier),]

#remove Empty_SCRPSY
genes_toplot<-genes_toplot[!grepl("SCRPSY",genes_toplot$Well_Identifier),]

#create plot
dotplot = ggplot(genes_toplot, aes(x=Species,y=Percent_VirusGrowth, fill=Species))+
  geom_dotplot(binaxis = "y",binwidth = 0.027,stackdir = "center",dotsize = 0.75, stroke = 0.5) +

geom_text_repel(aes(label=ifelse(zscore<threshold_growth_to_be_antiviral,as.character(GeneName),'')),size=2.5,color="bl
ack", max.overlaps = 20)+
              scale_y_continuous(trans = "log10", breaks = c(1, 10, 100, 1000))+
              labs(title=paste("OC43 Screen"), x = "Species", y = "Normalised Infection (%)") +
  scale_x_discrete(limits=c("Human", "Macaque", "Cow", "Mouse", "Rhinolophus affinis", "Rhinolophus sinicus")) +
theme_classic() +
              theme(panel.grid.major = element_blank(),
                    panel.grid.minor = element_blank(),
                    # panel.background = element_rect(fill = "white", color = "black"),
                    legend.position = "none")+
              scale_fill_manual(name = "Species",
```

```
                    values = c("blue", "skyblue", "deepskyblue", "purple", "yellow", "springgreen"))


#save dotplot as pdf
ggsave(paste(experiment_folder,"_scatterplot.pdf"),
      width = 20, height = 20, units = "cm")

#show dotplot
dotplot

#Transduction Plot
            dotplot_transduction = ggplot(genes_toplot, aes(x=Species,y=Percent_transduction, fill=Species))+
              geom_dotplot(binaxis = "y",binwidth = 0.027,stackdir = "center",dotsize = 0.75, stroke = 0.5) +
              #geom_text_repel(aes(label=ifelse(Percent_transduction<10,as.character(GeneName),'')), size=1, color="black",
max.overlaps = 30) +
              scale_y_continuous(trans = "log10", breaks = c(0.01, 0.1 ,1, 10, 100))+
              labs(title=paste("OC43 Screen"), x = "Species", y = "Transduction (%)") +
              scale_x_discrete(limits=c("Human", "Macaque", "Cow", "Mouse", "Rhinolophus affinis", "Rhinolophus sinicus")) +
theme_classic() +
              theme(panel.grid.major = element_blank(),
                    panel.grid.minor = element_blank(),
                    legend.position = "none")+
              scale_fill_manual(name = "Species",
                                values = c("red", "sienna1", "orangered", "tomato", "yellow", "orange"))


#save dotplot as pdf
ggsave(paste(experiment_folder,"_scatterplot_transduction.pdf"),
      width = 20, height = 20, units = "cm")

#show dotplot
dotplot_transduction

#low % transduction genes
low_transduction <- subset(Final_table, Percent_transduction < 10)
low_transduction <- low_transduction[!grepl("Virus",low_transduction$GeneName),]
low_transduction<-low_transduction[!grepl("Cells ",low_transduction$GeneName),]

#### Plot Genes with > 10% Transduction Efficiency

genes_toplot_10 <- subset(genes_toplot, Percent_transduction > 10)

#create plot
dotplot_10t <- ggplot(genes_toplot_10, aes(x=Species,y=Percent_VirusGrowth, fill=Species))+
              geom_dotplot(binaxis = "y",binwidth = 0.030,stackdir = "center",dotsize = 0.75, stroke = 0.5) +

geom_text_repel(aes(label=ifelse(zscore<threshold_growth_to_be_antiviral,as.character(GeneName),'')),size=3,color="blac
k", max.overlaps = 20)+
              scale_y_continuous(trans = "log10", breaks = c(1, 10, 100, 1000))+
              labs(title=paste("OC43 Screen"), x = "Species", y = "Normalised Infection (%)") +
              scale_x_discrete(limits=c("Human", "Macaque", "Cow", "Mouse", "Rhinolophus affinis", "Rhinolophus sinicus")) +
theme_classic() +
              theme(panel.grid.major = element_blank(),
                    panel.grid.minor = element_blank(),
                    # panel.background = element_rect(fill = "white", color = "black"),
                    legend.position = "none", axis.title = element_text(size = 16),
                    axis.text = element_text(size = 12))+
              scale_fill_manual(name = "Species",
                                values = c("blue", "skyblue", "deepskyblue", "purple", "yellow", "springgreen1"))

#save dotplot as pdf
ggsave(paste(experiment_folder,"_scatterplot_transduction10.pdf"),
                  width = 20, height = 20, units = "cm")

emf("_dotplot_transduction10.emf",
   height=10, width=15)
print(dotplot_10t)
dev.off()

#show dotplot
dotplot_10t
```

References

Abramson, J., Adler, J., Dunger, J., Evans, R., Green, T., Pritzel, A., Ronneberger, O., Willmore, L., Ballard, A.J., Bambrick, J., Bodenstein, S.W., Evans, D.A., Hung, C.-C., O'Neill, M., Reiman, D., Tunyasuvunakool, K., Wu, Z., Žemgulytė, A., Arvaniti, E., Beattie, C., Bertolli, O., Bridgland, A., Cherepanov, A., Congreve, M., Cowen-Rivers, A.I., Cowie, A., Figurnov, M., Fuchs, F.B., Gladman, H., Jain, R., Khan, Y.A., Low, C.M.R., Perlin, K., Potapenko, A., Savy, P., Singh, S., Stecula, A., Thillaisundaram, A., Tong, C., Yakneen, S., Zhong, E.D., Zielinski, M., Žídek, A., Bapst, V., Kohli, P., Jaderberg, M., Hassabis, D., Jumper, J.M., 2024. Accurate structure prediction of biomolecular interactions with AlphaFold 3. Nature 630, 493–500. https://doi.org/10.1038/s41586-024-07487-w

Akasaki, K., Nakamura, N., Tsukui, N., Yokota, S., Murata, S., Katoh, R., Michihara, A., Tsuji, H., Marques, E.T.A., August, J.T., 2004. Human dendritic cell lysosome-associated membrane protein expressed in lung type II pneumocytes. Archives of Biochemistry and Biophysics 425, 147–157. https://doi.org/10.1016/j.abb.2004.02.042

Alluwaimi, A.M., Alshubaith, I.H., Al-Ali, A.M., Abohelaika, S., 2020. The Coronaviruses of Animals and Birds: Their Zoonosis, Vaccines, and Models for SARS-CoV and SARS-CoV2. Front. Vet. Sci. 7. https://doi.org/10.3389/fvets.2020.582287

Almeida, J.D., Tyrrell, D.A.J., 1967. The Morphology of Three Previously Uncharacterized Human Respiratory Viruses that Grow in Organ Culture. Journal of General Virology 1, 175–178. https://doi.org/10.1099/0022-1317-1-2-175

Alspach, E., Lussier, D.M., Schreiber, R.D., 2019. Interferon γ and Its Important Roles in Promoting and Inhibiting Spontaneous and Therapeutic Cancer Immunity. Cold Spring Harb Perspect Biol 11, a028480. https://doi.org/10.1101/cshperspect.a028480

Atasheva, S., Akhrymuk, M., Frolova, E.I., Frolov, I., 2012. New PARP Gene with an Anti-Alphavirus Function. Journal of Virology 86, 8147–8160. https://doi.org/10.1128/jvi.00733-12

Avilov, S.V., Moisy, D., Munier, S., Schraidt, O., Naffakh, N., Cusack, S., 2012. Replication-Competent Influenza A Virus That Encodes a Split-Green Fluorescent Protein-Tagged PB2 Polymerase Subunit Allows Live-Cell Imaging of the Virus Life Cycle. Journal of Virology 86, 1433–1448. https://doi.org/10.1128/jvi.05820-11

Bamford, C.G.G., Aranday-Cortes, E., Sanchez-Velazquez, R., Mullan, C., Kohl, A., Patel, A.H., Wilson, S.J., McLauchlan, J., 2022. A Human and Rhesus Macaque Interferon-Stimulated Gene Screen Shows That Over-Expression of ARHGEF3/XPLN Inhibits Replication of Hepatitis C Virus and Other Flaviviridae. Viruses 14, 1655. https://doi.org/10.3390/v14081655

Barkhash, A., Babenko, V.N., Kobzev, V.F., Romaschenko, A.G., Voevoda, M.I., 2010a. Polymorphism of 2′-5′-oligoadenylate synthetase (OAS) genes,

associated with predisposition to severe forms of tick-borne encephalitis, in human populations of North Eurasia. Molecular Biology 44, 875. https://doi.org/10.1134/S002689331006004X

Barkhash, A., Perelygin, A.A., Babenko, V.N., Myasnikova, N.G., Pilipenko, P.I., Romaschenko, A.G., Voevoda, A.G., Brinton, M.A., 2010b. Variability in the 2′–5′-Oligoadenylate Synthetase Gene Cluster Is Associated with Human Predisposition to Tick-Borne Encephalitis Virus-Induced Disease. The Journal of Infectious Diseases 202, 1813–1818. https://doi.org/10.1086/657418

Bastard, P., Rosen, L.B., Zhang, Q., Michailidis, E., Hoffmann, H.-H., Zhang, Y., Dorgham, K., Philippot, Q., Rosain, J., Béziat, V., Manry, J., Shaw, E., Haljasmägi, L., Peterson, P., Lorenzo, L., Bizien, L., Trouillet-Assant, S., Dobbs, K., de Jesus, A.A., Belot, A., Kallaste, A., Catherinot, E., Tandjaoui-Lambiotte, Y., Le Pen, J., Kerner, G., Bigio, B., Seeleuthner, Y., Yang, R., Bolze, A., Spaan, A.N., Delmonte, O.M., Abers, M.S., Aiuti, A., Casari, G., Lampasona, V., Piemonti, L., Ciceri, F., Bilguvar, K., Lifton, R.P., Vasse, M., Smadja, D.M., Migaud, M., Hadjadj, J., Terrier, B., Duffy, D., Quintana-Murci, L., van de Beek, D., Roussel, L., Vinh, D.C., Tangye, S.G., Haerynck, F., Dalmau, D., Martinez-Picado, J., Brodin, P., Nussenzweig, M.C., Boisson-Dupuis, S., Rodríguez-Gallego, C., Vogt, G., Mogensen, T.H., Oler, A.J., Gu, J., Burbelo, P.D., Cohen, J.I., Biondi, A., Bettini, L.R., D'Angio, M., Bonfanti, P., Rossignol, P., Mayaux, J., Rieux-Laucat, F., Husebye, E.S., Fusco, F., Ursini, M.V., Imberti, L., Sottini, A., Paghera, S., Quiros-Roldan, E., Rossi, C., Castagnoli, R., Montagna, D., Licari, A., Marseglia, G.L., Duval, X., Ghosn, J., HGID Lab, NIAID-USUHS Immune Response to COVID Group, COVID Clinicians, COVID-STORM Clinicians, Imagine COVID Group, French COVID Cohort Study Group, Milieu Intérieur Consortium, CoV-Contact Cohort, Amsterdam UMC Covid-19 Biobank, COVID Human Genetic Effort, Tsang, J.S., Goldbach-Mansky, R., Kisand, K., Lionakis, M.S., Puel, A., Zhang, S.-Y., Holland, S.M., Gorochov, G., Jouanguy, E., Rice, C.M., Cobat, A., Notarangelo, L.D., Abel, L., Su, H.C., Casanova, J.-L., 2020. Autoantibodies against type I IFNs in patients with life-threatening COVID-19. Science 370, eabd4585. https://doi.org/10.1126/science.abd4585

Batra, J., Hultquist, J.F., Liu, D., Shtanko, O., Dollen, J.V., Satkamp, L., Jang, G.M., Luthra, P., Schwarz, T.M., Small, G.I., Arnett, E., Anantpadma, M., Reyes, A., Leung, D.W., Kaake, R., Haas, P., Schmidt, C.B., Schlesinger, L.S., LaCount, D.J., Davey, R.A., Amarasinghe, G.K., Basler, C.F., Krogan, N.J., 2018. Protein Interaction Mapping Identifies RBBP6 as a Negative Regulator of Ebola Virus Replication. Cell 175, 1917-1930.e13. https://doi.org/10.1016/j.cell.2018.08.044

Behera, A.K., Kumar, M., Lockey, R.F., Mohapatra, S.S., 2002. 2′-5′ Oligoadenylate Synthetase Plays a Critical Role in Interferon-γ Inhibition of Respiratory Syncytial Virus Infection of Human Epithelial Cells *. Journal of Biological Chemistry 277, 25601–25608. https://doi.org/10.1074/jbc.M200211200

Bisbal, C., Silverman, R.H., 2007. Diverse functions of RNase L and implications in pathology. Biochimie 89, 789–798. https://doi.org/10.1016/j.biochi.2007.02.006

Blanco-Melo, D., Nilsson-Payant, B.E., Liu, W.-C., Uhl, S., Hoagland, D., Møller, R., Jordan, T.X., Oishi, K., Panis, M., Sachs, D., Wang, T.T., Schwartz, R.E., Lim, J.K., Albrecht, R.A., tenOever, B.R., 2020. Imbalanced Host Response to SARS-CoV-2 Drives Development of COVID-19. Cell 181, 1036-1045.e9. https://doi.org/10.1016/j.cell.2020.04.026

Brass, A.L., Huang, I.-C., Benita, Y., John, S.P., Krishnan, M.N., Feeley, E.M., Ryan, B.J., Weyer, J.L., van der Weyden, L., Fikrig, E., Adams, D.J., Xavier, R.J., Farzan, M., Elledge, S.J., 2009. The IFITM proteins mediate cellular resistance to influenza A H1N1 virus, West Nile virus, and dengue virus. Cell 139, 1243–1254. https://doi.org/10.1016/j.cell.2009.12.017

Bréhin, A.-C., Casadémont, I., Frenkiel, M.-P., Julier, C., Sakuntabhai, A., Desprès, P., 2009. The large form of human 2′,5′-Oligoadenylate Synthetase (OAS3) exerts antiviral effect against Chikungunya virus. Virology 384, 216–222. https://doi.org/10.1016/j.virol.2008.10.021

Bresson, S., Sani, E., Armatowska, A., Dixon, C., Tollervey, D., 2025. The transcriptional and translational landscape of HCoV-OC43 infection. PLOS Pathogens 21, e1012831. https://doi.org/10.1371/journal.ppat.1012831

Burke, J.M., Moon, S.L., Matheny, T., Parker, R., 2019. RNase L Reprograms Translation by Widespread mRNA Turnover Escaped by Antiviral mRNAs. Molecular Cell 75, 1203-1217.e5. https://doi.org/10.1016/j.molcel.2019.07.029

Carey, C.M., Govande, A.A., Cooper, J.M., Hartley, M.K., Kranzusch, P.J., Elde, N.C., 2019. Recurrent Loss-of-Function Mutations Reveal Costs to OAS1 Antiviral Activity in Primates. Cell Host & Microbe 25, 336-343.e4. https://doi.org/10.1016/j.chom.2019.01.001

Carrique, L., Fan, H., Walker, A.P., Keown, J.R., Sharps, J., Staller, E., Barclay, W.S., Fodor, E., Grimes, J.M., 2020. Host ANP32A mediates the assembly of the influenza virus replicase. Nature 587, 638–643. https://doi.org/10.1038/s41586-020-2927-z

Carter, T., Iqbal, M., 2024. The Influenza A Virus Replication Cycle: A Comprehensive Review. Viruses 16, 316. https://doi.org/10.3390/v16020316

Channappanavar, R., Fehr, A.R., Vijay, R., Mack, M., Zhao, J., Meyerholz, D.K., Perlman, S., 2016. Dysregulated Type I Interferon and Inflammatory Monocyte-Macrophage Responses Cause Lethal Pneumonia in SARS-CoV-Infected Mice. Cell Host Microbe 19, 181–193. https://doi.org/10.1016/j.chom.2016.01.007

Chemudupati, M., Kenney, A.D., Bonifati, S., Zani, A., McMichael, T.M., Wu, L., Yount, J.S., 2019. From APOBEC to ZAP: Diverse mechanisms used by cellular restriction factors to inhibit virus infections. Biochim Biophys Acta

Mol Cell Res 1866, 382–394. https://doi.org/10.1016/j.bbamcr.2018.09.012

Chen, Y.G., Hur, S., 2022. Cellular origins of dsRNA, their recognition and consequences. Nat Rev Mol Cell Biol 23, 286–301. https://doi.org/10.1038/s41580-021-00430-1

Chu, L., Gong, Z., Wang, W., Han, G.-Z., 2023. Origin of the OAS–RNase L innate immune pathway before the rise of jawed vertebrates via molecular tinkering. Proceedings of the National Academy of Sciences 120, e2304687120. https://doi.org/10.1073/pnas.2304687120

Collins, A.R., 1994. Human Coronavirus OC43 Interacts with Major Histocompatibility Complex Class I Molecules at the Cell Surface to Establish Infection. Immunological Investigations 23, 313–321. https://doi.org/10.3109/08820139409066826

Corman, V.M., Muth, D., Niemeyer, D., Drosten, C., 2018. Hosts and Sources of Endemic Human Coronaviruses. Adv Virus Res 100, 163–188. https://doi.org/10.1016/bs.aivir.2018.01.001

Courtney, S.C., Di, H., Stockman, B.M., Liu, H., Scherbik, S.V., Brinton, M.A., 2012. Identification of Novel Host Cell Binding Partners of Oas1b, the Protein Conferring Resistance to Flavivirus-Induced Disease in Mice. J Virol 86, 7953–7963. https://doi.org/10.1128/JVI.00333-12

Crits-Christoph, A., Levy, J.I., Pekar, J.E., Goldstein, S.A., Singh, R., Hensel, Z., Gangavarapu, K., Rogers, M.B., Moshiri, N., Garry, R.F., Holmes, E.C., Koopmans, M.P.G., Lemey, P., Peacock, T.P., Popescu, S., Rambaut, A., Robertson, D.L., Suchard, M.A., Wertheim, J.O., Rasmussen, A.L., Andersen, K.G., Worobey, M., Débarre, F., 2024. Genetic tracing of market wildlife and viruses at the epicenter of the COVID-19 pandemic. Cell 187, 5468-5482.e11. https://doi.org/10.1016/j.cell.2024.08.010

Crow, Y.J., Stetson, D.B., 2022. The type I interferonopathies: 10 years on. Nat Rev Immunol 22, 471–483. https://doi.org/10.1038/s41577-021-00633-9

Cui, J., Li, F., Shi, Z.-L., 2019. Origin and evolution of pathogenic coronaviruses. Nat Rev Microbiol 17, 181–192. https://doi.org/10.1038/s41579-018-0118-9

Cusic, R., Burke, J.M., 2024. Condensation of RNase L promotes its rapid activation in response to viral infection in mammalian cells. Science Signaling 17, eadi9844. https://doi.org/10.1126/scisignal.adi9844

Daffis, S., Szretter, K.J., Schriewer, J., Li, J., Youn, S., Errett, J., Lin, T.-Y., Schneller, S., Zust, R., Dong, H., Thiel, V., Sen, G.C., Fensterl, V., Klimstra, W.B., Pierson, T.C., Buller, R.M., Gale Jr, M., Shi, P.-Y., Diamond, M.S., 2010. 2′-O methylation of the viral mRNA cap evades host restriction by IFIT family members. Nature 468, 452–456. https://doi.org/10.1038/nature09489

Dalskov, L., Gad, H.H., Hartmann, R., 2023. Viral recognition and the antiviral interferon response. EMBO J 42, e112907. https://doi.org/10.15252/embj.2022112907

Danziger, O., Patel, R.S., DeGrace, E.J., Rosen, M.R., Rosenberg, B.R., 2022. Inducible CRISPR activation screen for interferon-stimulated genes identifies OAS1 as a SARS-CoV-2 restriction factor. PLoS Pathog 18, e1010464. https://doi.org/10.1371/journal.ppat.1010464

de Haan, C.A.M., Masters, P.S., Shen, X., Weiss, S., Rottier, P.J.M., 2002. The Group-Specific Murine Coronavirus Genes Are Not Essential, but Their Deletion, by Reverse Genetics, Is Attenuating in the Natural Host. Virology 296, 177–189. https://doi.org/10.1006/viro.2002.1412

de Wilde, A.H., Raj, V.S., Oudshoorn, D., Bestebroer, T.M., van Nieuwkoop, S., Limpens, R.W.A.L., Posthuma, C.C., van der Meer, Y., Bárcena, M., Haagmans, B.L., Snijder, E.J., van den Hoogen, B.G., 2013. MERS-coronavirus replication induces severe in vitro cytopathology and is strongly inhibited by cyclosporin A or interferon-α treatment. Journal of General Virology 94, 1749–1760. https://doi.org/10.1099/vir.0.052910-0

Desforges, M., Desjardins, J., Zhang, C., Talbot, P.J., 2013. The Acetyl-Esterase Activity of the Hemagglutinin-Esterase Protein of Human Coronavirus OC43 Strongly Enhances the Production of Infectious Virus. J Virol 87, 3097–3107. https://doi.org/10.1128/JVI.02699-12

Desforges, M., Le Coupanec, A., Dubeau, P., Bourgouin, A., Lajoie, L., Dubé, M., Talbot, P.J., 2020. Human Coronaviruses and Other Respiratory Viruses: Underestimated Opportunistic Pathogens of the Central Nervous System? Viruses 12, 14. https://doi.org/10.3390/v12010014

Devaraj, S.G., Wang, N., Chen, Zhongbin, Chen, Zihong, Tseng, M., Barretto, N., Lin, R., Peters, C.J., Tseng, C.-T.K., Baker, S.C., Li, K., 2007. Regulation of IRF-3-dependent Innate Immunity by the Papain-like Protease Domain of the Severe Acute Respiratory Syndrome Coronavirus *. Journal of Biological Chemistry 282, 32208–32221. https://doi.org/10.1074/jbc.M704870200

Diamond, M.S., Farzan, M., 2013. The broad-spectrum antiviral functions of IFIT and IFITM proteins. Nat Rev Immunol 13, 46–57. https://doi.org/10.1038/nri3344

Dittmann, M., Hoffmann, H.-H., Scull, M.A., Gilmore, R.H., Bell, K.L., Ciancanelli, M., Wilson, S.J., Crotta, S., Yu, Y., Flatley, B., Xiao, J.W., Casanova, J.-L., Wack, A., Bieniasz, P.D., Rice, C.M., 2015. A serpin shapes the extracellular environment to prevent influenza A virus maturation. Cell 160, 631–643. https://doi.org/10.1016/j.cell.2015.01.040

Doench, J.G., Fusi, N., Sullender, M., Hegde, M., Vaimberg, E.W., Donovan, K.F., Smith, I., Tothova, Z., Wilen, C., Orchard, R., Virgin, H.W., Listgarten, J., Root, D.E., 2016. Optimized sgRNA design to maximize activity and minimize off-target effects of CRISPR-Cas9. Nat Biotechnol 34, 184–191. https://doi.org/10.1038/nbt.3437

Dong, B., Silverman, R.H., 1995. 2-5A-dependent RNase Molecules Dimerize during Activation by 2-5A (∗). Journal of Biological Chemistry 270, 4133–4137. https://doi.org/10.1074/jbc.270.8.4133

Dong, B., Xu, L., Zhou, A., Hassel, B.A., Lee, X., Torrence, P.F., Silverman, R.H., 1994. Intrinsic molecular activities of the interferon-induced 2-5A-dependent RNase. J Biol Chem 269, 14153–14158.

Donovan, J., Dufner, M., Korennykh, A., 2013. Structural basis for cytosolic double-stranded RNA surveillance by human oligoadenylate synthetase 1. Proceedings of the National Academy of Sciences 110, 1652–1657. https://doi.org/10.1073/pnas.1218528110

Donovan, J., Whitney, G., Rath, S., Korennykh, A., 2015. Structural mechanism of sensing long dsRNA via a noncatalytic domain in human oligoadenylate synthetase 3. Proceedings of the National Academy of Sciences 112, 3949–3954. https://doi.org/10.1073/pnas.1419409112

Dou, D., Revol, R., Östbye, H., Wang, H., Daniels, R., 2018. Influenza A Virus Cell Entry, Replication, Virion Assembly and Movement. Frontiers in Immunology 9, 1581. https://doi.org/10.3389/fimmu.2018.01581

Doudna, J.A., Charpentier, E., 2014. The new frontier of genome engineering with CRISPR-Cas9. Science 346, 1258096. https://doi.org/10.1126/science.1258096

Drappier, M., Michiels, T., 2015. Inhibition of the OAS/RNase L pathway by viruses. Curr Opin Virol 15, 19–26. https://doi.org/10.1016/j.coviro.2015.07.002

Drosten, C., Günther, S., Preiser, W., van der Werf, S., Brodt, H.-R., Becker, S., Rabenau, H., Panning, M., Kolesnikova, L., Fouchier, R.A.M., Berger, A., Burguière, A.-M., Cinatl, J., Eickmann, M., Escriou, N., Grywna, K., Kramme, S., Manuguerra, J.-C., Müller, S., Rickerts, V., Stürmer, M., Vieth, S., Klenk, H.-D., Osterhaus, A.D.M.E., Schmitz, H., Doerr, H.W., 2003. Identification of a novel coronavirus in patients with severe acute respiratory syndrome. N Engl J Med 348, 1967–1976. https://doi.org/10.1056/NEJMoa030747

Dugan, J.W., Albor, A., David, L., Fowlkes, J., Blackledge, M.T., Martin, T.M., Planck, S.R., Rosenzweig, H.L., Rosenbaum, J.T., Davey, M.P., 2009. Nucleotide oligomerization domain-2 interacts with 2′-5′-oligoadenylate synthetase type 2 and enhances RNase-L function in THP-1 cells. Molecular Immunology 47, 560–566. https://doi.org/10.1016/j.molimm.2009.09.025

Dyer, S.C., Austine-Orimoloye, O., Azov, A.G., Barba, M., Barnes, I., Barrera-Enriquez, V.P., Becker, A., Bennett, R., Beracochea, M., Berry, A., Bhai, J., Bhurji, S.K., Boddu, S., Branco Lins, P.R., Brooks, L., Ramaraju, S.B., Campbell, L.I., Martinez, M.C., Charkhchi, M., Cortes, L.A., Davidson, C., Denni, S., Dodiya, K., Donaldson, S., El Houdaigui, B., El Naboulsi, T., Falola, O., Fatima, R., Genez, T., Martinez, J.G., Gurbich, T., Hardy, M., Hollis, Z., Hunt, T., Kay, M., Kaykala, V., Lemos, D., Lodha, D., Mathlouthi, N., Merino, G.A., Merritt, R., Mirabueno, L.P., Mushtaq, A., Hossain, S.N., Pérez-Silva, J.G., Perry, M., Piližota, I., Poppleton, D., Prosovetskaia, I., Raj, S., Salam, A.I.A., Saraf, S., Saraiva-Agostinho, N., Sinha, S., Sipos, B., Sitnik, V., Steed, E., Suner, M.-M., Surapaneni, L., Sutinen, K., Tricomi, F.F., Tsang, I., Urbina-Gómez, D., Veidenberg, A., Walsh, T.A., Willhoft, N.L., Allen, J., Alvarez-Jarreta, J., Chakiachvili, M., Cheema, J., da Rocha,

J.B., De Silva, N.H., Giorgetti, S., Haggerty, L., Ilsley, G.R., Keatley, J., Loveland, J.E., Moore, B., Mudge, J.M., Naamati, G., Tate, J., Trevanion, S.J., Winterbottom, A., Flint, B., Frankish, A., Hunt, S.E., Finn, R.D., Freeberg, M.A., Harrison, P.W., Martin, F.J., Yates, A.D., 2025. Ensembl 2025. Nucleic Acids Research 53, D948–D957. https://doi.org/10.1093/nar/gkae1071

Elkhateeb, E., Tag-El-Din-Hassan, H.T., Sasaki, N., Torigoe, D., Morimatsu, M., Agui, T., 2016. The role of mouse 2',5'-oligoadenylate synthetase 1 paralogs. Infect Genet Evol 45, 393–401. https://doi.org/10.1016/j.meegid.2016.09.018

Espert, L., Degols, G., Gongora, C., Blondel, D., Williams, B.R., Silverman, R.H., Mechti, N., 2003. ISG20, a new interferon-induced RNase specific for single-stranded RNA, defines an alternative antiviral pathway against RNA genomic viruses. J Biol Chem 278, 16151–16158. https://doi.org/10.1074/jbc.M209628200

Fang, P., Fang, L., Zhang, H., Xia, S., Xiao, S., 2021. Functions of Coronavirus Accessory Proteins: Overview of the State of the Art. Viruses 13, 1139. https://doi.org/10.3390/v13061139

Feng, J., Wickenhagen, A., Turnbull, M.L., Rezelj, V.V., Kreher, F., Tilston-Lunel, N.L., Slack, G.S., Brennan, B., Koudriakova, E., Shaw, A.E., Rihn, S.J., Rice, C.M., Bieniasz, P.D., Elliott, R.M., Shi, X., Wilson, S.J., 2018. Interferon-Stimulated Gene (ISG)-Expression Screening Reveals the Specific Antibunyaviral Activity of ISG20. J Virol 92, e02140-17. https://doi.org/10.1128/JVI.02140-17

Forero, A., Moore, P.S., Sarkar, S.N., 2013. Role of IRF4 in IFN-stimulated gene induction and maintenance of KSHV latency in primary effusion lymphoma cells. J Immunol 191, 1476–1485. https://doi.org/10.4049/jimmunol.1202514

Froggatt, H.M., Harding, A.T., Chaparian, R.R., Heaton, N.S., 2021. ETV7 limits antiviral gene expression and control of influenza viruses. Sci Signal 14, eabe1194. https://doi.org/10.1126/scisignal.abe1194

Fukuyama, S., Katsura, H., Zhao, D., Ozawa, M., Ando, T., Shoemaker, J.E., Ishikawa, I., Yamada, S., Neumann, G., Watanabe, S., Kitano, H., Kawaoka, Y., 2015. Multi-spectral fluorescent reporter influenza viruses (Color-flu) as powerful tools for in vivo studies. Nat Commun 6, 6600. https://doi.org/10.1038/ncomms7600

Ganser-Pornillos, B.K., Pornillos, O., 2019. Restriction of HIV-1 and other retroviruses by TRIM5. Nat Rev Microbiol 17, 546–556. https://doi.org/10.1038/s41579-019-0225-2

Garcia-Cattaneo, A., Gobert, F.-X., Müller, M., Toscano, F., Flores, M., Lescure, A., Del Nery, E., Benaroch, P., 2012. Cleavage of Toll-like receptor 3 by cathepsins B and H is essential for signaling. Proc Natl Acad Sci U S A 109, 9053–9058. https://doi.org/10.1073/pnas.1115091109

Gaunt, E.R., Hardie, A., Claas, E.C.J., Simmonds, P., Templeton, K.E., 2010. Epidemiology and Clinical Presentations of the Four Human Coronaviruses 229E, HKU1, NL63, and OC43 Detected over 3 Years Using a Novel Multiplex Real-Time PCR Method. Journal of Clinical Microbiology 48, 2940–2947. https://doi.org/10.1128/jcm.00636-10

Ghosh, A., Sarkar, S.N., Guo, W., Bandyopadhyay, S., Sen, G.C., 1997. Enzymatic Activity of 2′–5′-Oligoadenylate Synthetase Is Impaired by Specific Mutations that Affect Oligomerization of the Protein*. Journal of Biological Chemistry 272, 33220–33226. https://doi.org/10.1074/jbc.272.52.33220

Ghosh, A., Sarkar, S.N., Sen, G.C., 2000. Cell growth regulatory and antiviral effects of the P69 isozyme of 2-5 (A) synthetase. Virology 266, 319–328. https://doi.org/10.1006/viro.1999.0085

Ghosh, S., Dellibovi-Ragheb, T.A., Kerviel, A., Pak, E., Qiu, Q., Fisher, M., Takvorian, P.M., Bleck, C., Hsu, V.W., Fehr, A.R., Perlman, S., Achar, S.R., Straus, M.R., Whittaker, G.R., de Haan, C.A.M., Kehrl, J., Altan-Bonnet, G., Altan-Bonnet, N., 2020. β-Coronaviruses Use Lysosomes for Egress Instead of the Biosynthetic Secretory Pathway. Cell 183, 1520-1535.e14. https://doi.org/10.1016/j.cell.2020.10.039

Gokul, A., Arumugam, T., Ramsuran, V., 2023. Genetic Ethnic Differences in Human 2′-5′-Oligoadenylate Synthetase and Disease Associations: A Systematic Review. Genes 14, 527. https://doi.org/10.3390/genes14020527

Goldstein, S.A., Thornbrough, J.M., Zhang, R., Jha, B.K., Li, Y., Elliott, R., Quiroz-Figueroa, K., Chen, A.I., Silverman, R.H., Weiss, S.R., 2017. Lineage A Betacoronavirus NS2 Proteins and the Homologous Torovirus Berne pp1a Carboxy-Terminal Domain Are Phosphodiesterases That Antagonize Activation of RNase L. J Virol 91, e02201-16. https://doi.org/10.1128/JVI.02201-16

Goubau, D., Deddouche, S., Reis e Sousa, C., 2013. Cytosolic Sensing of Viruses. Immunity 38, 855–869. https://doi.org/10.1016/j.immuni.2013.05.007

Grandvaux, N., Servant, M.J., tenOever, B., Sen, G.C., Balachandran, S., Barber, G.N., Lin, R., Hiscott, J., 2002. Transcriptional Profiling of Interferon Regulatory Factor 3 Target Genes: Direct Involvement in the Regulation of Interferon-Stimulated Genes. Journal of Virology 76, 5532–5539. https://doi.org/10.1128/jvi.76.11.5532-5539.2002

GTEx Consortium, 2015. Human genomics. The Genotype-Tissue Expression (GTEx) pilot analysis: multitissue gene regulation in humans. Science 348, 648–660. https://doi.org/10.1126/science.1262110

Haller, O., Arnheiter, H., Gresser, I., Lindenmann, J., 1979. Genetically determined, interferon-dependent resistance to influenza virus in mice. J Exp Med 149, 601–612. https://doi.org/10.1084/jem.149.3.601

Haller, O., Staeheli, P., Schwemmle, M., Kochs, G., 2015. Mx GTPases: dynamin-like antiviral machines of innate immunity. Trends in Microbiology 23, 154–163. https://doi.org/10.1016/j.tim.2014.12.003

Han, J.-Q., Barton, D.J., 2002. Activation and evasion of the antiviral 2′-5′ oligoadenylate synthetase/ribonuclease L pathway by hepatitis C virus mRNA. RNA 8, 512–525. https://doi.org/10.1017/S1355838202020617

Han, J.-Q., Townsend, H.L., Jha, B.K., Paranjape, J.M., Silverman, R.H., Barton, D.J., 2007. A phylogenetically conserved RNA structure in the poliovirus open reading frame inhibits the antiviral endoribonuclease RNase L. Journal of Virology 81, 5561–5572. https://doi.org/10.1128/JVI.01857-06

Hanners, N.W., Mar, K.B., Boys, I.N., Eitson, J.L., De La Cruz-Rivera, P.C., Richardson, R.B., Fan, W., Wight-Carter, M., Schoggins, J.W., 2021. Shiftless inhibits flavivirus replication in vitro and is neuroprotective in a mouse model of Zika virus pathogenesis. Proc Natl Acad Sci U S A 118, e2111266118. https://doi.org/10.1073/pnas.2111266118

Hardy, A., Bakshi, S., Furnon, W., MacLean, O., Gu, Q., Varjak, M., Varela, M., Aziz, M.A., Shaw, A.E., Pinto, R.M., Cameron Ruiz, N., Mullan, C., Taggart, A.E., Da Silva Filipe, A., Randall, R.E., Wilson, S.J., Stewart, M.E., Palmarini, M., 2023. The Timing and Magnitude of the Type I Interferon Response Are Correlated with Disease Tolerance in Arbovirus Infection. mBio 14, e00101-23. https://doi.org/10.1128/mbio.00101-23

Harioudh, M.K., Perez, J., Chong, Z., Nair, S., So, L., McCormick, K.D., Ghosh, A., Shao, L., Srivastava, R., Soveg, F., Ebert, T.S., Atianand, M.K., Hornung, V., Savan, R., Diamond, M.S., Sarkar, S.N., 2024. Oligoadenylate synthetase 1 displays dual antiviral mechanisms in driving translational shutdown and protecting interferon production. Immunity 57, 446-461.e7. https://doi.org/10.1016/j.immuni.2024.02.002

Harrison, C.M., Doster, J.M., Landwehr, E.H., Kumar, N.P., White, E.J., Beachboard, D.C., Stobart, C.C., 2023. Evaluating the Virology and Evolution of Seasonal Human Coronaviruses Associated with the Common Cold in the COVID-19 Era. Microorganisms 11, 445. https://doi.org/10.3390/microorganisms11020445

Hartmann, R., Justesen, J., Sarkar, S.N., Sen, G.C., Yee, V.C., 2003. Crystal Structure of the 2′-Specific and Double-Stranded RNA-Activated Interferon-Induced Antiviral Protein 2′-5′-Oligoadenylate Synthetase. Molecular Cell 12, 1173–1185. https://doi.org/10.1016/S1097-2765(03)00433-7

Hayn, M., Hirschenberger, M., Koepke, L., Nchioua, R., Straub, J.H., Klute, S., Hunszinger, V., Zech, F., Bozzo, C.P., Aftab, W., Christensen, M.H., Conzelmann, C., Müller, J.A., Badarinarayan, S.S., Stürzel, C.M., Forne, I., Stenger, S., Conzelmann, K.-K., Münch, J., Schmidt, F.I., Sauter, D., Imhof, A., Kirchhoff, F., Sparrer, K.M.J., 2021. Systematic functional analysis of SARS-CoV-2 proteins uncovers viral innate immune antagonists and remaining vulnerabilities. Cell Reports 35. https://doi.org/10.1016/j.celrep.2021.109126

Hill, V., Du Plessis, L., Peacock, T.P., Aggarwal, D., Colquhoun, R., Carabelli, A.M., Ellaby, N., Gallagher, E., Groves, N., Jackson, B., McCrone, J.T., O'Toole, Á., Price, A., Sanderson, T., Scher, E., Southgate, J., Volz, E., Barclay, W.S., Barrett, J.C., Chand, M., Connor, T., Goodfellow, I., Gupta,

R.K., Harrison, E.M., Loman, N., Myers, R., Robertson, D.L., Pybus, O.G., Rambaut, A., The COVID-19 Genomics UK (COG-UK) Consortium, 2022. The origins and molecular evolution of SARS-CoV-2 lineage B.1.1.7 in the UK. Virus Evolution 8, veac080. https://doi.org/10.1093/ve/veac080

Hilton, L., Moganeradj, K., Zhang, G., Chen, Y.-H., Randall, R.E., McCauley, J.W., Goodbourn, S., 2006. The NPro Product of Bovine Viral Diarrhea Virus Inhibits DNA Binding by Interferon Regulatory Factor 3 and Targets It for Proteasomal Degradation. J Virol 80, 11723–11732. https://doi.org/10.1128/JVI.01145-06

Houldcroft, C.J., Jackson, S.E., Lim, E.Y., Sedikides, G.X., Davies, E.L., Atkinson, C., McIntosh, M., Remmerswaal, E.B.M., Okecha, G., Bemelman, F.J., Stanton, R.J., Reeves, M., Wills, M.R., 2020. Assessing Anti-HCMV Cell Mediated Immune Responses in Transplant Recipients and Healthy Controls Using a Novel Functional Assay. Front. Cell. Infect. Microbiol. 10. https://doi.org/10.3389/fcimb.2020.00275

Hu, J., Wang, X., Xing, Y., Rong, E., Ning, M., Smith, J., Huang, Y., 2018. Origin and development of oligoadenylate synthetase immune system. BMC Evolutionary Biology 18, 201. https://doi.org/10.1186/s12862-018-1315-x

Hulswit, R.J.G., Lang, Y., Bakkers, M.J.G., Li, W., Li, Z., Schouten, A., Ophorst, B., van Kuppeveld, F.J.M., Boons, G.-J., Bosch, B.-J., Huizinga, E.G., de Groot, R.J., 2019. Human coronaviruses OC43 and HKU1 bind to 9-O-acetylated sialic acids via a conserved receptor-binding site in spike protein domain A. Proceedings of the National Academy of Sciences 116, 2681–2690. https://doi.org/10.1073/pnas.1809667116

Hur, S., 2019. Double-Stranded RNA Sensors and Modulators in Innate Immunity. Annual Review of Immunology 37, 349–375. https://doi.org/10.1146/annurev-immunol-042718-041356

Ibsen, M.S., Gad, H.H., Thavachelvam, K., Boesen, T., Desprès, P., Hartmann, R., 2014. The 2′-5′-Oligoadenylate Synthetase 3 Enzyme Potently Synthesizes the 2′-5′-Oligoadenylates Required for RNase L Activation. Journal of Virology 88, 14222–14231. https://doi.org/10.1128/jvi.01763-14

Isaacs, A., Lindenmann, J., 1987. Virus interference. I. The interferon. Journal of Interferon Research 7, 429–438. https://doi.org/10.1089/jir.1987.7.429

Ivashkiv, L.B., Donlin, L.T., 2014. Regulation of type I interferon responses. Nat Rev Immunol 14, 36–49. https://doi.org/10.1038/nri3581

Jackson, C.B., Farzan, M., Chen, B., Choe, H., 2022. Mechanisms of SARS-CoV-2 entry into cells. Nat Rev Mol Cell Biol 23, 3–20. https://doi.org/10.1038/s41580-021-00418-x

Jetten, A.M., 2009. Retinoid-related orphan receptors (RORs): critical roles in development, immunity, circadian rhythm, and cellular metabolism. Nucl Recept Signal 7, e003. https://doi.org/10.1621/nrs.07003

Johnson, B., VanBlargan, L.A., Xu, W., White, J.P., Shan, C., Shi, P.-Y., Zhang, R., Adhikari, J., Gross, M.L., Leung, Daisy.W., Diamond, M.S., Amarasinghe, G.K., 2018. Binding of IFIT1 by IFIT3 modulates protein stability and RNA

binding specificity. Immunity 48, 487-499.e5. https://doi.org/10.1016/j.immuni.2018.01.014

Jones, C.E., Tan, W.S., Grey, F., Hughes, D.J., 2021. Discovering antiviral restriction factors and pathways using genetic screens. Journal of General Virology 102, 001603. https://doi.org/10.1099/jgv.0.001603

Justesen, J., Hartmann, R., Kjeldgaard, N.O., 2000. Gene structure and function of the 2′-5′-oligoadenylate synthetase family. CMLS, Cell. Mol. Life Sci. 57, 1593–1612. https://doi.org/10.1007/PL00000644

Kakuta, S., Shibata, S., Iwakura, Y., 2002. Genomic Structure of the Mouse 2',5'-Oligoadenylate Synthetase Gene Family. Journal of Interferon & Cytokine Research 22, 981–993. https://doi.org/10.1089/10799900260286696

Kane, M., Zang, T.M., Rihn, S.J., Zhang, F., Kueck, T., Alim, M., Schoggins, J., Rice, C.M., Wilson, S.J., Bieniasz, P.D., 2016. Identification of Interferon-Stimulated Genes with Antiretroviral Activity. Cell Host Microbe 20, 392–405. https://doi.org/10.1016/j.chom.2016.08.005

Katiyar, H., Arduini, A., Li, Y., Liang, C., 2024. SARS-CoV-2 Assembly: Gaining Infectivity and Beyond. Viruses 16, 1648. https://doi.org/10.3390/v16111648

Kawai, T., Ikegawa, M., Ori, D., Akira, S., 2024. Decoding Toll-like receptors: Recent insights and perspectives in innate immunity. Immunity 57, 649–673. https://doi.org/10.1016/j.immuni.2024.03.004

Khan, H., Winstone, H., Jimenez-Guardeño, J.M., Graham, C., Doores, K.J., Goujon, C., Matthews, D.A., Davidson, A.D., Rihn, S.J., Palmarini, M., Neil, S.J.D., Malim, M.H., 2021. TMPRSS2 promotes SARS-CoV-2 evasion from NCOA7-mediated restriction. PLoS Pathog 17, e1009820. https://doi.org/10.1371/journal.ppat.1009820

Kim, J.H., Bryant, H., Fiedler, E., Cao, T., Rayner, J.O., 2022. Real-time tracking of bioluminescent influenza A virus infection in mice. Sci Rep 12, 3152. https://doi.org/10.1038/s41598-022-06667-w

Kmiec, D., Lista, M.J., Ficarelli, M., Swanson, C.M., Neil, S.J.D., 2021. S-farnesylation is essential for antiviral activity of the long ZAP isoform against RNA viruses with diverse replication strategies. PLOS Pathogens 17, e1009726. https://doi.org/10.1371/journal.ppat.1009726

Knoops, K., Kikkert, M., Worm, S.H.E. van den, Zevenhoven-Dobbe, J.C., van der Meer, Y., Koster, A.J., Mommaas, A.M., Snijder, E.J., 2008. SARS-coronavirus replication is supported by a reticulovesicular network of modified endoplasmic reticulum. PLoS Biol 6, e226. https://doi.org/10.1371/journal.pbio.0060226

Kodaka, M., Xu, X., Yang, Z., Maruyama, J., Hata, Y., 2017. Application of Split-GFP Reassembly Assay to Study Myogenesis and Myofusion In Vitro, in: Ryall, J.G. (Ed.), Skeletal Muscle Development. Springer, New York, NY, pp. 127–134. https://doi.org/10.1007/978-1-4939-7283-8_9

Kondratova, A.A., Cheon, H., Dong, B., Holvey-Bates, E.G., Hasipek, M., Taran, I., Gaughan, C., Jha, B.K., Silverman, R.H., Stark, G.R., 2020. Suppressing PARylation by 2′,5′-oligoadenylate synthetase 1 inhibits DNA damage-induced cell death. The EMBO Journal 39, e101573. https://doi.org/10.15252/embj.2019101573

Koul, A., Deo, S., Booy, E.P., Orriss, G.L., Genung, M., McKenna, S.A., 2020a. Impact of double-stranded RNA characteristics on the activation of human 2′–5′-oligoadenylate synthetase 2 (OAS2). Biochem. Cell Biol. 98, 70–82. https://doi.org/10.1139/bcb-2019-0060

Koul, A., Gemmill, D., Lubna, N., Meier, M., Krahn, N., Booy, E.P., Stetefeld, J., Patel, T.R., McKenna, S.A., 2020b. Structural and Hydrodynamic Characterization of Dimeric Human Oligoadenylate Synthetase 2. Biophysical Journal 118, 2726–2740. https://doi.org/10.1016/j.bpj.2020.04.025

Koul, A., Hui, L.T., Lubna, N., McKenna, S.A., 2024. Distinct domain organization and diversity of 2′-5′-oligoadenylate synthetases. Biochem. Cell Biol. 102, 305–318. https://doi.org/10.1139/bcb-2023-0369

Kristiansen, H., Gad, H.H., Eskildsen-Larsen, S., Despres, P., Hartmann, R., 2011. The Oligoadenylate Synthetase Family: An Ancient Protein Family with Multiple Antiviral Activities. Journal of Interferon & Cytokine Research 31, 41–47. https://doi.org/10.1089/jir.2010.0107

Kueck, T., Bloyet, L.-M., Cassella, E., Zang, T., Schmidt, F., Brusic, V., Tekes, G., Pornillos, O., Whelan, S.P.J., Bieniasz, P.D., 2019. Vesicular Stomatitis Virus Transcription Is Inhibited by TRIM69 in the Interferon-Induced Antiviral State. Journal of Virology 93, 10.1128/jvi.01372-19. https://doi.org/10.1128/jvi.01372-19

Kurhade, C., Xie, X., Shi, P.-Y., 2023. Reverse genetic systems of SARS-CoV-2 for antiviral research. Antiviral Res 210, 105486. https://doi.org/10.1016/j.antiviral.2022.105486

Kuroda, M., Halfmann, P.J., Hill-Batorski, L., Ozawa, M., Lopes, T.J.S., Neumann, G., Schoggins, J.W., Rice, C.M., Kawaoka, Y., 2020. Identification of interferon-stimulated genes that attenuate Ebola virus infection. Nat Commun 11, 2953. https://doi.org/10.1038/s41467-020-16768-7

Kwon, Y.-C., Kang, J.I., Hwang, S.B., Ahn, B.-Y., 2013. The ribonuclease L-dependent antiviral roles of human 2',5'-oligoadenylate synthetase family members against hepatitis C virus. FEBS Lett 587, 156–164. https://doi.org/10.1016/j.febslet.2012.11.010

Lazear, H.M., Schoggins, J.W., Diamond, M.S., 2019. Shared and Distinct Functions of Type I and Type III Interferons. Immunity 50, 907–923. https://doi.org/10.1016/j.immuni.2019.03.025

Le Pen, J., Paniccia, G., Kinast, V., Moncada-Velez, M., Ashbrook, A.W., Bauer, M., Hoffmann, H.-H., Pinharanda, A., Ricardo-Lax, I., Stenzel, A.F., Rosado-Olivieri, E.A., Dinnon, K.H., Doyle, W.C., Freije, C.A., Hong, S.-H., Lee, D., Lewy, T., Luna, J.M., Peace, A., Schmidt, C., Schneider, W.M.,

Winkler, R., Yip, E.Z., Larson, C., McGinn, T., Menezes, M.-R., Ramos-Espiritu, L., Banerjee, P., Poirier, J.T., Sànchez-Rivera, F.J., Cobat, A., Zhang, Q., Casanova, J.-L., Carroll, T.S., Glickman, J.F., Michailidis, E., Razooky, B., MacDonald, M.R., Rice, C.M., 2024. A genome-wide arrayed CRISPR screen identifies PLSCR1 as an intrinsic barrier to SARS-CoV-2 entry that recent virus variants have evolved to resist. PLoS Biol 22, e3002767. https://doi.org/10.1371/journal.pbio.3002767

Le Pen, J., Rice, C.M., 2024. The antiviral state of the cell: lessons from SARS-CoV-2. Current Opinion in Immunology 87, 102426. https://doi.org/10.1016/j.coi.2024.102426

Lee, D., Pen, J.L., Yatim, A., Dong, B., Aquino, Y., Ogishi, M., Pescarmona, R., Talouarn, E., Rinchai, D., Zhang, P., Perret, M., Liu, Z., Jordan, I., Bozdemir, S.E., Bayhan, G.I., Beaufils, C., Bizien, L., Bisiaux, A., Lei, W., Hasan, M., Chen, J., Gaughan, C., Asthana, A., Libri, V., Luna, J.M., Jaffré, F., Hoffmann, H.-H., Michailidis, E., Moreews, M., Seeleuthner, Y., Bilguvar, K., Mane, S., Flores, C., Zhang, Y., Arias, A.A., Bailey, R., Schlüter, A., Milisavljevic, B., Bigio, B., Voyer, T.L., Materna, M., Gervais, A., Moncada-Velez, M., Pala, F., Lazarov, T., Levy, R., Neehus, A.-L., Rosain, J., Peel, J., Chan, Y.-H., Morin, M.-P., Pino-Ramirez, R.M., Belkaya, S., Lorenzo, L., Anton, J., Delafontaine, S., Toubiana, J., Bajolle, F., Fumadó, V., DeDiego, M.L., Fidouh, N., Rozenberg, F., Pérez-Tur, J., Chen, S., Evans, T., Geissmann, F., Lebon, P., Weiss, S.R., Bonnet, D., Duval, X., Cohort, C.-C., Effort, C.H.G., Pan-Hammarström, Q., Planas, A.M., Meyts, I., Haerynck, F., Pujol, A., Sancho-Shimizu, V., Dalgard, C.L., Bustamante, J., Puel, A., Boisson-Dupuis, S., Boisson, B., Maniatis, T., Zhang, Q., Bastard, P., Notarangelo, L., Béziat, V., Diego, R.P. de, Rodriguez-Gallego, C., Su, H.C., Lifton, R.P., Jouanguy, E., Cobat, A., Alsina, L., Keles, S., Haddad, E., Abel, L., Belot, A., Quintana-Murci, L., 2023. Inborn errors of OAS–RNase L in SARS-CoV-2–related multisystem inflammatory syndrome in children. Science (New York, N.y.) 379, eabo3627. https://doi.org/10.1126/science.abo3627

Li, M.M.H., Aguilar, E.G., Michailidis, E., Pabon, J., Park, P., Wu, X., de Jong, Y.P., Schneider, W.M., Molina, H., Rice, C.M., MacDonald, M.R., 2019. Characterization of Novel Splice Variants of Zinc Finger Antiviral Protein (ZAP). Journal of Virology 93, 10.1128/jvi.00715-19. https://doi.org/10.1128/jvi.00715-19

Li, Yize, Banerjee, S., Wang, Y., Goldstein, S.A., Dong, B., Gaughan, C., Silverman, R.H., Weiss, S.R., 2016. Activation of RNase L is dependent on OAS3 expression during infection with diverse human viruses. Proceedings of the National Academy of Sciences 113, 2241–2246. https://doi.org/10.1073/pnas.1519657113

Li, Yongfeng, Li, L.-F., Yu, S., Wang, X., Zhang, L., Yu, J., Xie, L., Li, W., Ali, R., Qiu, H.-J., 2016. Applications of Replicating-Competent Reporter-Expressing Viruses in Diagnostic and Molecular Virology. Viruses 8, 127. https://doi.org/10.3390/v8050127

Liao, K.-C., Garcia-Blanco, M.A., 2021. Role of Alternative Splicing in Regulating Host Response to Viral Infection. Cells 10, 1720. https://doi.org/10.3390/cells10071720

Liao, X., Xie, H., Li, Shilin, Ye, H., Li, Shuang, Ren, K., Li, Y., Xu, M., Lin, W., Duan, X., Yang, C., Chen, L., 2020. 2′, 5′-Oligoadenylate Synthetase 2 (OAS2) Inhibits Zika Virus Replication through Activation of Type I IFN Signaling Pathway. Viruses 12, 418. https://doi.org/10.3390/v12040418

Lim, J.K., Lisco, A., McDermott, D.H., Huynh, L., Ward, J.M., Johnson, B., Johnson, H., Pape, J., Foster, G.A., Krysztof, D., Follmann, D., Stramer, S.L., Margolis, L.B., Murphy, P.M., 2009. Genetic Variation in OAS1 Is a Risk Factor for Initial Infection with West Nile Virus in Man. PLOS Pathogens 5, e1000321. https://doi.org/10.1371/journal.ppat.1000321

Lin, R.-J., Yu, H.-P., Chang, B.-L., Tang, W.-C., Liao, C.-L., Lin, Y.-L., 2009. Distinct Antiviral Roles for Human 2′,5′-Oligoadenylate Synthetase Family Members against Dengue Virus Infection. The Journal of Immunology 183, 8035–8043. https://doi.org/10.4049/jimmunol.0902728

Lin, Y.-T., Chiweshe, S., McCormick, D., Raper, A., Wickenhagen, A., DeFillipis, V., Gaunt, E., Simmonds, P., Wilson, S.J., Grey, F., 2020. Human cytomegalovirus evades ZAP detection by suppressing CpG dinucleotides in the major immediate early 1 gene. PLoS Pathog 16, e1008844. https://doi.org/10.1371/journal.ppat.1008844

Liu, B., Li, N.L., Wang, J., Shi, P.-Y., Wang, T., Miller, M.A., Li, K., 2014. Overlapping and distinct molecular determinants dictating the antiviral activities of TRIM56 against flaviviruses and coronavirus. J Virol 88, 13821–13835. https://doi.org/10.1128/JVI.02505-14

Liu, D.X., Liang, J.Q., Fung, T.S., 2021. Human Coronavirus-229E, -OC43, -NL63, and -HKU1 (Coronaviridae), in: Encyclopedia of Virology (Fourth Edition). Academic Press, Oxford, pp. 428–440. https://doi.org/10.1016/B978-0-12-809633-8.21501-X

Liu, G., Lee, J.-H., Parker, Z.M., Acharya, D., Chiang, J.J., van Gent, M., Riedl, W., Davis-Gardner, M.E., Wies, E., Chiang, C., Gack, M.U., 2021. ISG15-dependent activation of the sensor MDA5 is antagonized by the SARS-CoV-2 papain-like protease to evade host innate immunity. Nat Microbiol 6, 467–478. https://doi.org/10.1038/s41564-021-00884-1

Liu, Z., Chen, O., Wall, J.B.J., Zheng, M., Zhou, Y., Wang, L., Ruth Vaseghi, H., Qian, L., Liu, J., 2017. Systematic comparison of 2A peptides for cloning multi-genes in a polycistronic vector. Sci Rep 7, 2193. https://doi.org/10.1038/s41598-017-02460-2

Lopez-Cruzan, M., Sharma, R., Tiwari, M., Karbach, S., Holstein, D., Martin, C.R., Lechleiter, J.D., Herman, B., 2016. Caspase-2 resides in the mitochondria and mediates apoptosis directly from the mitochondrial compartment. Cell Death Discovery 2, 1–9. https://doi.org/10.1038/cddiscovery.2016.5

Mac Kain, A., Maarifi, G., Aicher, S.-M., Arhel, N., Baidaliuk, A., Munier, S., Donati, F., Vallet, T., Tran, Q.D., Hardy, A., Chazal, M., Porrot, F.,

OhAinle, M., Carlson-Stevermer, J., Oki, J., Holden, K., Zimmer, G., Simon-Lorière, E., Bruel, T., Schwartz, O., van der Werf, S., Jouvenet, N., Nisole, S., Vignuzzi, M., Roesch, F., 2022. Identification of DAXX as a restriction factor of SARS-CoV-2 through a CRISPR/Cas9 screen. Nat Commun 13, 2442. https://doi.org/10.1038/s41467-022-30134-9

Majdoul, S., Compton, A.A., 2022. Lessons in self-defence: inhibition of virus entry by intrinsic immunity. Nat Rev Immunol 22, 339–352. https://doi.org/10.1038/s41577-021-00626-8

Malaguarnera, L., Nunnari, G., Di Rosa, M., 2016. Nuclear import sequence identification in hOAS3 protein. Inflamm. Res. 65, 895–904. https://doi.org/10.1007/s00011-016-0972-8

Malathi, K., Dong, B., Gale, M., Silverman, R.H., 2007. Small self-RNA generated by RNase L amplifies antiviral innate immunity. Nature 448, 816–819. https://doi.org/10.1038/nature06042

Marié, I., Blanco, J., Rebouillat, D., Hovanessian, A.G., 1997. 69-kDa and 100-kDa Isoforms of Interferon-Induced (2′-5′)Oligoadenylate Synthetase Exhibit Differential Catalytic Parameters. European Journal of Biochemistry 248, 558–566. https://doi.org/10.1111/j.1432-1033.1997.t01-1-00558.x

Marié, I., Hovanessian, A.G., 1992. The 69-kDa 2-5A synthetase is composed of two homologous and adjacent functional domains. J Biol Chem 267, 9933–9939.

Marié, I., Rebouillat, D., Hovanessian, A.G., 1999. The expression of both domains of the 69/71 kDa 2′,5′ oligoadenylate synthetase generates a catalytically active enzyme and mediates an anti-viral response. European Journal of Biochemistry 262, 155–165. https://doi.org/10.1046/j.1432-1327.1999.00361.x

Marié, I., Svab, J., Robert, N., Galabru, J., Hovanessian, A.G., 1990. Differential expression and distinct structure of 69- and 100-kDa forms of 2-5A synthetase in human cells treated with interferon. Journal of Biological Chemistry 265, 18601–18607. https://doi.org/10.1016/S0021-9258(17)44794-6

Martinand, C., Salehzada, T., Silhol, M., Lebleu, B., Bisbal, C., 1998. RNase L inhibitor (RLI) antisense constructions block partially the down regulation of the 2-5A/RNase L pathway in encephalomyocarditis-virus-(EMCV)-infected cells. European Journal of Biochemistry 254, 248–255. https://doi.org/10.1046/j.1432-1327.1998.2540248.x

McDougal, M.B., De Maria, A.M., Ohlson, M.B., Kumar, A., Xing, C., Schoggins, J.W., 2023. Interferon inhibits a model RNA virus via a limited set of inducible effector genes. EMBO reports 24, e56901. https://doi.org/10.15252/embr.202356901

McManus, S., Ebert, A., Salvagiotto, G., Medvedovic, J., Sun, Q., Tamir, I., Jaritz, M., Tagoh, H., Busslinger, M., 2011. The transcription factor Pax5 regulates its target genes by recruiting chromatin-modifying proteins in committed B cells. EMBO J 30, 2388–2404. https://doi.org/10.1038/emboj.2011.140

McNab, F., Mayer-Barber, K., Sher, A., Wack, A., O'Garra, A., 2015. Type I interferons in infectious disease. Nat Rev Immunol 15, 87–103. https://doi.org/10.1038/nri3787

Merold, V., Bekere, I., Kretschmer, S., Schnell, A.F., Kmiec, D., Sivarajan, R., Lammens, K., Liu, R., Mergner, J., Teppert, J., Hirschenberger, M., Hammes, S., Buder, K., Weitz, M., Koenig, L.M., Pichlmair, A., Schwierz, N., Sparrer, K.M.J., Lee-Kirsch, M.A., Mann, C.C. de O., 2025. Structural Basis for OAS2 Regulation and its Antiviral Function. https://doi.org/10.1101/2025.01.28.635220

Minakshi, R., Padhan, K., Rani, M., Khan, N., Ahmad, F., Jameel, S., 2009. The SARS Coronavirus 3a Protein Causes Endoplasmic Reticulum Stress and Induces Ligand-Independent Downregulation of the Type 1 Interferon Receptor. PLOS ONE 4, e8342. https://doi.org/10.1371/journal.pone.0008342

Miorin, L., Kehrer, T., Sanchez-Aparicio, M.T., Zhang, K., Cohen, P., Patel, R.S., Cupic, A., Makio, T., Mei, M., Moreno, E., Danziger, O., White, K.M., Rathnasinghe, R., Uccellini, M., Gao, S., Aydillo, T., Mena, I., Yin, X., Martin-Sancho, L., Krogan, N.J., Chanda, S.K., Schotsaert, M., Wozniak, R.W., Ren, Y., Rosenberg, B.R., Fontoura, B.M.A., García-Sastre, A., 2020. SARS-CoV-2 Orf6 hijacks Nup98 to block STAT nuclear import and antagonize interferon signaling. Proceedings of the National Academy of Sciences 117, 28344–28354. https://doi.org/10.1073/pnas.2016650117

Mistry, B., Long, J.S., Schreyer, J., Staller, E., Sanchez-David, R.Y., Barclay, W.S., 2020. Elucidating the Interactions between Influenza Virus Polymerase and Host Factor ANP32A. Journal of Virology 94, 10.1128/jvi.01353-19. https://doi.org/10.1128/jvi.01353-19

Müller, M.A., Corman, V.M., Jores, J., Meyer, B., Younan, M., Liljander, A.M., Bosch, B.-J., Lattwein, E., Hilali, M., Musa, B.E., Bornstein, S., Park, S.S., 2014. MERS Coronavirus Neutralizing Antibodies in Camels, Eastern Africa, 1983–1997. Emerging Infectious Diseases 20. https://doi.org/10.3201/eid2012.141026

Neil, S.J.D., Zang, T., Bieniasz, P.D., 2008. Tetherin inhibits retrovirus release and is antagonized by HIV-1 Vpu. Nature 451, 425–430. https://doi.org/10.1038/nature06553

Oakes, S.R., Gallego-Ortega, D., Stanford, P.M., Junankar, S., Au, W.W.Y., Kikhtyak, Z., Korff, A. von, Sergio, C.M., Law, A.M.K., Castillo, L.E., Allerdice, S.L., Young, A.I.J., Piggin, C., Whittle, B., Bertram, E., Naylor, M.J., Roden, D.L., Donovan, J., Korennykh, A., Goodnow, C.C., O'Bryan, M.K., Ormandy, C.J., 2017. A mutation in the viral sensor 2'-5'-oligoadenylate synthetase 2 causes failure of lactation. PLOS Genetics 13, e1007072. https://doi.org/10.1371/journal.pgen.1007072

Owczarek, K., Szczepanski, A., Milewska, A., Baster, Z., Rajfur, Z., Sarna, M., Pyrc, K., 2018. Early events during human coronavirus OC43 entry to the cell. Sci Rep 8, 7124. https://doi.org/10.1038/s41598-018-25640-0

Panne, D., Maniatis, T., Harrison, S.C., 2007. An Atomic Model of the Interferon-β Enhanceosome. Cell 129, 1111–1123. https://doi.org/10.1016/j.cell.2007.05.019

Park, A., Iwasaki, A., 2020. Type I and Type III Interferons - Induction, Signaling, Evasion, and Application to Combat COVID-19. Cell host & microbe 27. https://doi.org/10.1016/j.chom.2020.05.008

Patterson, J.B., Samuel, C.E., 1995. Expression and regulation by interferon of a double-stranded-RNA-specific adenosine deaminase from human cells: evidence for two forms of the deaminase. Mol Cell Biol 15, 5376–5388.

Perelygin, A.A., Scherbik, S.V., Zhulin, I.B., Stockman, B.M., Li, Y., Brinton, M.A., 2002. Positional Cloning of the Murine Flavivirus Resistance Gene. Proceedings of the National Academy of Sciences of the United States of America 99, 9322–9327.

Perez-Favila, A., Sanchez-Macias, S., De Lara, S.A.O., Garza-Veloz, I., Araujo-Espino, R., Castañeda-Lopez, M.E., Mauricio-Gonzalez, A., Vazquez-Reyes, S., Velasco-Elizondo, P., Trejo-Ortiz, P.M., Montaño, F.E.M., Castruita-De la Rosa, C., Martinez-Fierro, M.L., 2024. Gene Variants of the OAS/RNase L Pathway and Their Association with Severity of Symptoms and Outcome of SARS-CoV-2 Infection. J Pers Med 14, 426. https://doi.org/10.3390/jpm14040426

Pfaender, S., Mar, K.B., Michailidis, E., Kratzel, A., Boys, I.N., V'kovski, P., Fan, W., Kelly, J.N., Hirt, D., Ebert, N., Stalder, H., Kleine-Weber, H., Hoffmann, M., Hoffmann, H.-H., Saeed, M., Dijkman, R., Steinmann, E., Wight-Carter, M., McDougal, M.B., Hanners, N.W., Pöhlmann, S., Gallagher, T., Todt, D., Zimmer, G., Rice, C.M., Schoggins, J.W., Thiel, V., 2020. LY6E impairs coronavirus fusion and confers immune control of viral disease. Nat Microbiol 5, 1330–1339. https://doi.org/10.1038/s41564-020-0769-y

Pinto, R.M., Bakshi, S., Lytras, S., Zakaria, M.K., Swingler, S., Worrell, J.C., Herder, V., Hargrave, K.E., Varjak, M., Cameron-Ruiz, N., Collados Rodriguez, M., Varela, M., Wickenhagen, A., Loney, C., Pei, Y., Hughes, J., Valette, E., Turnbull, M.L., Furnon, W., Gu, Q., Orr, L., Taggart, A., Diebold, O., Davis, C., Boutell, C., Grey, F., Hutchinson, E., Digard, P., Monne, I., Wootton, S.K., MacLeod, M.K.L., Wilson, S.J., Palmarini, M., 2023. BTN3A3 evasion promotes the zoonotic potential of influenza A viruses. Nature 619, 338–347. https://doi.org/10.1038/s41586-023-06261-8

Poston, D., Weisblum, Y., Hobbs, A., Bieniasz, P.D., 2022. VPS29 Exerts Opposing Effects on Endocytic Viral Entry. mBio 13, e0300221. https://doi.org/10.1128/mbio.03002-21

Quintás-Cardama, A., Vaddi, K., Liu, P., Manshouri, T., Li, J., Scherle, P.A., Caulder, E., Wen, X., Li, Y., Waeltz, P., Rupar, M., Burn, T., Lo, Y., Kelley, J., Covington, M., Shepard, S., Rodgers, J.D., Haley, P., Kantarjian, H., Fridman, J.S., Verstovsek, S., 2010. Preclinical characterization of the selective JAK1/2 inhibitor INCB018424: therapeutic implications for the

treatment of myeloproliferative neoplasms. Blood 115, 3109–3117. https://doi.org/10.1182/blood-2009-04-214957

Rabaan, A.A., Alenazy, M.F., Alshehri, A.A., Alshahrani, M.A., Al-Subaie, M.F., Alrasheed, H.A., Al Kaabi, N.A., Thakur, N., Bouafia, N.A., Alissa, M., Alsulaiman, A.M., AlBaadani, A.M., Alhani, H.M., Alhaddad, A.H., Alfouzan, W.A., Ali, B.M.A., Al-Abdulali, K.H., Khamis, F., Bayahya, A., Al Fares, M.A., Sharma, M., Dhawan, M., 2023. An updated review on pathogenic coronaviruses (CoVs) amid the emergence of SARS-CoV-2 variants: A look into the repercussions and possible solutions. Journal of Infection and Public Health 16, 1870–1883. https://doi.org/10.1016/j.jiph.2023.09.004

Randall, R.E., Goodbourn, S., 2008. Interferons and viruses: an interplay between induction, signalling, antiviral responses and virus countermeasures. Journal of General Virology 89, 1–47. https://doi.org/10.1099/vir.0.83391-0

Rasighaemi, P., Ward, A.C., 2017. ETV6 and ETV7: Siblings in hematopoiesis and its disruption in disease. Critical Reviews in Oncology/Hematology 116, 106–115. https://doi.org/10.1016/j.critrevonc.2017.05.011

Reineke, L.C., Lloyd, R.E., 2015. The stress granule protein G3BP1 recruits protein kinase R to promote multiple innate immune antiviral responses. J Virol 89, 2575–2589. https://doi.org/10.1128/JVI.02791-14

Richardson, R.B., Ohlson, M.B., Eitson, J.L., Kumar, A., McDougal, M.B., Boys, I.N., Mar, K.B., De La Cruz-Rivera, P.C., Douglas, C., Konopka, G., Xing, C., Schoggins, J.W., 2018. A CRISPR screen identifies IFI6 as an ER-resident interferon effector that blocks flavivirus replication. Nat Microbiol 3, 1214–1223. https://doi.org/10.1038/s41564-018-0244-1

Rihn, S.J., Aziz, M.A., Stewart, D.G., Hughes, J., Turnbull, M.L., Varela, M., Sugrue, E., Herd, C.S., Stanifer, M., Sinkins, S.P., Palmarini, M., Wilson, S.J., 2019. TRIM69 Inhibits Vesicular Stomatitis Indiana Virus. J Virol 93, e00951-19. https://doi.org/10.1128/JVI.00951-19

Rihn, S.J., Merits, A., Bakshi, S., Turnbull, M.L., Wickenhagen, A., Alexander, A.J.T., Baillie, C., Brennan, B., Brown, F., Brunker, K., Bryden, S.R., Burness, K.A., Carmichael, S., Cole, S.J., Cowton, V.M., Davies, P., Davis, C., Lorenzo, G.D., Donald, C.L., Dorward, M., Dunlop, J.I., Elliott, M., Fares, M., Filipe, A. da S., Freitas, J.R., Furnon, W., Gestuveo, R.J., Geyer, A., Giesel, D., Goldfarb, D.M., Goodman, N., Gunson, R., Hastie, C.J., Herder, V., Hughes, J., Johnson, C., Johnson, N., Kohl, A., Kerr, K., Leech, H., Lello, L.S., Li, K., Lieber, G., Liu, X., Lingala, R., Loney, C., Mair, D., McElwee, M.J., McFarlane, S., Nichols, J., Nomikou, K., Orr, A., Orton, R.J., Palmarini, M., Parr, Y.A., Pinto, R.M., Raggett, S., Reid, E., Robertson, D.L., Royle, J., Cameron-Ruiz, N., Shepherd, J.G., Smollett, K., Stewart, D.G., Stewart, M., Sugrue, E., Szemiel, A.M., Taggart, A., Thomson, E.C., Tong, L., Torrie, L.S., Toth, R., Varjak, M., Wang, S., Wilkinson, S.G., Wyatt, P.G., Zusinaite, E., Alessi, D.R., Patel, A.H., Zaid, A., Wilson, S.J., Mahalingam, S., 2021. A plasmid DNA-launched SARS-CoV-

2 reverse genetics system and coronavirus toolkit for COVID-19 research. PLOS Biology 19, e3001091. https://doi.org/10.1371/journal.pbio.3001091

Roesch, F., OhAinle, M., Emerman, M., 2018. A CRISPR screen for factors regulating SAMHD1 degradation identifies IFITMs as potent inhibitors of lentiviral particle delivery. Retrovirology 15, 26. https://doi.org/10.1186/s12977-018-0409-2

Romero-Brey, I., Bartenschlager, R., 2014. Membranous Replication Factories Induced by Plus-Strand RNA Viruses. Viruses 6, 2826–2857. https://doi.org/10.3390/v6072826

Roth-Cross, J.K., Martínez-Sobrido, L., Scott, E.P., García-Sastre, A., Weiss, S.R., 2007. Inhibition of the Alpha/Beta Interferon Response by Mouse Hepatitis Virus at Multiple Levels. Journal of Virology 81, 7189–7199. https://doi.org/10.1128/jvi.00013-07

Sa Ribero, M., Jouvenet, N., Dreux, M., Nisole, S., 2020. Interplay between SARS-CoV-2 and the type I interferon response. PLoS Pathog 16, e1008737. https://doi.org/10.1371/journal.ppat.1008737

Sanjana, N.E., Shalem, O., Zhang, F., 2014. Improved vectors and genome-wide libraries for CRISPR screening. Nat Methods 11, 783–784. https://doi.org/10.1038/nmeth.3047

Sarkar, S.N., Ghosh, A., Wang, H.W., Sung, S.S., Sen, G.C., 1999. The nature of the catalytic domain of 2'-5'-oligoadenylate synthetases. J Biol Chem 274, 25535–25542. https://doi.org/10.1074/jbc.274.36.25535

Saunders, N., Fernandez, I., Planchais, C., Michel, V., Rajah, M.M., Baquero Salazar, E., Postal, J., Porrot, F., Guivel-Benhassine, F., Blanc, C., Chauveau-Le Friec, G., Martin, A., Grzelak, L., Oktavia, R.M., Meola, A., Ahouzi, O., Hoover-Watson, H., Prot, M., Delaune, D., Cornelissen, M., Deijs, M., Meriaux, V., Mouquet, H., Simon-Lorière, E., van der Hoek, L., Lafaye, P., Rey, F., Buchrieser, J., Schwartz, O., 2023. TMPRSS2 is a functional receptor for human coronavirus HKU1. Nature 624, 207–214. https://doi.org/10.1038/s41586-023-06761-7

Schneider, W.M., Chevillotte, M.D., Rice, C.M., 2014. Interferon-Stimulated Genes: A Complex Web of Host Defenses. Annu. Rev. Immunol. 32, 513–545. https://doi.org/10.1146/annurev-immunol-032713-120231

Schneider, W.M., Luna, J.M., Hoffmann, H.-H., Sánchez-Rivera, F.J., Leal, A.A., Ashbrook, A.W., Pen, J.L., Ricardo-Lax, I., Michailidis, E., Peace, A., Stenzel, A.F., Lowe, S.W., MacDonald, M.R., Rice, C.M., Poirier, J.T., 2021. Genome-Scale Identification of SARS-CoV-2 and Pan-coronavirus Host Factor Networks. Cell 184, 120-132.e14. https://doi.org/10.1016/j.cell.2020.12.006

Schoggins, J.W., 2019. Interferon-Stimulated Genes: What Do They All Do? Annu Rev Virol 6, 567–584. https://doi.org/10.1146/annurev-virology-092818-015756

Schoggins, J.W., MacDuff, D.A., Imanaka, N., Gainey, M.D., Shrestha, B., Eitson, J.L., Mar, K.B., Richardson, R.B., Ratushny, A.V., Litvak, V., Dabelic, R.,

Manicassamy, B., Aitchison, J.D., Aderem, A., Elliott, R.M., García-Sastre, A., Racaniello, V., Snijder, E.J., Yokoyama, W.M., Diamond, M.S., Virgin, H.W., Rice, C.M., 2014. Pan-viral specificity of IFN-induced genes reveals new roles for cGAS in innate immunity. Nature 505, 691–695. https://doi.org/10.1038/nature12862

Schoggins, J.W., Wilson, S.J., Panis, M., Murphy, M.Y., Jones, C.T., Bieniasz, P., Rice, C.M., 2011. A diverse range of gene products are effectors of the type I interferon antiviral response. Nature 472, 481–485. https://doi.org/10.1038/nature09907

Schröder, H.C., Ugarković, D., Wenger, R., Reuter, P., Okamoto, T., Müller, W.E., 1990. Binding of Tat protein to TAR region of human immunodeficiency virus type 1 blocks TAR-mediated activation of (2'-5')oligoadenylate synthetase. AIDS Res Hum Retroviruses 6, 659–672. https://doi.org/10.1089/aid.1990.6.659

Shaw, A.E., Hughes, J., Gu, Q., Behdenna, A., Singer, J.B., Dennis, T., Orton, R.J., Varela, M., Gifford, R.J., Wilson, S.J., Palmarini, M., 2017. Fundamental properties of the mammalian innate immune system revealed by multispecies comparison of type I interferon responses. PLoS Biol 15, e2004086. https://doi.org/10.1371/journal.pbio.2004086

Shaw, B., Gatherer, D., 2023. Candidate historical events for the emergence of Human Coronavirus OC43: A critical reassessment of the molecular evidence. PLOS ONE 18, e0285481. https://doi.org/10.1371/journal.pone.0285481

Shen, L., Yang, Y., Ye, F., Liu, G., Desforges, M., Talbot, P.J., Tan, W., 2016. Safe and Sensitive Antiviral Screening Platform Based on Recombinant Human Coronavirus OC43 Expressing the Luciferase Reporter Gene. Antimicrob Agents Chemother 60, 5492–5503. https://doi.org/10.1128/AAC.00814-16

Shmerling, M., Chalik, M., Smorodinsky, N.I., Meeker, A., Roy, S., Sagi-Assif, O., Meshel, T., Danilevsky, A., Shomron, N., Levinger, S., Nishry, B., Baruchi, D., Shargorodsky, A., Ziv, R., Sarusi-Portuguez, A., Lahav, M., Ehrlich, M., Braschi, B., Bruford, E., Witz, I.P., Wreschner, D.H., 2022. LY6S, a New IFN-Inducible Human Member of the Ly6a Subfamily Expressed by Spleen Cells and Associated with Inflammation and Viral Resistance. Immunohorizons 6, 253–272. https://doi.org/10.4049/immunohorizons.2200018

Sievers, B.L., Cheng, M.T.K., Csiba, K., Meng, B., Gupta, R.K., 2024. SARS-CoV-2 and innate immunity: the good, the bad, and the "goldilocks." Cell Mol Immunol 21, 171–183. https://doi.org/10.1038/s41423-023-01104-y

Silverman, R.H., 2007. Viral Encounters with 2′,5′-Oligoadenylate Synthetase and RNase L during the Interferon Antiviral Response. Journal of Virology 81, 12720–12729. https://doi.org/10.1128/jvi.01471-07

Siu, Y.L., Teoh, K.T., Lo, J., Chan, C.M., Kien, F., Escriou, N., Tsao, S.W., Nicholls, J.M., Altmeyer, R., Peiris, J.S.M., Bruzzone, R., Nal, B., 2008. The M, E, and N Structural Proteins of the Severe Acute Respiratory Syndrome

Coronavirus Are Required for Efficient Assembly, Trafficking, and Release of Virus-Like Particles. J Virol 82, 11318–11330. https://doi.org/10.1128/JVI.01052-08

Sola, I., Almazán, F., Zúñiga, S., Enjuanes, L., 2015. Continuous and Discontinuous RNA Synthesis in Coronaviruses. Annu Rev Virol 2, 265–288. https://doi.org/10.1146/annurev-virology-100114-055218

Sorgeloos, F., Jha, B.K., Silverman, R.H., Michiels, T., 2013. Evasion of Antiviral Innate Immunity by Theiler's Virus L* Protein through Direct Inhibition of RNase L. PLOS Pathogens 9, e1003474. https://doi.org/10.1371/journal.ppat.1003474

Soveg, F.W., Schwerk, J., Gokhale, N.S., Cerosaletti, K., Smith, J.R., Pairo-Castineira, E., Kell, A.M., Forero, A., Zaver, S.A., Esser-Nobis, K., Roby, J.A., Hsiang, T.-Y., Ozarkar, S., Clingan, J.M., McAnarney, E.T., Stone, A.E., Malhotra, U., Speake, C., Perez, J., Balu, C., Allenspach, E.J., Hyde, J.L., Menachery, V.D., Sarkar, S.N., Woodward, J.J., Stetson, D.B., Baillie, J.K., Buckner, J.H., Gale, M., Jr, Savan, R., 2021. Endomembrane targeting of human OAS1 p46 augments antiviral activity. eLife 10, e71047. https://doi.org/10.7554/eLife.71047

Spence, J.S., He, R., Hoffmann, H.-H., Das, T., Thinon, E., Rice, C.M., Peng, T., Chandran, K., Hang, H.C., 2019. IFITM3 directly engages and shuttles incoming virus particles to lysosomes. Nat Chem Biol 15, 259–268. https://doi.org/10.1038/s41589-018-0213-2

Stertz, S., Reichelt, M., Spiegel, M., Kuri, T., Martínez-Sobrido, L., García-Sastre, A., Weber, F., Kochs, G., 2007. The intracellular sites of early replication and budding of SARS-coronavirus. Virology 361, 304–315. https://doi.org/10.1016/j.virol.2006.11.027

Takata, M.A., Gonçalves-Carneiro, D., Zang, T.M., Soll, S.J., York, A., Blanco-Melo, D., Bieniasz, P.D., 2017. CG dinucleotide suppression enables antiviral defence targeting non-self RNA. Nature 550, 124–127. https://doi.org/10.1038/nature24039

Talbot, H.K., Shepherd, B.E., Crowe, J.E.J., Griffin, M.R., Edwards, K.M., Podsiad, A.B., Tollefson, S.J., Wright, P.F., Williams, J.V., 2009. The Pediatric Burden of Human Coronaviruses Evaluated for Twenty Years. The Pediatric Infectious Disease Journal 28, 682. https://doi.org/10.1097/INF.0b013e31819d0d27

Thi Nhu Thao, T., Labroussaa, F., Ebert, N., V'kovski, P., Stalder, H., Portmann, J., Kelly, J., Steiner, S., Holwerda, M., Kratzel, A., Gultom, M., Schmied, K., Laloli, L., Hüsser, L., Wider, M., Pfaender, S., Hirt, D., Cippà, V., Crespo-Pomar, S., Schröder, S., Muth, D., Niemeyer, D., Corman, V.M., Müller, M.A., Drosten, C., Dijkman, R., Jores, J., Thiel, V., 2020. Rapid reconstruction of SARS-CoV-2 using a synthetic genomics platform. Nature 582, 561–565. https://doi.org/10.1038/s41586-020-2294-9

Thornbrough, J.M., Jha, B.K., Yount, B., Goldstein, S.A., Li, Y., Elliott, R., Sims, A.C., Baric, R.S., Silverman, R.H., Weiss, S.R., 2016. Middle East

Respiratory Syndrome Coronavirus NS4b Protein Inhibits Host RNase L Activation. mBio 7, e00258. https://doi.org/10.1128/mBio.00258-16

Torralba, S., Sojat, J., Hartmann, R., 2008. 2'-5' oligoadenylate synthetase shares active site architecture with the archaeal CCA-adding enzyme. Cell Mol Life Sci 65, 2613–2620. https://doi.org/10.1007/s00018-008-8164-5

Tyrrell, D. a. J., Bynoe, M.L., 1965. Cultivation of a Novel Type of Common-cold Virus in Organ Cultures. https://doi.org/10.1136/bmj.1.5448.1467

V'kovski, P., Kratzel, A., Steiner, S., Stalder, H., Thiel, V., 2021. Coronavirus biology and replication: implications for SARS-CoV-2. Nat Rev Microbiol 19, 155–170. https://doi.org/10.1038/s41579-020-00468-6

Wack, A., Terczyńska-Dyla, E., Hartmann, R., 2015. Guarding the frontiers: the biology of type III interferons. Nat Immunol 16, 802–809. https://doi.org/10.1038/ni.3212

Wang, M., Casey, P.J., 2016. Protein prenylation: unique fats make their mark on biology. Nat Rev Mol Cell Biol 17, 110–122. https://doi.org/10.1038/nrm.2015.11

Wang, Ruofan, Simoneau, C.R., Kulsuptrakul, J., Bouhaddou, M., Travisano, K.A., Hayashi, J.M., Carlson-Stevermer, J., Zengel, J.R., Richards, C.M., Fozouni, P., Oki, J., Rodriguez, L., Joehnk, B., Walcott, K., Holden, K., Sil, A., Carette, J.E., Krogan, N.J., Ott, M., Puschnik, A.S., 2021. Genetic Screens Identify Host Factors for SARS-CoV-2 and Common Cold Coronaviruses. Cell 184, 106-119.e14. https://doi.org/10.1016/j.cell.2020.12.004

Wang, Rong, Yang, X., Chang, M., Xue, Z., Wang, W., Bai, L., Zhao, S., Liu, E., 2021. ORF3a Protein of Severe Acute Respiratory Syndrome Coronavirus 2 Inhibits Interferon-Activated Janus Kinase/Signal Transducer and Activator of Transcription Signaling via Elevating Suppressor of Cytokine Signaling 1. Front. Microbiol. 12. https://doi.org/10.3389/fmicb.2021.752597

Wang, X., Hinson, E.R., Cresswell, P., 2007. The interferon-inducible protein viperin inhibits influenza virus release by perturbing lipid rafts. Cell Host Microbe 2, 96–105. https://doi.org/10.1016/j.chom.2007.06.009

WHO COVID-19 dashboard [WWW Document], 2025. . World Health Organisation. URL https://data.who.int/dashboards/covid19/cases (accessed 1.27.25).

Wickenhagen, A., Sugrue, E., Lytras, S., Kuchi, S., Noerenberg, M., Turnbull, M.L., Loney, C., Herder, V., Allan, J., Jarmson, I., Cameron-Ruiz, N., Varjak, M., Pinto, R.M., Lee, J.Y., Iselin, L., Palmalux, N., Stewart, D.G., Swingler, S., Greenwood, E.J.D., Crozier, T.W.M., Gu, Q., Davies, E.L., Clohisey, S., Wang, B., Trindade Maranhão Costa, F., Freire Santana, M., de Lima Ferreira, L.C., Murphy, L., Fawkes, A., Meynert, A., Grimes, G., ISARIC4C Investigators, Da Silva Filho, J.L., Marti, M., Hughes, J., Stanton, R.J., Wang, E.C.Y., Ho, A., Davis, I., Jarrett, R.F., Castello, A., Robertson, D.L., Semple, M.G., Openshaw, P.J.M., Palmarini, M., Lehner, P.J., Baillie, J.K., Rihn, S.J., Wilson, S.J., 2021. A prenylated dsRNA sensor protects against

severe COVID-19. Science 374, eabj3624. https://doi.org/10.1126/science.abj3624

Xia, H., Cao, Z., Xie, X., Zhang, X., Chen, J.Y.-C., Wang, H., Menachery, V.D., Rajsbaum, R., Shi, P.-Y., 2020. Evasion of Type I Interferon by SARS-CoV-2. Cell Reports 33. https://doi.org/10.1016/j.celrep.2020.108234

Xu, D., Jiang, W., Wu, L., Gaudet, R.G., Park, E.-S., Su, M., Cheppali, S.K., Cheemarla, N.R., Kumar, P., Uchil, P.D., Grover, J.R., Foxman, E.F., Brown, C.M., Stansfeld, P.J., Bewersdorf, J., Mothes, W., Karatekin, E., Wilen, C.B., MacMicking, J.D., 2023. PLSCR1 is a cell-autonomous defence factor against SARS-CoV-2 infection. Nature 619, 819–827. https://doi.org/10.1038/s41586-023-06322-y

Yadati, T., Houben, T., Bitorina, A., Shiri-Sverdlov, R., 2020. The Ins and Outs of Cathepsins: Physiological Function and Role in Disease Management. Cells 9, 1679. https://doi.org/10.3390/cells9071679

Yang, E., Li, M.M.H., 2020. All About the RNA: Interferon-Stimulated Genes That Interfere With Viral RNA Processes. Front. Immunol. 11. https://doi.org/10.3389/fimmu.2020.605024

Yang, Y., Zhang, L., Geng, H., Deng, Y., Huang, B., Guo, Y., Zhao, Z., Tan, W., 2013. The structural and accessory proteins M, ORF 4a, ORF 4b, and ORF 5 of Middle East respiratory syndrome coronavirus (MERS-CoV) are potent interferon antagonists. Protein & Cell 4, 951–961. https://doi.org/10.1007/s13238-013-3096-8

Zaki, A.M., van Boheemen, S., Bestebroer, T.M., Osterhaus, A.D.M.E., Fouchier, R.A.M., 2012. Isolation of a novel coronavirus from a man with pneumonia in Saudi Arabia. N Engl J Med 367, 1814–1820. https://doi.org/10.1056/NEJMoa1211721

Zang, R., Case, J.B., Yutuc, E., Ma, X., Shen, S., Gomez Castro, M.F., Liu, Z., Zeng, Q., Zhao, H., Son, J., Rothlauf, P.W., Kreutzberger, A.J.B., Hou, G., Zhang, H., Bose, S., Wang, X., Vahey, M.D., Mani, K., Griffiths, W.J., Kirchhausen, T., Fremont, D.H., Guo, H., Diwan, A., Wang, Y., Diamond, M.S., Whelan, S.P.J., Ding, S., 2020. Cholesterol 25-hydroxylase suppresses SARS-CoV-2 replication by blocking membrane fusion. Proceedings of the National Academy of Sciences 117, 32105–32113. https://doi.org/10.1073/pnas.2012197117

Zeberg, H., Pääbo, S., 2021. A genomic region associated with protection against severe COVID-19 is inherited from Neandertals. Proceedings of the National Academy of Sciences 118, e2026309118. https://doi.org/10.1073/pnas.2026309118

Zhang, Q., Bastard, P., Liu, Z., Le Pen, J., Moncada-Velez, M., Chen, J., Ogishi, M., Sabli, I.K.D., Hodeib, S., Korol, C., Rosain, J., Bilguvar, K., Ye, J., Bolze, A., Bigio, B., Yang, R., Arias, A.A., Zhou, Q., Zhang, Y., Onodi, F., Korniotis, S., Karpf, L., Philippot, Q., Chbihi, M., Bonnet-Madin, L., Dorgham, K., Smith, N., Schneider, W.M., Razooky, B.S., Hoffmann, H.-H., Michailidis, E., Moens, L., Han, J.E., Lorenzo, L., Bizien, L., Meade, P., Neehus, A.-L., Ugurbil, A.C., Corneau, A., Kerner, G., Zhang, P., Rapaport,

F., Seeleuthner, Y., Manry, J., Masson, C., Schmitt, Y., Schlüter, A., Le Voyer, T., Khan, T., Li, J., Fellay, J., Roussel, L., Shahrooei, M., Alosaimi, M.F., Mansouri, D., Al-Saud, H., Al-Mulla, F., Almourfi, F., Al-Muhsen, S.Z., Alsohime, F., Al Turki, S., Hasanato, R., van de Beek, D., Biondi, A., Bettini, L.R., D'Angio', M., Bonfanti, P., Imberti, L., Sottini, A., Paghera, S., Quiros-Roldan, E., Rossi, C., Oler, A.J., Tompkins, M.F., Alba, C., Vandernoot, I., Goffard, J.-C., Smits, G., Migeotte, I., Haerynck, F., Soler-Palacin, P., Martin-Nalda, A., Colobran, R., Morange, P.-E., Keles, S., Çölkesen, F., Ozcelik, T., Yasar, K.K., Senoglu, S., Karabela, Ş.N., Rodríguez-Gallego, C., Novelli, G., Hraiech, S., Tandjaoui-Lambiotte, Y., Duval, X., Laouénan, C., COVID-STORM Clinicians, COVID Clinicians, Imagine COVID Group, French COVID Cohort Study Group, CoV-Contact Cohort, Amsterdam UMC Covid-19 Biobank, COVID Human Genetic Effort, NIAID-USUHS/TAGC COVID Immunity Group, Snow, A.L., Dalgard, C.L., Milner, J.D., Vinh, D.C., Mogensen, T.H., Marr, N., Spaan, A.N., Boisson, B., Boisson-Dupuis, S., Bustamante, J., Puel, A., Ciancanelli, M.J., Meyts, I., Maniatis, T., Soumelis, V., Amara, A., Nussenzweig, M., García-Sastre, A., Krammer, F., Pujol, A., Duffy, D., Lifton, R.P., Zhang, S.-Y., Gorochov, G., Béziat, V., Jouanguy, E., Sancho-Shimizu, V., Rice, C.M., Abel, L., Notarangelo, L.D., Cobat, A., Su, H.C., Casanova, J.-L., 2020. Inborn errors of type I IFN immunity in patients with life-threatening COVID-19. Science 370, eabd4570. https://doi.org/10.1126/science.abd4570

Zhang, R., Wang, K., Ping, X., Yu, W., Qian, Z., Xiong, S., Sun, B., 2015. The ns12.9 Accessory Protein of Human Coronavirus OC43 Is a Viroporin Involved in Virion Morphogenesis and Pathogenesis. Journal of Virology 89, 11383–11395. https://doi.org/10.1128/jvi.01986-15

Zhang, Y., Hatziioannou, T., Zang, T., Braaten, D., Luban, J., Goff, S.P., Bieniasz, P.D., 2002. Envelope-Dependent, Cyclophilin-Independent Effects of Glycosaminoglycans on Human Immunodeficiency Virus Type 1 Attachment and Infection. J Virol 76, 6332–6343. https://doi.org/10.1128/JVI.76.12.6332-6343.2002

Zhang, Y., Yu, C., 2020. Prognostic characterization of OAS1/OAS2/OAS3/OASL in breast cancer. BMC Cancer 20, 575. https://doi.org/10.1186/s12885-020-07034-6

Zhao, L., Jha, B.K., Wu, A., Elliott, R., Ziebuhr, J., Gorbalenya, A.E., Silverman, R.H., Weiss, S.R., 2012. Antagonism of the interferon-induced OAS-RNase L pathway by murine coronavirus ns2 protein is required for virus replication and liver pathology. Cell Host Microbe 11, 607–616. https://doi.org/10.1016/j.chom.2012.04.011

Zhao, M., Wan, B., Li, H., He, J., Chen, X., Wang, L., Wang, Y., Xie, S., Qiao, S., Zhang, G., 2017. Porcine 2′, 5′-oligoadenylate synthetase 2 inhibits porcine reproductive and respiratory syndrome virus replication in vitro. Microbial Pathogenesis 111, 14–21. https://doi.org/10.1016/j.micpath.2017.08.011

Zhao, X., Guo, F., Liu, F., Cuconati, A., Chang, J., Block, T., Guo, J., 2014. Interferon induction of IFITM proteins promotes infection by human

coronavirus OC43. Proceedings of the National Academy of Sciences of the United States of America 111. https://doi.org/10.1073/pnas.1320856111

Zhao, X., Sehgal, M., Hou, Z., Cheng, J., Shu, S., Wu, S., Guo, F., Le Marchand, S.J., Lin, H., Chang, J., Guo, J.-T., 2018. Identification of Residues Controlling Restriction versus Enhancing Activities of IFITM Proteins on Entry of Human Coronaviruses. J Virol 92, e01535-17. https://doi.org/10.1128/JVI.01535-17

Zheng, S., Zhu, D., Lian, X., Liu, W., Cao, R., Chen, P., 2016. Porcine 2′, 5′-oligoadenylate synthetases inhibit Japanese encephalitis virus replication in vitro. Journal of Medical Virology 88, 760–768. https://doi.org/10.1002/jmv.24397

Zhong, X., Xie, T., Wang, S.-Y., Xu, Z.-S., Chi, X.-X., Lan, Q.-S., Xie, B.-W., Sun, Q.-L., Yuan, L., Lan, Q.-Y., Zhao, Z.-X., Pan, B.-R., Feng, H., Lu, L., Wang, Y.-Y., Wang, X., Dong, C., 2025. Alveolar macrophages critically control infection by seasonal human coronavirus OC43 to avoid severe pneumonia. Cell Reports 44. https://doi.org/10.1016/j.celrep.2025.115531

Zhou, H., Ji, J., Chen, X., Bi, Y., Li, J., Wang, Q., Hu, T., Song, H., Zhao, R., Chen, Y., Cui, M., Zhang, Y., Hughes, A.C., Holmes, E.C., Shi, W., 2021. Identification of novel bat coronaviruses sheds light on the evolutionary origins of SARS-CoV-2 and related viruses. Cell 184, 4380-4391.e14. https://doi.org/10.1016/j.cell.2021.06.008

Zhou, Z., Xue, Q., Wan, Y., Yang, Y., Wang, J., Hung, T., 2011. Lysosome-associated membrane glycoprotein 3 is involved in influenza A virus replication in human lung epithelial (A549) cells. Virol J 8, 384. https://doi.org/10.1186/1743-422X-8-384

Zhu, J., Zhang, Y., Ghosh, A., Cuevas, R.A., Forero, A., Dhar, J., Ibsen, M.S., Schmid-Burgk, J.L., Schmidt, T., Ganapathiraju, M.K., Fujita, T., Hartmann, R., Barik, S., Hornung, V., Coyne, C.B., Sarkar, S.N., 2014. Antiviral activity of human oligoadenylate synthetases-like (OASL) is mediated by enhancing retinoic acid-inducible gene I (RIG-I) signaling. Immunity 40, 936. https://doi.org/10.1016/j.immuni.2014.05.007

Zhu, N., Zhang, D., Wang, W., Li, X., Yang, B., Song, J., Zhao, X., Huang, B., Shi, W., Lu, R., Niu, P., Zhan, F., Ma, X., Wang, D., Xu, W., Wu, G., Gao, G.F., Tan, W., 2020. A Novel Coronavirus from Patients with Pneumonia in China, 2019. New England Journal of Medicine 382, 727–733. https://doi.org/10.1056/NEJMoa2001017

Zhu, Z., Fodor, E., Keown, J.R., 2023. A structural understanding of influenza virus genome replication. Trends in Microbiology 31, 308–319. https://doi.org/10.1016/j.tim.2022.09.015

Ziegler, T., Matikainen, S., Rönkkö, E., Österlund, P., Sillanpää, M., Sirén, J., Fagerlund, R., Immonen, M., Melén, K., Julkunen, I., 2005. Severe Acute Respiratory Syndrome Coronavirus Fails To Activate Cytokine-Mediated Innate Immune Responses in Cultured Human Monocyte-Derived Dendritic Cells. Journal of Virology 79, 13800–13805. https://doi.org/10.1128/jvi.79.21.13800-13805.2005

Zimmer, M.M., Kibe, A., Rand, U., Pekarek, L., Ye, L., Buck, S., Smyth, R.P., Cicin-Sain, L., Caliskan, N., 2021. The short isoform of the host antiviral protein ZAP acts as an inhibitor of SARS-CoV-2 programmed ribosomal frameshifting. Nat Commun 12, 7193. https://doi.org/10.1038/s41467-021-27431-0

Znaidia, M., Demeret, C., van der Werf, S., Komarova, A.V., 2022. Characterization of SARS-CoV-2 Evasion: Interferon Pathway and Therapeutic Options. Viruses 14, 1247. https://doi.org/10.3390/v14061247

Zoladek, J., El Kazzi, P., Caval, V., Vivet-Boudou, V., Cannac, M., Davies, E.L., Rossi, S., Bribes, I., Rouilly, L., Simonin, Y., Jouvenet, N., Decroly, E., Paillart, J.-C., Wilson, S.J., Nisole, S., 2024. A specific domain within the 3′ untranslated region of Usutu virus confers resistance to the exonuclease ISG20. Nat Commun 15, 8528. https://doi.org/10.1038/s41467-024-52870-w

Züst, R., Cervantes-Barragán, L., Kuri, T., Blakqori, G., Weber, F., Ludewig, B., Thiel, V., 2007. Coronavirus Non-Structural Protein 1 Is a Major Pathogenicity Factor: Implications for the Rational Design of Coronavirus Vaccines. PLOS Pathogens 3, e109. https://doi.org/10.1371/journal.ppat.0030109